# Observational Studies of Extreme Stellar Magnetic Activities: Spots, Flares, and Mass Ejections

**Kosuke Namekata**

A thesis presented for the degree of

Doctor of Science


Department of Astronomy

Kyoto University

Japan

December 2020

# Observational Studies of Extreme Stellar Magnetic Activities: Spots, Flares, and Mass Ejections

**Kosuke Namekata**

**Abstract**

Solar and stellar flares are sudden energetic explosions on the surfaces and occur by releasing the magnetic energy stored around the spots. Solar flares often produce X-ray/UV radiations, high-energy particles, and mass ejections, and they directly affect the Earth's environment and human technologies. Young and cool M-K dwarfs having gigantic spots often produce larger "superflares", possibly having great impacts on the exoplanet atmosphere. Moreover, superflares have been also observed on the old, slowly-rotating solar-type (G-type main-sequence) stars, which evokes a possibility of superflares on the current Sun. In this context, there is an increasing interest in the questions of what are the occurrence conditions of stellar superflares and how severely the stellar magnetic activities can affect the habitability and origins of lives on planets. However, fundamental processes and properties of such extreme stellar magnetic activities have been poorly understood. The main aim of this thesis is to investigate whether they can be explained by an extension of the solar physics, especially for the following three different topics: gigantic star spots (Chapters 2 and 3), stellar superflares (Chapters 4 and 5), and stellar mass ejections (Chapter 6).

Chapters 2 and 3 treat the occurrence mechanism of gigantic star spots on solar-type stars, which can trigger superflares. It is found that the emergence/decay rates of gigantic star spots correspond to those extrapolated from empirical and theoretical MHD models. This suggests common emergence and decay processes of large-scale star spots and small-scale sunspots. In contrast, variation rates of some of the gigantic star spots are a little smaller than predictions from solar relations (Chapter 2), which can come from the successive emergence of many unresolved spots. Gigantic star spots survive for 100 days – 1 yr, and this indicates that the extreme space weather events can continue for such long periods.

Chapter 4 reports the occurrence mechanism of stellar superflares on solar-type stars. The flare duration $\tau$ as a function of flare energy $E$ in the formula of $\tau \propto E^{\alpha}$ (as a proxy of energy release rates per time) is compared between solar flares and stellar superflares in white-light bands. The power-law index $\alpha \sim 1/3$ of stellar superflares is almost equal to that of solar flares, while the absolute values of the superflare durations are 10 times shorter than solar ones when compared at the same flare energy. The common power-law index can be explained by the magnetic reconnection model, which indicates a common flare mechanism of solar and stellar flares. This theory

also predicts that the magnetic field strength of superflares is $\sim$3 times stronger than that of solar flares.

Chapter 5 is dedicated to the radiation/heating mechanism of stellar superflares on an active M-dwarf AD Leonis. A superflare ($\sim$20 times the largest solar flares) was successfully detected by ground-based spectroscopy and photometry. It showed H$\alpha$ line broadenings and simultaneous intense white-light emission in the impulsive phase. This can be produced by the chromospheric regions compressed by non-thermal electrons. According to radiative hydrodynamic simulations, the superflare requires non-thermal high-energy electrons with the total flux of $10^{12}$ erg s$^{-1}$ cm$^{-2}$ and hard spectra of $\delta$ = 3 (d$N$/d$E$ $\propto$ $E^{-\delta}$, where $N$ is the number of electrons), which is much higher than the solar cases. It is also indicated that the heating changes to weak and/or thermal heating in the decay phase.

Chapter 6 describes the detection of stellar mass ejection from superflares. Our optical spectroscopic observation of the young solar-type star EK Draconis provided clear evidence of a stellar mass ejection associated with a superflare on a solar-type star for the first time. After the superflare ($\sim$20 times the largest solar flares), a blue-shifted hydrogen absorption component with a velocity of $-510 \pm 120$ km s$^{-1}$ appeared. The temporal changes in the spectra closely resemble that of solar mass ejections. The ejected mass of $1.1^{+4.2}_{-0.9} \times 10^{18}$ g is much larger than solar largest values ($\sim 10^{16}$ g) but consistent with the solar flare-energy/ejected-mass relation. These discoveries imply that a huge stellar mass ejection did occur in the same way as solar ones.

Based on a series of these results, I concluded that the extreme stellar magnetic activities analyzed in this thesis can occur in the same way as solar events, if different values of physical quantities are taken into account. The fundamental physical quantities of such extreme stellar events are found to be much larger than those of the largest solar events and can be used as initial conditions for numerical modelings. Moreover, the observational results presented in this thesis can improve researches in exoplanets, and possibly can provide a proxy for a possible extreme event on the Sun as follows: Chapters 2 and 3 provide information on the duration of the extreme space weather; Chapters 4 and 5 suggest the impulsive optical (and possibly X-ray/UV) radiations of superflares; and Chapter 6 shows the first observational example of stellar mass ejections on the young Sun. The detection of mass ejections also suggests significant mass loss of the past Sun, which is important for the general stellar evolution theory. In the future, multi-wavelength observations of stellar flares would become more and more important, and the approaches presented in this thesis will be helpful for future studies.

Supervisors: Kazunari Shibata and Daisaku Nogami

# Acknowledgements

I owe thanks to individuals who directly and indirectly contributed to this dissertation over the past five years. First of all, I would like to express my gratitude to my supervisors Prof. Kazunari Shibata and Prof. Daisaku Nogami. I could not finish my Ph.D. without a lot of helpful comments provided by them. Prof. Kazunari Shibata have kindly educated me and always encouraged me. They gave me an opportunity to use the Seimei Telescope for its initial observational periods. In addition, I would like to thank Prof. Hiroyuki Maehara, Prof. Satoshi Honda, Dr. Yuta Notsu, Prof. Adam F. Kowalski, Dr. James R. A. Davenport, Dr. Shin Toriumi, Prof. Kyoko Watanabe, Prof. Ayumi Asai, Prof. Kiyoshi Ichimoto, Kai Ikuta, Takahito Sakaue, Ryo Sasaki, and Hiroki Kawai for the insightful comments on my researches that significantly improved my studies. I also would like to thank all of my co-authors in my refereed papers.

I would like to thank all the members of Kwasan, Hida, and Okayama Observatories and the Department of Astronomy. Some of the data presented here were obtained at the Okayama Observatory of Kyoto University. Some of the data presented here were obtained at the Hida Observatory of Kyoto University. This work and operations of OISTER were supported by the Optical and Near-infrared Astronomy Inter-University Cooperation Program and the Grants-in-Aid of the Ministry of Education.

This work is supported by JSPS KAKENHI grant numbers JP18J20048. This work is also supported by the JSPS Overseas Challenge Program for Young Researchers.

Finally, I thank my supportive family for the constant encouragement that always empowered me.

# Contents

# List of Figures

# List of Tables

CHAPTER 1

# General introduction

## 1.1 Solar magnetic activity

### 1.1.1 Overview

The Sun is the nearest star and a hot sphere held by the self-gravitation and the nuclear reactions in the core. The solar interior is divided into the central radiative core and surface convective zone (Figure 1.1). The surface atmosphere above the convective zone consists of stratified plasma layers of the lower photosphere ($\sim$6000 K), middle chromosphere ($\sim 10^4$ K), and outer corona ($\sim 10^6$ K) as in Figure 1.1 (Rutten, 2003; Leenaarts, 2020). The solar age is known as 46 Gyr and is located at the middle age of its whole lifetime according to the stellar evolution theory (Güdel, 2007). The Sun has provided heat with the Earth for such a very long time and is highly related to the origins and maintenance of life on the early and current Earth. In this context, one of our motivations to study the Sun is to know how the Sun has influenced the early, current, and future Earth's environment and the human life.

Moreover, the Sun has a different aspect as a laboratory of magnetized plasma (Tajima & Shibata, 2002). Plasmas are everywhere in the universe and their behaviors are very complicated especially if there are magnetic fields. Since the Sun can be spatially resolved and is easy to observe, the solar observation has a very long history ($\sim$400 yr; Usoskin, 2017). It has provided the fundamental understandings of the magneto-hydrodynamics (MHD) of plasma. Although the physical scales and conditions of solar phenomena are quite limited compared to those of all kinds of phenomena in the universe, the scale-freeness of MHD model has enabled the application of solar physics to the other astronomical objects so far (e.g. magnetically active stars). Therefore, the fundamental understanding of magnetized plasma is one of the main goals in the solar community.

In this section, I will introduce the basic solar physics especially for solar flares, sunspots,

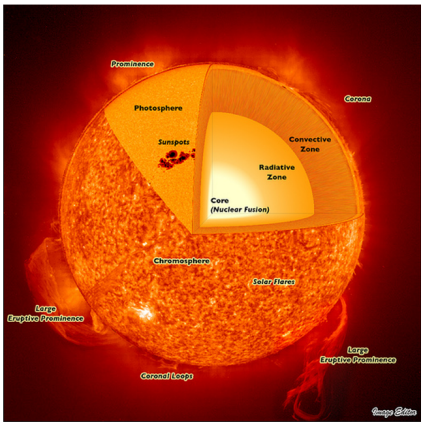


https://sites.ualberta.ca/~pogosyan/teaching/ASTRO_122/lect8/lecture8.html

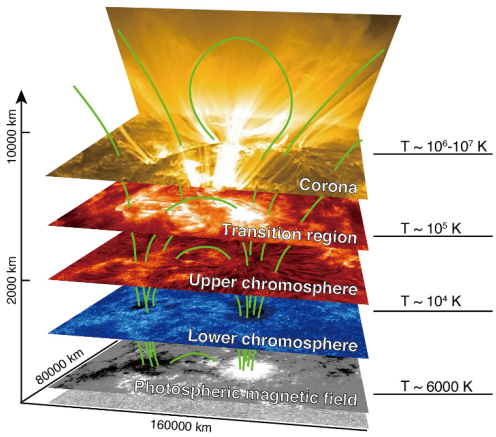


https://solar-c.nao.ac.jp/en/science.html

Figure 1.1: The schematic pictures of solar structure. Left: From the solar interior to the outer atmosphere (`https://sites.ualberta.ca/~pogosyan/teaching/ASTRO_122/lect8/lecture8.html`). Right: Surface structure from photosphere to corona (`https://solar-c.nao.ac.jp/en/science.html`). See also Figure 1.5 for solar active regions in different wavebands.

and mass ejections, which is helpful to understand stellar events introduced in Section 1.2.

### 1.1.2 Solar flares

**- Observations -**

Solar flares are phenomena that produce abrupt brightening on the solar surface (Shibata & Magara, 2011). The brightening of solar flares was firstly observed by Carrington (1859) with the visible continuum in 1859. The Carrington event finally produced one of the largest geomagnetic storms on the Earth that caused strong aurora and telegraph system troubles on the grounds (Usoskin, 2017).

Recent solar observations reveal that the released energy of solar flares is ranging from $\sim 10^{28}$ to $10^{32}$ erg, and the duration is ranging from minutes to hours (Benz, 2017). This is the most energetic phenomena in the solar system. The released energy takes various forms such as radiative, kinetic, thermal, and non-thermal energy (Aschwanden et al., 2017; Emslie et al., 2012). The radiations are observed across a wide wavelength range such as radio, visible, X-rays, and gamma rays as in Figure 1.2 (e.g. Kane, 1974; Benz, 2017).

Solar flares are known to often occur around sunspots, indicating that the magnetic field plays an important role in solar flares. They show several observational features as follows

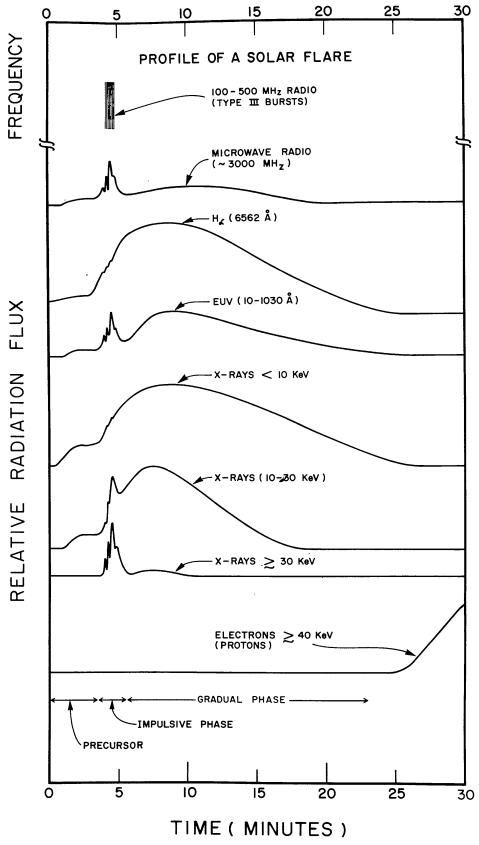


Figure 1.2: Multi-wavelength light curves of a typical solar flare. Radio to X-ray light curves are shown in the same panel. The light curves are usually divided into the initial impulsive phase and subsequent gradual phase. From (Kane, 1974).

(see Figure 1.3). During flares, expanding two ribbons are observed across the magnetic neutral lines of sunspots in chromospheric emissions such as H$\alpha$ and visible continuum (e.g. Svestka, 1976; Zirin & Liggett, 1987, see Figure 1.3B). In addition, bright soft X-ray arcades are observed in the corona above the two ribbons (Figure 1.3A), and cusp-like arcades are sometimes observed in the gradual phase of the long-duration flares (Tsuneta et al., 1991; Tsuneta, 1996; Forbes & Acton, 1996). Bright hard X-ray points are also observed above the top of the flaring soft X-ray loops (Masuda et al., 1994). A theoretical model of solar flares has been phenomenologically developed so that it can explain the above observational features (Shibata & Magara, 2011).

**- Theory -**

Nowadays the solar flares are believed to be caused by energy release through the magnetic reconnection (reconnection of the anti-parallel magnetic field lines) in the corona (e.g. Priest, 1981; Shibata & Magara, 2011, see Figure 1.3C), although a complete understanding of the relevant physics is still on the way. In the magnetic reconnection model,

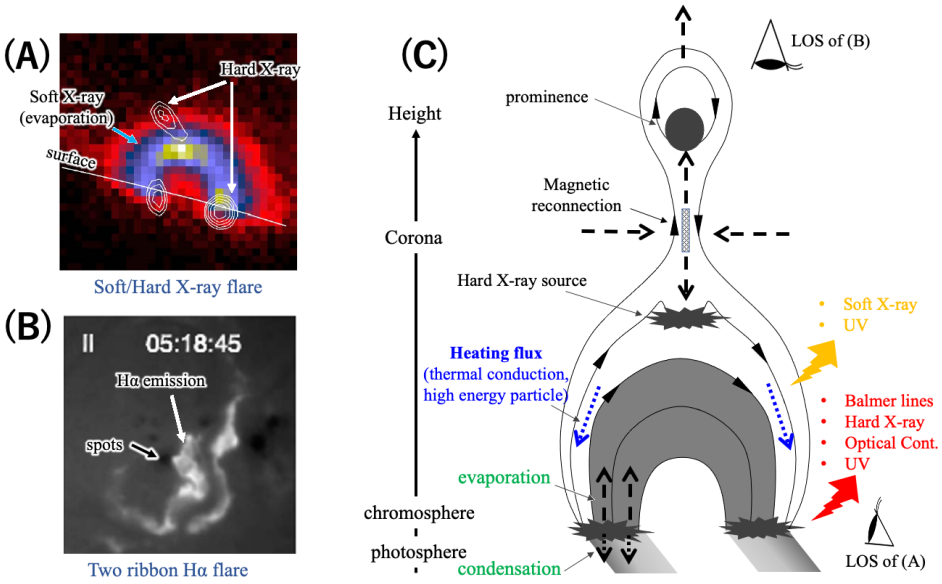


Figure 1.3: Observations and theoretical understandings of solar flares. (A) Soft and hard X-ray images of an impulsive solar flare on the solar limb (Masuda et al., 1994). The loop-shape soft X-ray source and the loop-top/foot-points hard X-ray sources are simultaneously plotted. (B) Two ribbon solar flare on the solar disk observed in H$\alpha$ (Asai et al., 2004). (C) Schematic picture of solar flares. The lines with arrows are the magnetic field connected to the photosphere, and the horizontal is the height of solar atmosphere. The filled regions with gray color indicates the magnetic loop filled with dense evaporated plasma observed by soft X-ray. The line of sight directions of panel images (A) and (B) are also indicated here.

the energy release timescales is considered to be proportional to the Alfvén time ($\tau_A$):

$$t_{\rm flare} \sim \tau_A / M_A \propto L / v_A / M_A, \tag{1.1}$$

where L is the loop length scale, $v_A$ is the Alfvén velocity, and $M_A$ is the dimensionless reconnection rate. The released energy can be characterized as stored magnetic energy:

$$E_{\rm flare} \sim f E_{\rm mag} \sim f (B^2/8\pi) L^3 \sim 10^{32} \left(\frac{f}{0.1}\right) \left(\frac{B}{10^3\,{\rm G}}\right)^2 \left(\frac{L}{3\times10^9\,{\rm cm}}\right)^3 {\rm erg}, \tag{1.2}$$

where $f$ is a fraction of energy released by a flare, B is the magnetic field strength.

The process of solar flares can be simply divided into three important factors: “energy build-up”, “energy release”, and “energy transport” (see Shibata & Magara, 2011). The flare process starts with the emergence of magnetic field into the surface, which carries magnetic energy from the interior to the atmosphere (“energy build-up”). Then, the rapid release of the magnetic energy accumulated via the energy build-up process occurs via magnetic reconnection (“energy release”). In the standard theory, the released energies are transported from the corona to the lower atmosphere by non-thermal high energy particles

and thermal conduction ("energy transport"). The high energy electrons injected to the chromosphere have been estimated to have the total flux of $10^{10-11}$ erg $s^{-1}$ $cm^{-2}$ and hard spectra of $\delta$ = 3-7 ($dN/dE \propto E^{-\delta}$, where $N$ is a number of electrons). As a result of the energy injection to the chromosphere, upward chromospheric evaporations and downward chromospheric condensations are thought to occur on the principle of action and reaction (e.g. Fisher et al., 1985). The chromospheric evaporation plays a fundamental role in soft X-ray emissions (Hirayama, 1974). The heat flux reaches the upper chromosphere and increases the gas pressure to produce an upflow toward the corona against the gravity. The upflows are observed as the blue shift of the coronal lines, and magnetic loops filled with the evaporated hot plasma ($>$ 10 MK) form the soft X-ray arcades (Fisher et al., 1984; Chen & Ding, 2010). As a response to the upward evaporation, the chromosphere is pushed downward by the high pressure. Because the temperature of the compressed plasma cannot increase owing to the radiation cooling, the density increases to form chromospheric condensation. The chromospheric condensation radiates the bright chromospheric emissions (e.g. Balmer series, Ca, Mg lines, visible continuum, and so on) showing red-shifted spectral shape (Ichimoto & Kurokawa, 1984).

One-dimensional hydrodynamic simulations successfully reproduce the picture of the bidirectional flows (Nagai, 1980; Nagai & Emslie, 1984; Fisher & Hawley, 1990; Allred et al., 2005, 2006, 2015; Kowalski et al., 2017). Later, two-dimensional magnetohydrodynamic (MHD) simulations also reproduced chromospheric evaporations driven by thermal conduction (Yokoyama & Shibata, 1998; Takasao et al., 2015). These pictures of solar flares are - not completely, but - relatively well-established by the recent space observations and numerical simulations, although there remain some unsolved problems such as the particle accelerations (Zharkova et al., 2011; Oka et al., 2010; Shibata & Magara, 2011), white-light flares (Kretzschmar, 2011; Watanabe et al., 2017; Martínez Oliveros et al., 2012; Machado et al., 1989), and so on. The established magnetic reconnection model has been applied not only to the micro-scale solar flare (called "microflare" or "nanoflare") but also to the various kinds of stellar and astronomical phenomena (e.g. stellar flares), and the examples are shown in the following sections.

The solar flares sometimes accompany upward magnetized-plasma ejections which consist of hot coronal mass ejections (CMEs, or CME leading edges; Figure 1.4A), and cool, dense prominence eruptions (which later become CME cores; Figure 1.4A). The plasma is gradually accelerated by the magnetic forces (e.g. Lorenz forces and/or reconnection outflows) in the corona even from before the flares are triggered (see Figure 1.3C, 1.4B for the model; Chen, 2011; Webb & Howard, 2012). The acceleration mechanism is not completely understood (Chen, 2011). The CMEs with high velocity travel through the interplanetary space and sometimes reach the Earth and the other planets, which sometimes severely affect the environments. The CMEs are also getting more and more attention in

stellar observations and the solar observations can be a clue to explore the stellar CMEs (see Section 1.2.5) The detailed effects on the Earth environments are summarized in the following sections.

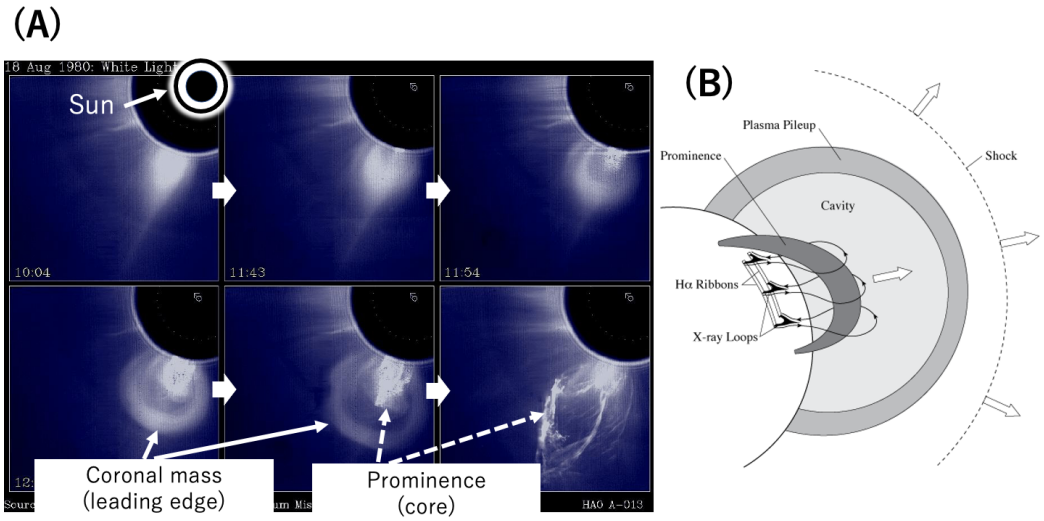


Figure 1.4: Observations and theoretical understandings of CME. (A) Temporal evolution of coronal mass ejections (CMEs) observed with the white-light coronagraph (van Driel-Gesztelyi & Culhane, 2009, `https://www.windows2universe.org/sun/images/aug1980cme.jpg`). The CMEs consist of the CME edges, cavity, and cores (∼prominences or filaments). (B) Schematic picture of solar CMEs. From Forbes (2000).

**- The effect on the Earth environment -**

The effect of solar activities on the Earth and nearby interplanetary space are often called “space weather" (see Schwenn, 2006; Pulkkinen, 2007, for review). While the Sun provides the heat and light necessary for our lives on the Earth, it also endangers the space environments and our human technologies in the form of irradiance of (1) X-ray and extreme ultraviolet radiations (hereafter, referred to as “XUV” in this thesis), (2) solar energetic particles (SEPs), and (3) magnetic storms via magnetized plasma ejections (CMEs).

Electromagnetic waves cause a photochemical reaction with the Earth’s atmosphere, and the upper part of the atmosphere is ionized to form the ionosphere. In addition, the mass ejections and solar wind exhibit a complicated aspect by interacting with the earth’s magnetic field and the ionosphere. When the magnetic field in the solar wind faces south, magnetic recombination occurs between the solar wind and the earth’s magnetosphere, and the energy of the solar wind reaches near the earth. In particular, solar flares and CMEs, and solar winds emitted from coronal holes have a significant impact on the earth.

(1) XUV increases the electron density in the Earth’s atmosphere, which significantly

hinders the use of communications, broadcasting, the satellite positioning, and the air traffic control radar (e.g. Schrijver et al., 2015). (2) Subsequently, SEPs can cause human exposure during manned activities in outer space and even at the altitude of international aircraft than on the ground (e.g. Schrijver et al., 2015). (3) Due to the influence of CME, the artificial satellite may be charged, resulting in functional deterioration or suspension of operation. In addition, a current is generated in the magnetosphere and the ionosphere to generate a large-scale aurora (e.g. Huttunen & Koskinen, 2004; Hayakawa et al., 2017), and an underground induced current is generated, which affects the power transmission network and the power supply system.

Actually, the magnetic storms produced by the large-arcade solar flare in 1989 severely affect the social infrastructure. For example, in the Quebec state, Canada, the power grid of an electric power company was destroyed and seriously damaged, and the communication of the US meteorological satellite was stopped (Allen et al., 1989; Rich & Denig, 1992).

### 1.1.3 Sunspots - a proxy of solar dynamo and an origin of solar flares -

**- Observations and theory -**

Sunspots are the most visible manifestations of solar magnetic fields, and are known as dark regions on the surfaces (Fig 1.5A; see Solanki, 2003, for review). The sunspots are observed by visible light and have been observed for 400 years by ground optical telescopes and naked eyes (see Usoskin, 2017, for review). Hale (1908) found the evidence of the magnetic field in the sunspots, and nowadays sunspots are well-known as a cross-section of the strong magnetic flux (1000$\sim$1500 G at average; Livingston, 2002) on the solar surfaces while the averaged magnetic field on the Sun is $\sim$5 G. The strong magnetic field suppresses the convective heating inside the large magnetic flux tube, and decreases the temperature ($\sim$4000 K, called “umbra") compared to the quiet regions ($\sim$6000 K); thus the spots look dark (see Solanki et al., 1993). The typical sunspots consist of a pair of two or more dark regions as in Fig 1.5A which have opposite magnetic polarities (therefore, sunspots are often called “sunspot group"). This means that the magnetic field of sunspots has dipole components whose edges are connected to the interior.

The sunspot has a diverse surface area ranging from a few to 6000 of millions of solar hemisphere (hereafter we call millions of solar hemisphere “MSH" where $10^6$ MSH = solar hemispheric area; the maximum area of 6000 MSH means 0.6 % of solar hemisphere = $1.8\times10^{20}$ cm$^2$; Aulanier et al., 2013; Toriumi et al., 2017; Hayakawa et al., 2017). The larger sunspots more rarely appear compared to smaller ones (Bogdan et al., 1988; Maehara et al., 2017). For example, large sunspots with the area of a few times 1000 MSH appear only once in about 10 years, whereas small ones with 10 - 100 MSH can be seen 200 - 300 times in one year on average.

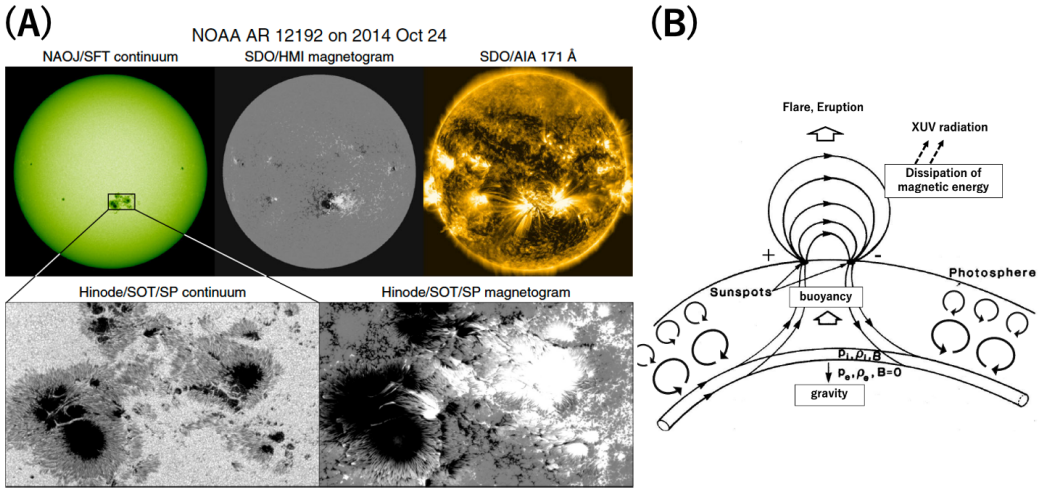


Figure 1.5: Observations and theoretical understandings of sunspots. (A) Observations of solar active regions and sunspots. Upper panels show the continuum, magnetogram, and 171 Å EUV images of the whole Sun and lower panels show the continuum and magnetogram images of an active region 12192 on 2014 Oct 24. From Toriumi & Wang (2019). (B) Schematic picture of the formations of sunspots and active regions. In the panel, the bottom indicates the solar interior where the magnetic fluxes of spots are generated by the dynamo process. The magnetic fluxes emerge to the surface by the magnetic buoyancy and form the sunspots and XUV-bright active regions. The figure is taken from Tajima & Shibata (2002). See also Figure 1.1 for visibility of active region in different wavebands.

The magnetic fluxes of sunspots are now believed to emerge from the deep convection zone to the solar surface thanks to the magnetic buoyancy and convection (see Fig 1.5B; e.g. Parker, 1955; Cheung & Isobe, 2014). This was confirmed by the time-resolved 2D observations of surface magnetic fields showing the emergence of the dipole magnetic field. It takes typically hours to days for sunspot formations ($<$ 5 days; Harvey & Zwaan, 1993), while the spot decay spends longer periods, typically weeks to months (Hathaway & Choudhary, 2008).

The occurrence frequency and locations of sunspots are known to show unique cyclic features with the period of 11 years (see Figure 1.6; Harvey, 1992, called “11-year cycle"), as firstly discovered in 1843. There is no single sunspot in the activity minimum, while large sunspots are commonly seen around the maxima. The appearance is usually restricted to the latitudinal belts from 5° to 40° on each side of the solar equator (see Figure 1.6). The typical latitudes largely change within one solar activity cycle: from high latitude to low latitude (Carrington, 1858). The sunspot typically has leading (West-side) and following (East-side) spots with opposite polarities, but the directions of magnetic fields are opposite

for the north and south hemispheres (Hale et al., 1919). Moreover, the polarities become inverse in the next 11-year cycle. These 11-year cyclic of sunspots have provided a key to understand the generation mechanism of large magnetic flux inside the Sun (called solar “dynamo"). For now, the so-called flux-transport dynamo has been proposed for the solar dynamo process (e.g. Dikpati & Charbonneau, 1999), although it is not complete. A review is given by Solanki (2003).

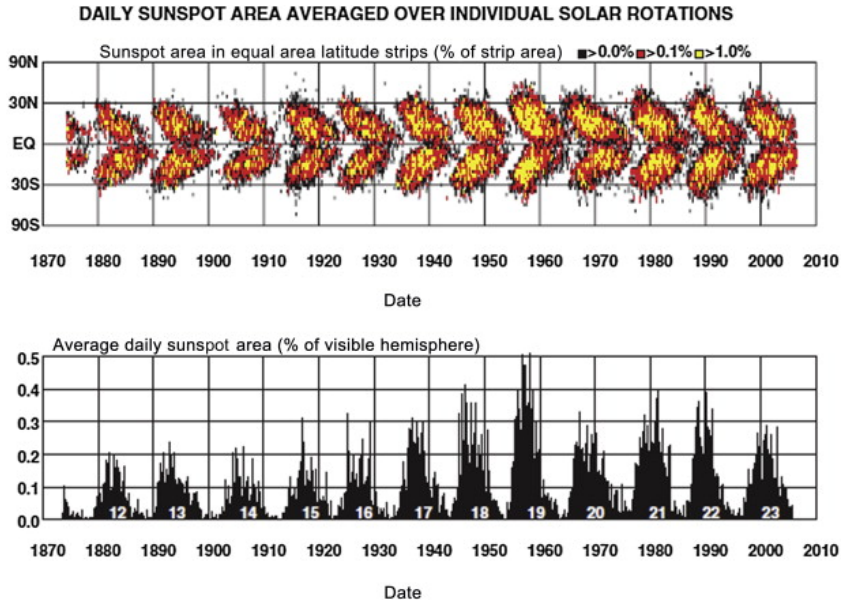


Figure 1.6: Long-term sunspot observations and the 11-year cycles (D. Hathaway, Solar Cycle Science; see `http://www.solarcyclescience.com/solarcycle.html`). Upper: Locations and area of sunspot emergence (known as “Butterfly diagram"). Lower: Daily sunspot area in the unit of % of visible hemisphere.

**- An origin of solar flares -**

Historically, magnetic fields of sunspots were discovered after the first solar flares are observed (Carrington, 1859; Hodgson, 1859). After the finding, the role of magnetic field in solar activity has been investigated extensively. Later, the bright soft X-ray regions are found to be well correlated with sunspots (Hildner et al., 1976). It is now widely accepted that the magnetic field of sunspots provides the main energy source of solar activity, such as solar flares and XUV radiation (see Figure 1.5A). The flare energy and spot area ($\sim$total magnetic energy) are found to be correlated with each other (see Figure 1.7; Sammis et al., 2000), and the upper limit of flare energy can be explained by the magnetic field stored in the sunspots, indicating that sunspots (and active regions) are the origins of the solar flares (Shibata et al., 2013).

We know there are flare-productive and flare-quiet sunspots and sunspots with very complex features (e.g. $\delta$-type spots) show larger flare frequently (see Figure 1.7; e.g. Sammis

et al., 2000). However, the occurrence conditions of solar flares on a given sunspot are not completely solved (Toriumi & Wang, 2019). Recently, the study of solar flare prediction have been intensively conducted based on the surface magnetic field distributions and the extrapolations of the coronal magnetic fields (e.g. Kusano et al., 2020).

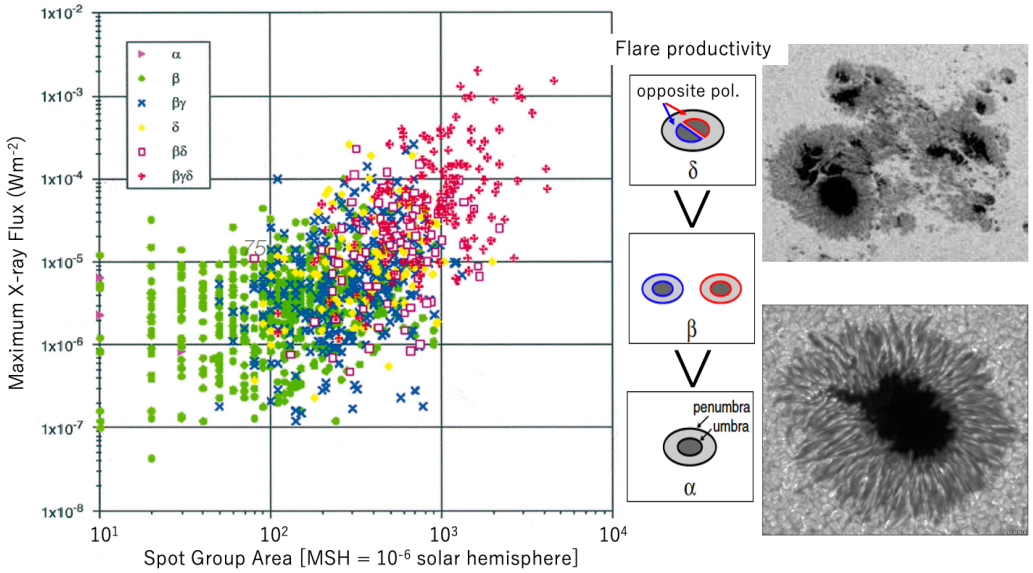


Figure 1.7: Comparison between maximum soft X-ray flux of solar flares and area of sunspot groups (in the unit of solar hemisphere) causing the solar flares. From Sammis et al. (2000). The colors and symbols indicates the complexity of sunspot shape (e.g. simple $\sim \alpha < \beta < \delta \sim$ complex). Note that the values of horizontal axis in the original figure have mistakes (Sammis et al., 2000), and they are revised in this panel. The complex sunspots are known to be flare-productive. Right is the schematic picture of sunspot classifications, and examples of simple and complex sunspots. Schematic pictures are taken from Toriumi & Wang (2019)

## 1.2 Stellar magnetic activity

### 1.2.1 Overview - why do we study stars? -

Magnetic activities explained in the preceding solar section are also observed in other stars, such as M-F dwarfs, young stellar objects, binary systems, and evolved giant stars. Figure 1.8A shows the stars that show stellar flares in the HR diagram (Van Doorsselaere et al., 2017). These flaring stars are expected to have the surface convective layers that generate the large magnetic fields. The magnetic field on those active stars has been well known via the Zeeman splitting observations (Johns-Krull & Valenti, 1996). The stellar phenomena on various types of stars are expected to share the same underlying process as

solar phenomena if we take into account the scale-freeness of MHD (Brun & Browning, 2017). However, many stars show much higher – or much lower – magnetic activity than the Sun, some of which have not been fully understood, even by using the knowledge of modern solar physics (Strassmeier, 2009; Wright et al., 2011; Maehara et al., 2012).

For example, it is known that rapidly-rotating stars show higher X-ray coronal emissions and the unexpected X-ray saturation (the rotation-activity relation in Figure 1.8B; Wright et al., 2011). According to the stellar rotational evolution of magnetic stars, the rotation periods ($P_{\rm rot}$) increase as the stellar ages ($t_{\rm age}$) increase via the magnetic breaking (cf. the gyrochronology relation of solar-type star, $P_{\rm rot} \propto (t_{\rm age})^{0.6}$; Ayres, 1997). Therefore, Figure 1.8B means that stellar activity decreases as a function of stellar ages, and this activity-age relation is consistent with the current solar activity. The consistency may indicate that the same underlying process is working for younger stars, but the activity evolution and the X-ray saturation is poorly understood.

The comparison between solar and stellar magnetic activities will be able to bridge the solar physics to stellar physics. I believe that the solar-stellar connections will be able to reveal the important astronomical questions on “Is our Sun special or normal in this universe?" (to know the Sun from stars) and “How do our solar-plasma physics have a universality or diversity?" (to know stars from the Sun). In the following, I will introduce important observations and history of stellar extreme magnetic activities, especially stellar flares (Section 1.2.2), star spots (Section 1.2.3), and stellar mass ejections (Section 1.2.4). These phenomena are often observed on the Sun, while the understandings are lacking in the case of active stars.

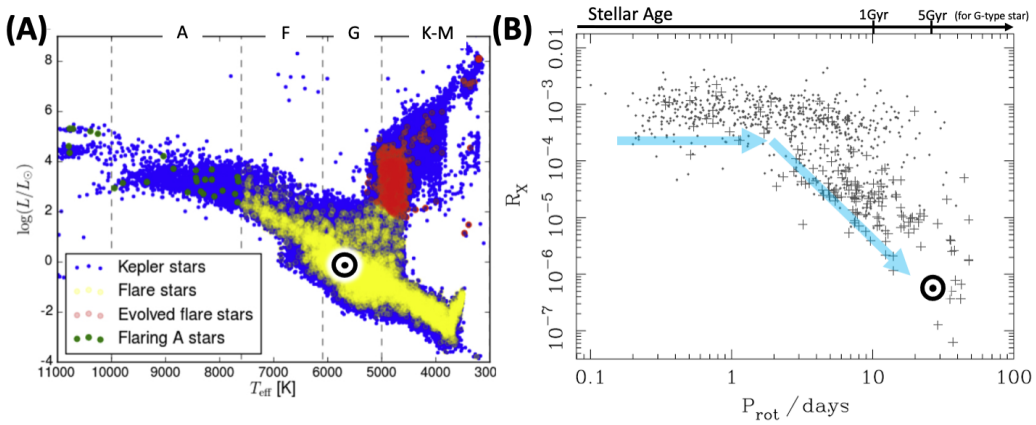


Figure 1.8: Magnetically active stars on various kinds of stars. (A) Flare stars on the HR diagram in *Kepler* field. From Van Doorsselaere et al. (2017). (B) Activity-rotation relation for FGKM-type stars. Horizontal axis indicates X-ray to bolometric luminosity ratio. Binary stars are shown as plus symbols, and the Sun with a solar symbol. From Wright et al. (2011).

### 1.2.2 Stellar flares

By solar analogy (cf. Section 1.1.2), other magnetically-active stars are known to show stellar flares. The first stellar flare event was seemingly found in Carina as a rapid enhancement of the luminosity (Hertzsprung, 1924). Since then, stellar flares are often observed in radio, visible, and X-ray ranges. Young T-tauri stars (Koyama et al., 1996; Benz & Güdel, 2010), M-type stars (e.g. Hawley & Fisher, 1992; Kowalski et al., 2013), and RS CVn-type binary stars (Walter & Bowyer, 1981), often show large flares, called “superflares", whose energies range from $10^{33}$ – $10^{38}$ erg. The superflares release much larger total energies than the largest solar flares ($\sim 10^{32}$ erg). Figure 1.9 shows the typical optical light curve of stellar superflares observed on an active M dwarf (Hawley & Pettersen, 1991). In the following, I will introduce the observational features and interpretations of the stellar flares reported before.

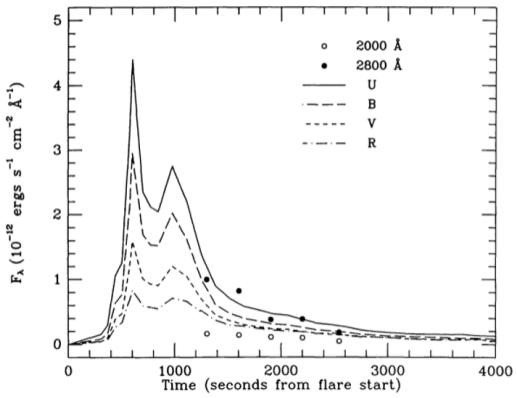


Figure 1.9: Light curves of a giant stellar flare on an M-dwarf AD Leo. From Hawley & Pettersen (1991). The flare lasted for more than 4 hr, and the total energy is estimated to be more than $10^{34}$ erg (i.e. a superflare). The effective temperature and emission line to continuum ratios are well determined for the superflare.

**- White-light emissions -**

Visible range is one of the most useful wavelengths to observe the stellar flares as in Figure 1.9. The white-light (optical continuum) components, as well as emission lines, have been detected from the ground. As mentioned in Section 1.1.2, even in the case of solar flares, the origin of the white-light emission component is a mystery. In the case of stellar flares, indeed, the white-light emissions are relatively most frequently observed, but the interpretation is much more difficult because of the lacking of spatial information. Here the observational features of white-light flares are summarized as follows: Most historically, the broad-band white-light spectral shapes as in Figure 1.10A were fitted with black-body radiation whose temperature of 9,000 $\sim$ 10,000 K (e.g. Hawley & Fisher, 1992; Kowalski

et al., 2013). The temperature is quite similar to the solar observations by Kretzschmar (2011), which may imply a common emission mechanism. Some stellar flares show such blackbody-like broadband spectra without an indication of the significant Balmer jump at $\lambda$ = 3646 Å (e.g. Hawley & Fisher, 1992; Hawley et al., 2003). Enhancements of the Balmer continuum on the hot blackbody components ($>$ 10,000K) were observed on M-dwarf (YZ CMi) flares (e.g. Kowalski et al., 2013). The NUV-optical spectra can be phenomenologically interpreted as a combination of the following three components (see Figure 1.10B; e.g. Kowalski et al., 2013, 2015, 2016): (1) 10,000 K blackbody components, (2) Balmer continuum (bound-free emission), and (3) pseudo-continuum of blended higher order Balmer lines. Later, by using a radiative hydrodynamics simulation (RADYN; Carlsson & Stein, 1992) with the heating flux of $10^{13}$ erg cm$^{-2}$ s$^{-1}$, Kowalski et al. (2015) self-consistently reproduced the observed continuum spectra around 3600 Å on M-dwarf flare spectra. However, in order to produce the optically thick chromospheric condensation with high density, the large heating fluxes ($10^{13}$ erg cm$^{-2}$ s$^{-1}$) are necessary, which are much higher than the observed values in solar flares ($\sim 10^{10-11}$ erg cm$^{-2}$ s$^{-1}$). The origin of stellar white-light emissions is therefore still a mystery and should be addressed in the future (cf. Chapters 4 and 5 in this thesis)

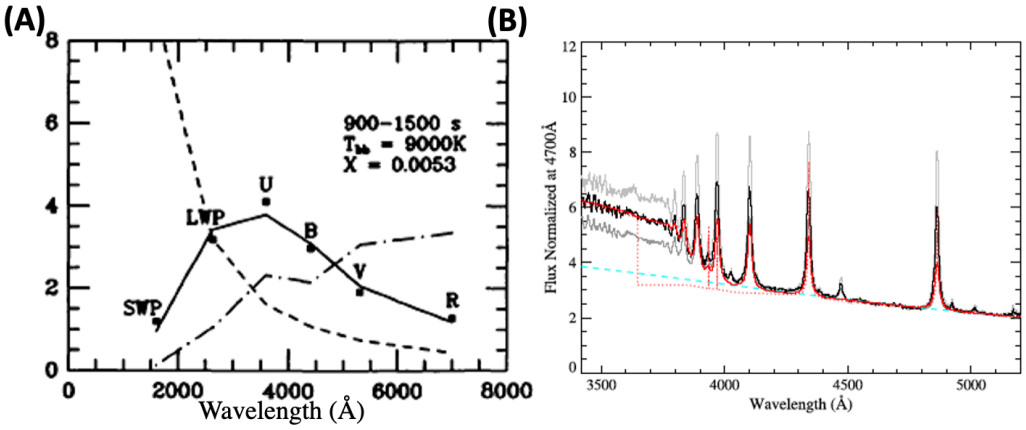


Figure 1.10: Observations of board-band spectra of stellar flares. (A) Broad-band optical to near UV spectrum during the stellar flare in the Figure 1.9 (black points). The solid line shows the black-body radiation with the temperature of 9000 K. From Hawley & Fisher (1992) (B) Spectroscopic observations of blue optical continuum during an M-dwarf stellar flare (black and gray) and the numerical simulation (red). From Kowalski et al. (2016).

**- Optical spectral lines -**

Optical spectra of stellar flares such as Balmer lines have been historically well observed. As often seen in solar flares (cf. Section 1.1.2), red asymmetries (red-wing enhancements) in the Balmer lines are observed during an M-dwarf (AD Leo) flare (e.g. Houdebine et al., 1993). This is interpreted as evidence of downward-moving chromospheric condensations

similar to those often seen in the solar flares. On the other hand, the blue enhancement of the wings of Balmer and Ca II H-K lines were also found during an M-dwarf flare (e.g. Gunn et al., 1994; Caballero-García et al., 2015). In addition, recent high time-cadence observations of an M-dwarf (EV Lac) flare showed that enhancement of H$\alpha$ blue wing was seen from the beginning to the end of a flare (Honda et al., 2018). These findings are surprising because blue asymmetries are rare and seen only in the early phase of solar flares. Phenomenologically, the blue asymmetry can be understood as (i) absorption of the emission from heated but static lower chromosphere by downward-moving cool plasma in the upper chromosphere or the post-flare loops, (ii) cool dense plasma goes up along with chromospheric evaporation, or (iii) cool-mass ejections (Honda et al., 2018; Tei et al., 2018; Maehara et al., 2020). These unexpected features may require a newly-developed idea to understand the gas dynamics of stellar flares (cf. Chapter 6 in this thesis).

The line broadenings of stellar flares have been also observed. Kowalski et al. (2017) reported the line broadening of the H$\gamma$ line of stellar flares, and they interpreted it as pressure broadenings (the Stark effect). The broadenings can be a possible way to diagnose the stellar flare parameters such as density and opacity (see Chapter 5 in this thesis in detail).

**- Stellar flare mechanism from X-ray observations -**

Thanks to developments of X-ray satellites (e.g. *ASKA*, *XMM-Newton*), many stellar X-ray flares have been observed on nearby young stars, M-dwarfs, and RS CVn stars (e.g. 1.11A; Tsuboi et al., 1998). The spectroscopic observations of the soft X-ray found that the flare temperatures are 10 –100 MK, and the emission measures are estimated to be $10^{51}$ – $10^{55}$ cm$^{-3}$. These values are much higher than those of solar flares. Interestingly, according to Feldman et al. (1995), Shimizu (1995), and Yuda et al. (1997), there is a universal correlation between the temperatures and emission measures among not only solar flares but also stellar flares (Figure 1.11B).

Moreover, Shibata & Yokoyama (1999; 2002) suggested a theoretical scaling law to explain the observed correlation based on the magnetic reconnection theory. Their theory is based on two-dimensional magnetohydrodynamic simulations of magnetic reconnection with heat conduction and chromospheric evaporation from a previous study (Yokoyama & Shibata, 1998), which showed that the reconnection heating ($B^2 v_A / 4\pi L$) is roughly balanced with the conduction cooling ($\kappa_0 T^{7/2} / 2L^2$) at the flare peak. They also assumed that the gas pressure ($p$) is comparable to the magnetic pressure ($B^2/8\pi$) in the evaporated plasma. Here, $v_A$ is the Alfvén speed and $\kappa_0$ is Spitzer's thermal conductivity. They then deduced the following scaling law:

$$EM = 10^{48} \left( \frac{B}{50\,\mathrm{G}} \right)^{-5} \left( \frac{n_0}{10^9 \mathrm{cm}^{-3}} \right)^{3/2} \left( \frac{T}{10^7 \mathrm{K}} \right)^{17/2} \mathrm{cm}^{-3} \tag{1.3}$$

where $B$ is the coronal magnetic field strength, $T$ is the temperature, $EM$ is the emission measure, defined as $EM = n^2L^3$, and $L$ is length scale of the magnetic loop. It should be noted that $n$ is the electron density of the evaporated plasma, whereas $n_0$ is the pre-flare coronal electron density around the reconnection region. If we assume magnetic field strength and pre-flare coronal density is not so different in different flares and stars, we can derive the $EM$-$T$ scaling law as $EM \propto T^{17/2}$. As in Figure 1.11B, this scaling law successfully explains the observed $EM$-$T$ diagram, which implies the stellar flares can be also explained by the model of magnetic reconnection theory. The theoretical scaling relations have been also observationally confirmed by my previous study (Namekata et al., 2017a), which also supports the unified model with the magnetic reconnection. Although simultaneous observations with X-ray and other wavebands are still difficult, the X-ray $EM$-$T$ measurement can be therefore a very strong tool to unveil the stellar flare properties (cf. Chapter 5).

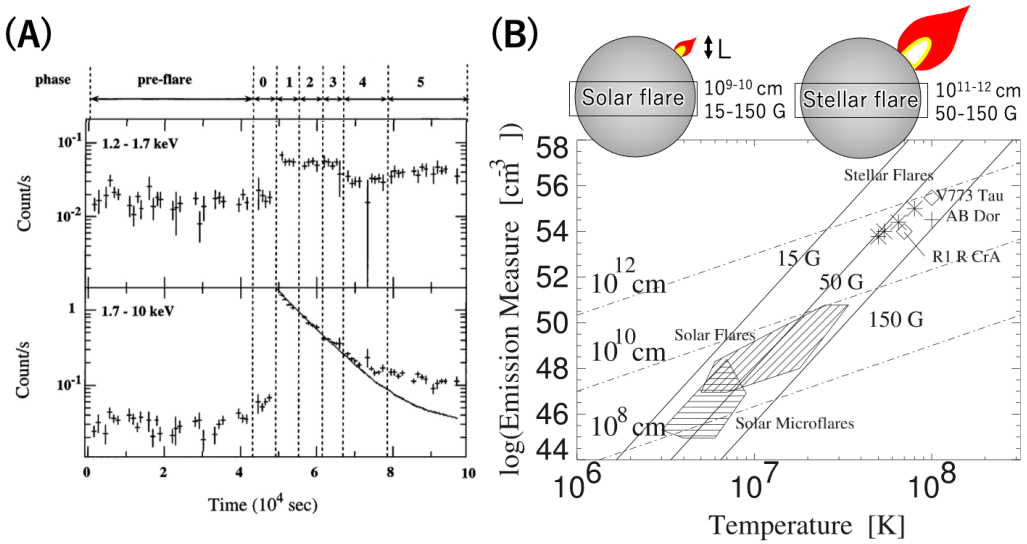


Figure 1.11: X-ray observations of solar and stellar flares. (A) Soft X-ray light curves of stellar flares on weak-lined T Tauri star V773 Tau (HD 283447) observed by *ASCA*. From Tsuboi et al. (1998). (B) Universal understanding of emission measure and temperature diagram for solar and stellar flares. The solid and dash-dotted lines indicate the theoretical scaling laws derived from the solar magnetic reconnection model. From Shibata & Yokoyama (1999; 2002).

**- Effects on the exoplanets -**

As mentioned in Section 1.1.2, solar flares often affect the Earth and planet atmosphere and magnetosphere in the form of XUV radiations, solar energetic particles (SEPs), solar winds, and coronal mass ejections (see Airapetian et al., 2020, for review). In the case

of other stellar systems hosting exoplanets, the central stars are expected to affect the exoplanet atmosphere in the same way as the Sun. Some stars show very high magnetic activities such as XUV radiations and superflares (Tsuboi et al., 1998; Maehara et al., 2012), which would much more severely affect the planetary atmosphere. In addition, in the case of M-dwarfs, the habitable zone where liquid water can survive is close to the central stars, and therefore even the small-scale stellar flares can be critical to the planet habitability (Kasting et al., 1993; Kopparapu et al., 2013). The characterization of the magnetic activity of the central star is becoming more and more important to evaluate its effects on the planetary systems. However, the XUV radiations from superflares have been rarely observed, and stellar energetic particles and mass ejections have been very difficult to observe.

Recently, some studies have reported the effect of the central star activity on the exoplanets with numerical simulations and solar empirical relations. As summarized by Airapetian et al. (2020), not only the XUV radiations but also the mass ejections can contribute to the atmospheric erosions of exoplanets. Segura et al. (2010) found that, with the high energy protons, the ozone depletion reaches a maximum of 94% two years after the flare for a planet with no magnetic field. Also, Yamashiki et al. (2019) found that when they take into account the effects of the possible maximum flares from the planet host stars such as TRAPPIST-1 e and Ross-128 b, the estimated dose reaches fatal levels at the terrestrial lowest atmospheric depth. Airapetian et al. (2016) suggested that the high-energy particles injected into the planet atmosphere can contribute to the generations of prebiotic chemistry and atmospheric warming (NOx) of early Earth by an active young Sun through the chemical reaction in Figure 1.12.

How do the large magnetic activities on central stars affect the planet's atmosphere and habitability? This question can be related to the mystery of the origins of life, one of the big mysteries in modern astronomy and astrobiology. For further realistic evaluations, it is necessary to investigate the properties of stellar magnetic activities (implications to the exoplanet habitability obtained throughout this paper and summarized in Chapter 7).

### 1.2.3 Superflares on Sun-like stars and the Sun

**- History: before the *Kepler* era -**

The Sun is old with the age of 46 Gyr, and relatively magnetically-moderate stars compared to the young stars, T-tauri stars, M-type stars, and RS CVn stars (cf. Figure 1.8), and superflares (and potential large sunspots) have never been observed on the Sun (e.g. Emslie et al., 2012; Aulanier et al., 2013). It has been widely known that young, rapidly rotating solar-type stars such as EK Dra and 47 Cas actually show superflares (see Figure 1.13; Audard et al., 1999). In the past, Schaefer et al. (2000) reported nine superflares on

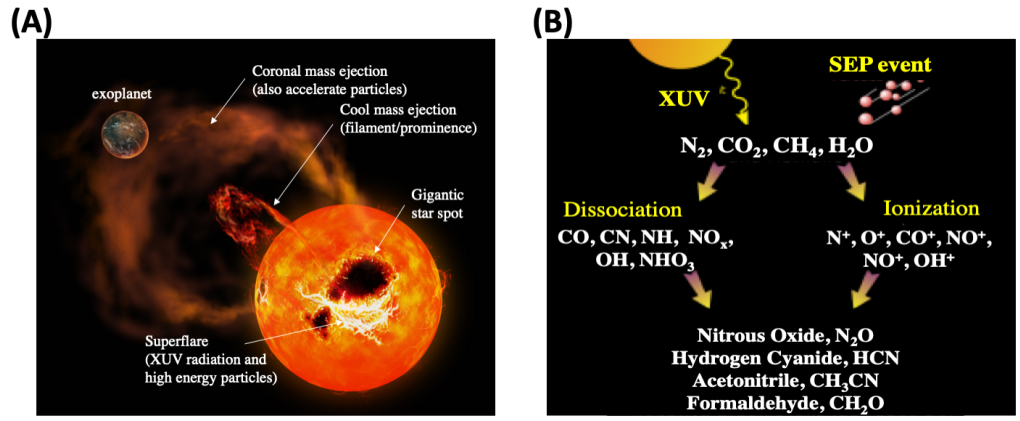


Figure 1.12: Imaginary and schematic pictures of the effect of stellar flares on the exoplanets. Left panel shows an imaginary picture of the stellar superflares affecting the planet atmosphere and magnetosphere via XUV irradiance, high energy particles (from stellar flares as well as stellar CMEs), and stellar CMEs (©National Astronomical Observatory of Japan; `https://www.nao.ac.jp/news/science/2020/20200710-okayama.html`). Right panel shows a schematic picture of how the high XUV radiations and flare/CMEs-related particles affect the atmospheric composition on the exoplanets. From Airapetian et al. (2016) and Airapetian et al. (2020).

solar-type stars (G-type main sequence stars)* including slowly rotating stars. However, the occurrence of superflares on the present Sun and slowly-rotating Sun-like stars have been cast doubt on for the following reasons:

- Stellar activity is highly related to the rotational period (see Figure 1.8B; Wright et al., 2011), and the Sun is relatively old and slowly rotating compared to the young solar-type stars showing superflares.
- The Sun has no companion that may enhance dynamo activity (Schaefer et al., 2000). Rubenstein & Schaefer (2000) argued that solar-type stars with any companion (e.g. hot Jupiter) are candidates of superflare stars.
- The Sun had had no historical record of superflares. Schrijver et al. (2012) suggest that solar flares with the energy of $> 10^{33}$ erg are unlikely based on historical records of sunspot size over the recent 400 years.

*In this thesis, 'solar-type stars' usually mean G-type main sequence stars with the effective temperature of 5000-6000 K in most cases, but in some cases the definition can be slightly different. 'Sun-like star' is a subclass of solar-type stars and has old age ($\sim$4.5 Gyr) and slow rotation ($>$ 20 days). 'Young solar analog' is also a subclass of solar-type stars, which is very young but has stellar properties similar to the young Sun. These definitions are not necessarily common among the previous studies but the difference is not significant in discussions of my thesis.

However, the universal occurrence frequency distribution of solar flares ($\mathrm{d}N/\mathrm{d}E \propto E^{-\alpha}$, $\alpha$ = 1.5 $\sim$ 1.9; Crosby et al., 1993) predicts that superflares with the energy of $\sim 10^{34}$ erg may occur only once in about 1,000 years. Therefore, such low occurrence rates of superflares keep us away from detecting superflares not only in the previous solar observations ($\sim$ 400 years) but also stellar observations of the Sun-like stars. In addition, the role of companions like hot Jupiter on stellar dynamo has not been validated before.

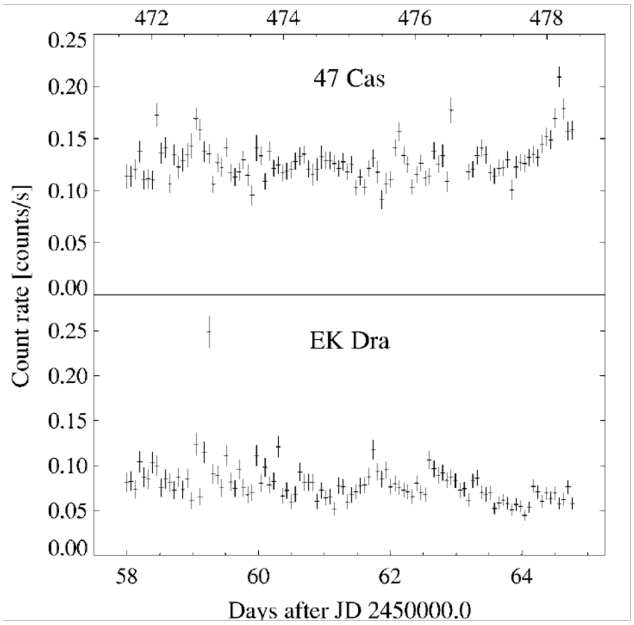


Figure 1.13: Stellar EUV superflares on the young solar analog 47 Cas and EK Dra observed by Extreme Ultraviolet Explorer (*EUVE*). Both are known to be very young ($\approx$ 100 Myr age). From Audard et al. (1999).

**- Discovery of superflares on Sun-like stars in *Kepler* Era -**

*Kepler* space telescope (launched in 2009 Koch et al., 2010) opened a new era to research statistical properties of the "rare" stellar superflares on cool stars (see Figure 1.8A for the flare stars in the *Kepler* field). *Kepler* conducted the long-term ($\sim$ 4 years) and high-precision (0.1-0.01 %) photometry and was originally designed for the exoplanet survey with exoplanet transits. The *Kepler* photometry is also useful for stellar flare survey because of plenty of observational periods and target stars including about 90,000 solar-type stars which are thought to be almost unbiased. In the case of the largest solar flares, the flare amplitude of optical continuum normalized by stellar luminosity is about 0.03 %, and the amplitude of a possible superflare on solar-type stars are expected to be $>$ 0.1 % by just assuming that the amplitude is proportional to the flare energy. Although this small amplitude is very difficult to detect by the ground-based survey, it is detectable by *Kepler* if there are.

Surprisingly, by analyzing the *Kepler* data, Maehara et al. (2012) and Shibayama et al. (2013) found 1547 superflares on 279 solar-type stars. Later, Okamoto et al. (2020) increase the number of superflares to 2341 superflares on 265 solar-type stars by using the full datasets of the *Kepler*. Spectroscopic observations shows that some of the superflare stars do not show any signature of binaries (Notsu et al., 2015a, 2019). Figure 1.14 shows an example of the light curve of detected superflares on the solar-type stars. The rotational period of the stars can be calculated by the quasi-periodic modulations which are thought to be caused by the stellar rotation with large star spots (see Section 1.2.4 for detailed discussions on star spots on superflare stars; also see McQuillan et al., 2014; Notsu et al., 2013). By measuring the rotational periods, it is confirmed that 15 old, slowly-rotating Sun-like stars (effective temperature is 5600 - 6000 K and rotation period is over 20 days in solar-type stars) show superflares up to $\sim 4 \times 10^{34}$ erg (Okamoto et al., 2020).

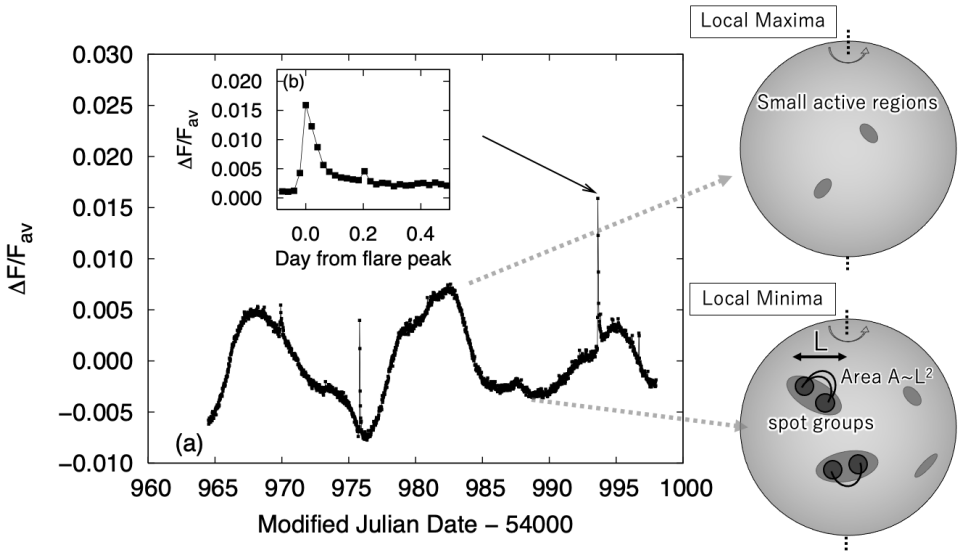


Figure 1.14: Stellar white-light superflares on an old solar-type star ($\approx$ 2 Gyr age) observed by *Kepler* space telescope. (a) Quasi-period brightness variation is caused by the stellar rotation with large star spots, and the sudden increase in the brightness with an arrow is a superflare. (b) Light curve of a superflare with the duration of $\sim$ 2 hr. From Maehara et al. (2012).

Statistical properties of superflares on solar-type stars and Sun-like stars are summarized as follows:

- The maximum flare energy decreases as the rotational period (stellar age) increases (Figure 1.15A), which can be expected from the activity-rotation relation (Figure 1.8B). The maximum energy of superflares on rapidly rotating stars is up to $\sim 10^{36}$ erg, and that on slowly rotating stars is up to $\sim 4 \times 10^{34}$ erg (Notsu et al., 2019;

Okamoto et al., 2020). This is surprising because it is still much higher than that of the largest solar flares $\sim 10^{32}$ erg. These are also related to the observations reporting that the spot surface filling factor is decreasing as the stellar age (rotation period of the star) increases (cf. Section 1.2.4; Maehara et al., 2017).

- The occurrence rate (dN/dE) of superflares on slowing-rotating Sun-like stars flare energy (E) shows a power-law distribution with $dN/dE \propto E^{\alpha}$, where $\alpha \sim 2$ (see Figure 1.15B; Notsu et al., 2019; Okamoto et al., 2020), which is very similar to solar ones (d$N$/d$E \propto E^{-\alpha}$, $\alpha$ = 1.5 $\sim$ 1.9; Crosby et al., 1993). This may indicate a possible common underlying mechanism of solar flares and superflares on Sun-like stars.

- The *Kepler* Sun-like stars are found to produce superflares of $10^{33-34}$ erg once in 1000 - 6000 yr (see Figure 1.15B; Okamoto et al., 2020). This quite low occurrence of superflares is consistent with those that we expect from solar flare occurrence frequency distributions. In contrast, the rapidly rotating stars have much higher superflare occurrence frequency, indicating that it is consistent with the past observations of superflares on the young stars (Audard et al., 1999).

- No hot Jupiter has been reported around the *Kepler* Sun-like superflare stars (Maehara et al., 2012; Okamoto et al., 2020), while it had been previously suggested that hot Jupiters are necessary to produce superflares (Schaefer et al., 2000).

These revealed the evidence that even the slowly-rotating Sun-like stars can cause superflares with very low occurrence frequency. These findings have raised a fundamental and important question "Can superflare occur on the Sun?" (e.g. Shibata et al., 2013; Aulanier et al., 2013; Schrijver et al., 2012)

Even the large solar flare ($10^{29-32}$ erg) has severely damaged human society so far (cf. Section 1.1.2). If the superflares occurred on the current Sun, it could affect the Earth environments and human society much more severely than our modern society has experienced in this half a century. The actual effect is difficult to estimate because we have no detailed observations of superflares (only stellar data). According to the simple solar scaling relation, there is an estimation that the magnetic storm can reach -2000 nT and can produce CMEs with the velocity of up to 9000 km/s (e.g. Takahashi et al., 2016). More exact effects on the Earth including social and economical effects are necessary to be investigated in the future (cf., Eastwood et al., 2017; Lingam & Loeb, 2017; Riley et al., 2018; Battersby, 2019).

Because of these backgrounds, there is an increasing interest in the characterizations of the superflares on solar-type stars and Sun-like stars. Shibata et al. (2013) theoretically

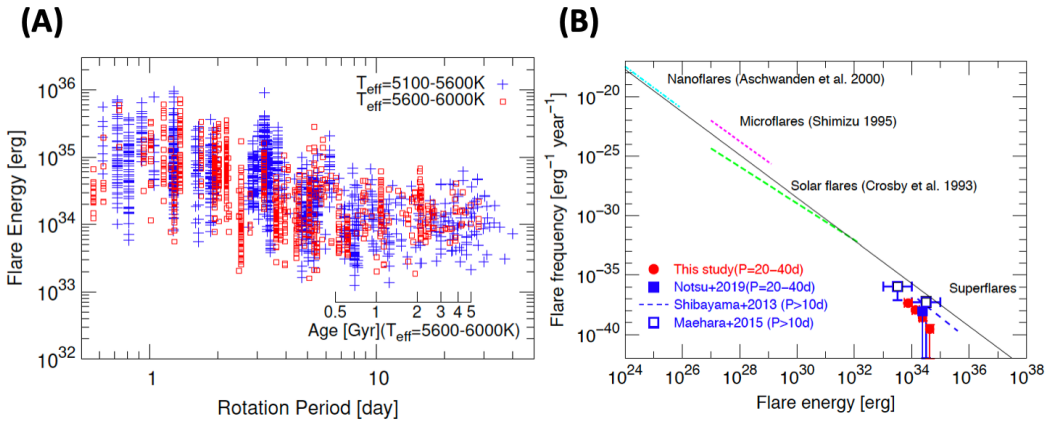


Figure 1.15: Evolution of flare energy and occurrence frequency from young Sun to current Sun. (A) Evolution of the stellar flare energy on solar-type stars found by *Kepler* space telescope as a function of rotation period (stellar age). (B) Flare occurrence frequency for solar flares and stellar superflares on the slowly-rotating Sun-like stars in the *Kepler* field. From Okamoto et al. (2020).

suggested that even the current Sun can produce superflares up to $10^{34}$ erg by considering the solar dynamo theory, although the stellar dynamo is one of the most mysterious topics in this field. Spectroscopic characterizations of the *Kepler* Sun-like superflare stars have not yet been conducted and there remains a possibility of the existence of low-mass companions near the stars.

How about the occurrence mechanism of superflares on solar-type star? It has not been confirmed yet, although they are expected to share the same underlying mechanism as solar flares (i.e. magnetic reconnection; in Section 1.1.2). In addition, the most superflares have been observed by *Kepler* photometry, but simultaneous observation of optical and X-ray (line/continuum) spectra have been seldom carried out. The number of spectroscopic observations of stellar superflares is still small, especially for superflares on solar-type stars (cf. Section 1.2.2). Therefore, whether the spectral features (i.e. chromospheric and coronal dynamics and radiations) are similar to solar flares or not should be addressed (cf. Chapters 4 and 5 in this thesis), which is also important to evaluate the effect of radiations on (exo)planets. The keywords for the remaining and important problems in stellar superflares (on solar-type stars) are listed as follows (cf. Section 1.1.2 for basic solar flare processes: “build-up”, “release”, and “transport”):

- Energy build-up (cf. Section 1.2.4 and Chapters 2, 3 and 5)
- Energy release (reconnection or not; cf. Chapter 4)
- Energy transport (e.g. particles accelerations, heating, radiations; cf. Chapter 5)

**- Possible superflares on the Sun?: Signature from different perspective -**

Is there any evidence of a superflare on the past Sun? Miyake et al. (2012) found the sudden increase in the carbon isotope $^{14}$C in the worldwide tree ring during A.D. 774 - 775 (see Figure 1.16A; Usoskin et al., 2013; Usoskin, 2017; Uusitalo et al., 2018). The carbon isotope $^{14}$C is related to the galactic and/or solar cosmic rays, and the sudden increase means the sudden increase in galactic and/or solar cosmic rays. Other events are also found during A.D. 993-994 and B.C. 660 (also see Figure 1.16A; Miyake et al., 2013; O'Hare et al., 2019). Moreover, the increase in the isotope $^{10}$Be and $^{36}$Cl in the ice core, a signature generated by the cosmic ray, is also found. The $^{10}$Be and $^{36}$Cl are less sensitive to the gamma-ray burst, and there is no signature of the supernova remnant near the solar system. Therefore, it is recently believed that the increase in the isotopes is generated by the sudden increase of the solar cosmic rays (called solar energetic particles, SEPs), which might be generated by superflares on the Sun.

In addition to these researches, by investigating old domestic and foreign documents, the signatures of extreme solar activity such as large sunspots sketches and low-latitudes aurora have been found (see Figure 1.16B; Hayakawa et al., 2017). This may indicate that the extreme solar magnetic events might have occurred in these 1000 years. However, there are large uncertainties for these studies on isotope and old documents, more studies are necessary to estimate the occurrence frequency and flare energy and to see the consistency between solar and stellar magnetic activities.

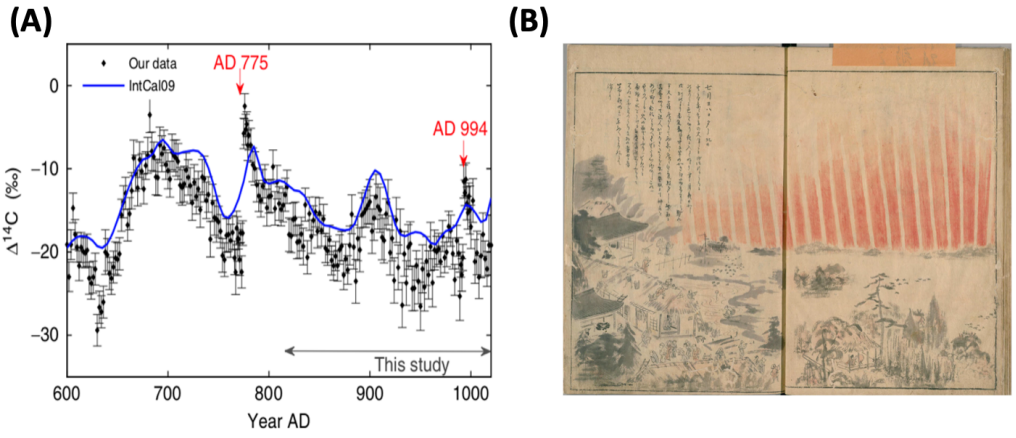


Figure 1.16: Signatures of superflares on the past Sun. (A) Amount of carbon isotope $^{14}$C in the tree ring as a function of the tree-ring year. Sudden increase in the $^{14}$C are found in A.D. 774 - 775 and A.D. 993 - 994. From Miyake et al. (2012; 2013). (B) The low-latitude aurora at Nagoya on 1770 September as e evidence of extreme space weather events (Courtesy: the National Diet Library). From Hayakawa et al. (2017).

### 1.2.4 Star spots - a key to stellar dynamo and superflares -

**- As a key to stellar dynamo -**

Star spots** are found after the findings of stellar flares. Kron (1947) seemingly considered for the first time the hypothesis that spots on the stellar surface. Nowadays star spots are universally observed on various kinds of stars, such as M-F dwarfs, young and evolved stars, and close binary stars (see Berdyugina, 2005; Strassmeier, 2009, for review). Star spot signature can be observed by both spectroscopy and photometry. In particular, the key observations of star spots to understand the stellar dynamo are considered to be as follows: sizes, locations (latitude and longitude), evolution, long-term activity cycles, and differential rotations. These keywords are important to solve the unsolved problem of the stellar dynamo (as seen in the case of the solar dynamo, see Section 1.1.3).

I first summarize the research on star spots obtained by ground-based telescopes. Photometric observations of stars having large spots usually show large quasi-periodic brightness variations caused by stellar rotations (e.g. Strassmeier et al., 1994; Hall & Henry, 1994; Maehara et al., 2017; Basri & Nguyen, 2018), which helps us investigate the star spot properties. Spectroscopic observations of the rapidly-rotating stars can resolve the rotational velocity components of stellar east and west side and enable us to reconstruct the star spot distribution on the surface (the method is called Doppler Imaging; e.g. Strassmeier et al., 1999; Hussain et al., 2007; Künstler et al., 2015). Moreover, spectroscopic observations with polarimetry have succeeded in the reconstruction of the surface map of magnetic field polarity (called Zeeman Doppler Imaging; Carroll et al., 2012; Waite et al., 2017). More recently, Roettenbacher et al. (2016) reported imaging of the old, magnetically active star using long-baseline infrared interferometry.

These developments of star-spot mapping methods have been conducted since the 1990s and found some features similar to – or sometimes very different from – sunspots observations. For example, some stars show solar-like long-term activity cycles according to the very-long term monitoring observations of Ca II emission (e.g. Baliunas et al., 1995). The Doppler Imaging revealed that sunspot-like dark spots appear on the various type of stars (summarized by Berdyugina, 2005). In contrast, Figure 1.17 shows the large star spot located on the stellar rotational pole on the active RS-CVn type star HD 12545 reconstructed by Doppler Imaging (Strassmeier et al., 1999). The spot radius is $\sim$ 10 solar radius, and the polar spots are not expected from solar observations (cf. Section 1.1.3 for solar observations). Some of the star spots (groups) are known to survive for more than 10 years while the lifetime of sunspots is much shorter (less than several months).

The recent *Kepler* space telescope has revealed many statistical properties of star spots

**Expressions of "star spot" and "starspot" have the same meaning. In this thesis, I use "star spot".

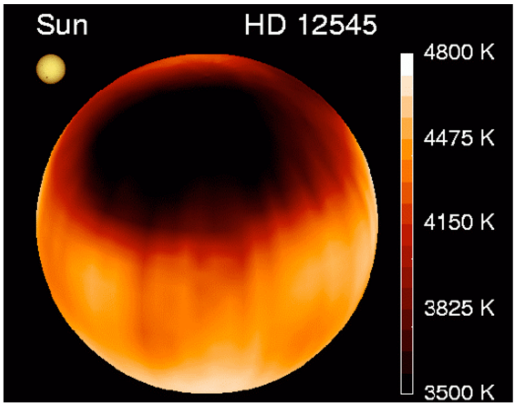


Figure 1.17: Doppler imaging of the stellar surface of the active RS-CVn type star HD 12545. The very large star spot (group) covering about the half of stellar hemisphere appears on the stellar pole. From Strassmeier et al. (1999).

with the various types of stars (especially, related to the spot sizes). These works were performed by assuming that the stellar quasi-periodic brightness variations are caused by the stellar rotation with gigantic star spots. This assumption was spectroscopically confirmed (e.g. Notsu et al., 2015b, 2019, for the *Kepler* solar-type stars) and the brightness variation amplitudes are found to correspond to spot area (coverage). Maehara et al. (2017) found that the spot activity decreases as the rotational period increases, which can be straightforwardly understood by considering the well-known activity rotation relations (Wright et al., 2011). Interestingly, even the Sun-like stars possess gigantic spots with areas of 10,000-100,000 MSH (millions of solar hemisphere, $10^6$ MSH = $2\pi R_{\odot}^2$ = $3.1\times10^{22}$ cm$^2$; Maehara et al., 2017; Notsu et al., 2019; Okamoto et al., 2020), which is by far larger than the largest sunspot ($\sim$6,000 MSH). The occurrence frequency of large star spots on Sun-like stars is found to be consistent with that of sunspots (Maehara et al., 2017, see the right panel of Figure 1.18). These can imply that the same dynamo process is working in the hyper-active Sun-like stars, which raises a new question of whether the solar dynamo (theory) can produce such gigantic spots (cf. Shibata et al., 2013). This is how the *Kepler* data have greatly improved statistics of spot area (coverage) compared to the past ground-based era.

In summary, ground/space-based observations have provided key information (snapshot and long-term variations) on gigantic star spot on various types of stars, although the number of stars are limited to the nearby active stars. Now the *Kepler* era has arrived and *Kepler* provided huge amount of long-term ($\sim$4 year) dataset suitable for the statistical analysis especially on spot size, location, rotation, differential rotations, and spot evolution. In my opinion, these have been well studied using *Kepler* data, except for the spot evolution and distribution. The spot evolution and distribution may be difficult to estimate

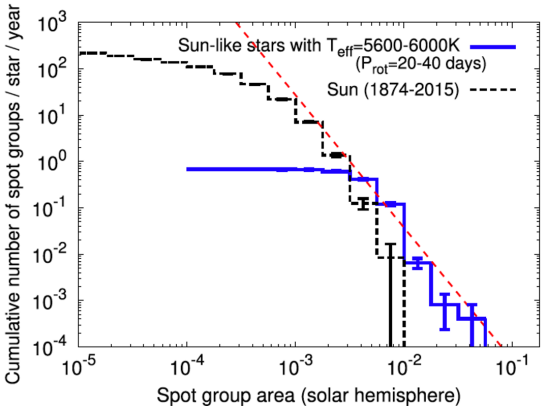


Figure 1.18: Occurrence frequency of sunspots (black) and star spots (blue) on the *Kepler* slowly-rotating Sun-like stars as a function of spot group area in the unit of solar hemisphere ($3.1\times10^{22}$ cm$^2$). Red dashed line is a common power-law relation for sunspots and star spots. Note that the saturation in the smaller spots of star spots is caused by the detection limit and that of sunspots is caused because the very small magnetic fluxes do not produce dark spots but bright area (known as “faculae"). From Maehara et al. (2017) and Notsu et al. (2019).

only from the photometry, but it should be addressed by using the precious Kepler data because they are one of the keys to stellar dynamo. The keywords for the problems treated in this thesis are listed as follows:

- Spot distribution (cf. Chapter 3)
- Spot evolution as a fundamental process of flux transport (cf. Chapters 2 and 3, and see the key question of “energy build-up” process of stellar flares raised in the Section 1.2.3)

**- As a key to stellar superflares -**

Can large star spots be the energy source of stellar superflares? The *Kepler* Sun-like stars showing superflares are found to have the large star spots (i.e. magnetic energy), indicating a possible link between flares and spots (Notsu et al., 2013; Hawley et al., 2014; Davenport et al., 2015; Maehara et al., 2017). Shibata et al. (2013) and Notsu et al. (2013) suggest that the energies of superflares can be explained by the magnetic energy stored around corresponding star spots. The flare energy described in Equation 1.2 can be rewritten as a function of the spot area ($A_{\rm spot} \sim L^2$; see Figure 1.14):

$$E \sim f E_{\rm mag} \sim 7\times10^{32} \left(\frac{f}{0.1}\right) \left(\frac{B}{10^3{\rm G}}\right)^2 \left(\frac{A_{\rm spot}/2\pi R_\odot}{10^{-3}}\right)^{3/2} [{\rm erg}], \tag{1.4}$$

where $f$ is a non-dimensional fraction of magnetic energy released by the flare, typically $\sim 0.1$ (Aschwanden et al., 2014). Figure 1.19 shows that the upper limit of the energies released by the flares are basically comparable to the stored magnetic energies around star spots, and the observed energy of solar and stellar flares are below a roughly the same theoretical lines (Equation 1.4). This implies that stellar superflares occur as a result of the energy release of magnetic energies around star spots.

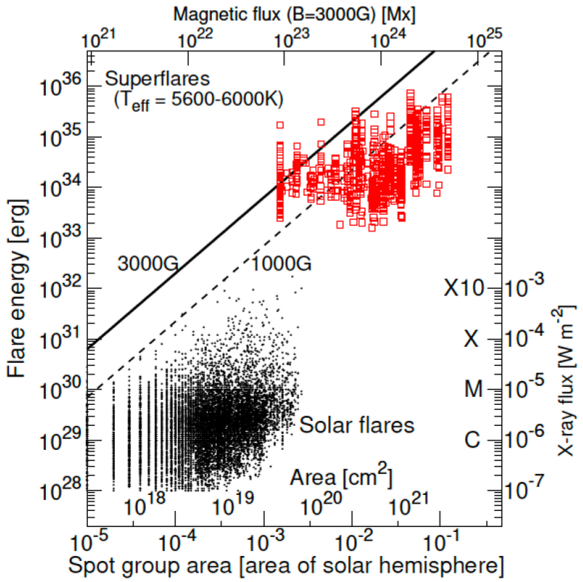


Figure 1.19: Relation between spot group area and flare energy for solar (black) and stellar flares (red). Dashed and solid line indicates the theoretical upper limit of flare energy when the flare release 10 % of magnetic energy stored around spots with the magnetic field of 1000 and 3000 G, respectively (Eq. 1.4). From Okamoto et al. (2020).

By considering the spot existence, the observational result for stellar superflares can be consistently understood. As described in Section 1.2.3, the occurrence frequency of large star spots on Sun-like stars are found to be consistent with that of sunspots (Maehara et al., 2017, see the right panel of Figure 1.18). This can be highly related to the common power-law distribution of flares (see Figure 1.16B). In addition, the decrease in maximum flare energy as a function of stellar age (see Figure 1.16A) can related to the decrease in maximum spot coverage as a function of stellar age (Maehara et al., 2017; Okamoto et al., 2020). These discoveries imply that gigantic star spots are essential to produce superflares.

In summary, the statistical properties of star spots and the relation between flares and spots have been largely improved by *Kepler* photometry. However, there would be some additional important factors to produce superflares. For example, in the above *Kepler* studies, only the spot size (or coverage) has been considered as a possible condition to produce superflares. The emergence/decay of star spots or complexity of star spots may

play an important role to produce stellar superflares as in solar cases (cf. Toriumi & Wang, 2019, for reviews). The mid-timescale variations such as spot evolution have not been well studied by the previous ground-based observations and it must be helpful to unveil the underlying stellar dynamo (cf. Brun & Browning, 2017, for reviews). The keywords for these important problems are listed as follows (cf. Chapters 2 and 3):

- Spot evolution as a role to trigger superflares
- Spot complexity as a role to trigger superflares

These topics correspond to the key questions on "energy build-up" process of flares raised in the Section 1.2.3.

### 1.2.5 Exploration of stellar mass ejections

The mass ejections are generally related to the "energy transport" process of flares raised in Section 1.2.3. As introduced in Section 1.1.2, solar mass ejections associated with solar flares releasing the energy of $10^{29}$ to $10^{32}$ erg often directly affect Earth's environment (Gopalswamy et al., 2003). Here, I generally define "mass ejections" as the phenomena including cool mass ejections (known as filament eruptions and surges) and hot mass ejections (outer-layer CMEs). Stellar mass ejections are considered to play a key role in affecting the exoplanets. However, the evidence of the mass ejection from stellar flares is quite rare and controversial. What is the best way to detect mass ejections? Here, I introduce previous studies reporting signatures on stellar mass ejections and a possible way to detect it by analogy with solar flares.

Figure 1.20 shows a summary of the detection methods of stellar mass ejections. In the case of solar flares, the CMEs can be mostly observed by coronagraph in the optical continuum (mostly via Thomson scattering; see Figure 1.20D). However, the detections of this continuum emission are very difficult due to the low contrast in the case of stellar observations.

Spectroscopic observations are possible and promising ways to detect the high-velocity ejection components from stellar flares (see Figure 1.20B). In the case of solar flares, the blue-shifted spectra in optical lines (mostly Balmer series) are well observed. Odert et al. (2020) calculate whether it can be detected by stellar spectroscopic observation and suggest that it is possible if the signal-to-noise ratio is enough high. In M-dwarf flares, there have been many reports that blue-shifted "emission" lines have been detected as possible evidence of prominence eruptions (Houdebine et al., 1990; Gunn et al., 1994; Fuhrmeister & Schmitt, 2004; Leitzinger et al., 2014; Vida et al., 2016; Korhonen et al., 2017; Honda et al., 2018; Muheki et al., 2020a; Maehara et al., 2020). Some of them

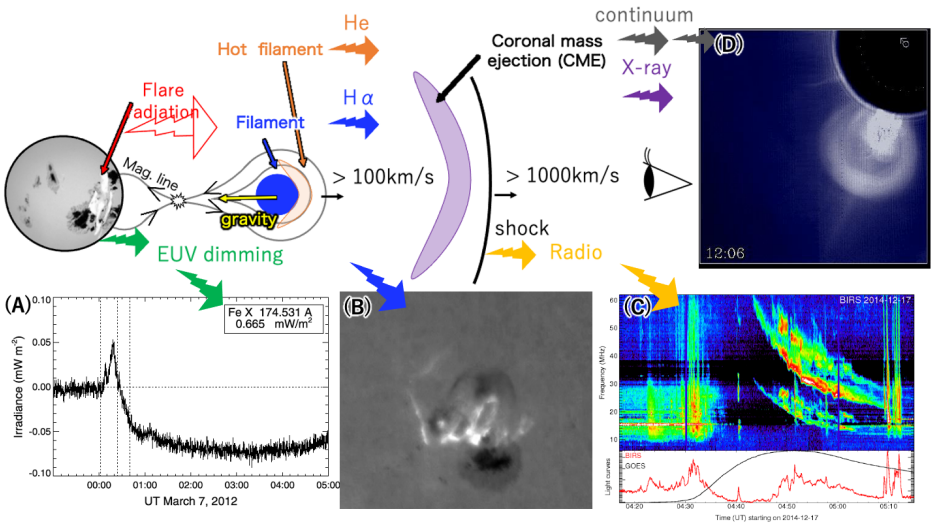


Figure 1.20: Schematic picture of possible ways to detect stellar mass ejection, one of a big mystery in stellar magnetic activities, on the basis of solar observations. (A) Post-flare EUV dimming on the stellar surface as an indirect signature of mass ejection (Harra et al., 2016). (B) Prominence eruption (©Hida Observatory). (C) Type-II radio burst as an evidence of CME shock propagating through the interplanetary space (Crosley et al., 2017). (D) CME observed by white-light coronagraph (van Driel-Gesztelyi & Culhane, 2009).

are characterized by higher velocities than the escape velocities. However, as introduced in Section 1.1.2, the blue-shifted emissions can come from upward flows in the flaring footpoints, which is often reported in solar flares (Švestka et al., 1962; Tei et al., 2018). In addition, Honda et al. (2018) proposed that the emission can come from the red-wing absorption of flaring emission by the overlying downward post-flaring loops. Therefore, we need to be careful for the understandings of the blue-shifted emission components.

A signature of CME has been reported from a blue-shifted emission component of the cool X-ray O VIII line (4 MK) in the late phase of stellar flare on an evolved giant star HR 9024 (Argiroffi et al., 2019). Although the time evolution of a blue-shifted velocity is not obtained there, they detected the blue-shifted emission component with the velocity of 90 km $s^{-1}$ (the escape velocity 220 km $s^{-1}$) and interpreted it as a coronal mass ejection. The blue-shifted plasma components with a few MK are also emitted from the flare-origin upward flow (called “chromospheric evaporation") in the case of solar flares, but they exclude the possibility considering the other hotter lines do not show the blue-shifted component in the post-flare phase. Although currently the X-ray spectroscopic data of O VIII line for solar CMEs is currently not available because of the lack of the instruments, the future solar observations may enable us to directly compare with the stellar X-ray observations.

Other signatures of kinematic characteristics of the ejected plasma are also inferred from

continuous X-ray absorption during stellar flares, which can be caused by neutral material above the flaring region, such as filament eruptions (Tsuboi et al., 1998; Moschou et al., 2019; Favata & Schmitt, 1999). However, on the Sun, X-ray absorption by prominences is uncommon (Schwartz et al., 2015; Odert et al., 2020), and instrumental calibration effects at low energy have been pointed out (Osten & Wolk, 2017). Other than this, pre-flare dips have been reported in optical photometry, which may suggest potential prominence eruptions, but possibly due to the opacity effects (Osten & Wolk, 2017). Radio observations have recently investigated the type-II radio bursts associated with shocks in front of coronal mass ejections as possible evidence of mass ejections (Figure 1.20C), but no significant signature has been obtained so far (Osten & Wolk, 2017). In addition, by a possible future work, there is a possibility that the post-flare dimming can be observed in EUV ranges (Figure 1.20A; Harra et al., 2016).

Recently, some numerical simulations of stellar mass ejections have been more and more performed (Airapetian et al., 2016; Alvarado-Gómez et al., 2018; Kay et al., 2019). Alvarado-Gómez et al. (2018) proposed that overlying large-scale magnetic fields on active stars suppress the mass ejections. In order to know the whole picture of stellar flare events and its effect on the exoplanets, it is necessary to reveal more detailed properties of stellar mass ejections from various perspectives (cf. Chapter 6).

## 1.3 Aim of this thesis

In the above sections, I introduced my research interest in the extreme stellar magnetic activities and their impact on the exoplanets (cf. Section 1.2). There are many observational studies reporting large-scale magnetic activities on various types of stars. However, most of the fundamental physical process of such extreme events have been poorly understood (see problems raised throughout Section 1.2). In addition, although extreme stellar magnetic activities have been getting more and more attention in the context of the recent surveys of habitable exoplanets (cf. Section 1.2.2, 1.2.3), the observational properties such as mass ejections, XUV flare radiations, and high energy particles that can directly affect the exoplanet atmosphere have not been well investigated.

The aim of this study is to estimate the physical properties of stellar flares, star spots, and mass ejections by conducting solar and stellar observations and numerical simulations. The main questions I address in this thesis are as follows:

- What is the occurrence mechanism of the gigantic star spots, stellar superflares, and stellar mass ejections?
- What is the effect of extreme magnetic activities of central stars on the exoplanet habitability?

In this thesis, I mainly focus on the active solar-type stars (G-type main-sequence stars), although in some parts I treat cooler M dwarfs (cf. Chapter 5). This is not only because of the importance of solar-type stars but also because the detailed researches on the "rare" extreme magnetic activities on solar-type stars have a potential to be dramatically improved thanks to the recent *Kepler* and *TESS* (Ricker et al., 2015) missions (cf. Section 1.2.3).

The keyword throughout this thesis is "time evolution" of stellar magnetic activities, which I regard as important to investigate the underlying mechanism. My main approaches are basically **(1)** to statistically analyze the photometric data provided by *Kepler* space telescope and **(2)** to conduce time-resolved multi-wavelength observations by using ground/space-based telescopes. **(1)** The *Kepler* data have the following originalities: long-term (4 years), high-cadence (1 min or 30 min), high-precision, and huge amount of unbiased photometric samples. Therefore, *Kepler* data are suitable for the statistical analyses of temporal evolution of star spots having the timescales of months to years as well as stellar flares having the timescales of minutes to hours. **(2)** In 2019, the Kyoto-University 3.8-meter Seimei Telescope started the flare-monitoring spectroscopic observations (Kurita et al., 2020), which provides a precious opportunity to investigate stellar flares with very high-time cadences ($\sim$ 1 min; flare monitoring usually takes more than $\sim$5 minutes in previous studies). Plenty of observational time of the 4m-class telescope, sometimes combined by *TESS* (targeting nearby stars much brighter than *Kepler*'s faint targets) photometry, has provided high-quality and high-time-cadence datasets of the "rare superflares", which enables us to unveil the dynamic changes in flaring emission and mass ejection (as raised in Section 1.2.3, 1.2.5).

In addition, throughout this thesis, I regard the idea of "solar-stellar connection" as important. This is because the comparison between solar and stellar observations is helpful to unveil the mysteries of stellar magnetic activities on the basis of well-established solar physics. The approaches taken in Chapters 2$\sim$6 therefore have been brought from the knowledge of solar observations (cf. Section 1.1). Also, one of my unique approaches is to analyze the Sun by spatially integrating solar observational data (called the "Sun-as-a-star" observations; cf. Chapters 4 and 6) to understand the stellar magnetic activities. The Sun-as-a-star approach is helpful for the stellar flare observations with no spatial information which is one of the biggest difficulties in stellar studies.

This dissertation addresses totally four kinds of stellar topics: (i) formation/decay of star spots, (ii) energy release of stellar flares, (iii) heating/radiation of stellar flares, and (iv) stellar mass ejections from superflares. In other words, these topics correspond to "energy build-up" (i), "energy release" (iii), and "energy transport" (iii)-(iv) in terms of the basic processes of flares (see Section 1.1.2). Chapters 2 and 3 describe the results based on two publications Namekata et al. (2019) and Namekata et al. (2020a), and deal with the formation/decay of star spots. Chapter 4 treats the energy release of stellar flares on

the basis of the published paper Namekata et al. (2017b). Chapter 5 handles the nature of heating/radiation of stellar flares on the basis of the published paper Namekata et al. (2020b). Chapter 6 is based on the submitted paper Namekata et al. (submitted), and is dedicated to stellar mass ejections. Chapter 7 draws conclusions.

In our studies, my role was to make research plans, to propose and conduct the observations, to perform data analyses, to interpret the results, and to write papers. In Chapters 5 and 6, many observers and advisors in our team helped me. I wrote the analytical code by myself except for the following two parts: In Section 3.3.3, James R.A. Davenport provided STSP code and revised data of Davenport (2015), and my role was to discuss the model input and analyze the model outputs. In the numerical works in Chapter 6, my role was to perform simulations and interpret the results. Adam F. Kowalski shared with me his numerical code RADYN and gave me much advice about coding.

CHAPTER 2

# Lifetimes and emergence/decay rates of star spots on solar-type stars estimated by *Kepler* data in comparison with those of sunspots

## 2.1 Introduction

As introduced in Section 1.2, most of flaring solar-type stars possess gigantic spots with areas of 10,000-100,000 MSH (millions of solar hemisphere, $10^6$ MSH = $2\pi R_\odot^2 = 3.1\times10^{22}$ cm$^2$, Maehara et al., 2017), which is by far larger than the largest sunspot (6132 MSH, Aulanier et al., 2013; Cliver & Dietrich, 2013; Hathaway, 2015; Toriumi et al., 2017; Hayakawa et al., 2017). However, little is known about the process to generate and decay the magnetic fields of the spots, which can be a trigger of superflares (Toriumi & Wang, 2019). In addition, observations of the spot properties may provide a clue to the universal understanding of the stellar dynamo (see Section 1.1.3; e.g. Shibata et al., 2013; Brun & Browning, 2017).

First we introduce the basic properties of sunspot emergence and decay physics. In the case of sunspots, the magnetic fluxes are generally thought to emerge from the deep convection zone to the solar surface thanks to the magnetic buoyancy and convection (e.g. Parker, 1955; Cheung & Isobe, 2014), and decay as soon as (even before) the sunspots are completely formed (McIntosh, 1981). As for the decay process, the granular motions can be a possible mechanism, though other processes such as surface flows (moat/Evershed flows, e.g. Kubo et al., 2008), subsurface convections and reconnections (Schrijver & Title, 1999) can also contribute to the spot decay. It takes typically hours to days for

the sunspot formations ($<$ 5 days; Harvey & Zwaan, 1993), while the spot decay spends longer periods, typically weeks to months (Hathaway & Choudhary, 2008). Since the decay phase is longer than the emerging phase, sunspot lifetimes have been discussed with regard to the decay mechanism. Spot decay rates ($dA/dt$) as a function of the spot area ($A$) have been best discussed so far. There are two models, a linear decay law ($dA/dt \propto$ constant; Bumba, 1963) and a parabolic decay law ($dA/dt \propto A^{1/2}$; Martinez Pillet et al., 1993). In the former case, a relation between the lifetime ($T$) and spot area ($A$) can be formulated into $T \propto A$, which is called "Gnevyshev-Waldmeier" (GW) law (Gnevyshev, 1938; Waldmeier, 1955). In the latter case, the lifetime-area relation can be expressed as $T \propto A^{1/2}$ (Martinez Pillet et al., 1993), while $T \propto A$ can be also derived by considering the maximum size dependency (Petrovay & van Driel-Gesztelyi, 1997). Observationally, lifetimes of sunspot groups are roughly consistent with the GW law, though the large scattering around the GW law can be seen (e.g. Henwood et al., 2010).

Star spots are also universally observed on various kinds of stars, including solar-type stars (see Berdyugina, 2005, for review). Stars having large spots show large quasi-periodic brightness variations caused by stellar rotations (Notsu et al., 2015b; Karoff et al., 2016), which helps us investigate the star spot properties. Although the temporal evolutions of star spots can be a clue to the understanding of the supply and dissipation of magnetic field on stellar surface, they have not been extensively investigated due to its difficulty in observation. However, investigations on temporal evolutions of star spots may exert a huge impact on a variety of research fields because of the following reasons. (1) It can be a tool to understand how the superflares are triggered, and enable us to estimate how long surrounding planets are exposed to the danger of flares and coronal mass ejections (e.g. Takahashi et al., 2016; Lingam & Loeb, 2017). (2) Estimating the diffusion coefficient of stellar surface would be helpful for numerical modelings on stellar dynamo. (3) It can provide a constraint for the light curve modeling calculations to reconstruct surface intensity distributions, which are helpful for detections of exoplanet transits (Giles et al., 2017).

In 1990s, several researches reported lifetimes of star spots on active young stars, cool stars (mainly M and K-type stars), and RS CVn-type stars (close binary stars) on the basis of ground-based observations (e.g. Hall & Henry, 1994; Henry et al., 1995; Strassmeier et al., 1994). They indicated that the lifetimes of star spots linearly increase with the spot area in the domain of small spots, while they decrease in the domain of large spots possibly because of differential rotations (Henry et al., 1995). For the huge spots, the estimated lifetimes are quite long and sometimes exceed 2 years (Strassmeier et al., 1994). Futheremor, the developments of Doppler Imaging techniques surprisingly revealed that active young stars have large polar spots which have persisted for more than decades (Strassmeier et al., 1999; Carroll et al., 2012). More recently, the light curve modelings have been carried out

by many authors (see, Strassmeier, 2009, for review) and an inversion modeling has beed developed (Savanov & Strassmeier, 2008), which may reveal the spot temporal evolutions although there may be more or less degeneracy in inversions.

How about the lifetime of star spot on solar-type stars? In 2009, the *Kepler* satellite was launched to observe a huge amount of long-term stellar light curves ($\sim$4 years), and the high-sensitivity observations have enabled us to research the temporal evolutions of star spots on solar-type stars by using several methods. The spot signals are relatively small in the case of the solar-type stars (Maehara et al., 2017), and it had been difficult to investigate the mid-term temporal evolution of star spot on solar-type stars have not well investigated from the ground-based telescope before the *Kepler* era. Fröhlich et al. (2012) and Bradshaw & Hartigan (2014) performed a light curve modeling to reconstruct the spot evolutions for two solar-type stars, though their applications have been limited to short observational periods ($\sim$ 130 days), which does not clearly cover the whole spot lifetimes. Davenport (2015) estimated lifetimes and area of star spots on solar-type stars on the basis of the surface distributions reconstructed by the stellar brightness variation during exoplanet transits. More recently, Giles et al. (2017) developed a method to derive an indicator to characterize the star spot lifetime on solar-type stars by applying the auto-correlation function to the *Kepler* light curves. Although this is only a proxy of the typical spot decay time of the star, it enables a statistical study for large samples and interestingly shows a trend similar to that in Davenport (2015). All of them showed that star spots with area of 10,000–100,000 MSH have much shorter lifetimes ($\sim$10–200 day) than those expected from the solar GW relation (1,000–10,000 day). Based on the historical GW relation, Bradshaw & Hartigan (2014) suggest that the shorter lifetime can be explained by the turbulent magnetic diffusivity different from solar ones, and proposes the magnetic diffusivity in the supergranule size is working in spot decay. However, the comparison in lifetimes have the following two difficulties: First, the lifetimes can be underestimated due to the sensitivity of the method and data. Second, the lifetime is a superposition of the emergence phase and decay phase, and it may not be explained only by the decay process. In addition, although Giles et al. (2017) report the global decay timescales of star spots by using large numbers of data, we still need more statistical analyses of the detailed temporal evolutions of "individual" star spots for revealing the underlying physics.

Our basic idea to solve the difficulties in lifetime is to measure the variation rates of star spot area (i.e. emergence/decay rates). The variation rates are not affected by the detection limit of the spot area, and it can be discussed for emergence and decay phase separately. In addition, the emergence and decay rates as a function of spot area are relatively better studied than lifetimes not only by the solar observations but also the simple solar MHD models as introduced above (see also Section 2.3). In this study, we develop a method to measure temporal evolutions of star spot area on solar-type stars by tracing local minima

of the *Kepler* light curves, which enables us to statistically estimate not only lifetime–area relation but also emergence and decay rates of "individual" star spots (groups). In addition, we focus on the comparison between sunspots and spots on the solar-type stars in this study as a first step (see Section 1.3). In Section 2.2, we introduce our sample selection, method, and detection criteria. We also describe how to calculate lifetimes, areas, and emergence and decay rates. In Section 2.3, we show several results of our analysis and comparisons with the solar data. Finally, we discuss the results in Section 2.4.

## 2.2 Data and analysis method

### 2.2.1 Sample selection

It is expected that the spot emergence, its decay, and dynamo mechanism are all closely related to the stellar surface temperature and gravity (e.g. Kippenhahn & Weigert, 1990). In order to assess the diversity and similarity of the star spots by comparing them with the sunspots, we here selected solar-type stars (G-type main sequence stars) as target stars from the *Kepler* data set on the basis of the stellar effective temperature ($T_{\rm eff}$) and surface gravity ($\log\ g$) listed in *Kepler* Input Catalog (Kepler Data Release 25 Notes, Thompson & Caldwell, 2016). In this study, we defined solar-type stars with a criteria of 5000 K $<$ $T_{\rm eff}$ $<$ 6000 K and $\log g > 4.0$. For each star, we used all the available *Kepler* pre-search data conditioning (PDC) long-cadence (30 min) data (Kepler Data Release 25, Thompson & Caldwell, 2016), in which instrumental effects are removed.

The active stars show quasi-periodic variations due to stellar rotations with large dark star spots, which form local minima in the light curves corresponding to times when star spots are on the visible side of the stars. The brightness variation amplitude corresponds to the spot area compared to stellar disk (e.g. Notsu et al., 2013, 2015b). The idea of this study is that temporal evolutions of the star spots are measurable if we can trace the local minima in time series, as introduced in the following section. In inactive stars, it is difficult to detect and trace the local minima because of the low signal to noise ratio. We therefore only selected stars showing high magnetic activity with an additional criterion: amplitude of periodic variability taken from McQuillan et al. (2014) are above 1%. The 5356 active solar-type stars are finally selected as our target stars.

### 2.2.2 Detection and tracing of local minima

We used a simple method similar to that of Hall & Henry (1994) to measure the temporal evolutions of star spots. In this method, each star spot can be identified by the repetition of the local minima over the rotational phases (see below Figure 2.1). The light curve

of a rotating star with star spots shows several local minima when the spots are on the visible side (Figure 2.1(a)). The time separation of each local minimum corresponds to the rotational period. For example, if a star has two large star spots at separated longitudes, the light curve exhibits two local minima during one rotational period, and the separation of the two local minima give the difference of the longitudes. This difference makes it possible to identify longitudinally-separated star spots. In the time-phase diagram of local minima (Figure 2.1(c)), an individual star spot is distinguishable as a common straight line (e.g. the gray line in Figure 2.1(c)). This is how the individual star spots are identified and their temporal evolutions are measured from the light curves (Figure 2.1(d)). This method is our basic idea to discuss the temporal evolution of star spots, and has been applied to the ground-based observation of young stars, cool stars, and RS-CVn stars (e.g. Henry et al., 1995).

However, this method contains a problem caused by the stellar differential rotation. If two spots are located at the different latitudes, the time separation of two local minima changes in time because of the differential rotation (see, e.g. Strassmeier & Bopp, 1992). The differential rotation finally makes the two local minima combined to one. This difficulty prevents us from tracing the whole time evolutions of the identical star spots from the appearance to disappearance. Therefore, this method cannot distinguish whether the spot disappears or combines with other spots at the same longitude. Moreover, changes in relative longitudes of the spots lead to changes in depths of local minima, which makes it difficult to estimate variation rates of the spot area (see Notsu et al., 2013).

To overcome these difficulties, we introduce the following conditions: we focus on light curves that have a pair of spots (1) rotating with a common period and (2) located on the reverse rotational phase (i.e. a longitude separation of the two spots of approximately 180 degree). As for the pair of spots satisfying the condition (1), the absolute values of spot latitudes are considered the same. When a light curve satisfies the conditions (1) and (2), the local minima can be traced without being disturbed by the differential rotation as well as brightness variations of the other spots. Although this method can contain some selection biases, the simplicity enables an application to a huge amount of the *Kepler* dataset.

Based on the above idea, we developed an algorithm to automatically detect such star spots as follows. First, we derived rotational periods by the discrete Fourier transform of the whole light curves. We here selected stars with their rotational periods more than 1 day and less than 30 day because too rapid or slow rotations complicate tracing local minima for a long time. Investigating a dependence of rotational periods on lifetimes is not our main purpose in this paper, though it should be investigated in our future works. Next, we obtained the smoothed light curve by using locally weighted polynomial regression fitting (LOWESSFIT; Cleveland, 1979) to remove flare signature and noise. In the LOWESSFIT

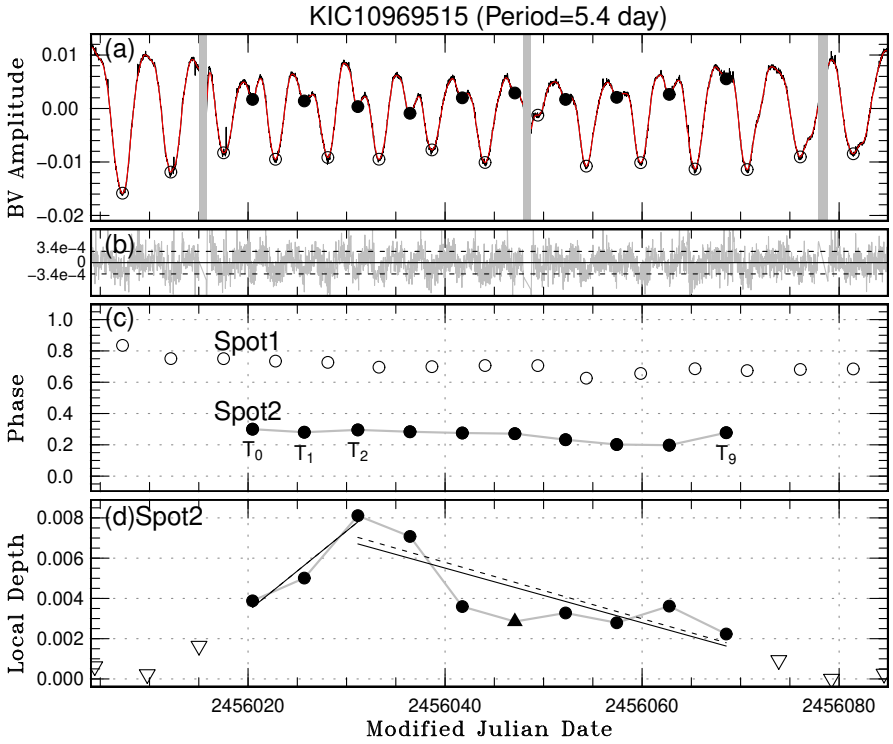


Figure 2.1: An example of the temporal evolution of one star spot successfully measured in this study. (a): Background black line is the observed *Kepler* light curves, and red line is the fitted one. Vertical gray lines correspond to the observational gaps longer than 5 hours. Filled circles are the local minima of a detected spots candidate, and the open circles are the local minima of another spot. (b): The residual errors between the original *Kepler* light curve and fitted one. (c): Phase-time diagram, where the vertical axis corresponds to phases of the local minima detected in the upper panels compared to the rotational period (cf., Carrington longitude). Symbols are the same as the above. Open circles correspond to another spot candidates, but they are not included in our catalog because their temporal evolutions are not well measurable. (d): The temporal evolution of the depth of the local minima from the nearby local maximums of the spot candidates that we focus on. The filled upward triangle is the local minima near the observational gaps. The open downward triangles indicate the upper limit of the brightness variation before the spot emerge and after the spot disappear. The black solid lines are fitted lines of the emergence and decay phase (for data unaffected by data gaps), and dashed lines are the same as solid one but fitted only for black circles. Figures for all the other 55 spot candidates are available in the online version of the Journal.

algorithm, a low degree polynomial is fitted to the data subset by using weighted least squares, where more weights are given to the nearby points. We used the $lowess$ function incorporated to the R package. The fitting passbands were selected to be $4\times P_{\rm rot}$ to avoid the over- and under-smoothing. We detected the local minima as downward convex points of the smoothed light curve; i.e. the smoothed stellar fluxes $F(t)$ satisfy $F(t_{\rm (n\text{-}m)}) < F(t_{\rm (n\text{-}m\text{-}1)})$ and $F(t_{\rm (n+m)}) < F(t_{\rm (n+m+1)})$. Here, m takes a value of [0, 1, 2], $t$ is time, and n is time step. [A] We start to trace them from an arbitrary local minimum ($T_0$), and at first search another local minimum whose time is between $T_0 + 0.8 \times P_{\rm rot}$ and $T_0 + 1.2 \times P_{\rm rot}$ (see Figure 2.2 for the visual explanations of the procedure [A] $\sim$ [E]). This range was determined to be able to cover the range of the solar-like differential rotation ($\Delta P/P_{\rm rot} \sim 0.2$). In case we find the next local minimum, we identify it as a next one ($T_1$). If we successfully trace more than three local minima in the same manner, we identify them as a single spot candidate, and continue the tracking. [B] After $T_2$, we decide to search the next local minimum as time in between $T_2 + 0.9 \times P_{\rm spot}$ and $T_2 + 1.1 \times P_{\rm spot}$, where $P_{\rm spot}$ is a rotational period of the spot candidate which is obtained in the procedure [A]. [C] In case that there are some observational data gaps, our algorithm is designed to be able to search a next local minimum until three rotational period ahead. The algorithm also search the local minima before the start point ($T_0$) by the same manner. If there is no local minimum in the next rotational phase, the algorithm stops to trace and switches to the next starting point ($T_0$).

After searching the spot candidates in a given star, the dubious candidates are automatically removed in the following procedure. [D] First, for a given spot candidate, if there are other local minima within $\pm 0.35 \times P_{\rm rot}$ of each $T_{\rm n}$ (n = 0$\sim$N, N+1 is the total number of local minima of the spot candidate), we remove the candidate because the spot area can be largely affected by the other spots. [E] Second, we extrapolated the "virtual" local minima for 3 period ahead and behind ($T_{-3,-2,-1}$ = $T_0$ - m$\times P_{\rm rot}$, $T_{N+1,N+2,N+3}$ = $T_N$ + m$\times P_{\rm rot}$, m is 1,2,3). If there are other local minima within $\pm 0.3 \times P_{\rm rot}$ of each "virtual" local minimum, we also remove the candidate because the spot can survive or combine with the other spot in longitude which is originally located at the different longitude. The values of 0.35 and 0.3 are longitude separation over which we regard a pair of spots as located on reverse phase (i.e. longitude separation $> 126°$, $108°$), and were determined based on the number of miss detections. If the values become smaller, the contaminations and mergings of other spots would not be negligible. Lastly, we measure the local depth of the local minima from the near local maxima as an indicator of spot area. To investigate the nature of a single star spot as well as to remove the beating spot candidate, we also remove the spot candidates whose local depth variation do not show clear emergence and decay phases. Here we simply use chi-squared test to judge whether it shows emergence or decay phase or not.

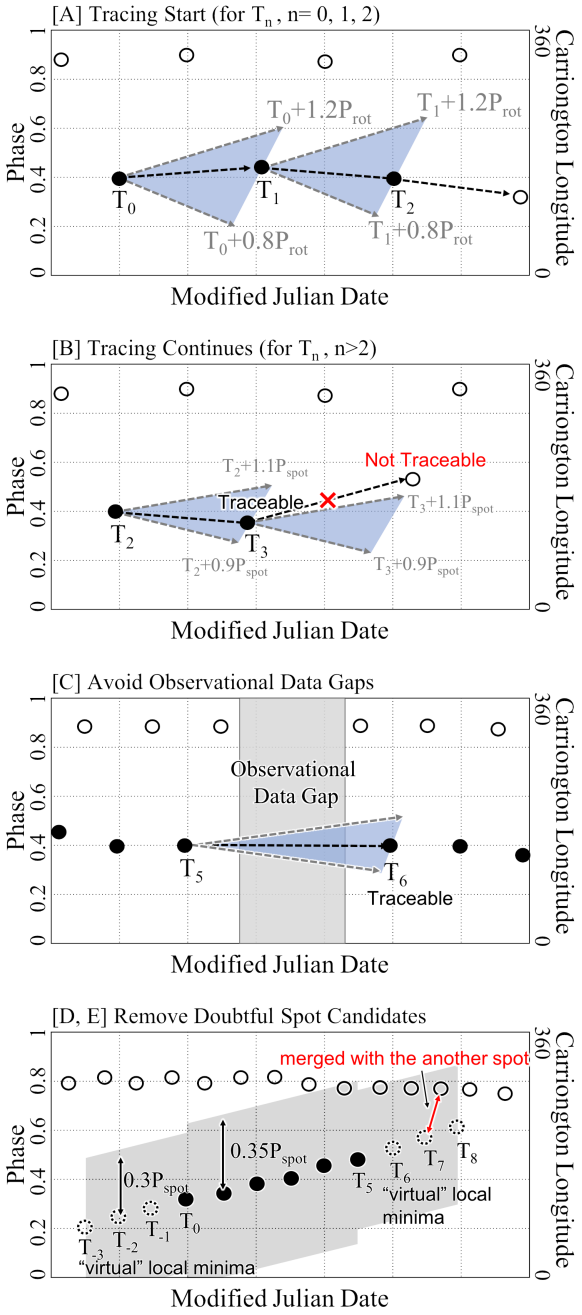


Figure 2.2: Schematic pictures to explain the method ([A] $\sim$ [E]) of tracing the local minima described in Section 2.2.2. All panels correspond to the phase-time diagram of local minima, which is similar to Figure 2.1(c). Each panel describe the following; [A] explains how to start the tracing and identification of spots, [B] how to continue the tracing after the identifications, [C] how to avoid the observational data gaps, and [D, E] how to remove the spot candidates that can merge with other spots in longitudes which are originally located at the separated longitudes. If there are other local minima in the gray region, the spot candidates are removed in our algorithm.

We applied the above automatical detection method to the 5356 solar-type target stars observed by the Kepler, and obtained 147 spot candidates. Visually checking all the light curves, phase-time diagrams of local minima, and temporal variations of local depth, we selected spot candidates that satisfy the following conditions: (1) The temporal variations show clear emergence and decay phases. We use a threshold that the first spot area $A(T_0)$ and final one $A(T_{\rm N})$ should be smaller than 70 % of the maximum size ($A_{\rm max}$), i.e. $A(T_0)$ $< 0.7 \times A_{\rm max}$ and $A(T_{\rm N}) < 0.7 \times A_{\rm max}$. See Section 2.2.3 for the detailed definitions of the spot area $A(t)$. This threshold was determined to exclude the doubtful spot candidates (e.g. a pair of beating spots). For example, if we choose 90 % as a threshold, we need to expect contaminations by considerable amount of dubious spot candidates. If the light curve satisfies this condition, it is easy to accurately measure the emergence and decay rates and extrapolate the variations to estimate the lifetimes. This threshold has been determined by trial and error. (2) The temporal evolutions of spot area show apparent single peaks. Note that we do not remove candidates whose temporal evolutions can be separated from the other spot candidates. (3) The observational noise is apparently much smaller than the spot amplitude. (4) The light curves show no apparent beat features during the lifetimes. (5) The observational gaps do not largely disturb the detection of local minima. (6) The local minima should not disappear during the lifetime for reasons other than observational gaps. (7) The local minima do not include any apparent miss detections of local minima. We conducted these treatments (1) – (7) with manual checking by more than three of the authors. According to this procedure, we successfully identified the temporal evolutions of 56 star spots listed in Table 1. As for the spot candidates, we also improved the light curve fittings. To avoid overfitting the flare signals, we simply detected large flare-like signals by using the threshold of superflare detections based on Maehara et al. (2012), and remove them with spline interpolation. After this process, we fit the long-period spot modulations by LOWESSFIT, where the fitting parameter are manually adjusted for each light curve. Then we re-detected the local minima and trace them in the same manner. These re-detected values are listed in Table 1.

### 2.2.3 Area estimation

We estimated the area of star spots based on the brightness depth of each local minimum ($\Delta F$) from the nearby local maximum. Deriving the spot area from the $\Delta F$ requires measurements of the spot temperature (e.g. Poe & Eaton, 1985). However, since the *Kepler* conducted single-bandpass observations, we cannot distinguish a decrease of the spot temperature from an increase of the spot area and vice versa. Here, we used the following empirical relation of spot temperature as a function of stellar effective temperature. According to Maehara et al. (2017), the area ($A_{\rm spot}$) can be derived as a function of the normalized amplitude ($\Delta F/F_{\rm star}$), stellar effective temperature ($T_{\rm star}$), and stellar radius

Table 2.1: Physical parameters of star spots and the host stars.

| *Kepler* ID | $T_{\rm eff}$* [K] | log $g^{\dagger}$ | $R_{\rm star}{}^{\ddagger}$ [$R_{\odot}$] | $P_{\rm rot}{}^{\S}$ [day] | $T^{\parallel}$ [day] | $A_{\rm max}{}^{\#}$ [$10^3$MSH] | $\Phi_{\rm max}{}^{\#}$ [$10^{23}$Mx] | $d\Phi_{\rm e}/dt^{**}$ [$10^{20}$Mx/h] | $d\Phi_{\rm d}/dt^{**}$ [$10^{20}$Mx/h] |
|---|---|---|---|---|---|---|---|---|---|
| 10186360 | 5994 | 4.48 | 0.92 | 7.3 | $73.7 \pm 8.3$ | $2.7^{+0.9}_{-0.6}$ | $1.4^{+0.8}_{-0.4}$ | $1.0^{+1.0}_{-0.6}$ | $1.4^{+1.3}_{-0.7}$ |
| 10328375[1] | 5631 | 4.48 | 2.07 | 5.1 | $63.9 \pm 1.7$ | $27.7^{+8.9}_{-6.7}$ | $72.1^{+43.6}_{-27.1}$ | $86.6^{+67.4}_{-38.9}$ | $102.2^{+73.5}_{-43.4}$ |
| 10736868 | 5505 | 4.44 | 1.16 | 6.3 | $57.2 \pm 20.1$ | $9.1^{+2.0}_{-1.7}$ | $7.5^{+2.9}_{-2.2}$ | $9.1^{+7.8}_{-4.9}$ | $6.8^{+3.8}_{-2.6}$ |
| 10802309[1] | 5403 | 4.61 | 1.43 | 2.0 | $65.0 \pm 21.7$ | $17.5^{+4.1}_{-3.5}$ | $21.7^{+9.4}_{-6.9}$ | $26.8^{+14.4}_{-9.9}$ | $15.3^{+9.5}_{-6.3}$ |
| 10818810 | 5869 | 4.38 | 0.96 | 6.0 | $17.0 \pm 5.1$ | $3.6^{+0.9}_{-0.6}$ | $2.0^{+0.9}_{-0.5}$ | - | - |
| 10936008 | 5271 | 4.58 | 0.75 | 9.3 | $37.2 \pm 18.5$ | $2.2^{+1.0}_{-0.7}$ | $0.7^{+0.6}_{-0.3}$ | - | - |
| 10969515 | 5380 | 4.50 | 0.95 | 5.5 | $58.6 \pm 10.5$ | $4.9^{+1.2}_{-0.9}$ | $2.7^{+1.2}_{-0.8}$ | $5.5^{+4.1}_{-2.5}$ | $1.9^{+1.5}_{-0.9}$ |
| 11033729 | 5399 | 4.59 | 0.74 | 10.2 | $244.4 \pm 19.3$ | $4.8^{+1.1}_{-0.9}$ | $1.6^{+0.7}_{-0.5}$ | $0.3^{+0.2}_{-0.1}$ | $1.1^{+0.6}_{-0.4}$ |
| 11046341 | 5597 | 4.39 | 0.84 | 16.3 | $111.1 \pm 29.9$ | $6.3^{+1.3}_{-1.1}$ | $2.7^{+1.1}_{-0.8}$ | $1.6^{+1.8}_{-1.1}$ | $1.7^{+0.7}_{-0.5}$ |
| 11080702 | 5307 | 4.58 | 0.88 | 9.2 | $86.7 \pm 3.7$ | $4.2^{+0.6}_{-0.5}$ | $2.0^{+0.5}_{-0.4}$ | $2.3^{+1.0}_{-0.7}$ | $1.4^{+0.6}_{-0.4}$ |
| ... | ... | ... | ... | ... | ... | ... | ... | ... | ... |
| 9408373 | 5782 | 4.49 | 0.91 | 5.1 | $31.7 \pm 1.6$ | $2.8^{+0.7}_{-0.5}$ | $1.4^{+0.7}_{-0.4}$ | $2.9^{+2.4}_{-1.4}$ | $5.0^{+4.2}_{-2.4}$ |
| 9579266 | 5164 | 4.60 | 0.83 | 10.6 | $63.2 \pm 10.0$ | $2.6^{+1.0}_{-0.7}$ | $1.1^{+0.7}_{-0.4}$ | - | $0.8^{+0.7}_{-0.4}$ |

[1] Subgiant or main-sequence binary candidates (Berger et al., 2018). [2] cool main-sequence binary candidates (Berger et al., 2018).
*Stellar effective temperature taken from *Kepler* Input Catalog (Kepler Data Release 25 Notes, Thompson & Caldwell, 2016).
†Stellar surface gravity taken from *Kepler* Input Catalog. ‡Corrected stellar radii by Berger et al. (2018).
§Stellar rotational periods. ‖Lifetimes of star spots.
#Maximum star spot area and magnetic flux in the unit of MSH and Mx, respectivitly.
**Emergence and decay rates of star spots in the unit of Mx per hour.

($R_{\rm star}$):

$$A_{\rm spot} = \left(\frac{R_{\rm star}}{R_{\odot}}\right)^2 \frac{T_{\rm star}^4}{T_{\rm star}^4 - \{T_{\rm star} - \Delta T(T_{\rm star})\}^4} \frac{\Delta F}{F_{\rm star}}, \quad (2.1)$$

$$\Delta T(T_{\rm star}) = T_{\rm star} - T_{\rm spot} = 3.58 \times 10^{-5} T_{\rm star}^2 + 0.249 T_{\rm star} - 808, \quad (2.2)$$

where $\Delta T$ is temperature difference between photosphere and spot derived based on Berdyugina (2005). The spot temperature is basically estimated by the Doppler imaging technique of several main-sequence stars. Since this relation is just an empirical one, the spot area can change if the actual spot temperature varies. However, the variation of the temperature by ± 500 K (± 1000 K) could vary the spot area by only 11 % (23 %). Therefore, our results would not be significantly affected by the assumption of temperature. Here, the stellar effective temperature (T) is based on the *Kepler* Input Catalog (Kepler Data Release 25, Thompson & Caldwell, 2016). As for the stellar radius, we use the radius values updated by using recent *Gaia* satellite Data Release 2 (Berger et al., 2018; Lindegren et al., 2018).

Note that the estimated area can be somewhat underestimated due to inclinations of the stellar rotational axes and the contaminations of brightness from other spots. The latter may be corrected by modeling the light curves, but we simply use the local depth of light curves as an indicator of spot area. Moreover, the faculae on the stellar surface can also contribute to the over- and under-estimation of the star spot area. In Section 2.4.5, the uncertainties by those effects are clarified, while they are not incorporated to the estimations

in this paper. In Appendix A.1, we simply evaluated accuracies of the area estimations on the basis of the Sun-as-a-star analysis.

### 2.2.4 Lifetime estimation

We measured the lifetimes ($T_1$) of the 56 star spots based on how long the local minima are detectable (i.e. $t_N - t_1$). The lifetimes ($T_1$) can be, however, underestimated because the detectable limits of amplitude can largely suffer from noises and contaminations of other spots. Therefore, we fitted the emergence and decay phases with linear relations (solid lines in Figure 2.1(d)) and estimated the lifetimes ($T_2$) from spot emergence to disappearance. In the following section, we defined the lifetime ($T$) as ($T_1 + T_2$)/2, the lower limit as $T_1$, and the upper limit as $T_2$. Note that $T_2$ are not exactly the upper limit values, but extrapolated ones by assuming the linear emergence and decay. As mentioned in the following, it may be better to fit by assuming parabolic decay. However, the decay phases do not necessarily show the clear parabolic decay curves, so we use this assumption.

### 2.2.5 Calculation of emergence and decay rates of star spots

We estimated the emergence ($d\Phi_{\rm e}/dt$) and decay rates ($d\Phi_{\rm d}/dt$) of the star spots based on the variation rates of star spot area. The variation rates are considered to be better indices when comparing with sunspot properties because they are unaffected by the detectable limits of local minima unlike the lifetimes. We derived the variation rates of star spot area (emerging rate $dA_{\rm e}/dt$ and decay rate $dA_{\rm d}/dt$) by applying the linear regression fitting method to spot area variations. Many papers have reported variation rates of sunspots in the unit of Mx = G$\cdot$ cm$^2$ (e.g. Norton et al., 2017). Taking this fact into account, we calculated the emergence and decay rates by assuming that the mean magnetic field of star spots is 2000 G considering the typical magnetic field strength of sunspots (Solanki, 2003):

$$\frac{d\Phi_{\rm e,d}}{dt} = 2000 \times \frac{dA_{\rm e,d}}{dt}. \tag{2.3}$$

The error values are mainly estimated based on the errors of the fitted slopes, stellar effective temperature, and stellar radius.

## 2.3 Result

### 2.3.1 Temporal evolutions of star spots

Figure 2.1 shows an example of the temporal evolutions of star spots in our catalog. Figure 2.1(a) shows a light curve and circles are the detected local minima. Figure 2.1(c) shows

time-phase diagram, where the vertical axis is the rotational phase of the detected local minima. The gray solid line is an individual spot component that we detected. Figure 2.1(d) shows the temporal evolution of the local depth of each local minima that correspond to the star spot area. As described in Section 2.2, we selected star spots showing clear emergence and decay, and such features can be also seen in Figure 2.1.

As a result of these analyses, the area of the detected star spots are 1500–23000 MSH at the maximum, and the lifetimes are 10–350 days (see Table 1). The lifetime of one year is the longest ever observed for the solar-type stars ($\lesssim$ 200 days in the previous studies: Bradshaw & Hartigan, 2014; Davenport, 2015; Giles et al., 2017). In the case of the sunspots, there is a notable asymmetry in emergence and decay phase as mentioned in Section 2.1. However, in the case of star spots, the averaged emergence rates $6.6 \times 10^{20}$ Mx·hr$^{-1}$ (11 MSH·hr$^{-1}$) are not so much different from the averaged decay rates $5.2 \times 10^{20}$ Mx·hr$^{-1}$ (8.5 MSH·hr$^{-1}$). Interestingly, in several spots, emergence phase are longer than the decay phase (see the figures in the online version of the Journal for the detail). There is a possibility that not only the area but also lifetimes can have some uncertainties caused by the data sensitivity and analytical method. The uncertainties are discussed in Section 2.4.5.

### 2.3.2 Star spot properties versus stellar properties

Figure 2.3 shows stellar radius as a function of the effective temperature (i.e. HR diagram). Background black shades indicate distributions of *Kepler* stars and colored symbols indicate our catalog. The vertical axis values are plotted with revised radii based on quite recent Gaia DR2 parallaxes provided by Berger et al. (2018). According to Berger et al. (2018), four of our “solar-type" stars are classified into subgiant stars or main-sequence binaries stars (green triangles), and two are classified into main-sequence binary star candidates (blue diamonds), although they are solar-type stars according to the *Kepler* Input Catalog. In the following figures and discussions, we only focus on the temporal evolutions of star spots on main-sequence stars.

Figure 2.4 shows a comparison between stellar effective temperature and lifetimes of star spots. There seems to be no clear temperature dependence even for a given spot size, although Giles et al. (2017) have reported that cooler stars have spots that last much longer. This might be due to our small number of samples and small range of temperature. We focus only on G-stars while they analyzed F, G, K, M-stars. In this paper, we do not discuss the relation between stellar effective temperature and star spot properties because of shortage of samples and range of stellar properties. Nevertheless, the dependence of temperature on the lifetimes is quite interesting to investigate the role of differential rotation

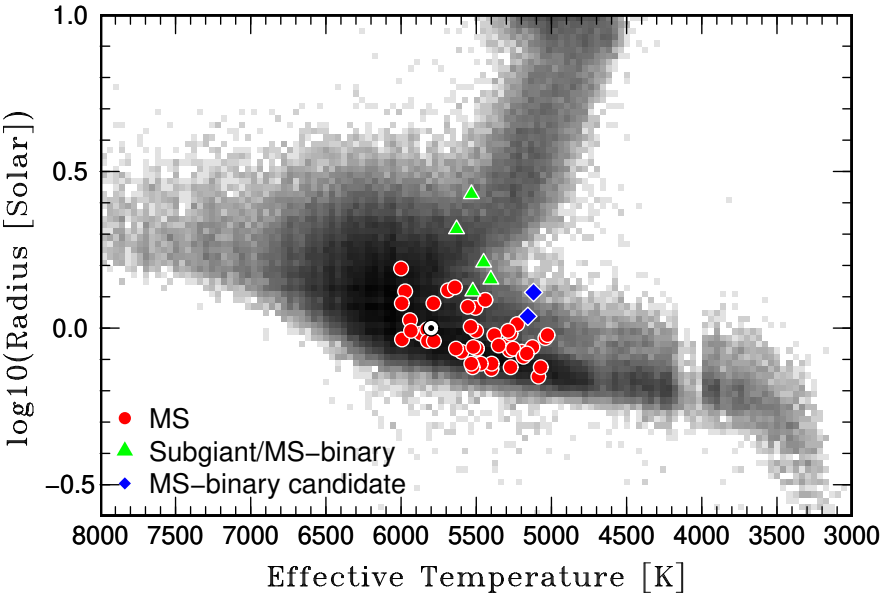


Figure 2.3: Radius versus effective temperature. Background black shades indicate distributions of *Kepler* stars with revised radii based on Gaia DR2 parallaxes presented in Berger et al. (2018). Red circles, green triangles, and blue diamonds are solar-type stars in our catalog, which had been judged as solar-type stars in *Kepler* Input Catalog (Kepler Data Release 25 Notes, Thompson & Caldwell, 2016). They are classified as main-sequence stars, subgiant stars/main-sequence binary stars, and main-sequence binary stars, respectively (Berger et al., 2018). Solar value is also plotted for reference (the circled dot).

and convection in the spot fragmentations. This dependence is subjected to consideration in the future study.

Figure 2.5 shows a comparison between rotational periods and lifetimes of star spots and there looks to have a positive correlation. Please note that there are an undetectable region because our algorithm can detect spots whose lifetimes are longer than a couple of rotational periods.

### 2.3.3 Comparison with sunspot I: lifetime versus maximum area

Figure 2.6 shows a comparison between the maximum area and lifetimes of the star spots in our catalog. We plotted the star spot data for slowly rotating stars ($P_{\rm rot} > 7$ days) and rapidly rotating ones ($P_{\rm rot} < 7$ days), separately. There seems to be a weak positive correlation between them.

Figure 2.7 shows a comparison between the maximum area and lifetime of sunspots and star spots on solar-type stars. Black and gray points are sunspot data taken from Petrovay & van Driel-Gesztelyi (1997) and Henwood et al. (2010), respectively. These sunspot data

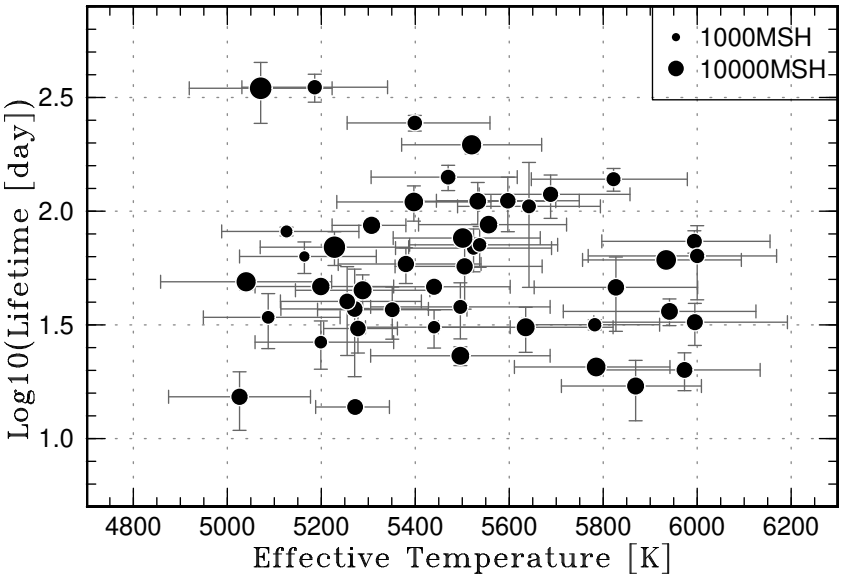


Figure 2.4: Comparison between the stellar effective temperatures ($T_{\rm eff}$) and lifetimes of star spots. The size of each circle corresponds to the maximum area of the star spot. The temperatures and the error bars are taken from *Kepler* Input Catalog (Kepler Data Release 25 Notes, Thompson & Caldwell, 2016).

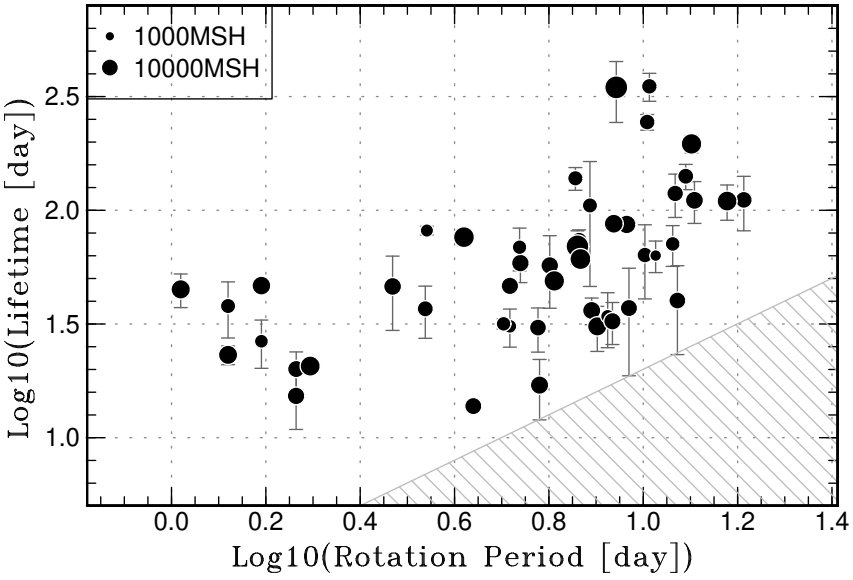


Figure 2.5: Comparison between the stellar rotation period ($P$) and lifetimes of star spots. The size of each circle represents the maximum area of the star spot.

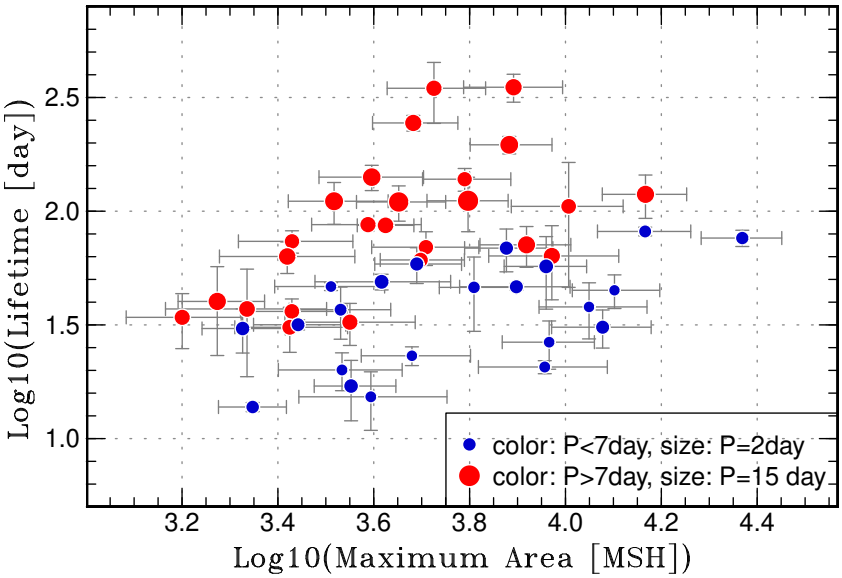


Figure 2.6: Comparison between maximum areas and lifetimes ($T$) of the detected star spots on solar-type stars. The area is plotted in the unit of million solar hemisphere (1MSH = $10^{-6} \times 2\pi R_{\odot}^2$). The size of each circle represents the stellar rotational period. Blue and red colors correspond to the spots with $P_{\rm rot} < 7$ day and $P_{\rm rot} > 7$ day, respectively.

are basically measured by using the Debrecen Photoheliographic Results and Greenwich Photoheliographic Results, respectively. They are available upon the databases recording day–to–day individual sunspot areas. Note that, since the identification of recurrent sunspots is based only on its longitude and latitude, the succeeding spot emergence in the decaying active regions can be identified as a single spot. For example, Kopecky (1984) have reported long-lived sunspot groups surviving during 8 solar rotation by use of Greenwich Photoheliographic Results. The temporal development of spot area shows, however, several peaks, which indicates successive episodes of spot emergence in the same region. Our main purpose is to reveal a star spot physics from the basic sunspot physics, and the comparison with such sunspots with several emergence would lead to more complex discussions. Therefore, as for the data of Henwood et al. (2010), we have excluded the sunspots whose temporal evolutions show multiple growths for matching our star spots that have only simple emergence-decay patterns. The resulting lifetimes of sunspots are up to 6 solar rotational period ($\sim$200 days) and the area is up to $\sim$6000 MSH. The dashed line indicates the GW relation mentioned in Section 2.1 ($A = DT$, $D \sim 10$ MSH·day$^{-1}$).

In Figure 2.7, we also plotted star spots on solar-type stars with red and blue filled circles for slowly ($P_{\rm rot} > 7$ days) and rapidly rotating stars ($P_{\rm rot} < 7$ days), respectively. We found that the lifetimes of large star spots (10$\sim$350 day) are shorter than those expected from the GW relation (300$\sim$1000 day). This trend is similar to the results reported in the other

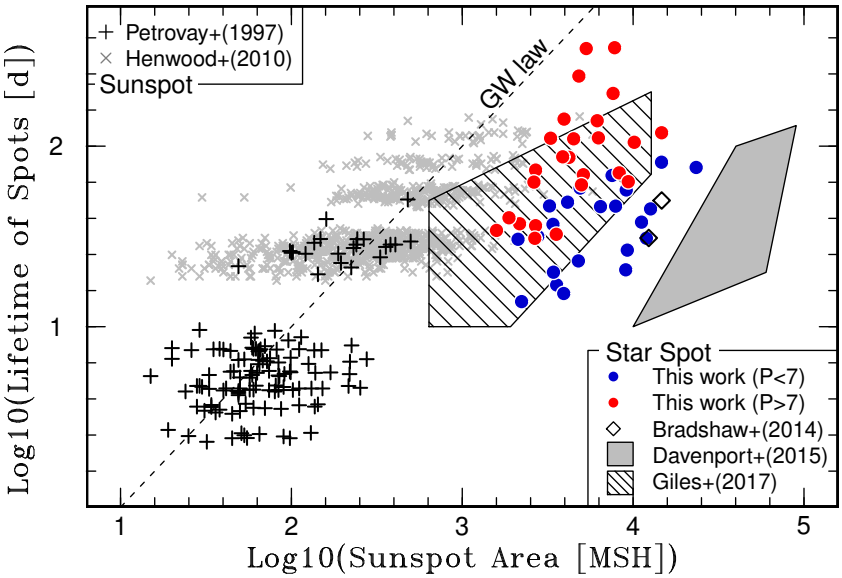


Figure 2.7: Comparison between maximum spot area and lifetime of sunspots and star spots on solar-type stars. Black and gray crosses are sunspots data taken from Petrovay & van Driel-Gesztelyi (1997) and Henwood et al. (2010), respectively. The dashed line indicates the solar GW relation ($A = DT$, $D \sim 10$ MSH·day$^{-1}$). Blue and red circles correspond to the spots analyzed in this study with $P_{\rm rot} < 7$ day and $P_{\rm rot} > 7$ day, respectively. Open diamonds are star spots on G-type stars (Kepler-17 and CoRoT-2) taken from Bradshaw & Hartigan (2014). A grayed filled region indicates star spots on Kepler-17 detected in Davenport (2015). Note that the area and lifetimes of star spots on Kepler-17 are also estimated in Bradshaw & Hartigan (2014), but there is a factor gap in spot area between Bradshaw & Hartigan (2014) and Davenport (2015). A region filled with diagonal lines indicates the result of Giles et al. (2017).

previous researches. We plotted the star spots that were reported in Bradshaw & Hartigan (2014), Davenport (2015), and Giles et al. (2017). Note that the data of Giles et al. (2017) are given in the unit of brightness variation amplitude in their paper, so we plotted their G-type star data by assuming that all of the effective temperatures and radii are the same as the solar values. As a result, we found that our results are consistent with that of Giles et al. (2017), and partly similar to that of Bradshaw & Hartigan (2014). The spot area of Davenport (2015) are much larger than our data, while the lifetimes are similar to our results.

### 2.3.4 Comparison with sunspot II: emergence rates versus maximum flux

Figure 2.8 shows a comparison between the emergence rates and maximum fluxes of sunspots and star spots on solar-type stars. The solar values are based on the magnetogram

observation carried out by Otsuji et al. (2011), Toriumi et al. (2014), and Norton et al. (2017). The grayed dotted lines are the 95% confidence intervals of the sunspot observational data. As a result of comparison, 76% of the star spots are consistently included inside the extrapolated 95% confidence intervals of sunspots. Particularly, the emergence rates of star spots are consistent with an empirical line ($d\Phi_e/dt \propto \Phi^{0.3}$) derived by Norton et al. (2017). The standard deviations of difference between star spot observations and the empirical line are $7.1\times10^{20}$ Mx·h$^{-1}$. On the other hand, they are mostly smaller than those expected from a simple theoretical line ($d\Phi_e/dt \propto \Phi^{0.5}$) derived by Otsuji et al. (2011). The standard deviations of difference between star spot observations and the theoretical line are $9.5\times10^{20}$ Mx·h$^{-1}$. Moreover, the emergence rates of star spots looks to be dependent of the stellar rotational period dependence. The star spots on slowly rotating stars shows relatively small values, which is similar to the case of the lifetimes of star spots.

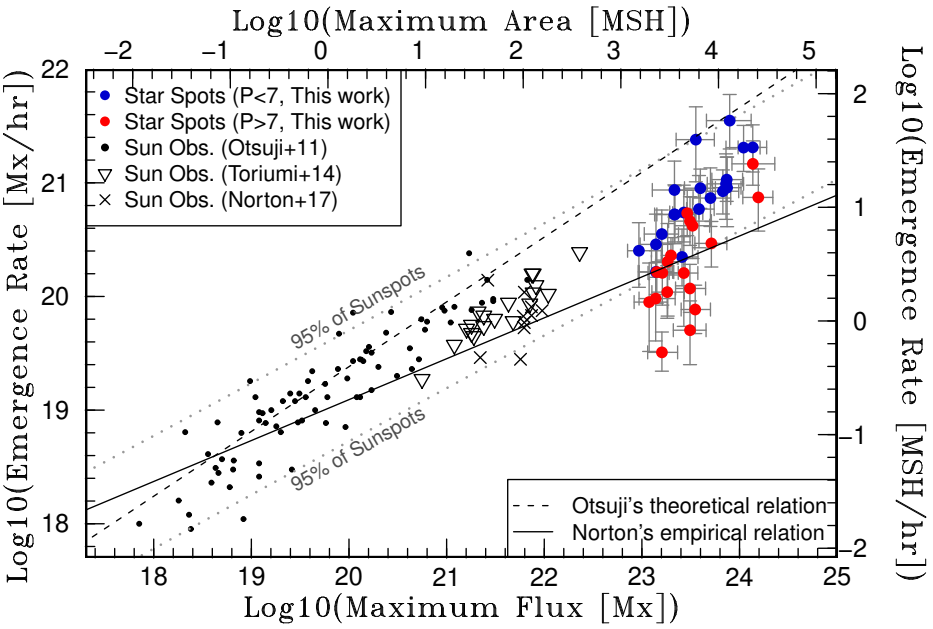


Figure 2.8: Comparison between maximum magnetic flux ($\Phi$) and emergence rate ($d\Phi_e/dt$) of sunspots and star spots on solar-type stars. Black points, downward triangles, and crosses are sunspots observational data taken from Otsuji et al. (2011), Toriumi et al. (2014), and Norton et al. (2017), respectively. Blue and red circles correspond to the spots analyzed in this study with $P_{\rm rot} < 7$ day and $P_{\rm rot} > 7$ day, respectively. A solid ($d\Phi_e/dt \propto \Phi^{0.3}$) and dashed line ($d\Phi_e/dt \propto \Phi^{0.5}$) is a scaling relation derived by Norton et al. (2017) and Otsuji et al. (2011), respectively. The standard deviations of the star spot data compared with the scaling laws are $7.1\times10^{20}$ and $9.5\times10^{20}$ for Norton's and Otsuji's scaling law, respectively. Dotted lines are upper and lower of the 95% confidence interval for the sunspot observations. 76% of the star spots are located in the extrapolation of this 95% confidence interval.

### 2.3.5 Comparison with sunspot III: decay rate versus maximum flux

Figure 2.9 shows a comparison between the decay rates and maximum fluxes of sunspots and star spots on solar-type stars. Black points are based on the visible sunspot observations (Hathaway & Choudhary, 2008; Petrovay & van Driel-Gesztelyi, 1997), while the green points are based on the magnetogram observations (Kubo et al., 2008; Norton et al., 2017). The grayed dotted lines are the 95% confidence intervals of the sunspot observational data of Hathaway & Choudhary (2008). The order of the confidence intervals is about one order of magnitude, which is roughly the same as those of emergence rates. As a result, the decay rates of star spots are also consistent with those of sunspots, while some parts are smaller than those expected from the sunspot distributions. 89% of the star spots are included inside the extrapolated 95% confidence intervals of sunspots data of Hathaway & Choudhary (2008). The decay rates, including simulations, are roughly on the same lines (a solid line in Figure 2.9; $d\Phi_{\rm d}/dt \propto \Phi^{0.5}$) over a wide range of magnetic flux ($10^{21}$–$10^{24}$ Mx, 20–20000 MSH). Also, a rotational period dependence can be also seen in the case of decay rates.

## 2.4 Discussion

### 2.4.1 Emergence of star spots

We showed that the emergence and decay rates of star spots as a function of maximum fluxes are mostly consistent with those extrapolated from the sunspot observations. This may suggest that the temporal evolutions of sunspot and star spot can be universally explained by the same underlying physical processes. As for the emergence, we found that the emergence rates of star spots favor the empirical relation $d\Phi_{\rm e}/dt \propto \Phi^{0.3}$ (Norton et al., 2017), but are smaller than those expected from the theoretical scaling relation $d\Phi_{\rm e}/dt \propto \Phi^{0.5}$ (Otsuji et al., 2011).

Otsuji et al. (2011) derived the simple theoretical scaling law $d\Phi_{\rm e}/dt \propto \Phi^{0.5}$ by assuming that (1) the emerging flux is self-similar in its size ($\Phi_{\rm e} \propto wh \propto w^2$: $w$ is horizontal, and $h$ is vertical length of its cross section) and (2) the rise velocity ($v$) is independent of its size ($d\Phi_{\rm e}/dt \propto vw \propto w$). In spite of these rough assumptions, the scaling law agrees with their own observational data.

If we discuss the results on the basis of the theoretical scaling law ($d\Phi_{\rm e}/dt \propto \Phi^{0.5}$), there is a possibility that the emergence rates of star spots are suppressed to lower values for some reasons. One explanation for the lower values is that the observed large star spots ($\sim 3 \times 10^{23}$ Mx, $\sim 5000$ MSH) can be conglomerates of relatively smaller sunspot-scale spots (e.g. $\sim 10^{22}$ Mx, $\sim 160$ MSH). If the large star spots are conglomerates of

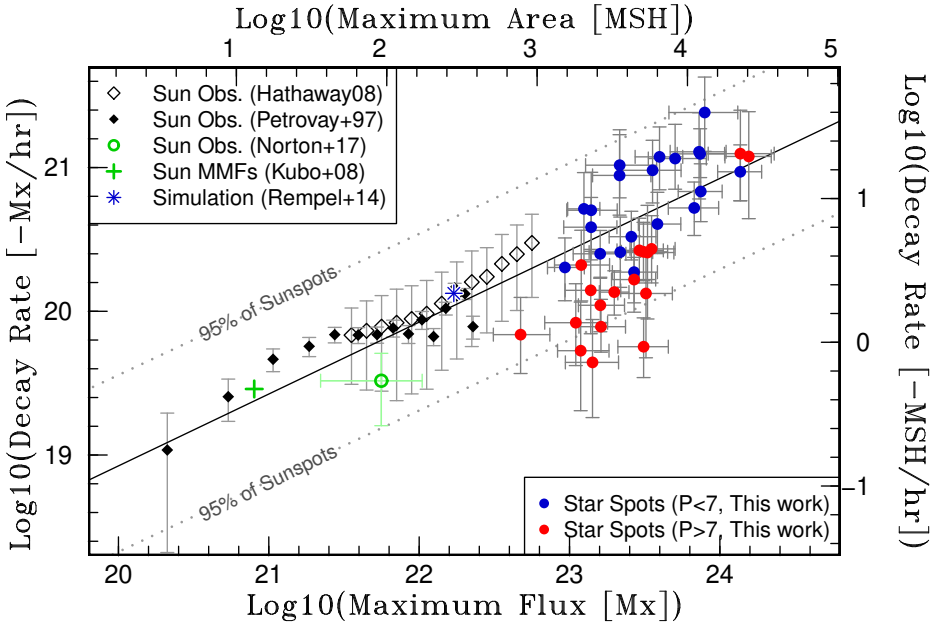


Figure 2.9: Comparison between maximum magnetic flux ($\Phi$) and decay rate ($d\Phi_{\rm d}/dt$) of sunspots and star spots on solar-type stars. Black open and filled diamonds are sunspot's observations by Hathaway & Choudhary (2008) and Petrovay & van Driel-Gesztelyi (1997), respectively. Note that the error bars of Hathaway & Choudhary (2008) indicate 1-$\sigma$ level of their data, and those of Petrovay & van Driel-Gesztelyi (1997) indicate 3-$\sigma$ level. As for the data of Petrovay & van Driel-Gesztelyi (1997), the area is not the maximum area but the area when the decay rates are measured. A green circle shows sunspot observations with *SDO* magnetogram (Norton et al., 2017), and a green cross is a sunspot decay rate owing to moving magnetic features (MMFs; Kubo et al., 2008). Blue and red circles correspond to the spots analyzed in this study with $P_{\rm rot} < 7$ day and $P_{\rm rot} > 7$ day, respectively. Blue asterisks are the result of a simulation performed by Rempel & Cheung (2014). Dotted lines are upper and lower of 95% confidence levels for the sunspot observations (Hathaway & Choudhary, 2008). 89% of the star spots are located in this extrapolation of 95% confidence interval. A solid line is the line of $d\Phi_{\rm d}/dt \propto \Phi^{0.5}$, where the absolute values are derived based on mean values of the sunspot observations (Hathaway & Choudhary, 2008).

smaller spots and the smaller spots emerge successively, the smaller emergence rates can be understood by extrapolating the emergence rates of sunspots.

On the other hand, from the standpoint of the solar empirical relation ($d\Phi_{\rm e}/dt \propto \Phi^{0.3}$; Norton et al., 2017), some corrections of the Otsuji's scaling law are necessary to theoretically understand the small power-law index. For example, if emerging velocity has a negative dependence on the total flux (i.e. $v \propto \Phi^{\rm a}$, a $< 0$), the empirical relation could be theoretically explained. One explanation for the negative dependence is that the flux emergence could be suppressed to some extent if the surfaces are already filled with relatively strong magnetic fields. As another hypothesis, since the emergence of a weak flux tube can be affected by convective motions (Weber et al., 2011), emergence velocity of small weak flux becomes faster if the field strengths have a positive relation with the total fluxes.

As discussed above, the flux emergence process can be universally explained over a wide range of spot sizes including sunspots and star spots ($10^{18\sim24}$ Mx, $0.02 \sim 20000$ MSH), although the detailed understanding is not enough. It should be noted that our results may contain some uncertainties and they can be updated by further studies. The emergence process of sunspots inside the convection zone is not well understood observationally even by the local helioseismology. Although a comparison with numerical simulations can help us interpret the observations (e.g. Rempel & Cheung, 2014), the realistic ones with deep convection zone have not been done. More researches on spot emergence by sunspot observations and simulations are necessary.

### 2.4.2 Decay of star spots

Our results show that the decay rates of star spots are consistent with those of sunspots, and the sunspot distributions ($d\Phi_{\rm d}/dt \propto \Phi^{\sim0.49}$) almost correspond to the parabolic decay law ($d\Phi_{\rm d}/dt \propto \Phi^{\sim0.5}$, Martinez Pillet et al., 1993). This may suggest that sunspot and star spots are universally explained by the parabolic decay model, where spots decay by the erosion of the spot boundaries.

It should be noted here that Petrovay & van Driel-Gesztelyi (1997) suggested a corrected parabolic decay law in the form of $dA/dt \propto (A/A_{\rm max})^{0.5}$. This may not match our data because the theory predicts that $dA/dt|_{A=A_{\rm max}}$ is a constant value independent of the spot size.

On the other hand, if we want to justify the linear decay theory ($dA/dt \propto$ constant), some excuses may be necessary. In this case, decay rates should be, possibly apparently, enhanced only for large spots to explain the observations. Possible interpretations can be explained as follows: (1) The decay rates of large spots are apparently enhanced because large sunspots can consist of many small sunspots (e.g. Hathaway & Choudhary, 2008) or

different active regions on opposite latitudes. In addition, many of large sunspots are classified into complex shapes, which can enhance flux cancellations (Martinez Pillet et al., 1993), although surface flux transport simulations are unsupportive for this (Işık et al., 2007). (2) Stellar differential rotation can also contribute to high decay rate of large spots (Hall & Henry, 1994). Işık et al. (2007) also showed that differential rotations can accelerate flux cancelations depending on the tilt angle of bipole. (3) Bradshaw & Hartigan (2014) tried to explain the high magnetic diffusivity on stellar surface by assuming that supergranular scales determine the decay timescales, though the roles of supergranule are not well understood.

Recent MHD numerical simulations can give us more insights into the star spot decay. Rempel & Cheung (2014) performed 3-dimensional numerical simulations of spot emergence and decay. The decay rate obtained by their simulations is also plotted in this Figure 2.9. In the first decay phase in their simulations, the dispersal of flux is mainly due to the downward vertical convection motion. In the late phase, intrusions of plasma in subsurface accelerate the spot fragmentations. Their result indicates that the subsurface large-scale convectional flows can play a significant role in spot decay. However, numerical box is limited only for the surface of convection zone and the subsurface morphology is little known observationally (Rempel & Schlichenmaier, 2011). Further development of numerical simulations including a deep convection zone may reveal the spot decay mechanism.

Usage of the Doppler imaging technique can let us measure the temporal evolutions of star spots as well. A decay rate of the red giant star XX Triangulum was estimated to be -5.6$\times10^{22}$ Mx·h$^{-1}$ (-920 MSH·h$^{-1}$) with the area of 1.2$\sim$6.2$\times10^{26}$ Mx (2$\sim$10$\times10^{6}$ MSH) according to the Doppler imaging method (Künstler et al., 2015). The decay rate is surprisingly consistent with the parabolic decay relation in our paper (Figure 2.9), although its surface effective temperature (4,620 K) and gravity (log $g$ = 2.82) are quite different from those of solar-type stars. Red giant stars or cooler stars will be subjected to consideration in our next paper, as these stars are currently beyond the scope of this paper.

This is an incipient research on the temporal evolutions of unresolved star spots. Further development in sunspot and star spots observations as well as numerical simulations are required for the understandings of decay process of star spots.

### 2.4.3 Lifetime of star spots

Historically, the spot evolutions have been discussed in terms of the lifetimes, and the simple GW law ($T \propto A$) has been used in the solar community (see Section 2.1). In contrast, the lifetimes (10 days $\sim$ 350 days) of star spots on solar-type stars are much shorter than those extrapolated from the GW relation (300 days $\sim$ 1000 days).

If we assume that the emergence and decay rates are independent of the (total) spot fluxes ($d\Phi_{\mathrm{e,\,d}}/dt$ = constant), spot lifetimes naturally follow the GW law (Meyer et al., 1974), which is inconsistent with star spot data. However, as discussed in Section 2.4.1 and 2.4.2, the emergence and decay rates clearly depend on the spot area across wide ranges of total fluxes ($d\Phi_{\mathrm{e,\,d}}/dt \propto \Phi^{0.3\sim0.5}$). This dependence of variation rates on the maximum sizes would be one reason why the lifetimes of star spots are much less than those expected from the GW law. In this case, the relation between lifetimes and area can be expressed as $T \propto A^{0.5\sim0.7}$. We discuss detection limits and method dependences on star spot lifetimes in Section 2.4.5.

Interestingly, ground based observations have revealed that HR 7275, a RS CVn-type K1 III-IV star, has spots with much longer lifetimes ($\sim$2.2 years on average, Strassmeier et al., 1994), although the spot areas are also huge. Moreover, cooler stars are reported to have longer lifetimes (Giles et al., 2017). The differences in lifetimes can reveal the role of surface convection in spot decay. Moreover, in the rapidly rotating young star V410 Tau, a large spot near the pole has persisted for at least 20 yr (Carroll et al., 2012), and FK Comae giant HD 199178 has a polar spot whose lifetime is more than 12 yr (Strassmeier et al., 1999). These properties of polar spots can be different from the solar-like spots at lower latitude. The comparison between different types of stars are beyond the scope of this paper, but will be addressed in future.

### 2.4.4 Rotational period dependence

Since the rotational period is a good indicator of the stellar ages, the dependence on the temporal evolutions can be a hint to the understandings of the evolutions of stellar dynamo. As in Section 2.3, the star spots on rapidly rotating stars tend to show more rapid emergences and decays compared to the spots on the slowly rotating ones. The rapid decay can be explained by the stellar differential rotation because rapidly rotating stars are thought to have a strong differential rotations (e.g. Hotta & Yokoyama, 2011; Balona & Abedigamba, 2016). Here, we only selected star spot pairs whose relative longitude are considered to be unaffected by the stellar differential rotation. Since the rotational periods of the pairs are not completely the same value, there is a possibility that the strong surface differential rotations on rapidly rotating stars makes it difficult to trace the local minima for a long time, which can result in short lifetimes in rapidly rotating stars. On the other hand, according to Giles et al. (2017), there is no clear dependence on the rotational period on the decay timescale of star spots. They however analyzed only the relatively slowly rotating stars (10 and 20 days), and the application to the more rapidly rotating stars have not yet been done. The detailed dependence of rotational periods should be researched in future.

### 2.4.5 Uncertainties on the measurements of lifetime and area

Let us summarize here uncertainties and biases of the results which can be caused by our method. First, we do not correct the star spot area for the stellar inclination angles. The star spot area, as well as variation rates, can be somewhat underestimated if the stellar inclination angles (sin *i*) are small (Notsu et al., 2015b) or the spots are located on the high latitude. Under the assumption of the random orientation of rotational axes, the average inclination angle ($i$) can be derived as 1 radian. If we assume this typical inclination angle, the stellar inclination reduces the statistical values of star spot area by $\sim$30% for the sun-like star spot distribution (latitude $\sim$ 10-30°; Solanki, 2003).

Second, the determination of the unspotted brightness levels of the stars is subjected to difficulty, affected by the existence of faculae and large polar spots, and the inevitable Kepler's long-term observational trend. However, we calculate the spot area from the brightness differences from the local maxima and minima. These are the relative values and less affected by the zero-levels. Even if the stellar unspotted level becomes brighter by 1% (e.g. solar faculae; Solanki et al., 2013), the spot size can decrease only by a few per cent. Likewise, we ignore the contributions of stellar faculae to the stellar brightness variations because the distributions and filling factors are not well known. If the faculae are localized in a single hemisphere and the brightness contributions of faculae are comparable to those of spots, the spot area can be both over- and under-estimated to some extent.

Third, since we used the local depth as the spot area, contaminations of other spots are not corrected in this analysis. This also contribute the uncertainties of the estimation of spot area. To avoid this effect, light-curve modelings with several star spots would be necessary for more detailed analyses.

Moreover, it should be noted here that lifetimes can have some uncertainties due to observational and analytical problems. The star spots become difficult to detect as the spot area decrease depending on the photometric errors and analysis methods, which leads to the underestimations of the spot lifetimes. Although we extrapolated the lifetimes by assuming linear emergence and decay, it is just an assumption. In addition, there can be a selection bias that long-lived spots with lifetimes of $\gtrsim$1,000 days can be missed because the *Kepler* observational period is limited to only $\sim$4 years. In this case, the emergence and decay rates can be smaller than our results.

Davenport (2015) have reported the lifetime of star spots by using exoplanet transits, and their results are somewhat different from our results. Their methods have an advantage that they can spatially resolve the stellar surface, and their lifetime and star spot area may more clearly represent the single star spot properties (see Chapter 3 for the detailed comparison and collaborations with Davenport (2015)).

## 2.5 Summary

The subject of this study is to investigate the emergence and decay processes of large star spots on solar-type stars by comparing them with well-known sunspot properties. We have developed a method to measure the temporal evolutions of single star spots by tracing local minima of visible continuum brightness variations. By applying this method to a huge amount of *Kepler* data, we have successfully detected temporal evolutions of star spots showing clear emergence and decay phase.

We mainly obtained the following three results:

**(i)** the emergence rates of star spots are consistent with those extrapolated from the sunspots ($d\Phi_{\rm e}/dt \propto \Phi^{0.3\sim0.5}$) under the assumption of the spot magnetic field strengths of 2000 G;

**(ii)** the decay rates of star spots are consistent with those extrapolated from the sunspots ($d\Phi_{\rm e}/dt \propto \Phi^{\sim0.5}$), which might be understood as an erosion from the edge;

**(iii)** the lifetime of star spots are much shorter than those extrapolated from the empirical GW relation of sunspots ($T \propto A$), though the lifetimes are up to 1 year.

Based on the results (i) and (ii), it can be concluded that emergence and decay of sunspots ($10^{18-23}$ Mx, 0.02-2000 MSH) and large star spots on solar-type stars ($10^{23-24}$ Mx, 2000-20000 MSH) can be universally explained by the same underlying process, i.e. a flux emergence from stellar interior and a following flux diffusion in stellar surface.

The result (iii) is basically similar to the previous studies (Giles et al., 2017; Bradshaw & Hartigan, 2014, e.g.). The works by Giles et al. (2017) is not the spot lifetimes of "individual" spot (groups) but the global trends, but our result is surprisingly consistent with them. Bradshaw & Hartigan (2014) proposed that the short timescales of gigantic star spots can be due to the different turbulent magnetic diffusivity based on the solar GW relation $T \propto A$. However, we confirmed that the dependence of the emergence/decay rates of star spots has a positive correlation with spot area for solar and stellar spots (results (i)-(ii)). Based on the equations in the results (i)-(ii), we derived the new scaling relations $T \propto A^{0.5-0.7}$. The relation can naturally explain the observed lifetimes of star spots without any assumption of magnetic diffusivity in Bradshaw & Hartigan (2014). We then propose that not only the emergence/decay rates but also the lifetimes can be explained universally by solar models for sunspots and star spots on solar-type stars. It should be notable that the scatters of the area-lifetime relation are very large, and there may be additional factors to determine the lifetimes of spots. The discussion will be revisited in Chapter 3.

We also found that star spots on slowly rotating stars show more slow temporal evolutions than those on rapidly rotating stars and solar scaling relations. These dependence on the rotational period can be real and should be considered. However, in fact, the spatial resolution of the method employed here is not good ($\sim 100^{\circ}$), and there is a possibility that the spot emergence and decay rates can be changed if the local minima consist of several large spots (spot groups or active longitude). Therefore, it is necessary to perform the spot modelings (e.g. Fröhlich et al., 2012), inversion modelings (e.g. Savanov & Strassmeier, 2008), and follow-up spectroscopic observations for the further evaluations of the error bars of the derived parameters. In Chapter 3, we will perform further studies by using not only the local minima tracing method but also the spot modeling and exoplanet transit methods, which solves some uncertainties raised here.

Finally, we comment on the importance of lifetimes of star spots (result (iii)). It should be notable that the lifetimes can be used as an indicator of the durations of the extreme space whether events. The large star spots ($\sim$10,000 MSH) potential to produce superflares ($\sim 10^{34}$ erg, Shibata et al., 2013) are found to survive for up to $\sim$1 year. This implies that the surrounding exoplanets can be exposed to danger of superflares for such a long time once one big spot (group) emerges. Moreover, according to frequency distributions of superflares, superflares of $10^{34}$ erg can occur about once a year on the star spots with area $\sim$10,000 MSH (Maehara et al., 2017). This may indicate that superflares can occur once in the lifetime with a high probability if such large spots (groups) emerge on the stellar surfaces. These should be a key information for evaluating the exoplanet habitability around the active stars (see also Section 3.5.3 in Chapter 3).

CHAPTER 3

# Temporal evolution of spatially-resolved individual star spots on a planet-hosting solar-type star: Kepler-17

## 3.1 Introduction

In Chapter 2, we extended the simple local minima tracing method introduced by Hall & Henry (1994) to a huge amount of solar-type stars observed by *Kepler* Space Telescope, and found 56 favorable cases of the individual star spot evolutions on the solar-type stars. The results show some consistency between sunspots and star spots in the relations of the emergence/decay rates and spot area. In Chapter 2, we selected only favorable spots separated from other spots in longitude, but still have the following two problems: (1) uncertainties due to several assumptions and (2) selection biases.

First, there would be large uncertainties due to several causes: stellar inclination, the extent of polar spotting, the extent of contamination from other spots at different positions, and the number of spots that local minima have (see, Basri, 2018; Basri & Nguyen, 2018) as in Chapter 2. Also, the unspotted stellar brightness level is unknown in the *Kepler* light curves (e.g. Basri, 2018). To evaluate those effects, the development of and comparison with light curve modeling method are necessary, but even these suffer from severe degeneracies that make it unlikely to discover the true spot distribution only from a light curve.

Moreover, since we selected only favorable spots separated from other spots in longitude in Chapter 2, so there can be selection biases. Most light curves are highly disturbed by stellar differential rotations and some have long-lived active longitudes (or active nests Zwaan, 1987; Berdyugina & Usoskin, 2003), so the validation of our results is difficult on

the other stars. In addition, the criteria of Chapter 2 can miss long-lived spots ($>$ 1 year) because of the stellar differential rotations and limited *Kepler*'s observational time ($\sim$ 4 years).

In this Chapter, our purposes are to partly solve the above problems and to investigate the star spot emergence/decay from a new perspective. In order to achieve these purposes, we take two new approach using (1) an exoplanet transits method and (2) a light curve modeling method. First, we introduce the simplified idea of exoplanet transits method as follows: It is sometimes reported that, during the exoplanet transit, the additional small brightness variations can be detected which are caused by an exoplanet passing in front of dark spots on the stellar surface (Silva, 2003). By analyzing the brightness variations, the spot locations and area can be estimated with the spatial scale as small as the exoplanet diameter (Davenport, 2015; Estrela & Valio, 2016; Valio et al., 2017; Morris et al., 2017). In addition, we developed a simple light curve modeling method to reconstruct the spot emergence and decay. The purpose of this new modeling is to confirm whether the sophisticated models can deduce the same estimate or not. We compared the results with the spots detected by the local minima tracing method (performed in Chapter 2) as well as those detected in transits.

Kepler-17 is a hot-Jupiter-hosting rotating active solar-like star, and it is a good target to estimate the spot evolutions by using the transit data (Davenport, 2015). In Kepler-17, the transit path of the hot Jupiter (Kepler-17b) is almost parallel to the rotational direction and the same spots can be detectable for many times. Therefore, by using the transit of Kepler-17 data, we can estimate the temporal evolution of spatially resolved individual star spots. Because of this unique feature, Kepler-17, as well as its planet, has been well-studied (Désert et al., 2011; Bonomo et al., 2012; Valio et al., 2017). Bonomo et al. (2012) performed the light curve inversion from the rotational modulation to the stellar surface filling factor, Estrela & Valio (2016) estimated the stellar magnetic cycles by using the transit data, and Valio et al. (2017) estimated the stellar differential rotation in this star. Later, Lanza et al. (2019) compared the results of the transit method with those of the light curve inversion method, and discussed their consistency, especially the differential rotation and activity cycles. Davenport (2015) showed some examples of the temporal evolution of the spots in transit, but did not show the detailed comparisons with sunspots.

In this Chapter, we discuss relations of spots derived by the three different methods: (a) local minima tracing method, (b) light curve modeling method, and (c) transit method. In particular, the discussions on spot emergence and decay dealt with in Chapter 2 are revisited by comparing these different methods. Because long-lived active longitudes have been reported on Kepler-17 by Lanza et al. (2019), the star is also a good target to confirm to what extent we can measure the spot area and variation rates of individual spots based on the *Kepler*'s rotational light curve. In Section 3.2, we introduce the data set and the stellar

parameters of Kepler-17 and Kepler-17b. In Section 3.3, we show our analysis methods: (a) local minima tracing method, (b) light curve modeling method, and (c) transit method. In Section 3.4, we show the results of our analysis, and in Section 3.5 we discuss the results.

## 3.2 Stellar parameters and data

Kepler-17 is a solar-like main sequence star with spectral type G2V. Its mass is $1.16 \pm 0.06$ $M_{\odot}$, radius is $1.05 \pm 0.03$ $R_{\odot}$, effective temperature is $5780 \pm 80$ K (Désert et al., 2011; Bonomo et al., 2012; Valio et al., 2017), and the stellar age is estimated to be less than 1.78 Gyr (Bonomo et al., 2012). The star has rotational brightness variations with its star spots whose rotational period is about 12.4 days (Bonomo et al., 2012). The large amplitude of these brightness variations show that this star has large star spots covering about 7% of the surface (Lanza et al., 2019), which is much larger than the observed maximum sizes of sunspots.

In the Kepler-17 system, a hot-Jupiter was first detected with *Kepler* space telescope. The planet mass is $2.45 \pm 0.01$ $M_{Jup}$, planet radius is $0.138 \pm 0.001$ $R_{\rm star}$, and orbital period is 1.4857108 days (Désert et al., 2011; Bonomo et al., 2012; Valio et al., 2017). During the exoplanet transits, small brightness enhancement can be observed, and this is thought to be caused by the exoplanet hiding the star spots on the stellar photosphere. By modeling the transit light curve, individual star spot sizes and locations can be estimated with much smaller spatial resolution ($\sim R_{\rm plant}/R_{\rm star} \sim 0.1 \sim 20^{\circ}$, see e.g. Davenport, 2015; Morris et al., 2017; Valio et al., 2017) than the rotational modulation methods ($\sim 100^{\circ}$, Basri & Nguyen, 2018). Notable features of this system are as follows: (1) the inclination angle of the star is $\sim 90^{\circ}$; (2) exoplanet path is almost perpendicular to the stellar rotational axis ($\sim 89^{\circ}$), and the projected latitude beneath the exoplanet transit chord is near the equator ($\sim$ -4.6°); and (3) the transits occur every 1.5 days (significantly shorter than stellar rotational period $\sim$ 12 days). Thanks to these unique features, the same star spots can be detectable several times within the one rotational period, and even the recurrent spots can be traced over time. Therefore, Kepler-17 is the best target to measure the temporal evolutions of the individual star spot areas (Davenport, 2015).

For the rotational modulations, we used all the available *Kepler* pre-search data conditioning (PDC) long-cadence ($\sim$30 min) data (*Kepler* Data Release 25, Thompson & Caldwell, 2016), in which instrumental effects are removed. As for the transit, we used PDC short-cadence data. Since the long-term light curve modeling is very expensive, we only analyzed the long-cadence data from Quarter 4 to 6, when the short cadence mode began to observe Kepler-17. The in-transit star spot analysis method was applied to only observations taken at short cadence.

## 3.3 Analysis method

We investigate temporal evolutions of star spots on Kepler-17 by using the rotational modulations with simple traditional local minima tracing modeling (hereafter local minima tracing method; see Section 3.3.1 and Chapter 2; Hall & Henry, 1994; Namekata et al., 2019) and an MCMC-based simple light curve modeling (hereafter light curve modeling method; see Section 3.3.2). We also measured the temporal evolution of the starspots by transit modeling with the STSP code (hereafter in-transit method; see Section 3.3.3; Davenport, 2015; Morris et al., 2017).

### 3.3.1 Method I: local minima tracing method

The first method is a local minima tracing method which is firstly proposed by Hall & Henry (1994) to measure the temporal evolutions of star spots. In this method, each star spot can be identified by the repetition of the local minima over the rotational phases. The light curve of a rotating star with star spots shows several local minima when the spots are on the visible side (Notsu et al., 2013; Maehara et al., 2017). By tracing the local minima with the rotational period of the star, we can estimate the lifetimes of the large-scale spot patterns. We can estimate the temporal evolution of star spot coverage by measuring the local depth of the local minima from the nearby local maxima as an indicator of spot area. We first obtained the smoothed light curve by using locally weighted polynomial regression fitting (LOWESSFIT; Cleveland, 1979) to remove flare signature and noise. In the LOWESSFIT algorithm, a low degree polynomial is fitted to the data subset by using weighted least squares, where more weight is given to nearby points. We used the $lowess$ function incorporated in the `statsmodels` python package. We detected the local minima as downward convex points of the smoothed light curve; i.e. the smoothed stellar fluxes $F(t)$ satisfy $F(t_{\text{(n-m)}}) < F(t_{\text{(n-m-1)}})$ and $F(t_{\text{(n+m)}}) < F(t_{\text{(n+m+1)}})$. Here, $m$ takes a value of [0, 1, 2], $t$ is time, and $n$ is time step. When we estimate the spot area from the local depth of the light curve, we assume that the spot contrast is 0.3. The advantage of this method is its low computational cost, so it is suitable for statistical analyses, as discussed in Chapter 2 (Namekata et al., 2019). This star is a good candidate to evaluate how the simple method can estimate the temporal evolution of star spot areas by comparing with the other methods.

### 3.3.2 Method II: light curve modeling method

Light curve modeling methods for a rotating, spotted star have been developed by several authors (e.g. Croll, 2006; Fröhlich et al., 2012; Lanza et al., 2014). Here, we also developed a light curve modeling method under some simple assumptions (cf. Ikuta et al.,

2020).[††] The spot contrast is assumed to be constant (=0.3) because it is highly degenerate with spot area (Walkowicz et al., 2013). We are interested in the spot evolution, so each spot area is assumed to emerge and decay linearly for simplicity. The real spot evolution may be more complex, but it will not give a significant effect on our results because we will focus on the relations of spot maximum size and mean variation rate as presented in Chapter 2 (Namekata et al., 2019). A more realistic spot evolution model should be done in our future works.

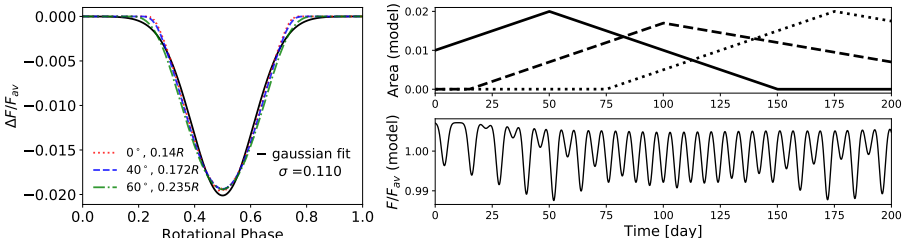


Figure 3.1: A detailed explanation of our model of out-of-transit rotational modulation. Left: light curves of a rotating star with (red) a spot of 0.14 $R_{\rm star}$ on the equator of stellar surface, (blue) a spot of 0.172 $R_{\rm star}$ on 40° and (green) a spot of 0.235 $R_{\rm star}$ on 60°. The black solid line behind is the model light curve that we use in our MCMC modeling, which is derived by fitting the mean of the color lines with a gaussian function. Upper right: one model of the temporal evolution of star spot. The values of the vertical axis is just a fraction in the light curves ($A(t)$ in the equation of Equation 3.2). Lower right: the light curve generated from the upper temporal evolutions by using our gaussian model.

In the left panel of Figure 3.1, modeled stellar light curves are plotted in several cases of spot size and latitude. In the model, we use the stellar surface model separated with grids by assuming linear-limb darkening (see Notsu et al., 2013). As one can see, the stellar light curve of a low-latitude small spot is highly degenerate with those of high-latitude large spots within the *Kepler* photometric errors of 0.1% (see also Walkowicz et al., 2013). By considering this, we did not consider the latitude information, so there should be uncertainty in area estimations caused by the projection effect at higher latitudes.

There are analytical models which reproduce stellar light curves from the spot parameters (e.g. Kipping, 2012). In this study, we adopt an approach to use a Gaussian function to approximate stellar rotational light curves. As in Figure 3.1, all of the light curve in the different cases show similar light curves in Kepler-17, which can be fitted by a Gaussian function as indicated in black line, with the *Kepler*'s photometric errors ($\sim$ 0.1 %). We

[††]As in the original paper (Namekata et al., 2020a), the basic concept of MCMC is the same as that of Ikuta et al. (2020), but the code and model of light curves are different. The code used here is developed by the author of this Ph.D. thesis (K. Namekata).

used the following function as a standard light curve:

$$\Delta F(t) = -A \times \exp\left(-\frac{(t-t_0)^2}{(\sigma P_{\rm rot})^2}\right), \tag{3.1}$$

where $A$ is spot area, $\sigma$ is non-dimensional factor (=0.110) derived by the Gaussian fitting, $t$ is time, $t_0$ is the standard time when the spot are on the visible side, and $P_{\rm rot}$ is the rotational period of a given spots. The right of Figure 3.1 is an example of the application of this Gaussian light curve to the multi-spot case. In this case, the model light curve $\Delta F(t)$ can be obtained as

$$\Delta F(t) \;=\; \sum_{n=1}^{\rm N_{spot}} \sum_{\rm m=-\infty}^{\infty} \left(-A^{\rm n}(t) \times \exp\left(-\frac{(t-t_0^{\rm n}+mP_{\rm rot}^{\rm n})^2}{(\sigma P_{\rm rot}^{\rm n})^2}\right)\right). \tag{3.2}$$

Here, $A(t)$ is a spot area as a function of time $t$, and $n$ is the spot number.

Here, the following six parameters are necessary for each spot: maximum area, emergence rate, decay rate, maximum timing, standard longitude ($t_0$), and rotational period ($P_{\rm rot}$). The total number of parameters is six times the number of spots (here, the number of spots is set to be five). We carried out a parameter search to estimate the most-likely parameters well reproducing the observed light curve with Markov chain Monte Carlo (MCMC). MCMC methods have become an important algorithm in not only astronomical (Sharma, 2017) but also various scientific fields (e.g. Liu, 2001). It can generate samples that follow a posterior distribution by selecting the sampling way based on the likelihood function $L$ in the Bayesian theorem. Here, we take the likelihood function as a product of Gaussian function on each time:

$$L = \prod_{i=1}^{N_{\rm data}} \frac{1}{\sqrt{2\pi\sigma_0^2}} \exp\left(-\frac{\left(\left(\frac{F(t_i)}{F_{\rm av}}\right)_{\rm obs} - \left(\frac{F(t_i)}{F_{\rm av}}\right)_{\rm model}\right)^2}{2\sigma_0^2}\right). \tag{3.3}$$

We adopt the traditional Metropolis-Hastings algorithm (Metropolis et al., 1953; Hastings, 1994). We also adopt the Gaussian function as the proposal distribution, and the step length (proposal variance) of the Gaussian was adaptively-tuned for each step by considering the acceptance ratio of MCMC sampling converged to be 0.2 (Gilks, 1998; Araki & Ikeda, 2013; Yamada et al., 2017, so-called adaptive MCMC algorithm, e.g.). A uniform distribution is adopted as a prior distribution.

In our case, when sampling from a multi-modal distribution with a large number of parameters, the chains theoretically can converge to the posterior distribution, but practically seapking, the chains may not converge because of the limited sampling times. They can be trapped in a local mode for a very long time. In order to avoid this, we apply the Parallel Tempering (PT) algorithm to our MCMC estimations (e.g. Hukushima & Nemoto, 1996; Araki & Ikeda, 2013). The PT algorithm introduces auxiliary distribution by using the

so-called inverse temperature ($\beta$), runs multiple MCMC samplings (hereafter "replica") simultaneously for each inverse temperature, and sometimes, exchange replica with a certain percentage. The tempering procedure and exchange processes help samples to escape from a local maximum. In practice, each Markov chain is controlled by the inverse temperature $\beta_i$ ($1 = \beta_0 > \beta_1 > \beta_2 ... > \beta_n > 0$), and the auxiliary likelihood for each replica is expressed as $L_i^{\beta_i}$. The higher-order replica has, therefore, the smaller valley to another local maximum than the lower-order one, and the parameters are easy to be searched across the wide range of the parameter space without being trapped in local maxima. By repeating the exchange between the orders, the highest-inverse-temperature replica (= the target samples) can sample around the maximum likelihood within finite computation times.

We run the MCMC sampler for 500,000 steps after the exchanges no longer occur, and set the burn-in period as the first 100,000 steps. As noted above, the replica change can occur theoretically even when sampling around the highest likelihood, but actually did not. We finally take the parameter showing the highest likelihood value in the 400,000 steps, and the error bars are estimated from the posterior distributions. For the parameter range, we take [0.001, 0.05] for maximum spot fraction ($A_{\rm max}$), [-5, -1] for emergence rate ($\Delta A$/day) in log scale, [-5, -1] for decay rate ($\Delta A$/day) in log scale, [start time, end time] for maximum timing, [0°, 360°] for standard Carrington longitude, and [11.63, 12.86] for rotational period ($P_{\rm rot}$). In this study, we adopt a four-spot model by considering the model evidence and its output. We also carried out five spot model and no significant new information was obtained. Initial input values are randomly selected in the parameter range and independently selected for each replica. The convergence was checked by visually checking the parameter changing for each step and marginalized posterior distribution with one parameter or two parameters. The MCMC method can estimate the parameters to best reproduce the light curve, but the reproduced spots do not necessarily have much to do with the spots that are actually present as we describe in the following paragraph.

### 3.3.3 Method III: transit method ( STSP code )

We modeled the spots occulted during the exoplanet transit (hereafter in-transit spots) by using STSP code[†] (Davenport, 2015; Morris et al., 2017). The spot modeling approach applied in the present study is the same as that already described in Chap. 5 of Davenport (2015) and L. Hebb et al. *i*n preparation, to which we refer the reader for details. In brief, STSP is a C code for quickly modeling the variations in the flux of a star due to circular spots, both in and out of the path of a transiting exoplanet. Static star spots are currently assumed in the code, and evolution of spot activity is typically analyzed by modeling many windows (e.g. individual transits) independently. STSP also allows the user

[†]The source code of STSP can be seen here: `https://github.com/lesliehebb/stsp`

to fit light curves with arbitrary sampling for the maximum-likelihood spot positions and size parameters using MCMC, and has been used for modeling systems with no transiting exoplanets (Davenport et al., 2015), as well as transiting systems with a range of geometries (e.g. Morris et al., 2017). Note that this application of MCMC algorithm is different from that described in the section 3.3.2 (see, Morris et al., 2017). The MCMC technique allows us to properly explore the degeneracies between star spot positions and sizes. The modeled data is mostly taken from the work by Davenport (2015). Please note that the model by Davenport (2015) was originally carried out by assuming by the stellar radius of 1.1 $R_{\odot}$ and planet radius of 0.10 $R_{\rm star}$, which is slightly different from reported from the other study (Désert et al., 2011; Bonomo et al., 2012; Valio et al., 2017). This can lead to 10 % errors in the estimated area and variation rates of area, but these do not significantly affect our results, because we will discuss much trends that are much larger than this difference. For the STSP outputs, we remove solutions of spots which are located on the stellar limb (i.e. distance from the disk center $>$ 1 - 2 $R_{\rm planet}$) and spots with the too large size (i.e. radius $>$ 0.25 $R_{\rm star}$) because the solutions in the ranges are likely to be biased. We also calculated the error bars of the estimated spot parameters based on the posterior distributions of MCMC samplings.

## 3.4 Results

### 3.4.1 Local minima tracing method in comparison with transit reconstruction

Figure 3.3 shows the result of local-minima spots and a comparison with in-transit spots. The middle panel shows the temporal evolution of local-minima spots. As described by Lanza et al. (2019), there are two active longitudes in this star as indicated with the different colors, and spot group Group A (red) is dominant compared to the spot group B (blue) in this period. We use this notation because local light curve minima on the Sun are sometimes due to spot groups or “active longitudes” (e.g. Berdyugina, 2005; Lanza et al., 2019). In general these terms may be misleading because the source of light curve minima might not be either of these phenomena. Minima can easily arise (even on the Sun) from a scattered configuration where more spots are on one hemisphere than the other. We have chosen to use conventional terminology, but one can more accurately read “spot group A" as “side A". The temporal evolution of the area of spot group A shows a clear emergence and decay phase, while spot group B does not.

The bottom panel of Figure 3.3 is a comparison of spot locations between local-minima spots and in-transit spots. Two local minima are dominant in one rotational phase, while there are 5-6 spots are visible in the transit path. The longitude of the local minima well

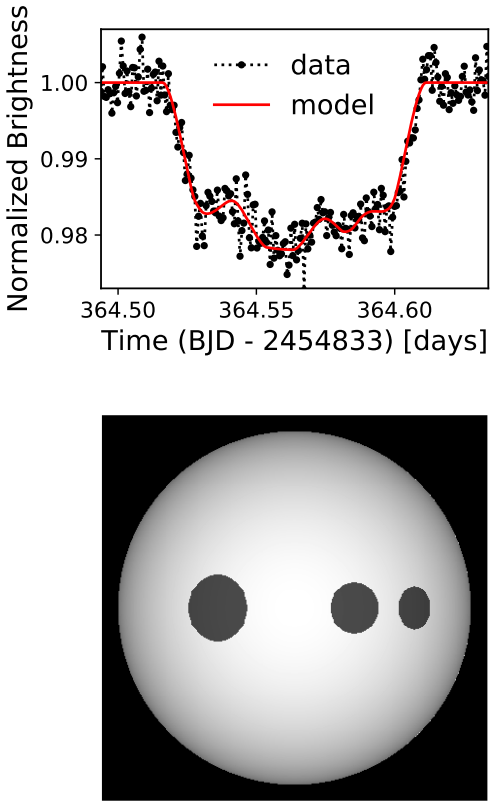


Figure 3.2: A example of the result of the transit modeling. Upper panel is one example of the high quality fits of our MCMC modeling (red line) to the high cadence in-transit data (black lines). Bottom panel is the reconstructed surface distribution of star spot.

matches those where in-transit spots are crowded, especially in the first 200 days (BJD 350 to 550+245833). On the other hand, after BJD 550+245833, the red and blue circles lose track of most of the transit spots, and the longitude of local minima becomes delayed compared to the in-transit spots (i.e. the slower rotation period than that of the equator). It could be due to the complex spot distribution changing, but could be caused by the new emergence of star spot on the higher latitude where spots are rotating slower because of the solar-like differential rotation of the star (see, Lanza et al., 2019).

Figure 3.4 indicates the comparison of the area of local-minima spots and in-transit spots. The upper left panel shows a comparison between *Kepler* light curve and the reconstructed one from the in-transit spots. Note that the reconstructed light curve in Figure 3.4 is subtracted by its mean value, and the zero level for the calculation of the reconstructed light curves is around $(F\text{-}F_{\rm av})/F_{\rm av} \sim 0.28$. The differential amplitude of the observed light curve is comparable to or a little smaller than the one reconstructed from the spots

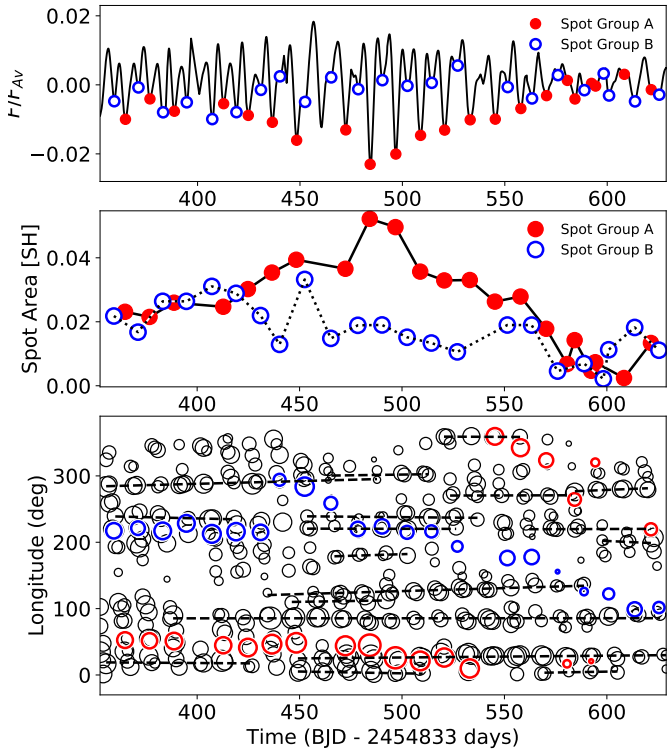


Figure 3.3: Upper: the black line is the smoothed light curve of Kepler-17 during quarter 4–6. Circles indicate the local minima of the light curve, and the different symbols mean the different spot groups identified based on the rotational phase. Middle: the temporal evolution of the star spot area for each spot group. Bottom: the comparison on the spot distribution between in-transit spots (black) and local minima spots (colors). The longitude are calculated as the Carrington longitude with the rotational period of 11.92 days (Valio et al., 2017). The dashed lines are the series of long-lived recurrent spot candidate identified by the DBSCAN package in *python*.

in-transit.

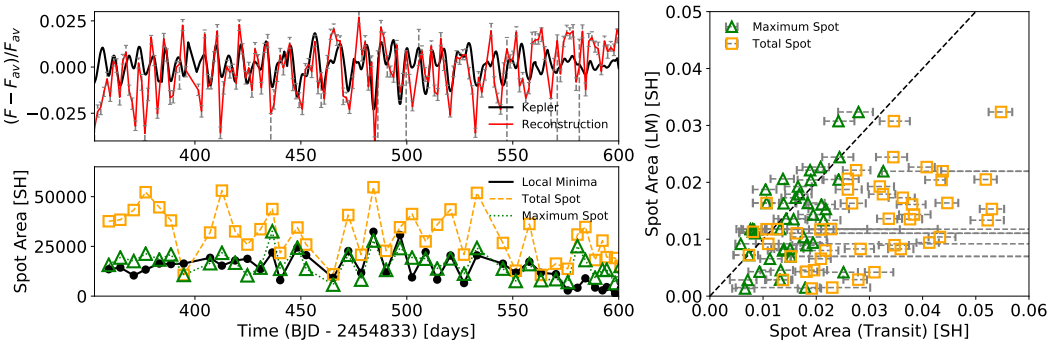


Figure 3.4: Comparison between in-transit spots and local-minima spots. Left upper: the comparison between the smoothed light curve of Kepler-17 (black) and reconstructed light curve by spots occulted by transits (red). In this figure, the vertical axis values are those relative to their averaged values. The *Kepler* light curve is subtracted by the average flux values for each quarter, while the reconstructed light curves are subtracted by the average value ($F_{\rm av}$) for all period, so both of them do not necessary match with each other. The error bars are estimated based on the posterior distributions of the spot area. A zero-level value for the reconstructed light curve is $\sim 0.028$ which is slightly higher than the local maxima. Left lower: temporal evolution of the spot area derived by local minima tracing method (black), total spot area derived by transit method (orange), and maximum spot area derived by transit method (green). Right: comparisons between spot area derived by local minima tracing method and total spot area derived by transit method (orange), and comparisons between spot area derived by local minima tracing method and maximum spot area derived by transit method (green).

The lower left panel of Figure 3.4 shows the comparison of temporal evolutions of the local-minima spot area (black), maximum visible area of in-transit spot (green), and total spot coverage in transit path on half the star (orange). The total spot coverage in the transit chord was calculated for the closest transits to the local minima. The right panel of Figure 3.4 is the comparison for each data point of the lower left panel of Figure 3.4. The area of local-minima spots is consistent with the maximum spot area in-transit. The area of local-minima spots also have a positive correlation with the total spot area in transit, although the former is smaller by a factor of two. This tendency can be also seen in the case of the Sun (Basri, 2018).

### 3.4.2 Light curve modeling method in comparison with local-minima-tracing/transit method

Figure 3.5 shows the results of light-curve-modeling spots in comparison with in-transit spots. The upper panel shows a comparison between *Kepler* light curve and the modeled one. The *Kepler* light curve is reproduced by our simple Gaussian model. That is because

| | Maximum Area [MSH] | Emergence Rate [MSH·h$^{-1}$] | Decay Rate [-MSH·h$^{-1}$] | Rotation Period [d] |
|---|---|---|---|---|
| Spot 1 | $20600^{+1.1}_{-200}$ | $2.83^{+0.47}_{-0.21}$ | $21.4^{+0.23}_{-0.52}$ | $11.99^{+0.0047}_{-0.00045}$ |
| Spot 2 | $22600^{+130}_{-36}$ | $2.2^{+0.48}_{-0.39}$ | $6.23^{+0.084}_{-0.017}$ | $12.02^{+0.0048}_{-0.0034}$ |
| Spot 3 | $8670^{+91}_{-65}$ | $3.16^{+0.055}_{-0.01}$ | $0.363^{+0.028}_{-0.0024}$ | $12.34^{+0.017}_{-0.016}$ |
| Spot 4 | $10700^{+120}_{-240}$ | $0.97^{+0.15}_{-0.26}$ | $0.362^{+0.00063}_{-0.0018}$ | $12.34^{+0.017}_{-0.016}$ |

Table 3.1: The spot parameters estimated by our MCMC-based light curve modeling for the rotational modulation. The values are taken as parameter showing the highest likelihood, and the error bars are estimated from 68 % of the posterior distribution.

there is only hemispheric information in the light curve, which is straightforward to model (but not so accurate). The middle panel shows the estimated areal evolution of the light-curve-modeling spots. The estimated parameters are listed on Table 3.1. The bottom panel shows that the estimated location of the light-curve-modeling spots matches that of the in-transit spots, especially for the red and purple spots. This would be because the purple and red spots are located near the equator. On the other hand, green and blue spots are not rotating with the same rotational period as the equator, so there is no corresponding spot occulted by transit. If we compare Figure 3.3 and 3.5, we can see that the locations of the local minima and the estimated spot are quite similar to each other.

We also tried a five-spot model and no significant new information was obtained. Here, we note that long-term spot modeling, covering over a quarter ($\sim$ 90 days), should be done carefully because *Kepler* light curves have an inevitable long-term instrumental trend in the light curve, and the absolute values may be unreliable.

### 3.4.3 Comparison of temporal evolutions of star spot area among different methods

We estimated the location and area of star spots occulted by the planet for all *Kepler* short time cadence data (16 quarters in total). The estimated result is plotted in Figure 3.6. There are many long-lived recurrent spots that are located on the same longitude for a long time. To pick up candidates of long-lived spots, we apply DBSCAN, a commonly-used data clustering algorithm, in the Python package `scipy` (Martin, 1996; Davenport, 2015). In brief, this algorithm finds the core points which have more than $N$ satellite points within the length of $\epsilon$, and find clusters by connecting the core points with each other. The detected clusters are plotted with the colored symbols in Figure 3.6. We interpret these clusters as the long-lived spots and measure the temporal evolution of the spot area in each cluster. Most of the spots show very complex areal evolutions probably due to the consecutive flux emergence events in the same place, while some of them show clear emergence and decay phases as plotted in Figure 3.7.

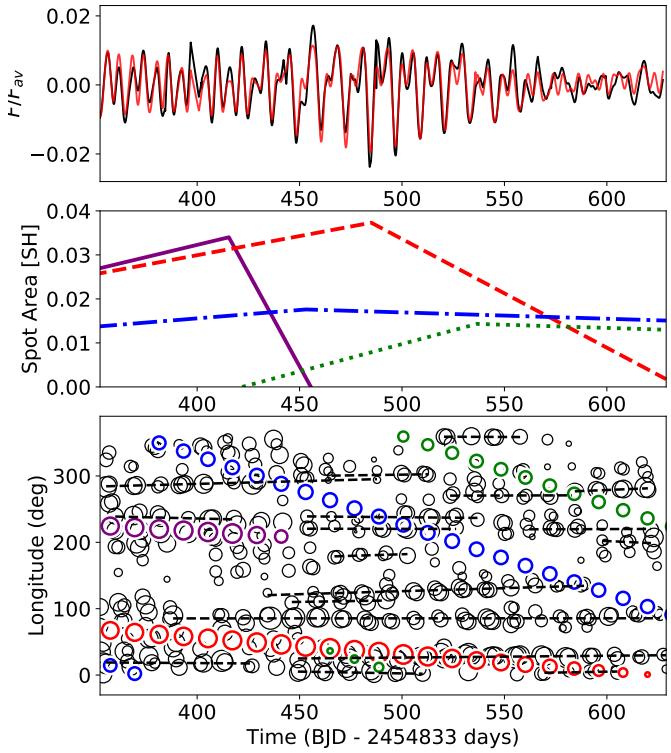


Figure 3.5: Spot evolution derived by light curve model and transit method. Upper: the black line is the smoothed light curve of Kepler-17 during quarter 4–6, and the red line is the modeled light curve with four-spots light curve modeling method. Middle: the temporal evolution of the star spot area estimated in our model. Bottom: the comparison on the spot distribution between the spots occulted by the transit and the those estimated by light curve model. The dashed lines are the series of long-lived recurrent spot candidate identified by the DBSCAN package in *python*.

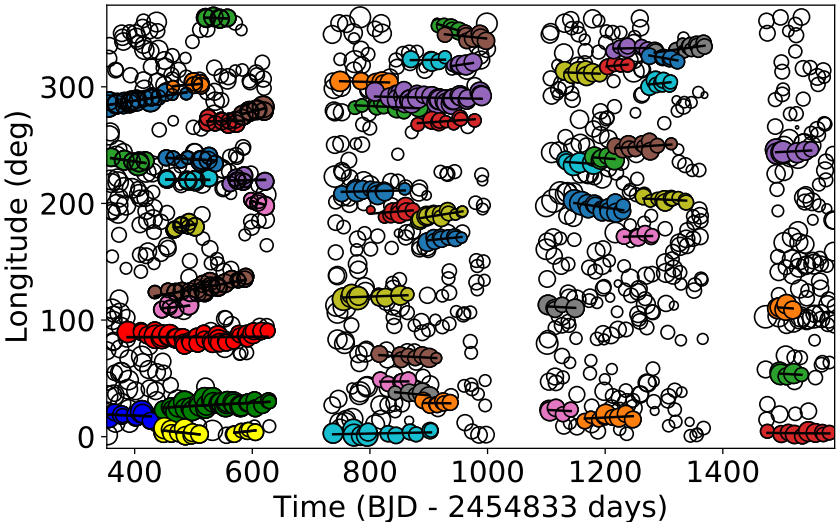


Figure 3.6: Spot locations derived from transit data. Symbols shows all spots detected by the STSP code (Davenport, 2015; Morris et al., 2017) on the time-longitude diagram. The color symbols are the series of long-lived recurrent spot candidate identified by the DBSCAN package in *python*.

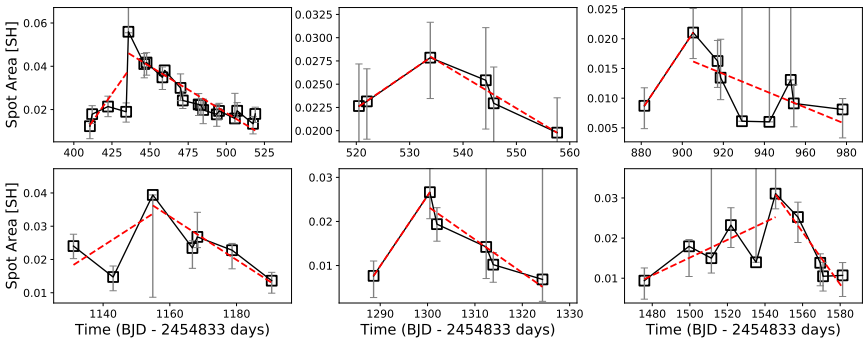


Figure 3.7: Several examples of the temporal evolution of star spot estimated from the exoplanet transit model which show clear emergence and decay phase. The solid error bars are estimated from 68 % of the posterior distribution.

We then compared the evolution of star spot areas detected by (a) local minima tracing method, (b) light curve modeling method, and (c) transit method in Figure 3.8. We focus on the spot group A in Figure 3.3 to see how the temporal evolution of star spot areas computed by the different methods compare. In panel (a) the spot group A indicated in Figure 3.3 is plotted. In panel (b) the corresponding spot evolution estimated by light-curve modeling is plotted on the basis of the location in Figure 3.8. As we expected, both of them show very similar temporal evolutions. This is very natural because both are obtained from the same data, but important for the validation of the local minima tracing method. In panel (c) we plot the temporal evolution of the selected spot area estimated by the transit method which is located on the longitude between $0^\circ$ and $100^\circ$ in the bottom panel of Figure 3.3. As one can see, the spot group A actually consists of at least four spots (two spots at the same time), and the temporal evolution of in-transit spots does not match with that of spot group A. The red circle shows the most dominant spot showing a clear emergence/decay phase, but the peak time is different from those seen in panel (a) and (b). This means that the temporal evolutions of the individual spots are different from those of spot groups (active longitudes), especially in this period.

We estimated the temporal evolution of individual star spot areas occulted by the planet and compared with those derived by other methods. We estimated the evolution of star spot area shown in Figure 3.7 with linear fitting (see red lines in Figure 3.7), and calculated the maximum area (flux), emergence rate, decay rates, and lifetime in the same manner as Chapter 2 (Namekata et al., 2019). We assume the mean magnetic field is about 2000 G when we compare them with the solar values. The estimated emergence rate is $1.1 \times 10^{21}$ Mx·h$^{-1}$ on average, and the decay rate is $-7.8 \times 10^{20}$ Mx·h$^{-1}$, for the spot area of $1.3 \times 10^{24}$ Mx. On the other hand, the emergence/decay rates of spot group derived from local minima is $3.8 \times 10^{20}$ Mx·h$^{-1}$ and $-5.6 \times 10^{10}$ Mx·h$^{-1}$ for the spot area of $2.0 \times 10^{24}$ Mx, respectively. Likewise, the emergence/decay rates of spot group derived from light curve modeling is $1.1 \times 10^{20}$ Mx·h$^{-1}$ and $-3.9 \times 10^{20}$ Mx·h$^{-1}$ for the spot area of $1.4 \times 10^{24}$ Mx, respectively. The spot area is quite similar, but the flux emergence/decay rates derived from rotational modulations are smaller by one order of magnitude than those derived from the transit method. Here, the spot group A has an equatorial rotational period and expected to be on round the equator, so the latitudinal effects are negligible. Each data are plotted in Figure 3.9 in comparison with those of sunspots and star spot in our previous work. As you can see, however, the emergence/decay rates of star spot occulted by transit look consistent with sunspots and star spots in our previous work, although they scatter by an order of magnitude. The emergence rates can be explained by the solar scaling relation ($d\Phi/dt \propto \Phi^{0.3-0.5}$, Otsuji et al., 2011; Norton et al., 2017), and the decay rates can be also explained by the solar relation ($d\Phi/dt \propto \Phi^{\sim 0.5}$, Petrovay & van Driel-Gesztelyi, 1997).

We also compared the lifetime-area relation in Figure 3.10. As a result, the lifetimes

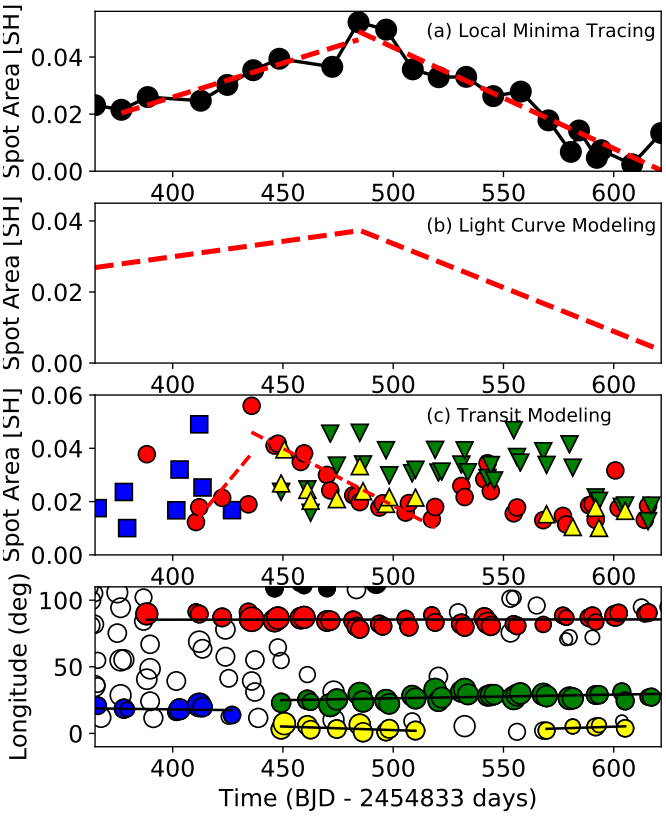


Figure 3.8: The temporal evolutions of star spot area derived by (a) local minima tracing method, (b) light curve modeling method, and (c) STSP transit method. In panel (a), the emergence and decay phases are fitted and indicated with the red dashed line. In panel (b), the corresponding star spots are indicated by red lines. In panel (c), the derived areas of the spots in the first observing period between longitude 0° and 100° are shown; the primary growth and decay of the spot near 100° is marked with the red dashed line. In the bottom panel, we show the extended figure of Figure 3.6 whose longitude is between 0° - 100°.

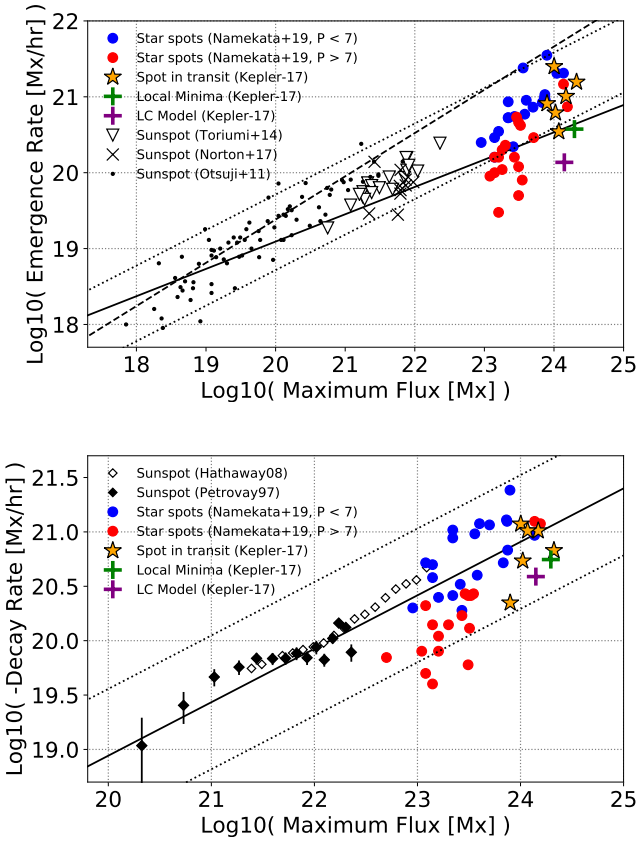


Figure 3.9: Maximum spot flux v.s. variation rates of spots. Left: comparison between maximum magnetic flux and emergence rate of sunspots and star spots on solar-type stars. Black points, downward triangles, and crosses are sunspots observational data taken from Otsuji et al. (2011), Toriumi et al. (2014), and Norton et al. (2017), respectively. Blue and red circles correspond to the spots analyzed in Chapter 2 (Namekata et al., 2019) with Prot $<$ 7 day and Prot $>$ 7 day, respectively. The yellow star symbols indicates the star spot occulted by transit derived in this study. A solid and dashed line is a scaling relation derived by Norton et al. (2017) and Otsuji et al. (2011), respectively. The dotted lines are the 95 % confidence level of solar data taken from Chapter 2 (Namekata et al., 2019). Right: Comparison between maximum magnetic flux and decay rate of sunspots and star spots on solar-type stars. Black open and filled diamonds are sunspot's observations by Hathaway & Choudhary (2008) and Petrovay & van Driel-Gesztelyi (1997), respectively. Blue and red circles correspond to the spots analyzed in Chapter 2 (Namekata et al., 2019) with Prot $<$ 7 day and Prot $>$ 7 day, respectively. A solid line is the line of the power law index of 0.5, where the absolute values are derived based on mean values of the sunspot observations (Hathaway & Choudhary, 2008). The yellow star symbols indicates the in-transit star spots derived in this study. The green and purple crosses indicates the star spot on Kepler-17 derived by using local minima tracing method and light curve modeling method for the red lines in Figure 3.8 (a) and (b), respectively. The dotted lines are the 95 % confidence level of solar data taken from Chapter 2 (Namekata et al., 2019).

of star spots occulted by transit are consistent with previous star spot studies (Bradshaw & Hartigan, 2014; Davenport, 2015; Giles et al., 2017; Namekata et al., 2019), and the lifetimes of star spot are much shorter than extrapolated from the solar empirical relations ($T \propto A$, so-called Gnevyshev-Waldmeier law; Gnevyshev, 1938; Waldmeier, 1955). On the other hand, the area-lifetime relation is roughly derived to be $T$ [d] $\sim$ C ($A$ [MSH])$^{0.5}$, where C is $\sim 0.8$, from the above dependence of emergence/decay rates on the total flux. This empirical relation would be more consistent with the stellar observations than the Gnevyshev-Waldmeier law as discussed in the following section.

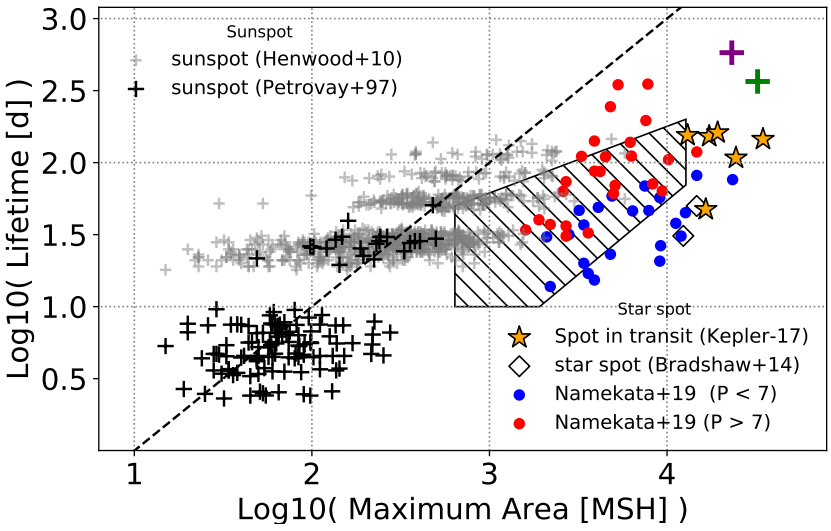


Figure 3.10: Comparison between maximum spot area and lifetime of sunspots and star spots on solar-type stars. Black and gray crosses are sunspots data taken from Petrovay & van Driel-Gesztelyi (1997) and Henwood et al. (2010), respectively. The dashed line indicates the solar GW relation (A = DT, D =10 MSH/day). Blue and red circles correspond to the spots analyzed in Chapter 2 (Namekata et al., 2019) with Prot $<$ 7 day and Prot $>$ 7 day, respectively. Open diamonds are star spots on G-type stars (Kepler-17 and CoRoT 2) taken from Bradshaw & Hartigan (2014). A region filled with diagonal lines indicates the result of Giles et al. (2017). The star symbols indicates our data in Kepler-17. The green and purple crosses indicates the star spot on Kepler-17 derived by using local minima tracing method and light curve modeling method, respectively.

## 3.5 Discussion

### 3.5.1 Spot area

In this section, we summarize and discuss the locations and spot areas on Kepler-17. In Section 3.4.1, we showed that one local minimum actually consists of several dominant

spots in the case of Kepler-17, which has been already indicated by Lanza et al. (2019). This can be easily understood in analogy with sunspot distributions where we can see several active regions at the same time during the maximum activity. The locations of local minima sometimes nicely match those of (nearly equatorial) transited dominant spots; in those cases we can pin much of the light curve modulations to those spots (see, Figure 3.4).

We also showed the amplitudes of local minima values also have a positive correlation with the visible maximum spot area in transit and the total projected spot area in transit in this observational period. This positive correlation may imply that (1) the unseen spots are randomly distributed and so have a relatively small effect on the brightness variation and the dominant spots (group) in transit mainly create the rotational modulation (e.g. Eker, 1994) or (2) the unseen spots follow the same general hemispheric pattern as the transited spots. In the case of (2), the unseen spots are perhaps part of the same general active areas, but not always, because sometimes the areas trend away from each other.

We also showed that the amplitudes of local minima match the visible maximum spot area in transit, while they are smaller by a factor of 2 than the total projected spot area in transit. This factor difference would be caused because spots are widely distributed in longitude (see Figure 3.6), which decreases the brightness variation amplitude as well demonstrated by Eker (1994).

The consistency between the amplitudes of local minima and the visible maximum spot area in transit indicates that the spot area derived from local minima (or amplitude of the brightness variations) can be still a good indicator of that of the largest spot on the disk, but do not always correspond to the total filling factor. The similar properties can be seen in the case of the Sun as Basri (2018) showed.

### 3.5.2 Temporal evolution of individual star spot areas

In this section, we discuss the temporal evolution of star spot area in comparison with those of sunspots and results obtained in Chapter 2 (Namekata et al., 2019). In Figure 3.9, it is clear that the emergence/decay rates of spatially resolved star spot (resolution is still $\sim$ 10-20 deg) are consistent with those of sunspots within one order of magnitude of error bars of solar data. Also, this result is roughly consistent with our previous study within one order of magnitude. (red and blue circles, see Chapter 2; Namekata et al., 2019), which measured the variations rates of the favorable individual spots (i.e. isolated local-minima series showing clear emergence and decay). This possibly supports that the spot emergence/decay can be explained by the same mechanism, and imply a possibility to apply solar physics to star spot emergence/decay. However, the solar ($P_{\rm rot} \sim 25$ d) and Kepler-17 ($P_{\rm rot} \sim 12$ d) data is more consistent with the rapid rotators ($P_{\rm rot} < 7$ d; blue

circles) and larger than the slowly rotators ($P_{\rm rot} > 7$ d; red circles). We speculate that the discrepancy between spatially resolved and non-resolved spots on the slowly rotating stars can be a result of the superposition effect of the several spot evolutions, as showed in Section 3.4.3 and discussed in the next paragraph. As for the rotational period dependence, we have discussed some possible mechanisms of the dependence of the rotational period on the spot evolution (e.g. decay due to the differential rotations of the stars) in Chapter 2, although it is still debated.

How about the comparison between the in-transit (spatially-resolved) and rotational-modulation (spatially-unresolved) spots? In the Kepler-17 system, it is reported that the two active longitudes are prominent, whose lifetimes are over the *Kepler* observational period ($\sim$ 1400 days), while the brightness variation amplitude is varying every moment (Lanza et al., 2019). This is partly due to intermittent flux emergence and decay on the stellar surface. In fact, in Section 3.4.3, we also showed that the temporal evolution of individual star spot area in transit looks different from those derived from the local minima tracing method and light curve modeling method. These results would imply that the temporal evolution of star spot derived from out-of-transit light curves (i.e. rotational modulations) can be actually a superposition of the several dominant spots existing at the same active longitude. As a result of the superposition effect, as in Figure 3.9, the emergence/decay rates of the star spots in transits ($\sim \pm 1 \times 10^{21}$ Mx·h$^{-1}$) are larger by more than a factor of two (up to one order of magnitude) than those derived from out-of-transit light curves ($\sim \pm$1-$6 \times 10^{20}$ Mx·h$^{-1}$), although the maximum spot area is quite similar ($\sim 10^{24}$ Mx). This is a feature discovered only on Kepler-17, but can be applicable to the other stars. So far, most of the star spot evolutions are estimated based on the Kepler/COROT rotational modulations (Bradshaw & Hartigan, 2014; Giles et al., 2017; Namekata et al., 2019), our results propose that there is a certainty that the superposition effect changes the lifetime and variation rates by some factor, and the lifetimes may not be those of spot groups but those of active longitudes. Even though we carefully chose the favorable targets as in Chapter 2, we therefore have to be careful on the qualitative discussions.

In fact, most of the in-transit spots do not show clear emergence/decay phase. This may mean that there are continuous flux emergences and as a result they do not show clear emergence/decay phase, but can mean that the we may pick up only spots having rapid emergence/decay and the variation rates can actually have much larger diversity (more than one order of magnitude).

We also comment on the difference between the light curve modeling method and the local minima tracing method. In Section 3.4.3, the temporal evolution of star-spot area derived by light curve modeling are consistent with those derived by the local minima tracing method, and they have similar values of the variation rates ($\sim \pm$1-$6 \times 10^{20}$ Mx·h$^{-1}$) and the maximum spot sizes ($\sim 10^{24}$ Mx). The reasons for the small difference in variation

rates (a factor of $\sim 5$) are as follows. First, the light curve modeling method improves the results of the local minima tracing method by considering the contamination of different spots. Second, the *Kepler* light curves have inevitable long-term trends, so the relative values between different observational quarters are not reliable. In our light curve, the mean value is set to be zero for each quarter. Because of this, the light curve modeling method can generate a pseudo-long-lived spots, which result in the above difference (see, Basri, 2018, for more detais).

Finally, we comment on the star spot lifetime. Figure 3.10 shows that the lifetimes of detected star spots are smaller than those expected from solar empirical relation (T = A/D; D=10), and the result is consistent with the other studies. This is not surprising because the positive correlations of the variation rates and spot area ($\mathrm{d}A/\mathrm{d}t \propto A^{\alpha}$, $\alpha$=0.3-0.5) result in more small power-law relations $T \propto A^{1-\alpha}$ (the detail about the star spot lifetimes are discussed in Chapter 2 (Namekata et al., 2019)). Please note that Figure 3.6 that all of the individual star spots seem to appear for only several hundred days (see also Davenport, 2015; Lanza et al., 2019). This fact can be a strong restriction on the spot-evolution physics because we could not exclude the existence of individual spots with lifetimes of more than 1,000 days as predicted from the solar Gnevyshev-Waldmeier relation as in Chapter 2 (Namekata et al., 2019).

### 3.5.3 Implication for the stellar superflares

In the Kepler-17, we cannot find any stellar flares in the light curve, although the stellar brightness variations indicate the existence of large star spots that have a potential to produce a superflare ($> 10^{34}$ erg). Also, Maehara et al. (2017) reported solar-type stars that do not show any superflares but have large star spots. The reason why such stars with large star spots do not show any superflares is an open question. Statistically, stars with such large star spots $> 10^{-1.5}$ cause superflares 0.1-1 times per one year (Maehara et al., 2017), so such stars without superflares during *Kepler*'s observational period can be classified to have relatively less flare-productive spots. One possibility is that the large spots without any flares, like spots on Kepler-17, can have a simple polarity shape (e.g. $\alpha$-type or $\beta$-type spots), which is known to rarely produce extreme flares in the case of the sunspots (e.g. Toriumi & Wang, 2019). On sunspots, complex spots show relatively fast decay, so that lifetimes of star spots can be an indicator of spot complexity and flare productivity. The comparison of star-spot lifetimes between flare-productive and less flare-productive stars would be important for why and how stellar superflares occur.

Roettenbacher & Vida (2018) reported that the stellar superflares do not appear to be correlated with the rotational phase on solar-type stars. They tried to explain this result by the existence of large polar spots, visible large flares over the limb, or the flares between the

active longitudes. Our transit model reveals that there are, more or less, visible spots on the disk regardless of its rotational phase, and the local maxima are not always the unspotted brightness level. These observations imply that, even if we assume that the superflares are accompanied with the solar-like low-latitude spots, superflares can apparently occur regardless of its rotational phase because large spots are always visible to some extent.

## 3.6 Summary and conclusion

In this Chapter, we investigated the temporal evolution of individual spot areas by using the local minima tracing method, light curve modeling method, and transit method. By using the transit method, we can estimate the properties of the (partially) spatially resolved star spots on . Kepler-17 is one of the best targets to analyze the temporal evolution of star spots by the transit method. The main results in this Chapter (and Chapter 2) are summarized as follows:

**(i)** On Kepler-17, although two series of local minima are prominent based on the rotational light curve, there are clearly many spots present on the star based on the exoplanet transits. The location, area, and temporal evolution of one local-minima spot does not necessary correspond to those of in-transit spots. This means that we have to be careful when we derive the spot information based on the rotational modulations.

**(ii)** Nevertheless, the estimated area from the local minima tracing method is consistent with the maximum in-transit spots. This indicates that the *Kepler* light curve amplitude is a good indicator of the maximum visible spot size.

**(iii)** The emergence/decay rates of in-transit spots are within an order of magnitude of error bars of those derived for sunspots, although the temporal evolution derived from the rotational modulation somewhat differs from those of in-transit spots to a certain degree. This consistency possibly supports the possibility of applications of sunspot emergence/decay physics (e.g. Otsuji et al., 2011; Norton et al., 2017; Petrovay & van Driel-Gesztelyi, 1997) to star spot evolutions. It is also consistent with that based on rotational modulations (see results (i)-(ii) in Chapter 2; Namekata et al., 2019) within one-order of magnitude, but slightly different for slowly rotating stars ($P_{\rm rot} > 7$ days). This may be because the evolution of local minimum can be a superposition of that of a few large spots, which produces a difference between spatially-resolved and spatially-unresolved star spot evolution.

**(iv)** The star spot distribution derived by the light curve modeling method is well consistent with that of local minima tracing method in terms of spot location and area. This

implies that even the simple local minima tracing method can capture the essential feature of the rotational modulation.

**(v)** The lifetime of spatially-resolved star spots in-transit are up to $\sim$ 200 days, although the spot size was about 10 times larger. The lifetimes are found to be not so much different from those obtained in Chapter 2, and much smaller than those extrapolated from the empirical GW relation of sunspots (see also Chapter 2). We would like to emphasize again that this implies that the surrounding exoplanets can be exposed to danger of superflares for such a long time once one big spot (group) emerges, which will be helpful to evaluate the effect on the extreme space weather on the exoplanets.

By considering the results in Chapters 2 and 3, it can be concluded that the emergence and decay process of gigantic star spots can share the same processes as sunspots (e.g. the results (ii)-(iv)). The results is important not only as an evidence of the fundamental MHD plasma physics but also as a confirmation of the origins of the magnetic flux of gigantic spots that can produce superflares. It should be noted that the result (i) is the finding which was not considered in Chapter 2 and we may need to be careful about the results we obtained in Chapter 2. In addition, we also have provided the important informations on the exoplanet habitability (result (v)).

Here we revisit the lifetimes of star spots (see also Section 2.5). The result (v) is basically similar to the previous studies (Giles et al., 2017; Bradshaw & Hartigan, 2014, e.g.). The works by Giles et al. (2017) is not the spot lifetimes of "individual" spot (groups) but the global trends, but our results in Chapters 2 and 3 are surprisingly consistent with them. Bradshaw & Hartigan (2014) proposed that the short timescales of gigantic star spots can be due to the different turbulent magnetic diffusivity based on the solar GW relation $T \propto A$. However, we confirmed that the dependence of the emergence/decay rates of star spots has a positive correlation with spot area for solar and stellar spots (results (iii)). Based on the equations in the results (iii), we derived the new scaling relations $T \propto A^{0.5-0.7}$. The relation can naturally explain the observed lifetimes of star spots without any assumption of magnetic diffusivity in Bradshaw & Hartigan (2014). We then propose that not only the emergence/decay rates but also the lifetimes can be explained universally by solar models for sunspots and star spots on solar-type stars.

Here, I summarize the important and remaining problems for the main topic described in Chapters 2 and 3 as follows:

- Relation between spot emergence and suerpflare (cf. Section 3.5.3)
- Study in other stars with different rotational period and temperature
- Comparison with solar observations and numerical modelings.

It should be noted that the above results are found only for Kepler-17, and it's not obvious that these are applicable to the other stars. Kepler-17 is a solar-type star with the medium rotation period ($P_{\rm rot} \sim 12$ days), and main physics to determine the spot emergence and decay can be different from those of younger more rapidly rotating star ($P_{\rm rot} \sim$ a few days) and older slowly-rotating stars like the Sun ($P_{\rm rot} \sim 25$ days), as suggested in Chapter 2 (Namekata et al., 2019). Actually, the obtained dependence of lifetimes on rotational periods is still a mystery for now. Therefore, the validations on other stars with the transit method would be necessary for further universal understandings of the star spot physics. Up to present, the number of good targets is quite limited in the *Kepler* field because this kind of research requires suitable inclinations of the stars and planets and high-time cadence data. Nowadays *TESS* (Transiting Exoplanet Survey Satellite, Ricker et al., 2015) have provided us with mid-term (27 days - 1 year) stellar photometric data, and is expected to find many transiting exoplanets with two-minute cadence. This may be good candidates to confirm our results on other stars, not only solar-type stars but also cooler stars (cf. Chapter 6).

Currently, we hardly observe the magnetic flux configurations of spots below the photosphere, even on the Sun, although the local helio-seismology has a potential to estimate them. As a future work, comparisons with numerical simulations on spot evolution would be important. Recently, calculations to investigate spot evolution have been widely carried out (e.g. Cheung et al., 2008; Rempel & Cheung, 2014), but the evolution in the limited numerical box are still influenced by the initial and bottom-boundary conditions. Numerical simulations of spot evolution covering from the convection zone have been performed (Hotta et al., 2019; Toriumi & Hotta, 2019), which may reveal the spot emergence and decay mechanism. Some of the key future topics presented here are listed again in Section 7.2.

CHAPTER 4

# Statistical study of solar white-light flares and comparison with superflares on solar-type stars

## 4.1 Introduction

As introduced in Chapter 1, one of the mysteries in stellar flares is the origin of white-light emission. The recent space-based optical telescopes found many stellar white-light flares (hereafter WLFs) even on solar-type stars as overviewed in Section 1.2.2-1.2.3, but the origin of white-light emissions have been poorly understood, even in the solar flares. It is obvious that the difficulty in interpretations of white-light emission has kept us away from unveil the mechanism of the stellar superflare events.

Here we introduce the historical observations of white-light flares and its interpretations. The white-light components in solar flares were firstly observed by Carrington (1859). Solar WLFs are usually rare events compared to the H$\alpha$ and soft X-ray flares because of the short durations (typically a few minutes; Hudson et al., 1992; Xu et al., 2006) and the low contrast (typically 5-50%, at most 300%; Lin & Hudson, 1976; Jess et al., 2008). It is widely accepted that white-light (WL) emissions are well correlated with hard X-ray and radio emissions spatially (e.g. Krucker et al., 2011) and temporally (e.g. Hudson et al., 2006). These properties imply that high energy electrons are essential to the WL emissions. However, while the high energy electrons can penetrate into the chromosphere, they hardly reach the photosphere where optical photospheric continua originate (Najita & Orrall, 1970). For this reason, some portions of WL emissions are considered to be radiated through hydrogen recombination continuum (Paschen) at the directly heated and ionized upper chromosphere (Machado et al., 1989; Svestka, 1976; Heinzel et al., 2017).

On the other hand, the absence of strong chromospheric Balmer-continuum emission in some WLFs (so-called "type-II" WLFs, Machado et al., 1986) is considered to suggest another WL emission source (Ding et al., 1999), which is $H^-$ continuum from the heated photosphere (also see Machado et al., 1989; Svestka, 1976; Heinzel et al., 2017, for review). The energy transportation to such a lower atmosphere is still debated. A strong downward irradiation by XUV or hydrogen Balmer continuum is proposed to heat the lower atmosphere ( the so-called "back-warming"). In addition to this, other energy injections have been also proposed, such as *Alfvén* waves (Fletcher & Hudson, 2008) or high energy protons (Neidig, 1989).

It is obvious that the lack of information on the emission heights and spectra keep us away from identifying the emission mechanism of white-light flares. Although many authors have reported the emission heights compared to hard X-ray (e.g. Martínez Oliveros et al., 2012) and chromospheric line emission (Watanabe et al., 2013), there is no agreement due to its difficulty in observation. The broad-band spectroscopic observations of solar WLFs are quite sparse (e.g. Mauas, 1990), but enable us to fit the continuum with blackbody radiation. Some studies reported the emission temperature of 5,000–6,000 K (e.g. Watanabe et al., 2013; Kerr & Fletcher, 2014; Kleint et al., 2016), and the others 9,000 K (Kretzschmar, 2011). The blackbody fitting would enable us to roughly estimate the radiation energies in the optical continuum, but it does not consider the Balmer recombination continuum whose large enhancement is proposed by some observations (e.g. Heinzel & Kleint, 2014) and simulations (e.g. Kowalski et al., 2017).

In the case of stellar flares, the interpretations of the white-light components are more controversial, although some of them shows similar features to solar WLFs (summarized in Section 1.2.2 'White-light emissions'). Interestingly, the large superflares on solar-type stars ($10^{33-36}$ erg) was detected as WLFs with the optical photometry by *Kepler* (see Section 1.2.3; Maehara et al., 2012; Shibayama et al., 2013). It has been found that superflares are also phenomena where magnetic energies are released (Notsu et al., 2013). However, the origin of the white-light emissions of the superflares has been not known, and therefore whether the superflares are essentially the same phenomena as solar flares (i.e. release of magnetic energy via magnetic reconnection) is a mystery.

Maehara et al. (2015) reported that there is a correlation between the energies radiated in WL ($E$) and durations ($\tau$) of superflares: $\tau \propto E^{0.39}$. They found that the power-law relation is surprisingly consistent with those of solar flares observed with hard/soft X-rays: $\tau \propto E^{0.2-0.33}$ (Veronig et al., 2002; Christe et al., 2008). A similar relation is also found between stored magnetic energies ($E_{\rm mag}$) and soft X-ray flare decay time ($\tau_{\rm decay}$): $\tau_{\rm decay} \propto E_{\rm mag}^{0.41}$ (Toriumi et al., 2017). These similarities on the $E$–$\tau$ relation indicate a common mechanism of energy release among solar flares and supreflares. Maehara et al. (2015) moreover suggested that the observed power law relations can be explained by the

magnetically driven energy release mechanism (magnetic reconnection) as follows. As in Equation 1.2, since flares are the mechanism that releases stored magnetic energies ($E_{\rm mag}$), flare energy ($E$) is expressed as a function of magnetic field strength ($B$) and length scale ($L$) of flares:

$$E_{\rm flare} \sim f E_{\rm mag} \propto f B^2 L^3, \tag{4.1}$$

where $f$ is a fraction of energy released by a flare. As in Equation 1.1, the duration of flares ($\tau$) is thought to be comparable to the reconnection time scale ($\tau_{\rm rec}$):

$$\tau \sim \tau_{\rm rec} \sim \tau_A / M_A \propto L / v_A / M_A, \tag{4.2}$$

where $\tau_A = L/v_A$ is the Alfvén time, $v_A$ is the Alfvén velocity, and $M_A$ is the dimensionless reconnection rate which takes the value of 0.1-0.01 in the case of the Petschek-type fast reconnection (Shibata & Magara, 2011). Assuming that stellar properties ($B$ and $v_A$) are not so different among the same spectral-type stars (solar-type stars), the values of both $E$ and $\tau$ are determined by the length scale ($L$). On the basis of this assumption, the relation between $E$ and $\tau$ can be derived by deleting $L$ from Equation 4.1 and 4.2:

$$\tau \propto E^{1/3}. \tag{4.3}$$

This similarity between the theory and solar and stellar flare observations indirectly indicates that solar and stellar flares can be explained by the same mechanism of magnetic reconnection.

The purpose of this chapter is to confirm observationally this suggestion by Maehara et al. (2015). We consider that a remaining key observation is to confirm whether both solar and stellar flares can be explained by the common $E$–$\tau$ scaling laws in the same wavelength range. This is because the origins of white-light emission is not well known and the durations and radiated energy in each band is largely different for each wavelength (see Section 1.1.2; e.g. Emslie et al., 2012; Kane, 1974). Therefore, in this study, we carried out a statistical research on 50 solar WLFs and compared the $E$–$\tau$ relations in the WL wavelength range, aiming to confirm the above expectation that solar and stellar flares can be universally explained by the same theoretical relation (Equation 4.3). We introduce analysis methods in Section 4.2, show the results in Section 4.3 and discuss the obtained results in Section 4.4

## 4.2 Analysis

We carried out statistical analyses of temporal variations of 50 solar WLFs observed by *Solar Dynamics Observatory* (*SDO*)/Helioseismic and Magnetic Imager (HMI; Scherrer

et al., 2012) in the continuum channel with 45 sec cadence. It is necessary to carefully subtract the background trend since the emission of solar WLFs is difficult to detect due to much lower contrast to the photosphere. On the basis of the previous studies (e.g. Kuhar et al., 2016; Matthews et al., 2003), we identified the WL emissions inside the region with strong HXR emissions observed by *RHESSI* (*Reuven Ramaty High Energy Solar Spectroscopic Imager;* Lin et al., 2002). The radiated energies and decay times were calculated from the extracted light curves of WLFs. In the following subsections, we introduce these analysis methods.

### 4.2.1 Selection

Our WLF catalogue contains M and X class solar flares which occurred from 2011 to 2015 and were observed by both *SDO*/HMI and *RHESSI*. The 43 flares in our catalogue which occurred from 2011 to 2014 were taken from Kuhar et al. (2016), we enlarged the sample by adding 10 flares which occurred in 2015. The newly added flares satisfy the following three conditions.

- The *GOES* X-ray class is above M2.
- The overall light curve of a flare was observed by *RHESSI*.
- The WL emissions can be clearly recognized with the pre-flare-subtracted images.

The reason why we added only above M2 class flares is that the increase in numbers of weak flares would not improve statistics due to the difficulty in measurements of the emission. After the imaging process of HXR with the *RHESSI* data, we finally selected 50 solar flares (Table B.1-B.5) whose HXR emissions are well spatially correlated with the WLF emissions.

### 4.2.2 Time evolution of WLF

As mentioned above, it is necessary to appropriately decide the area where we measure the enhancement of WLF to avoid the disturbance from granule or p-mode ocsillations. In this study, we extracted WL emissions inside the area identified by the HXR emissions observed with *RHESSI*. In the imaging process of the *RHESSI* data, we used the CLEAN algorithm (Hurford et al., 2002). Detectors were carefully chosen on the basis of the *RHESSI* detector spectrum (see, Table B.6). The energy band was determined to be 30-80 keV because the HXR around 50 keV is well correlated with WLF emissions (e.g. Kuhar et al., 2016). The integration time ranges were set from the beginning to the end of HXR

flares. As for the events whose loop-top sources have too strong HXR emissions, the initial impulsive phases were excluded to make clear maps of footpoint sources.

Comparing the images of the HXR flares and WLFs, we decided to make the light curves of WLFs by summing up the brightness variations of the HMI images inside the $30\%$ contour of HXR emissions. This contour level is large enough to cover the enhancements of WLF emissions. In order to make the light curves with high precision, the contour levels were adjusted to $10\%$, $20\%$, $50\%$, or $70\%$ for some events whose HXR emissions are too large or too small (Table B.6). We determined the WLF's start and end time on the basis of the obtained light curves ($L_{\rm obs}$) and the pre-flare-subtracted WL movies (Table B.6). We subtracted the global trend as follows. First, we replaced the light curves during the flares with linear interpolation of the quiescence ($L_{\rm bg}$). Second, we obtained global background trends ($L_{\rm bg\text{-}trend}$) by performing a smoothing process (across 5 points of data) for the obtained background light curves ($L_{\rm bg}$). Lastly, we subtracted the global background trends ($L_{\rm bg\text{-}trend}$) from the original light curves ($L_{\rm obs}$) and obtained the light curves of WLFs ($L_{\rm WL} = L_{\rm obs} - L_{\rm bg\text{-}trend}$). This analysis could hide meaningful trends such as increase in photospheric activity or gradual cooling components. Considering these effects, we estimated the expected error bars in the Section 4.3.2.

Figure 4.1 shows the examples of the time evolutions of WLFs. (a) is one of the most powerful WLFs in our catalogue which occurred on 23th October 2012 (a X1.8 class flare). In the panel, light curves observed by *GOES*, *RHESSI* and *SDO*/HMI are plotted in the left, and the pre-flare-subtracted images of the evolution of the WLF in the right. In the images, the time are indicated with arrows in the *SDO*/HMI light curve, and the black components show the WL emissions over $1\sigma$ levels. (b) and (c) show one of the long and short WLFs in our catalogue, respectively. (d) is a disk-center event, and the WL kernel can be seen in the pre-flare subtracted images in the HXR contour. As one can see, the main enhancement can be detected inside the *RHESSI* contours, and the decay phases are usually a few minutes, as many previous studies also reported (e.g. Kuhar et al., 2016; Hudson et al., 1992; Xu et al., 2006; Matthews et al., 2003)

To present whether the cadence of *SDO*/HMI is short enough to resolve the evolution of WLFs, we compared the obtained light curves with those observed by the *Solar Magnetic Activity Research Telescope* (SMART; Ishii et al., 2013) at Hida Observatory of Kyoto University for one event and *Hinode*/Solar Optical Telescope (SOT; Tsuneta et al., 2008) for four events. In our catalogue, a flare on 5th May 2015 was also observed by SMART. The SMART observes partial images of the Sun with a continuum filtergram (center 6470 Å, width 10 Å), and the time cadence is $\sim$0.04 sec. We made a light curve by the same way as the above analysis and compared the time evolution with that obtained from HMI in Figure 4.3. These light curves, as in Figure 4.3, look consistent with each other, which indicates that the cadence of HMI is enough to follow the evolution of solar WLFs. There

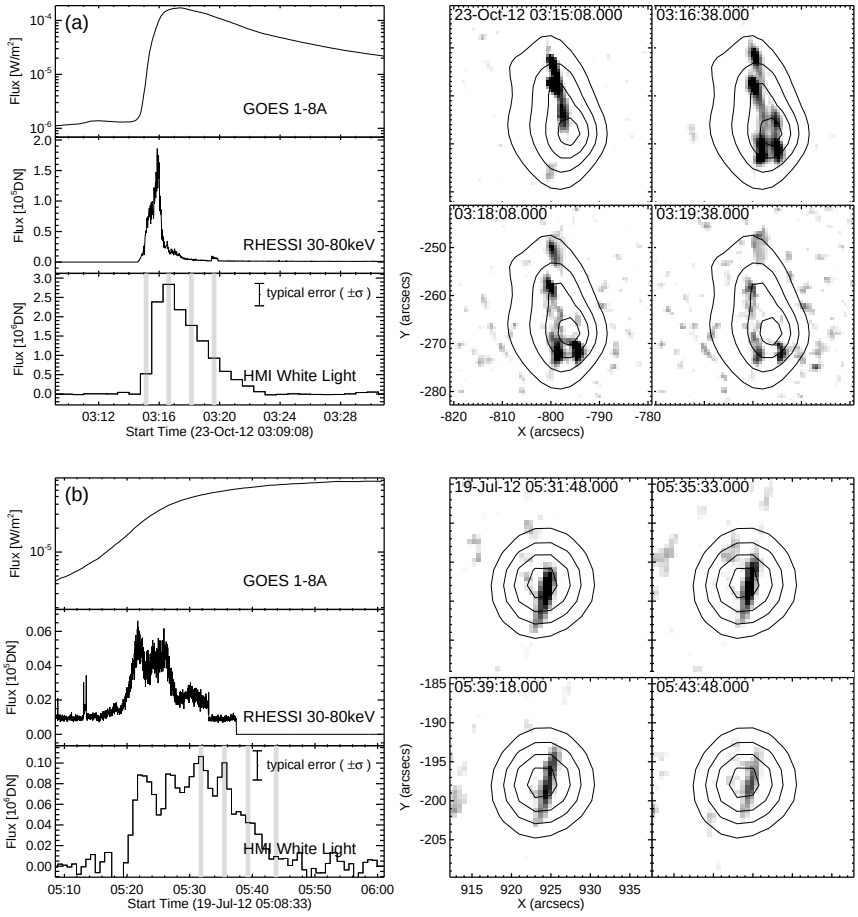


Figure 4.1: Light curves and intensity maps of solar flares observed in white-light, hard X-ray, and soft X-ray bands. (a) The left panels are the light curves of a solar flare which occurred on 23th October 2012 observed by *GOES* (1-8 Å; upper), *RHESSI* (30-80keV; middle) and HMI (white light; lower). A typical error of WL emission is calculated on the basis of brightness variation outside the HXR contour of the HMI images. The right panels show the evolution of the pre-flare-subtracted images observed by HMI continuum and each time corresponds to that marked with gray line in the left lower panel. The black components show white-light emissions above $1\sigma$ of each image and the black lines show the *RHESSI* contours of 30%, 50%, 70% and 90% of the maximum emission in 30-80keV. (b) A long-duration solar flare on 19th July 2012, but the black lines show the *RHESSI* contours of 10%, 30% 50%, 70% and 90%.

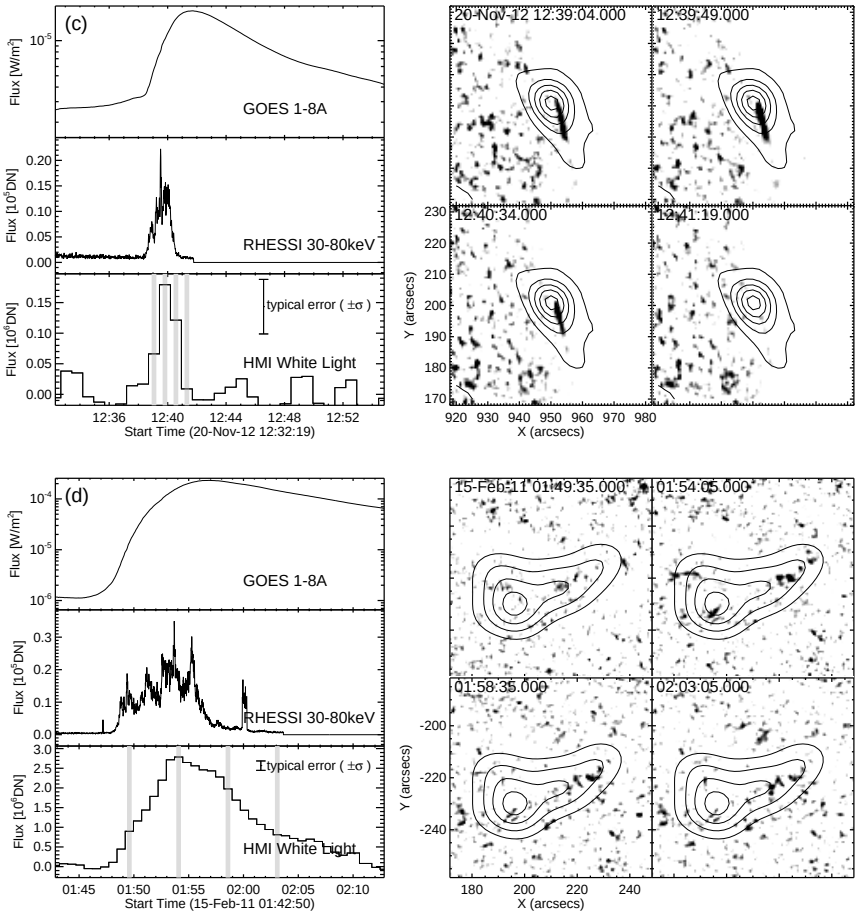


Figure 4.2: Light curves and intensity maps of solar flares observed in white-light, hard X-ray, and soft X-ray bands (Continued from Figure 4.1). (c) A short-duration solar flare on 20th November 2012. (d) A disk-center solar flare on 15th Feb 2011.

are also 4 events whose time profiles are clearly observed by *Hinode*/SOT in the continuum channels (a red channel at 6684.0 Å, and a green at 5550.5 Å, a blue at 4504.5 Å) among our catalogue (see, Table B.7). Figure 4.4 shows that the obtained light curves well match each other.

### 4.2.3 Calculation of energy and duration

The main aim is to compare the energy ($E$) and duration ($\tau$) of solar and stellar WLFs. We then calculated the energy and duration by the same way as Shibayama et al. (2013) and Maehara et al. (2015). There are two different things between solar and stellar observations, time cadences and pass bands. *SDO*/HMI observes the overall Sun with a 45 sec cadence and a narrow-band filtergram around a 6173.3 Å FeI line, while *Kepler* carried

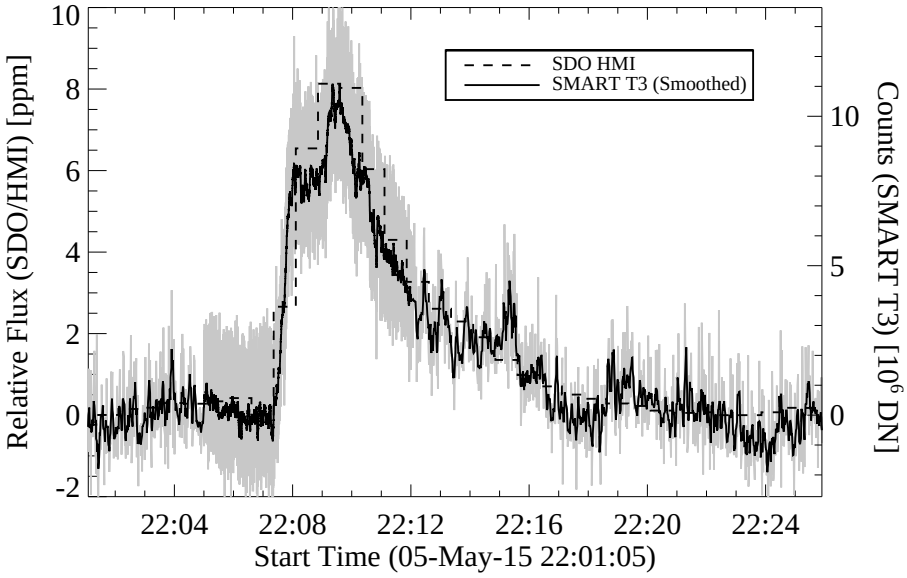


Figure 4.3: Comparisons of the light curves of a solar white-light flare on 5th May 2015 observed by HMI continuum (6173 Å; a dashed line) and SMART at Hida Observatory (continuum at 6470 Å; a solid line). As for the SMART data, the gray solid line is the observed data, and the black one is the smoothed data. SMART usually observes partial images of the Sun with 1 second cadence, but with 0.04 seconds cadence from 22:04:30 to 22:12:00 in the panel. Therefore, we obtained the black solid line by smoothing the gray line across 5 data points for the 1 second cadence data, and across 50 data points for 0.04 second cadence data. Note that the vertical axes of the SMART and HMI data are fitted with the each peak value. Although the 45 seconds cadence of HMI is worse than the 0.04 seconds (and 1 second) cadence of SMART, the light curve observed by HMI matches well that observed by SMART. The flare energy and duration ($2.5\times10^{30}$ erg and 2.9 min) calculated by HMI data were comparable to those ($2.3\times10^{30}$ erg and 2.5 min) calculated by SMART data. This indicates that the cadence of HMI is enough to follow the evolution of solar white-light flares.

out 1 min cadence observations with 4000-9000 Å broad-band filters. We calculated the energy of solar WLF assuming it is radiated by $T_{\rm flare}$ =10,000 K blackbody (see Katsova & Livshits, 2015, for this assumption):

$$E = \sigma_{\rm SB} T_{\rm flare}^4 \int A_{\rm flare}(t) dt \tag{4.4}$$

$$A_{\rm flare}(t) = \frac{L_{\rm flare}}{L_{\rm sun}} \pi R^2 \frac{\int R_\lambda B_\lambda(5800{\rm K}) d\lambda}{\int R_\lambda B_\lambda(T_{\rm flare}) d\lambda}, \tag{4.5}$$

where $\sigma_{\rm SB}$ is *Stefan-Boltzmann* constant, $L_{\rm flare}/L_{\rm sun}$ is the flare luminosity to the overall solar luminosity, $R$ is the solar radius, $R_\lambda$ is a response function of *SDO*/HMI and $B_\lambda(T)$ is the *Planck* function at a given wavelength $\lambda$. Since it is not confirmed how strongly the WL emission of flare is affected by the limb darkening effect (e.g. Watanabe et al., 2013),

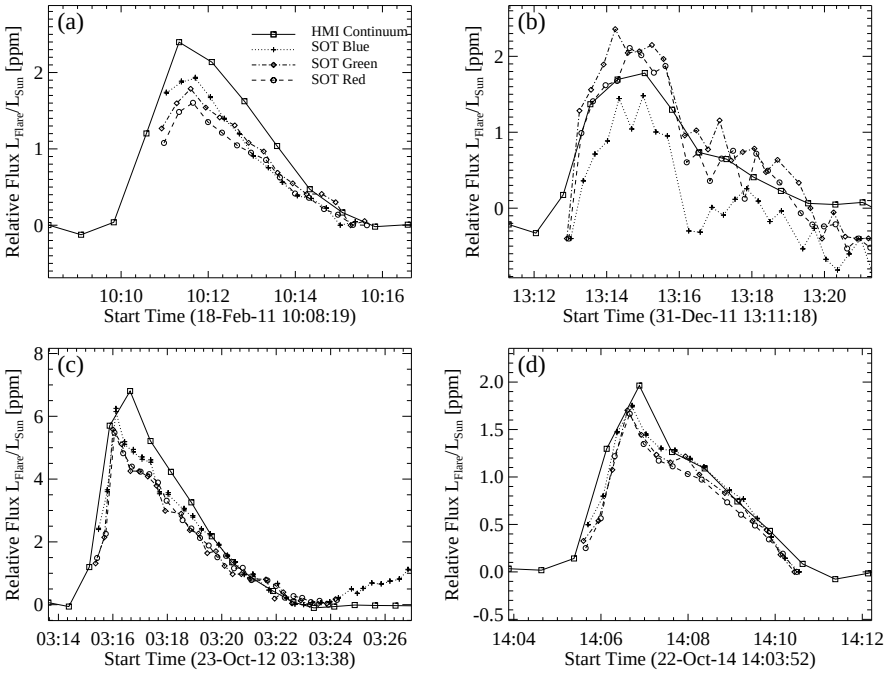


Figure 4.4: Comparisons of the light curves of solar white-light flares observed with HMI continuum (open squares; solid lines) and with *Hinode* SOT red (open circles; dashed lines), green (open diamonds; dash-dotted lines) and blue continuum (crosses; dotted lines). (a) is a flare on 18th Feb 2011, (b) a flare on 31th Dec 2011, (c) a flare on 23th Oct 2012, and (d) a flare on 22th Oct 2014.

we obtained WL fluxes and energies with and without correcting for the limb darkening of a plane parallel atmosphere at 6000 Å. On the other hand, the durations of flares are also calculated as e-folding decay time of light curves as in Maehara et al. (2015). If we use the 45 sec cadence data, the decay time may be overestimated especially in the case of the flares with very short duration such as in the lower panels of Figure 4.1. We therefore calculated the decay time by using the light curves corrected for a linear interpolation of 1 sec cadence.

## 4.3 Result

### 4.3.1 Relation between WLF flux, energy and SXR flux

First, we show statistical properties concerning the WL fluxes, energies, and *GOES* SXR fluxes. In our catalogue, more than 40 flares were also analyzed by Kuhar et al. (2016), and the values of WL fluxes obtained in this study are quite consistent with those obtained by Kuhar et al. (2016). The left panel in Figure 4.5 shows comparisons between WL fluxes

($F_{\rm WL}$) and *GOES* soft X-ray fluxes ($F_{\rm SXR}$) at the flare peak, and the right panel shows the same but the WL fluxes are limb-darkening corrected fluxes. We fitted the relation between $F_{\rm WL}$ and $F_{\rm SXR}$ in the form of $F_{\rm WL} \propto (F_{\rm SXR})^a$ with the following two methods for comparison, a linear regression method (LR) and a linear regression bisector method (LRB; Isobe et al., 1990). By the linear regression method, the power-law indexes of the left panel are $a = 0.63 \pm 0.04$, and those of the right panel are $a = 0.59 \pm 0.04$.

Likewise, the left panel in the Figure 4.6 shows comparisons between WL energies ($E_{\rm WL}$) and *GOES* soft X-ray fluxes, and the right shows the same but the WL energies are the limb-darkening corrected ones. The power-law relations ($E_{\rm WL} \propto (F_{\rm SXR})^b$) are obtained with the indexes $b = 0.87 \pm 0.04$, and those of the right panel with $b = 0.84 \pm 0.04$.

### 4.3.2 Relation between WLF energy and duration

Figure 4.7 shows comparisons between the radiated energies ($E$) and durations ($\tau$) of solar WLFs. The errors of flare durations are calculated by assuming that the pre-flare continuum levels fluctuated by $1\sigma$. There can be seen a positive correlation between flare energy and its duration and we can get the relation of $\tau \propto E^{0.38\pm0.06}$ by fitting the data with a linear regression method (the same fitting method as Maehara et al., 2015). Note that the relatively shorter durations of the *Hinode*'s flares are due to a selection bias that the *Hinode*'s observational intervals cannot cover the overall light curves of long duration flares. In fact, the decay time obtained from *Hinode* data is only 12 $\%$ shorter than that obtained from *SDO* data (also see, Table B.7).

### 4.3.3 Comparison between solar flares and superflares on solar-type stars

We compared the solar WLFs and superflares on solar-type stars in Figure 4.8. The data of superflares were basically taken from Maehara et al. (2015), which reports 187 superflares on 23 solar-type stars. In figure 4.8, however, we excluded all flares (19 events in total) on KIC 7093428. This is because KIC 7093428 was found to be a sub-giant star (surface gravity $\log g \sim 2.77$) in the latest version of the *Kepler* Input Catalog (Mathur et al., 2017), which includes the results of new estimations of $\log g$ values using the granulation amplitude data in *Kepler* light curve (cf. Flicker method; Bastien et al., 2016). The other 22 superflare stars in Maehara et al. (2015) are still in the range of solar-type stars in this revised *Kepler* Input Catalog, and we use these stars in the plot in Figure 4.8.

The left panel shows the distribution of WLF fluxes and durations of solar flares (filled squares) and superflares with short cadence data (open squares). The solar WLF fluxes $L_{\rm WL}$ are about $10^{-5}$–$10^{-6} L_{\rm sun}$, where $L_{\rm sun}$ is the solar luminosity. These values are

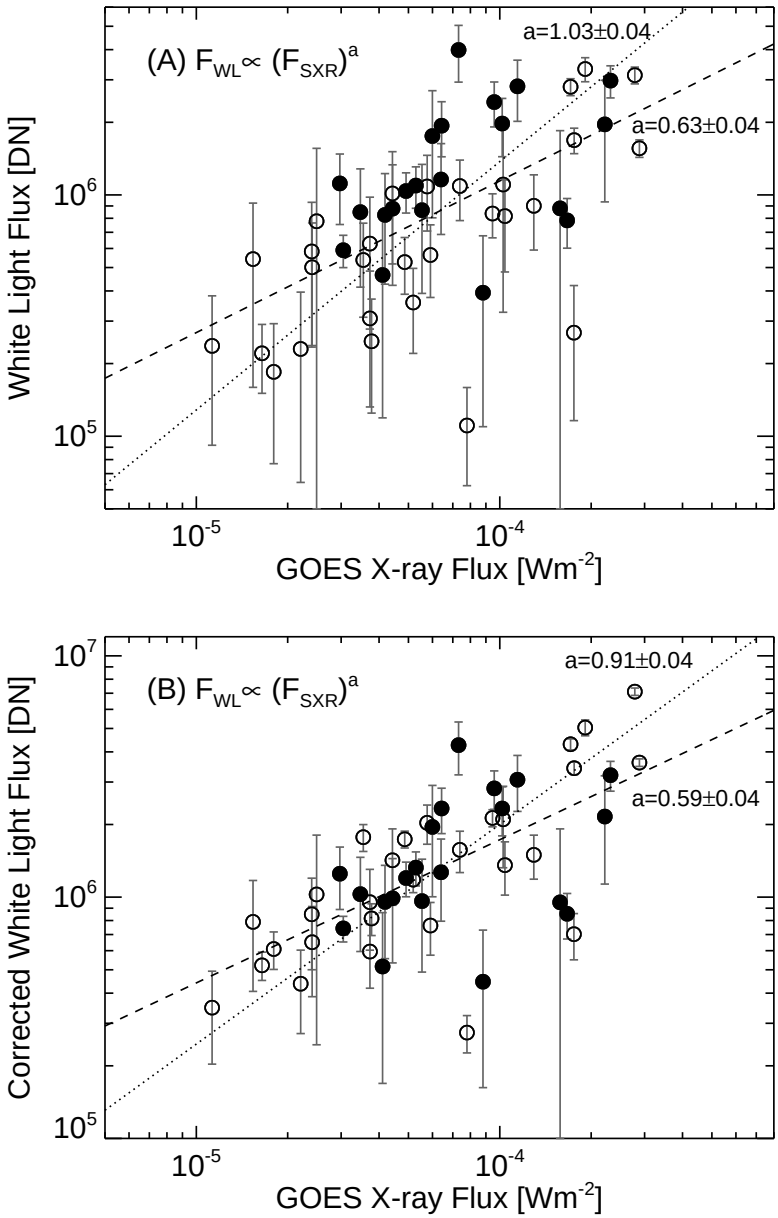


Figure 4.5: Comparison between GOES soft X-ray peak flux and white-light flare peak count. (A) The left panel shows the comparisons of the GOES soft X-ray fluxes at the flare peak time and the HMI white-light fluxes. (B) The right panel shows the same as the left panel, but the white-light emissions are corrected assuming the limb-darkening of the plane-parallel atmosphere. In each panel, the filled symbols are flares on the disk center whose distances from the solar center are less than 700 arcsec, and open ones are flares on the limb. Dashed and dotted lines are fitted lines with linear regression method (LR) and a linear regression bisector method (LRB; Isobe et al., 1990), respectively. The error bars shows $3\sigma$ components of the light curve in quiescence. The power-law indexes of the left panel are $a = 0.63 \pm 0.04$ (LR) and $a = 1.03 \pm 0.04$ (LRB), and those of the right panel are $a = 0.59 \pm 0.04$ (LR) and $a = 0.91 \pm 0.04$ (LRB).

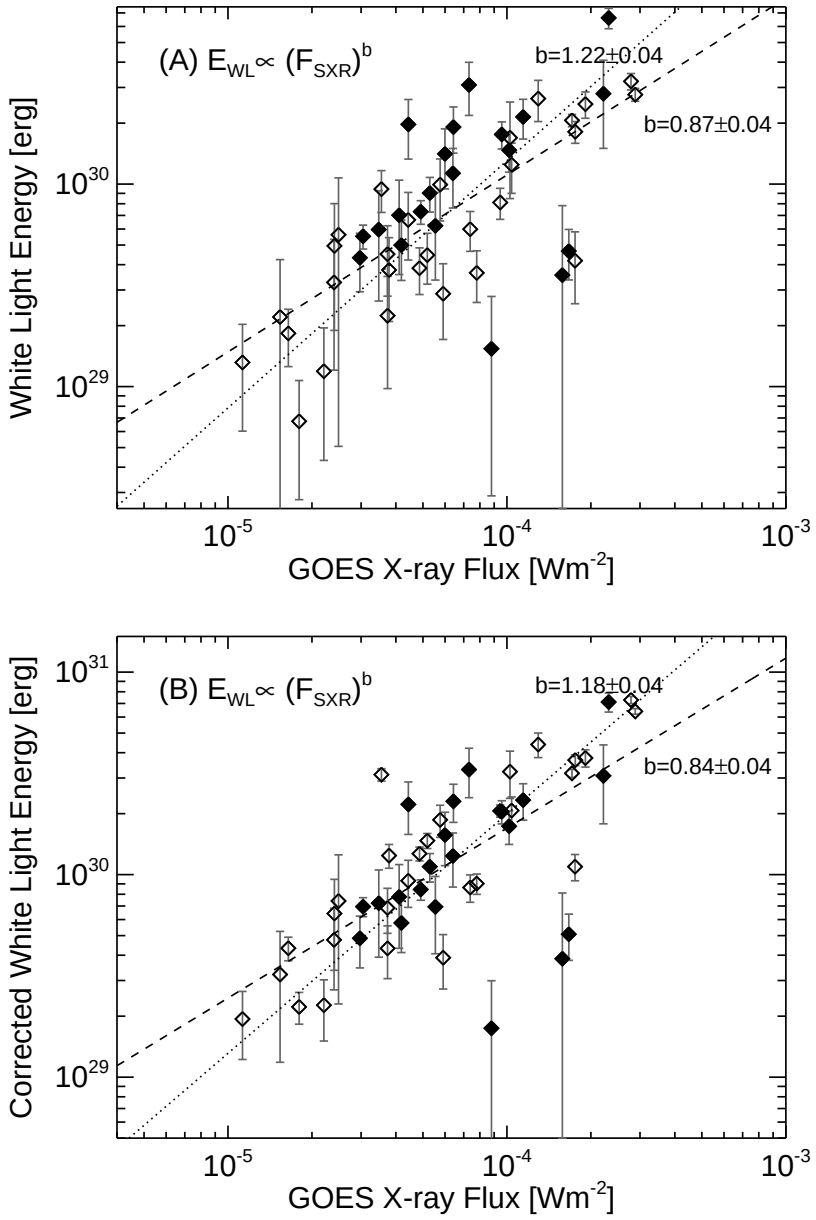


Figure 4.6: Comparison between GOES soft X-ray peak flux and white-light flare energy. (A) The left panel shows the comparisons of the GOES soft X-ray fluxes at the flare peak time and the HMI white-light energies. (B) The right panel shows the same as the left panel, but the white-light energies are corrected assuming the limb-darkening of the plane-parallel atmosphere. In each panel, the filled symbols are flares on the disk center whose distances from the solar center are less than 700 arcsec, and open ones are flares on the limb. Dashed and dotted lines are fitted lines with linear regression method (LR) and a linear regression bisector method (LRB; Isobe et al., 1990), respectively. The error bars were calculated from $1\sigma$ components of the light curve in quiescence. The power-law relations ($E_{\rm WL} \propto (F_{\rm SXR})^b$) are obtained with the indexes $b = 0.87 \pm 0.04$ (LR) and $b = 1.22 \pm 0.04$ (LRB), and those of the right panel with $b = 0.84 \pm 0.04$ (LR) and $b = 1.18 \pm 0.04$ (LRB), which shows that the WL energy is proportional to *GOES* soft X-ray flux.

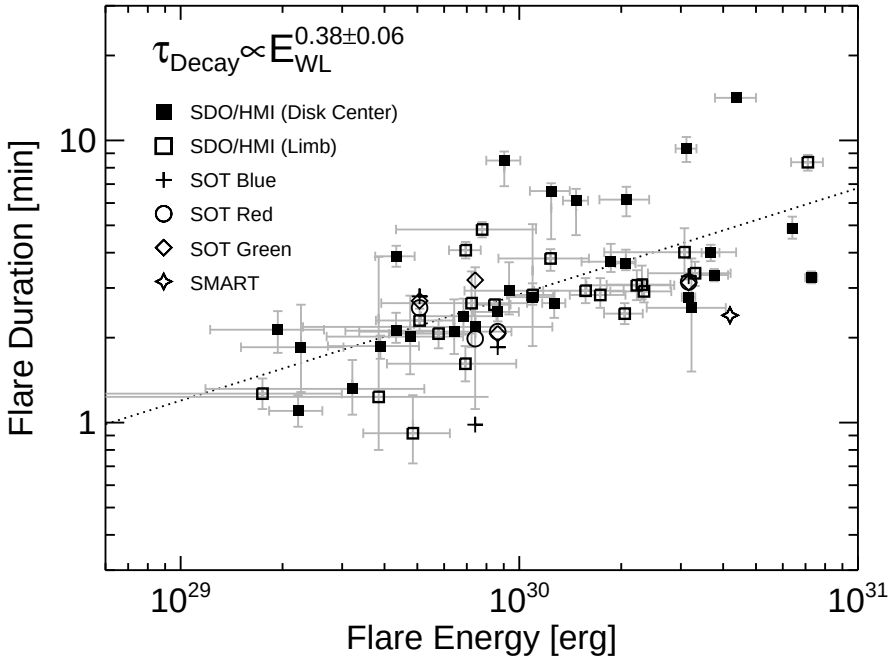


Figure 4.7: Comparison between the flare energy and duration. The squares show solar white-light flares analyzed in this paper and the dotted line is a fitting result for these data with a linear regression method. The filled squares are flares on the disk center whose distances from the solar center are less than 700 arcsec, and open ones are flares on the limb. The data whose durations were observed by *Hinode* SOT blue, red and green continuum were also plotted with crossed, open circles and open diamonds, respectively. The data observed by SMART is also plotted with a star symbol.

consistent with the result of flare observations using the total solar irradiance data (e.g. Kretzschmar, 2011).

Likewise, the right panel shows the distribution of radiated energies and durations. The power-law index of the superflares (without KIC 7093428) is $0.38 \pm 0.02$. This is not so different from the original value (0.39), which includes the data points of KIC 7093428. As in the above section, we found that a power-law index of solar WLFs (0.38) is found to be consistent with that of the superflares (0.38). However, these distributions of solar and stellar flares cannot be explained by a same power-law relation (cf, Equation 4.3, Maehara et al., 2015), and the durations of superflares are one order of magnitude shorter than those extrapolated from the power-law relation of solar WLFs.

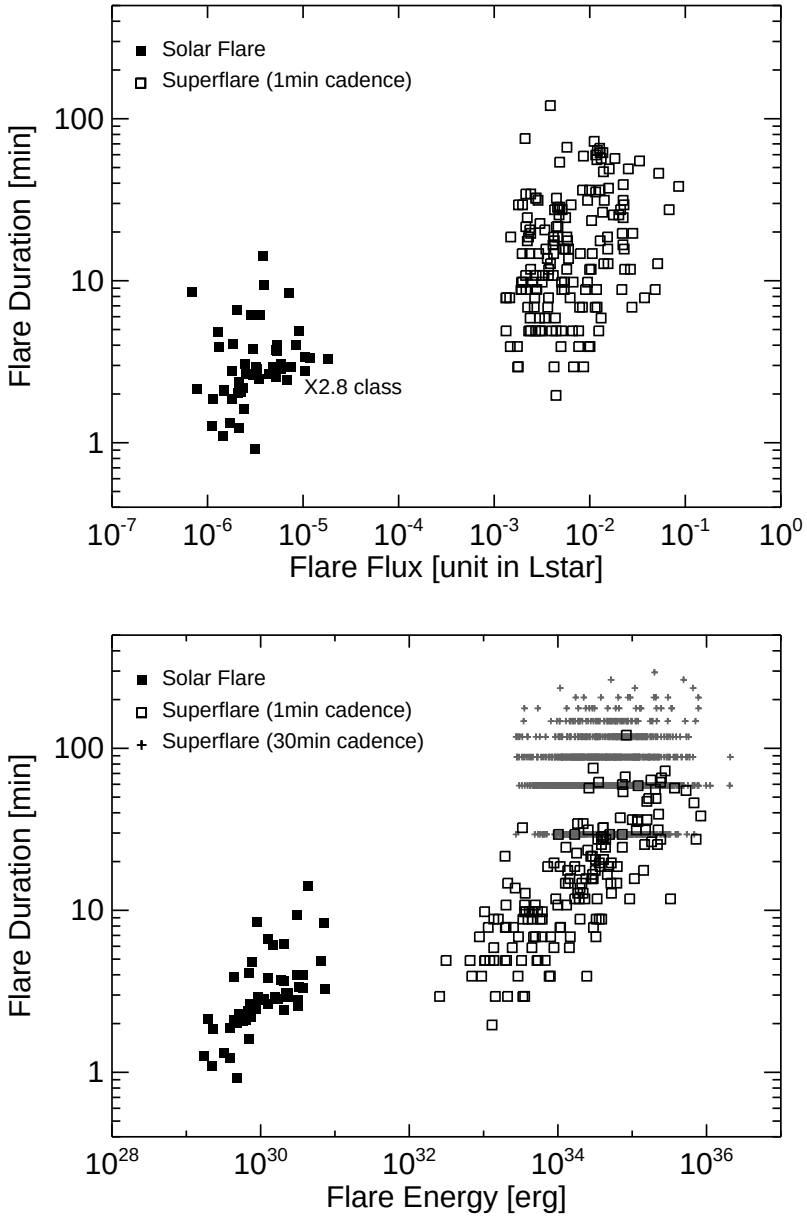


Figure 4.8: Comparison between the flare flux/energy and duration for solar and stellar flares. Upper: Comparison between the flare flux and duration. Lower: Comparison between the flare energy and duration. The open squares show solar white-light flares analyzed in this paper and the filled squares and crosses show superflares on solar-type stars obtained from *Kepler* 1 minutes and 30 minutes cadence data, respectively. The data of superflares are taken from Maehara et al. (2015).

## 4.4 Discussion

### 4.4.1 Energetics of solar flares

Many stellar flares are recently observed especially as WLFs thanks to the *Kepler* data, and the properties of stellar WLFs have been studied. In contrast, the energy scales of solar flares are mainly classified by the *GOES* X-ray flux (a few % of the total radiated energy; Emslie et al., 2012). To compare the properties of solar and stellar flares and understand the energetics of flares, it is necessary to investigate the relation between the *GOES* soft X-ray fluxes and WLF energies.

Our results of comparisons between WLF flux and *GOES* soft X-ray flux ($F_{WL} \propto F_{SXR}^{0.59\pm0.04}$) well match the relation ($F_{WL} \propto F_{SXR}^{0.65}$) obtained by Kretzschmar (2011). Even if the relation is universal across to wide energy ranges, the absence of a linear correlation is not surprising and can be explained as follows. The relation between HXR and SXR flux is expressed as $F_{HXR} \propto dF_{SXR}/dt \propto F_{SXR}/\tau$ in the impulsive phase, which is known as Neupert effect (Neupert, 1968). By considering that WLFs are well correlated with HXR flares and using the relation $\tau \propto E^{1/3}$, the relation between WL fluxes and SXR fluxes is derived as $F_{WL} \propto F_{HXR} \propto F_{SXR}/\tau \propto F_{SXR}^{2/3}$, which is in agreement with the above observed $F_{WL}$–$F_{SXR}$ relations.

Against these observations, Shibayama et al. (2013) suggested that the flare energy-frequency distribution cannot be explained by the Krezschmar's relation but by proportional relation ($F_{WL} \propto F_{SXR}$). However, the relation between flare energy and soft X-ray flux can be calculated as $E_{WL} \sim F_{WL} \times \tau_{\rm dur} \propto F_{WL}^{3/2} \propto F_{SXR}$ by using the Krezschmar's relation and the relation of $\tau \propto E^{1/3}$. Hence, there is in fact no contradiction between the observed flare energy-frequency distributions and the Krezschmar's relation. As in Figure 4.6, we found that the relation between the flare energy and *GOES* flux is in $E_{WL} \propto F_{SXR}^{0.84\pm0.04}$ with a linear regression method. Note that this power-law index may not be universal among wide energy ranges because it significantly depends on the fitting method due to such a narrow x-y range (e.g, $E_{WL} \propto F_{SXR}^{1.18\pm0.04}$ with a linear regression bisector method; Isobe et al., 1990).

### 4.4.2 The energy and duration diagram

As mentioned in Section 4.1, the relations between flare energies and durations have been found to be universal among solar X-ray flares ($\tau \propto E^{0.2-0.33}$) and stellar WLFs ($\tau \propto E^{0.39}$), and the relation well matches the theoretical relation consistent with magnetic reconnection ($\tau \propto E^{1/3}$). Our result also showed that the relation of solar WLFs ($\tau \propto E^{0.38\pm0.06}$) well matches these previous studies (Figure 4.7). This consistency supports

the suggestion that both solar and stellar flares are caused by the magnetic reconnection. However, as in Figure 4.8, it was also found that WLFs on the Sun and the solar-type stars were not on a same line though the power-law indexes are the same ($\tau \propto E^{1/3}$). This discrepancy indicates that solar and stellar WLFs cannot be simply explained by the relation derived by Maehara et al. (2015). We propose two possibilities to explain such a discrepancy:

- properties of cooling or heating mechanisms unique to WLFs (Section 4.4.2.1).
- differences in physical parameters between solar and stellar flares (Section 4.4.2.2)

Of course some analysis problems cannot be completely excluded. Nevertheless, the result can have a potential to know the difference between solar flares and superflares as well as the unsolved mechanism of WLFs. In the following sections, we discuss the above two possibilities in detail.

#### 4.4.2.1 Properties of cooling or heating mechanisms of WLFs

The first interpretation of the $E$-$\tau$ diagram is that the difference between solar and stellar flares is related to the properties unique to WLFs, especially cooling effect. It is observationally known that solar WLFs have two emission components: a "core" structure which is a candidate of direct chromospheric heating, and a "halo" structure which is a candidate of backwarming (Isobe et al., 2007). High-time-resolution observations also reveal that, in the "halo" structure, there are long ($\sim$500 sec) decay components and the timescales correspond to coronal cooling timescales (Kawate et al., 2016). We should note that it is not confirmed whether such decay time originates in the cooling timescale or the long lasting reconnection. However, if it does correspond to the cooling timescale, the 500 sec cooling time ($t_{\rm cool}$) is not negligible compared to the reconnection timescale ($t_{\rm rec}$) and could elongate the decay time of WLFs. Therefore, there is a possibility that the decay time of solar WLFs (below $\sim 10^{32}$ erg) are elongated by cooling effect because $t_{\rm cool} >> t_{\rm rec}$, but those of superflares (above $\sim 10^{33}$ erg) are not elongated because $t_{\rm cool} << t_{\rm rec}$, which would result in the observed $E$–$\tau$ discrepancy.

We consider that comparisons of the durations of solar WLFs and HXR flares can provide us a hint to cooling effect because the HXR nonthermal emissions are not affected by cooling time. We then measured the decay time of HXR emissions (30–80 keV) as a proxy of the reconnection timescale by using *RHESSI* data. In Figure 4.9, open circles are solar flares whose durations are replaced for those of HXR flares. The durations of solar HXR flares are shorter by a factor of 5 at average than those of WLFs. This indicates that the durations of solar WLFs are somewhat elongated by any cooling effect. Also, Figure

4.9 shows that the distribution is roughly on the line extrapolated from the distribution of the superflares. If we could assume that $t_{\rm cool} << t_{\rm rec}$ in the case of superflares, then we might explain the observed $E$–$\tau$ diagram and conclude that both solar flares and stellar superflares are explained by the magnetic reconnection theory.

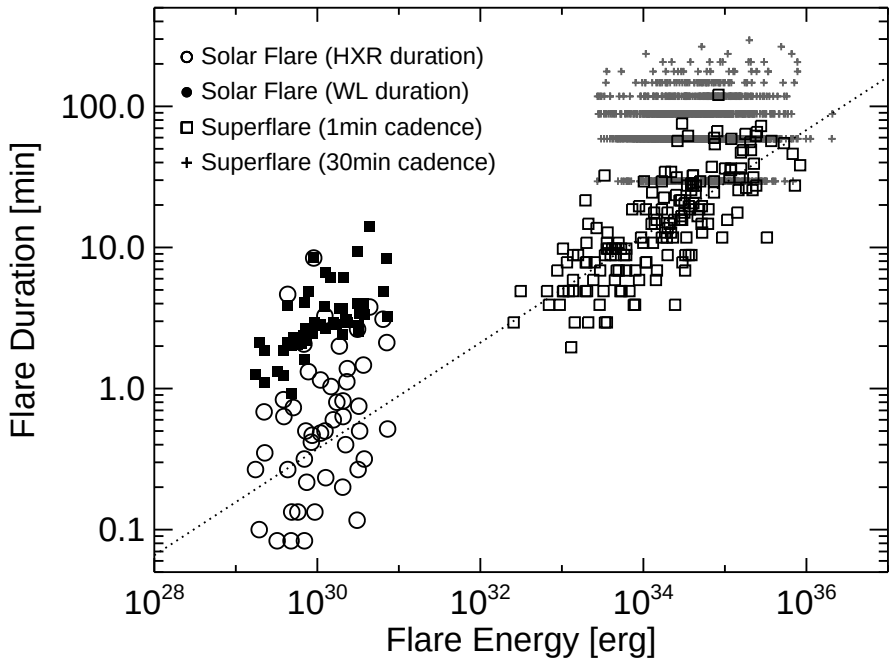


Figure 4.9: Physical understandings of relation between the flare energy and duration for solar and stellar flares (I). The symbols are basically the same as those in right panel of Figure 4.8, but open circles are solar flares whose durations are replaced for those of HXR flares. The HXR durations are defined as those from the peak time to the maximum time whose intensity are over 1/e of the peak values.

Note that we cannot completely support the above suggestion due to the following reasons. First, we have no knowledge about the relation between HXR durations and WL ones of superflares. Therefore, we cannot exclude a possibility that WL emissions of stellar superflares are also affected by cooling effect. Secondly, as in Figure 4.8, the $E$-$\tau$ relation of solar WLFs can be explained by the same theoretical line ($\tau \propto E^{1/3}$) as the large part of long-duration superflares observed by *Kepler* 30 min cadence. This may indicate that the WL cooling effect is not enough to explain the $E$–$\tau$ diagram.

In this section, we examined the possibility that the cooling timescale might be important in the understandings of the observed $E$-$\tau$ diagram. This may resolve the observed discrepancy except for some problems. To conclude how essential the cooling effect is, we have to (i) reveal the emission mechanism of solar WLFs, or to (ii) carry out multi-wavelength observations (WL and HXR) of superflares.

#### 4.4.2.2 Difference in physical parameters between solar and stellar flares

We present here the second interpretation of the observed $E$–$\tau$ diagram. Maehara et al. (2015) derived the theoretical scaling law $\tau \propto E^{1/3}$ assuming that the Alfvén velocity ($v_A = B/\sqrt{4\pi\rho}$) around reconnection region is constant among each flare on solar-type stars. This assumption would be roughly appropriate according to solar and stellar observations (e.g. Shibata & Yokoyama, 1999, 2002). When considering the dependence on Alfvén velocity, the scaling law can be expressed as follows:

$$\tau \propto E^{1/3} B^{-5/3} \rho^{1/2}. \tag{4.6}$$

On the basis of this scaling law, the one order of magnitude shorter durations of superflares can be understood by (1) two orders of magnitude lower coronal density of superflares, or (2) about a factor of 2–4 stronger coronal magnetic field strength of superflares than that of solar flares. The former possibility is less likely because superflare stars are rapidly rotating ones which are expected to have higher coronal densities based on the large emission measures of the X-ray intensity (e.g. Wright et al., 2011). On the other hand, the latter well accounts for the $E$–$\tau$ distributions without any contradiction with observations that superflare stars show high magnetic activities (e.g. Notsu et al., 2015b). On the basis of such a scaling relation, we proposed that the discrepancy can be caused by the strong coronal magnetic field strength of superflares.

By assuming pre-flare coronal density is a constant value, Equations 4.1 and 4.2 give the following new scaling laws:

$$\tau \propto E^{1/3} B^{-5/3} \tag{4.7}$$

$$\tau \propto E^{-1/2} L^{5/2}. \tag{4.8}$$

To simply determine the coefficients, we observationally measured the average values of $B$ and $L$ on the basis of the method introduced by Namekata et al. (2017a). $B$ is extrapolated from the photospheric magnetic fields using *SDO*/HMI magnetogram, and $L$ is calculated as square roots of the flaring area observed with *SDO*/Atmospheric Imaging Assembly (AIA; Lemen et al., 2012) 94 Å (see in detail Appendix B.1). As a result, the coefficients can be obtained as $B_0 = 57$ G, $L_0 = 2.4 \times 10^9$ cm, $\tau_0 = 3.5$ min and $E_0 = 1.5 \times 10^{30}$ erg from the average among the solar flares in our catalogue. On the basis of such values, we applied the scaling laws to the observed $E$–$\tau$ diagram as in Figure 4.10, and found that solar flares and stellar flares have coronal magnetic field strength of 30–400 G. This range is roughly comparable to the observed values (40–300 G) of solar and stellar flares (Rust & Bar, 1973; Dulk, 1985; Tsuneta, 1996; Grosso et al., 1997) and those (15–150 G) estimated by Shibata & Yokoyama (1999, 2002). Moreover, it is reasonable that the estimated loop length of superflares ($\sim 10^{10}$–$10^{11}$ cm) is less than the solar diameter ($1.4 \times 10^{11}$ cm).

These consistencies support our suggestions. According to the scaling law, superflares observed with short time cadence have 2–4 times stronger coronal magnetic field strength than solar flares. Although it would be controversial whether such strong coronal magnetic fields can be really formed and sustained in the stellar coronae, it may be possible that, in the case of the superflare stars, the stronger fields of the surrounding quiet regions or the large star spots suppress the magnetic loops of active regions, and then sustain such strong magnetic fields. Note that this does not mean that all of stellar flares can be caused in such strong magnetic fields. As seen in the left and right panels of Figure 4.8, the upper limit of $E$-$\tau$ diagram is determined by the detection limit of superflares, implying a selection bias that the detection method by Maehara et al. (2015) tends to select relatively impulsive superflares. Therefore, it is natural that there are expected to be long-duration superflares with field strengths of a few 10 G .

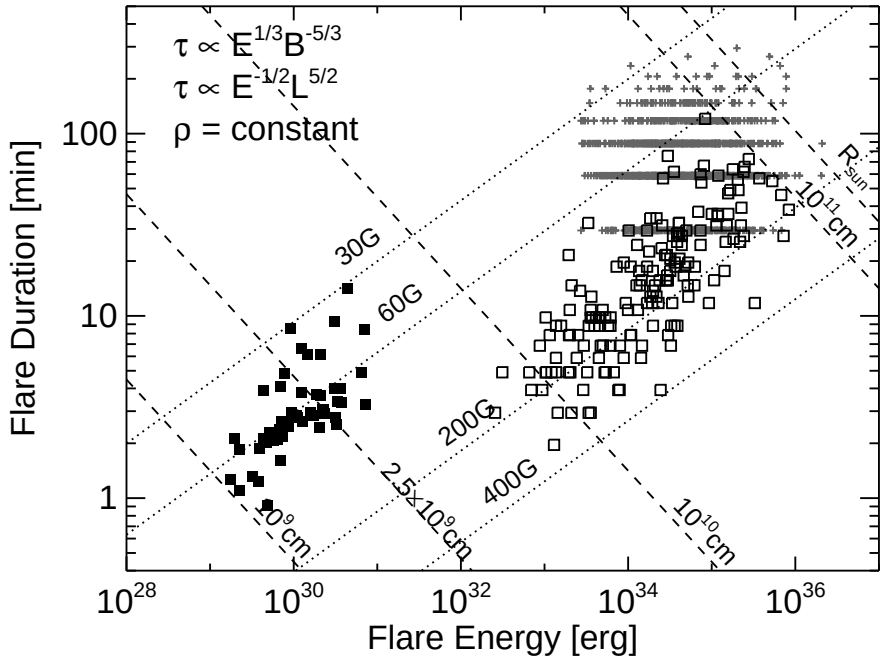


Figure 4.10: Physical understandings of relation between the flare energy and duration for solar and stellar flares (II). Theoretical $E$–$\tau$ relations (Equation 4.7, 4.8) overlaid on the observed $E$–$\tau$ relation in this study and Maehara et al. (2015). Theoretical lines are plotted with dotted lines for the different magnetic field strength $B$ = 30, 60 (an observational value of the solar flares), 200 and 400 G. The flare loop length $L$ = constant lines are also plotted with dashed lines for $L$=$10^9$, $2.5 \times 10^9$ (an observational), $10^{10}$, $10^{11}$ cm and a solar diameter.

To explain the observed $E$-$\tau$ diagram more realistically, we incorporated the dependence of the pre-flare coronal density ($\rho$) into the scaling law in the following two ways: (1) RTV (Rosner–Tucker–Vaiana) scaling law $\rho \propto L^{-3/7}$ (2) gravity stratification $\rho \propto L^{-1}$.

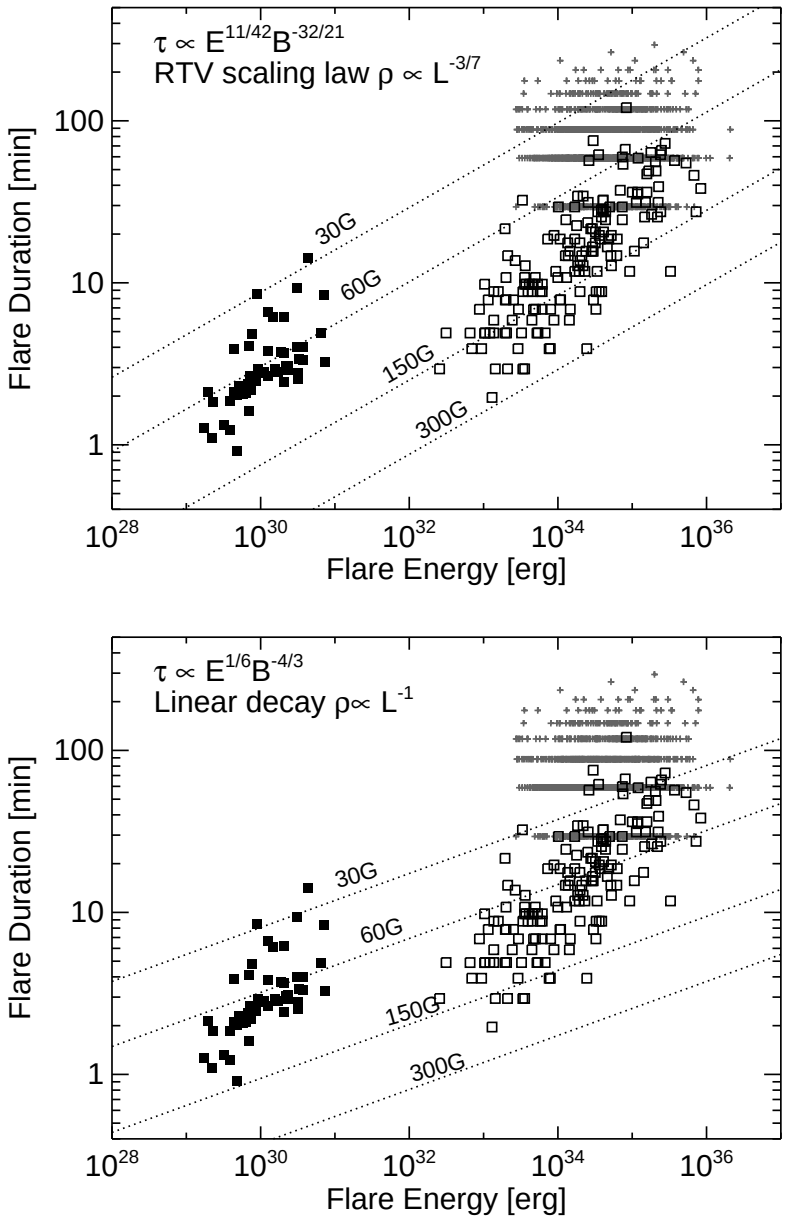


Figure 4.11: Physical understandings of relation between the flare energy and duration for solar and stellar flares (III) based on the revised theoretical scaling law. The figure shows the theoretical $E$–$\tau$ relations (Equation 4.9) considering the dependence of the pre-flare coronal density, as well as the observed data. Four theoretical lines are plotted for the different magnetic field strength $B$ = 30, 60, 150 and 300 G.

RTV scaling law ($T \propto (pL)^{1/3}$; $T$ is temperature, $p$ is gas pressure; Rosner et al., 1978) are well adopted to the static magnetic loop on the solar surface and can be deformed to $\rho \propto F^{4/7}L^{-3/7}$, where $F$ is coronal heating flux. In the case of gravity stratification, the coronal density linearly decreases as the height increases by a simple approximation (Takahashi et al., 2016). In both cases, a pre-flare coronal density can be expressed as $\rho \propto L^{-a}$ (a $> 0$). When the density dependence is considered, the scaling relation is written as:

$$\tau \propto E^{1/3-a/6}B^{-5/3+a/3}. \tag{4.9}$$

Although we ignored the $F$ dependence, it would be negligible due to the weak dependence of $F^{2/7}$. In Figure 4.11 , the theoretical scaling laws are plotted as well as the observed data. We found that the scaling law can explain the solar and stellar observation with roughly the same magnetic field strength (30–300 G). The power-law distributions of solar and stellar flares imply that the magnetic field strengths decrease as the magnetic loops expand, and the different distributions of solar and stellar flares can also be explained by the different magnetic field strength at a given height. In the case of comparison among different spectral types, the problem would become complex because the $F$ dependence cannot be negligible. The validity of the scaling law will be examined in Appendix B.1, and the comparison between the different spectral type will be discussed in Appendix B.2.

In this section, we derived the scaling laws on the basis of magnetic reconnection theory, and suggested that the observed $E$–$\tau$ distribution can be explained by the different magnetic field strength of solar and stellar flares, regardless of the WL cooling effect. These discussions in turn imply that the stellar properties can be estimated by using the scaling law from the most simply observable physical quantities (flare energy and duration). This would be helpful for researches on stellar properties in the further photometric observations (e.g. *TESS*, Ricker et al. 2015; see Chapter 6). It is, however, not clear that the scaling law can be applicable to the real observations due to the lack of the validation. As a future study, the measurements of magnetic field of superflare stars would be necessary to ascertain whether the observed $E$–$\tau$ diagram are caused by magnetic field strength or cooling effect.

## 4.5 Summary and conclusion

We conducted a statistical research on solar WLFs with the purpose of confirm the result proposed by Maehara et al. (2015). The relation of flare energy ($E$) and duration ($\tau$) is compared with those of superflares on solar-type stars in the white-light ranges. We found that superflares have one order of magnitude shorter durations than those extrapolated from the power-law relation of the obtained solar WLFs as in Figure 4.8. This discrepancy

between solar and stellar flares may have a potential to understand the detailed energy release mechanism of superflares or properties of the unsolved origin of WL emissions. We proposed the following two physical interpretations on the $E$–$\tau$ diagram to under the magnetic reconnection theory and white-light mechanism:

**(i)** Ratio of cooling timescales of white-light emission to reconnection timescales can be responsible for the discrepancy as follows: First, we assume that the reconnection timescale ($t_{\rm cool}$) can be shorter than the cooling timescale of the white-light emission source ($t_{\rm reconnection}$) in the case of small-scale solar flares, while it is reverse in the case of stellar flares. Under this assumption, the e-folding decay time of stellar WLFs can be shorter than expected from solar WLFs.

**(ii)** Coronal magnetic fields of the observed superflares are 2-4 times stronger than those of solar flares, under the scaling law ($\tau \propto E^{1/3}B^{-5/3}$) obtained from the magnetic reconnection theory. The scaling laws can predict the unresolved stellar parameters, the magnetic field strength $\sim$200 G and loop length $\sim 10^{10-11}$ cm.

Based on the above two possibilities, it can be concluded that the stellar superflares can be explained by the magnetic reconnection theory if we consider the different physical conditions or white-light flare mechanism.

In this study, we proposed new scaling relations that can estimate the physical parameters of spatially-unresolved stellar flares (Equation 4.7). These kinds of methods have been also proposed by Shibata & Yokoyama (2002) via X-ray observations, but the optical photometry is the easiest way to detect stellar flares, indicating versatility of our methods. This would be helpful for investigations on stellar properties in the future photometric observations (e.g. *TESS*; Ricker et al., 2015), and this method has been actually applied to recent observations (e.g. Brasseur et al., 2019; Maehara et al., 2020).

It should be noted that in the above conclusion, we need to unveil the white-light emission mechanism. The lack of our understanding of WLFs may keep us away from conclusion although it is based on the recent solar observations (Kawate et al., 2016), and it can be raised as a key topics in future works (see Section 7.2 'Future Perspective'). It is therefore necessary to reveal the emission mechanism or to detect the hard X-ray emission of superflares (cf. Chapter 5).

Here, we clarified some part of the energy release process of the *Kepler* superflares on solar-type stars There remains many problems in the energy transport, heating, dynamics, and radiation mechanism. In Chapter 5, some parts of these topics are dealt with based on the multi-wavelength observations of stellar superflares.

CHAPTER 5

# Optical and X-ray observations of stellar flares on an active M dwarf AD Leonis with Seimei Telescope, SCAT, NICER and OISTER

## 5.1 Introduction

Chapter 4 describes the "energy release" mechanism of stellar superflares. This chapter deals with the "energy transport" in stellar (super)flares, especially the heating and radiation mechanism in stellar flaring atmosphere. Considering the solar history that the energy transport in solar flares have been well-understood thanks to the multi-wavelength observations of solar flares, the further understandings of the whole picture of stellar superflares can be advanced by them. More samples of multi-wavelength observations are required to reveal the properties of stellar flares. As in the Section 1.2.2, magnetically active M dwarfs are one of the best targets for monitoring flares and increasing the samples of multi-bands observations. The small continuum levels of M-dwarfs enables the detection of even the small flares, and M-dwarfs have relatively deep convection zone generating large magnetic flux to produce superflares. In the planetary community, the extreme event on M-dwarfs has been getting more and more attention in terms of the exo-planet habitability around active young stars (Segura et al., 2010; Lingam & Loeb, 2017). By considering these situations, in this chapter, we will focus on the M-dwarf stellar superflares as a first approach using spectroscopic observations

As in the Section 1.1.2, the flaring atmosphere (mostly means the chromosphere in this chapter) are heated mainly by thermal conductions and the non-thermal electrons in the

case of solar flares. In the case of the stars, it is not easy to directly detect the emission from the non-thermal particles and heating flux (maybe possible with radio), some indirect approaches have been often done via chromospheric lines and X-ray emissions, although the number of observations is small. Stellar flares often produce greatly enhanced emission in chromospheric lines, such as the hydrogen Balmer series, Ca II H and K. These lines have been widely used as flare diagnostics because they represent various kind of flaring activities (e.g. chromospheric dynamics or mass ejections; cf. Sections 1.1.2 and 1.2.2) and are observable from the ground. The hydrogen lines tend to have a relatively fast rise phase, but the peak is often delayed compared to the continuum emission (Kahler et al., 1982; Hawley & Pettersen, 1991). The radiated energy in hydrogen lines is relatively small compared to the continuum (Hawley & Pettersen, 1991). The Balmer line broadening up to 20 Å has been observed during stellar flares (Hawley & Pettersen, 1991), which is interpreted as the non-thermal broadening or Stark (pressure) broadening. Recent numerical simulation shows that the broadenings of the higher-order Balmer lines (e.g. H$\gamma$) are good tools to estimate the chromospheric density, which can be a clue to the injected accelerated particles (Allred et al., 2006; Paulson et al., 2006; Kowalski et al., 2017). They sometimes report that the very impulsive (super)flares require the heating of chromosphere via high-energy electron beam fluxes of $10^{12-13}$ erg s$^{-1}$ cm$^{-2}$ (e.g. Kowalski et al., 2016). These values are much larger than those of typical solar flares ($10^{10-11}$ erg s$^{-1}$ cm$^{-2}$).

However, in almost all previous studies, the temporal evolution of the Balmer line widths has not been well investigated although the flaring atmosphere dramatically changes during flares. In addition, the heating fluxes have been estimated indirectly by observing optical lines, but the number of such kind of study is still small and statistical properties are not known. Moreover, the energy budget for each wavelength is not confirmed for stellar flares, although it is known that there is diversity even in solar flares. The keywords that will be addressed here are (1) temporal evolution, (2) more diagnostics of heating fluxes, and (2) energy budget.

Our main purpose of this chapter is to investigate the change in flaring atmosphere during stellar flares and its heating mechanism via multi-wavelength observations. In this study, we conducted the optical and X-ray monitoring observation of an M-dwarf flare star AD Leo during 8.5 nights by Seimei-OISTER campaign to reveal the features of stellar flares. In this campaign, we mainly used a low-resolution spectrograph on the 3.8-m Seimei Telescope (Kurita et al., 2020). We also conducted optical spectroscopy and photometric observations with the help of the OISTER (Optical and Infrared Synergetic Telescopes for Education and Research[‡]) program and with the SCAT at the Chuo University. We obtained the X-ray monitoring data from NICER (Neutron Star Interior Composition Explorer) during this observational period. In Section 5.2, we review observations and

[‡]http://oister.kwasan.kyoto-u.ac.jp/

Table 5.1: Observing Log.

| Telescope/Instrument (Data type) | UT Date (JD) | Time (hr) | Exp Time (s) | Flares # |
|---|---|---|---|---|
| Spectroscopy | | | | |
| 3.8m Seimei/KOOLS-IFU | 2019 Mar 22 (2458565) | 2.6 | 60 | #1 |
| (5000-8000 Å; R∼2000) | 2019 Mar 23 (2458566) | 4.6, 1 | 30 | - |
| | 2019 Mar 24 (2458567) | 4.1 | 60 | #2, 3 |
| | 2019 Mar 25 (2458568) | 2.5 | 30, 60 | - |
| | 2019 Mar 26 (2458569) | 7.3 | 30 | #4, 5 |
| | 2019 Mar 27 (2458570) | 5.1 | 30 | #6 |
| | 2019 Apr 12 (2458586) | 5.9 | 30 | #7, 8, 9, 10 |
| 2m Nayuta/MALLS (OISTER) | 2019 Mar 24 (2458567) | 5 | 120 | #2, 3 |
| (6350-6800 Å; R∼10000) | 2019 Mar 26 (2458569) | 5 | 120 | #4, 5 |
| 36cm SCAT | 2019 Mar 23 (2458566) | 2.5 | 600 | |
| (3520-8040 Å; R∼600; | 2019 Mar 24 (2458567) | 4.5 | 600 | #2, 3 |
| covering H$\alpha$, H$\beta$, H$\gamma$, and H$\delta$) | 2019 Mar 26 (2458569) | 5.5 | 600 | #4, 5 |
| | 2019 Mar 27 (2458570) | 2.5 | 600 | |
| Photometry | | | | |
| 50cm MITSuME (OISTER) | 2019 Mar 22 (2458565) | 6.9 | 5 | #1 |
| (g'/Rc/Ic-band photometry)$^{\dagger}$ | 2019 Mar 23 (2458565) | 6.0 | 5 | |
| | 2019 Mar 24 (2458567) | 6.8 | 5 | -* |
| | 2019 Mar 25 (2458568) | 4.8 | 5 | |
| | 2019 Mar 26 (2458569) | 7.0 | 5 | -* |
| | 2019 Mar 28 (2458571) | 7.0 | 5 | |
| | 2019 Apr 11 (2458585) | 4.5 | 5 | |
| | 2019 Apr 12 (2458586) | 4.5 | 5 | -* |
| | 2019 Apr 13 (2458587) | 4.6 | 5 | |
| 40cm KU Telescope (OISTER) | 2019 Apr 12 (2458586) | 5 | 10 | #7, 9, 10 |
| (B-band photometry)$^{\dagger}$ | | | | |
| X-ray | | | | |
| ISS/NICER | 2019 Mar 22-28 (2458565-71) | $\sim$0.5 × 26 | - | #4 |
| (0.2-12 keV X-ray) | 2019 Apr 11-13 (2458585-87) | $\sim$0.5 × 10 | - | #8, 11, 12 |

analyses. In Section 5.3, we introduce features of the observed stellar flares. In Section 5.4, we show the rotational modulations of the AD Leo. In Section 5.5, we perform one-dimensional hydrodynamic simulations of stellar flares to understand the flare properties. Finally, we discuss the observations and numerical simulations in Section 5.6.

## 5.2 Observations and data reductions

### 5.2.1 Target star

In 2019, we carried out large campaign monitoring observations on the nearby M dwarf AD Leo (GJ 388). AD Leo is classified to a dMe 3.5 star (Shkolnik et al., 2009), whose distance from the Earth is about 4.9 pc. Frequent stellar flares have been observed on AD Leo with the several wavelength ranges (Hawley et al., 1995, 2003; Kowalski et al., 2013), and an extremely large superflare was also observed (Hawley & Pettersen, 1991). The flare occurrence frequency is reported to have a power-law distributions, causing 0.76 flares per day (Pettersen et al., 1984).

### 5.2.2 Spectral data

We mainly used the Seimei Telescope located at Okayama Observatory, Japan, for spectroscopic data. The Seimei Telescope is 3.8 m optical and infrared telescope (Kurita et al. (2020)). We used the KOOLS-IFU instrument (Matsubayashi et al., 2019), which is a low-resolution spectrograph (KOOLS) with an optical-fiber integral field unit (IFU), on the Nasmyth focus. The grism we used covers 6150 to 7930 Å, and the spectral resolution (R) is $\sim$ 2,000. We conducted the 8.5 nights of spectroscopic monitoring observation of AD Leo with Seimei Telescope/KOOLS-IFU during March to April 2019 (Table 1). The time resolutions are 42 or 72 seconds including the 12-sec read-out time to achieve the signal to noise $\sim$ 100. The spectroscopic data of the KOOLS-IFU are two-dimensional spectroscopic data, and we use only the fiber array where stellar integrated brightness is more than 50 % than that of the maximum fiber. Data reduction was done using the package of the IRAF[§] and PyRAF[2] software and the data reduction packages developed by Matsubayashi et al. (2019). [¶]

During this observational period of Seimei Telescope, we also conducted monitoring observations of the Balmer lines of AD Leo with optical telescope SCAT (Spectroscopic Chuo-university Astronomical Telescope). SCAT is mounted on a building in Korakuen campus of Chuo University in Japan. It consists of an MEADE 36 cm diameter telescope and an ATIK 460EX CCD camera with an Shelyak Alpy 600 spectrometer. The spectrometer covers 3700 to 7500 Å, and the spectral resolution, R, is 600. About 600-sec exposure was required to get the signal to noise of $>$ 100. We executed the data reduction using the twodspec package of the IRAF software in the standard manner (dark subtraction, flat fielding, spectral extraction, sky subtraction, and wavelength calibration).

In the OISTER program, the spectroscopic observations were carried out with the Nayuta 2 m telescope at the Nishi-Harima Astronomical Observatory for two days (Table 1). The MALLS (Medium And Low-dispersion Long-slit Spectrograph) was used with a resolving power (R) of $\sim$10000 at 6500 Å, covering 6350 - 6800 Å. We aimed to use this instrument to detect line asymmetries of the Balmer lines (e.g. Honda et al. (2018)), but the changes in the H$\alpha$ profiles were too small, and the significant line asymmetries were not detected.

### 5.2.3 Photometric data

In the OISTER program, time-resolved photometry was performed during this period by using MITSuME 50 cm telescope at Okayama Observatory and the 40-cm telescope at

[§]IRAF and PyRAF are distributed by the National Optical Astronomy Observatories, which are operated by the Association of Universities for Research in Astronomy, Inc., under cooperate agreement with the National Science Foundation.

[¶]http://www.kusastro.kyoto-u.ac.jp/ kazuya/p-kools/reduction-201806/index.html

Kyoto University. MITSuME 50cm-telescope can acquire $g'$, $R_{\rm C}$, and $I_{\rm C}$-band images simultaneously by using two dichroic mirrors and three CCD cameras (Kotani et al., 2005). We described the observational log of MITSuME in Table 1. Note that although the location is the same as that of Seimei Telescope, the photometry has better sensitivity than the spectroscopy of Seimei. The CCDs of MITSuME have deteriorated recently, and the photometric sensitivity has become worse if we divide the images by flat flames. Therefore, most flares except for one large superflare could not be detected by MITSuME photometry even in $g'$-band where flare amplitude is expected to be the largest among the three bands of MITSuME. Also, B-band photometric observations on AD Leo was conducted by the 40-cm telescope at Kyoto University only on April 12th, and the data are shown in Appendix C.1.

### 5.2.4 X-ray data

NASA's Neutron Star Interior Composition Explorer (NICER; Gendreau et al. (2016)) has conducted the monitoring observations on AD Leo during this period. NICER is the soft X-ray instrument onboard the International Space Station, and observed AD Leo for about 1 ksec for each orbital period of ISS (about 90 minutes). The observation has been carried out for several times during each night. NICER is not an imaging instrument, so background spectra must be subtracted to get the stellar spectra. The data were processed using NICER software version 2019-10-30, which can estimate the background spectra at a given NICER observational orbit.[‖]

In making the light curves, we used 0.5-8 keV band corresponding channels 50 through 800. Below channel $\sim$ 50 and above $\sim$ 800, there is optical contamination due to the ambient light. For two flares clearly detected by NICER (Flare #4 and #12), we also analyzed X-ray spectra in flare phases. The integrated times are indicated by the error bars of the derived emission measure (EM) and temperature as in Figure 5.7. We fitted the pre-flare subtracted X-ray spectra (0.5-8.0 keV) with a simple thin-thermal model of single-temperature plasma where the abundance ratios of heavy elements are fixed to the solar values (e.g. Tsuboi et al. (2016)). We derived the emission measures, temperatures, and radiation flux by using the $apec$ models in *XSPEC* installed in HEASoft [**], and the parameters are summarized in Table 5.2.

### 5.2.5 Emission line/continuum fluxes

Emission fluxes were calculated for the hydrogen Balmer lines (H$\alpha$, H$\beta$, H$\gamma$, H$\delta$), and the He I line 6678.15Å, and the $g'$, $R_{\rm C}$, and $I_{\rm C}$-band continuum. For the emission lines, the

[‖] https://heasarc.gsfc.nasa.gov/docs/nicer/tools/nicer_bkg_est_tools.html
[**] https://heasarc.gsfc.nasa.gov/xanadu/xspec/

Table 5.2: X-ray spectral best-fit parameters for flare #4.

| Parameters | time 1 | time 2 | time 3 |
|---|---|---|---|
| $N_{\rm H}$ [$10^{20}$ cm$^{-2}$] | 3.48 | 8.50 | 5.23 |
| $kT$ [keV] | 2.62 | 1.31 | 1.27 |
| norm | $8.14 \times 10^{-2}$ | $5.07 \times 10^{-2}$ | $3.10 \times 10^{-2}$ |

flux ($F_{\rm line}$) is calculated from equivalent width (EW) and the local continuum enhancement levels ($F_{\rm flare}/F_{\rm pre\text{-}flare}$), and the local continuum enhance level is calculated based on $g'$-band and $R_{\rm C}$-band (c.f. the Appendix of Hawley & Pettersen (1991)). First, the synthetic $g'$-band flux, $R_{\rm C}$-band flux, and local continuum flux ($F_{\rm local\text{-}cont.}$) at each emission line in quiescence is calculated based on the flux-calibrated AD Leo spectra taken by SCAT. Second, the local-continuum enhancement levels at each line (i.e. $F_{\rm flare}/F_{\rm pre\text{-}flare}$) is calculated based on the $g'$- and $R_{\rm C}$-band enhancements level obtained from photometry. Finally, the line emission flux is calculated from the equivalent width and local-continuum enhancements level (i.e. $F_{\rm line}$ = EW $\times$ $F_{\rm flare}/F_{\rm pre\text{-}flare}$ $\times$ $F_{\rm local\text{-}cont.}$). H$\alpha$ and He I line 6678.15Å refer to the $R_{\rm C}$-band flux, and the others do to the $g'$-band flux. The fluxes of line emissions can have errors because of the contamination of line emissions on the broad-band continuum fluxes. However, for example, as for the flare #1, the effect would be less effective because the enhancement of equivalent width was 10 Å at most while the continuum bands have $>$ 100 % enhancement in $\sim$ 1000 Å bandwidth.

## 5.3 Flare atlas: light curves and spectra

### 5.3.1 Observational summary

We carried out the monitoring observations on AD Leo for 8.5 days, and the clear-sky ratio was about 50 %. Figure 5.1 indicates the overall light curve during this campaign. 12 flares were detected by eye mainly with the H$\alpha$ monitoring with Seimei/KOOLS-IFU (see Table 1) although there could be a larger amount of small flares which could not be identified by eye. The Balmer lines show emission even in quiescence, indicating very high atmospheric heating. The H$\alpha$ equivalent width in quiescence is about -3.5 Å, and the enhancement during flares are typically 1-1.5 Å. Only one flare (flare #1) shows very high enhancement of H$\alpha$ $\sim$ 10 Å. The number of flares detected by Balmer lines is 10. Even though the simultaneous photometry is limited, four of them are clearly detected by optical photometry, while five of them did not clearly show the white-light emissions (one of them has no photometry). Four of them are also detected by higher resolution

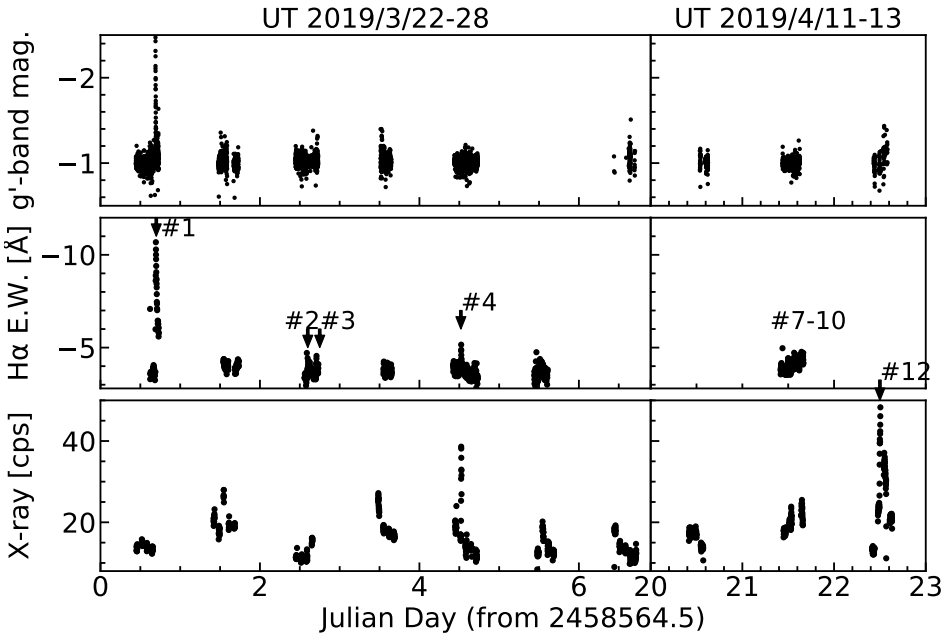


Figure 5.1: Overall light curves of AD Leo during this campaign observation. Top: the light curve in $g'$-band magnitude. Middle: the H$\alpha$ E.W.. Bottom: X-ray count rates [cps; count per sec] in 0.5-8 keV.

spectroscopy by Nayuta/MALLS, but are too weak to identify clear line asymmetry like Honda et al. (2018). Two of them are detected by NICER X-ray detector. The count rates of 0.5-8.0 keV in quiescence is about 18 counts per second. Besides, two additional flares are detected by NICER X-ray although there are no clear H$\alpha$ observations (flare #11, #12). In the following sections, we show the typical and prominent stellar flares detected (flare #1, #2, #3, and #4), and the other all flares are shown in the Appendix.

### 5.3.2 Flare #1: A superflare showing large line broadening

Figure 5.2 shows the light curve of the flare #1 observed by Seimei spectroscopy and MITSuME photometry. Unfortunately, there were no X-ray observations during this flare. The panel (A) shows that the equivalent width of H$\alpha$ becomes -12 from -3.5 Å. The $g'$-band continuum becomes four times brighter than the quiescence, and the contrast is largest among the three filters. This can indicate very blue spectra of white-light continuum emissions, but M dwarfs are also very red so a flat spectrum leads to larger flux enhancements as well. The panel (B) shows the temporal evolution of the radiated flux for each wavelength. The energies radiated in the continuum bands are much larger than the line emissions. The total radiated energies (and ratios relative to the g-band energy) in $g'$-band, $R_{\rm C}$-band, $I_{\rm C}$-band continuum, H$\alpha$, and He lines are calculated to be $1.4\times10^{33}$ erg, $4.7\times10^{32}$ erg (0.34), $7.0\times10^{31}$ erg (0.05), $2.5\times10^{31}$ erg (0.018), and $1.3\times10^{30}$ erg (0.0093), respectively, and

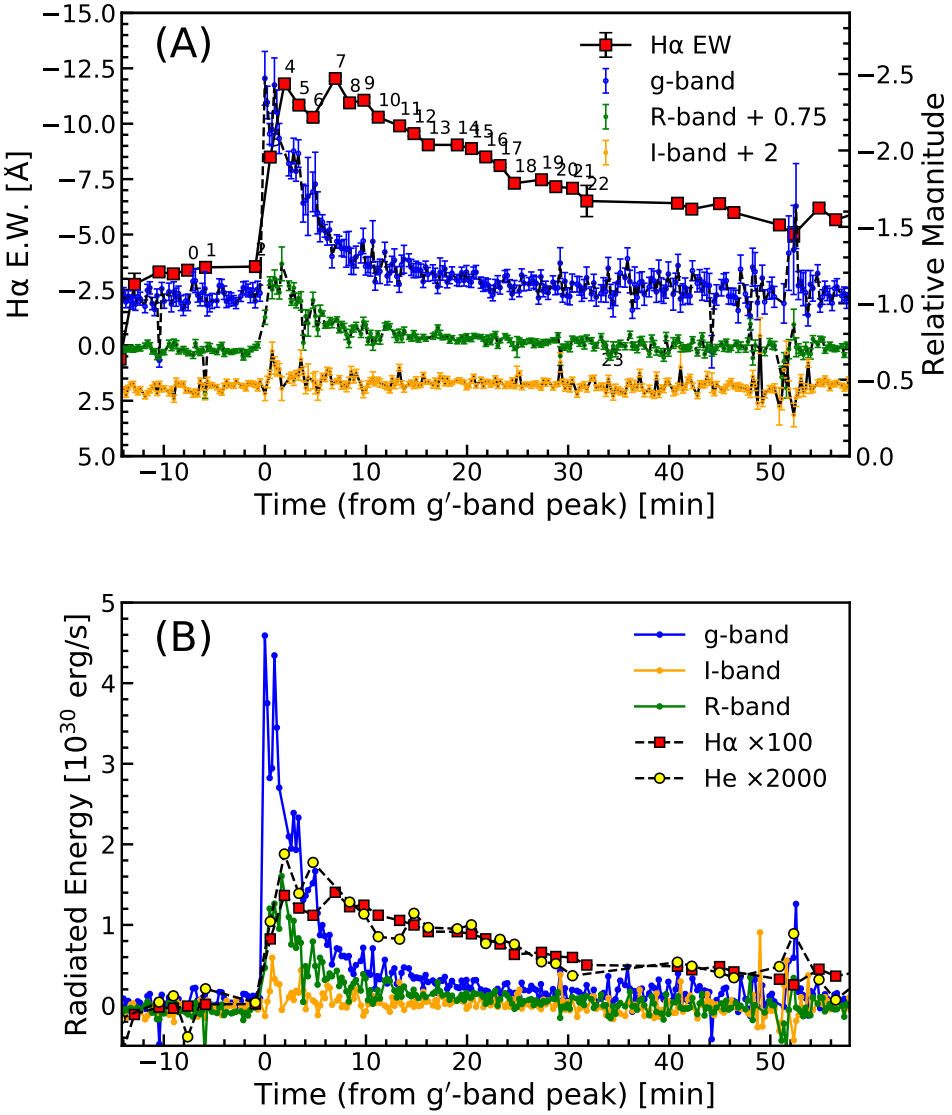


Figure 5.2: (A) Light curve of the flare #1 observed by Seimei Telescope/KOOLS-IFU (H$\alpha$) and MITSuME ($g^{'}$, $R_{\rm c}$, $I_{\rm c}$). The equivalent width is corrected by the continuum enhancements (B) Light curve of flare #1 in the unit of erg·s$^{-1}$.

the flare is classified to be a superflare (a flare with the total energy of more than $10^{33}$ erg $\sim$ ten times larger energy than the largest scale of solar flares; Maehara et al. (2012)). Here, to calculate the flare energies, the flare fluxes in continuum and line emission in Figure 5.2 (B) were time-integrated between -2.6 min and 36 min and between -2.6 min and 58 min, respectively. Because the observations finished before the H$\alpha$ and He line flare emissions completely decayed, the energies of line emissions would be underestimated to some extent. The duration of the H$\alpha$ flare is more than one hour, while those of white-light flares are about 15 minutes. The continuum fluxes have shorter durations than the chromospheric line emission, which can be an indication of the Neupert effect in the case of solar flares (Neupert, 1968). The color temperature of the white-light emission during the flare is calculated to be typically 14,000 $^{+17,000}_{-8,000}$ K if we assume the black-body radiation for $g'$-band and $R$-band fluxes. Note that the continuum flux ratio was very noisy during the flare, so the error bar of the emission temperature is very large. The temporal evolution of the white-light emission temperature is therefore not significantly found. However, it is reported that broad-band continua, especially $g'$-band, could be affected by emission lines (e.g. Kowalski et al. (2019)), so we need to be careful about the interpretations of the emission temperatures derived here.

Figure 5.3 shows the temporal evolution of the low-resolution H$\alpha$ spectra during this flares. The panel (A) is the spectra normalized by the continuum level, and the panel (B) is the pre-flare subtracted spectra. First, we could not find any line asymmetry during this flare, although the blue and red asymmetries are frequently observed during not only stellar flares but also solar flares (e.g. Ichimoto & Kurokawa (1984); Tei et al. (2018) ;Honda et al. (2018); Muheki et al. (2020b)). Second, we found significant line-wing broadenings of H$\alpha$ line during the flare, as you can see in Figure 5.3 (B). The line broadening is prominent especially in the initial phase of the flare, but it is not prominent in the later decay phase. Figure 5.4 shows the temporal evolution of the line width and line peak intensity. As you can see, both line width and intensity largely increase in the initial phase of the flare when the white-light emissions are seen. In the decay phase, the line width dramatically decreases while the line peak intensity does not largely change.

### 5.3.3 Flare #2 (and #3): a flare showing clear Balmer-line decay

Figure 5.5 shows the light curve of flare #2 and #3, observed by Seimei/KOOLS-IFU and SCAT. There were photometric observations by MITSuME during this flare, but no significant white-light enhancement can be seen. The equivalent width change of the higher level Balmer line (e.g. H$\delta$ and H$\gamma$) is larger than the lower level (e.g. H$\alpha$), which would be because there is a lower continuum in the blue. However, the decay timescale for each line is quite similar to each other. The decay timescale for each Balmer lines is not easy to in-

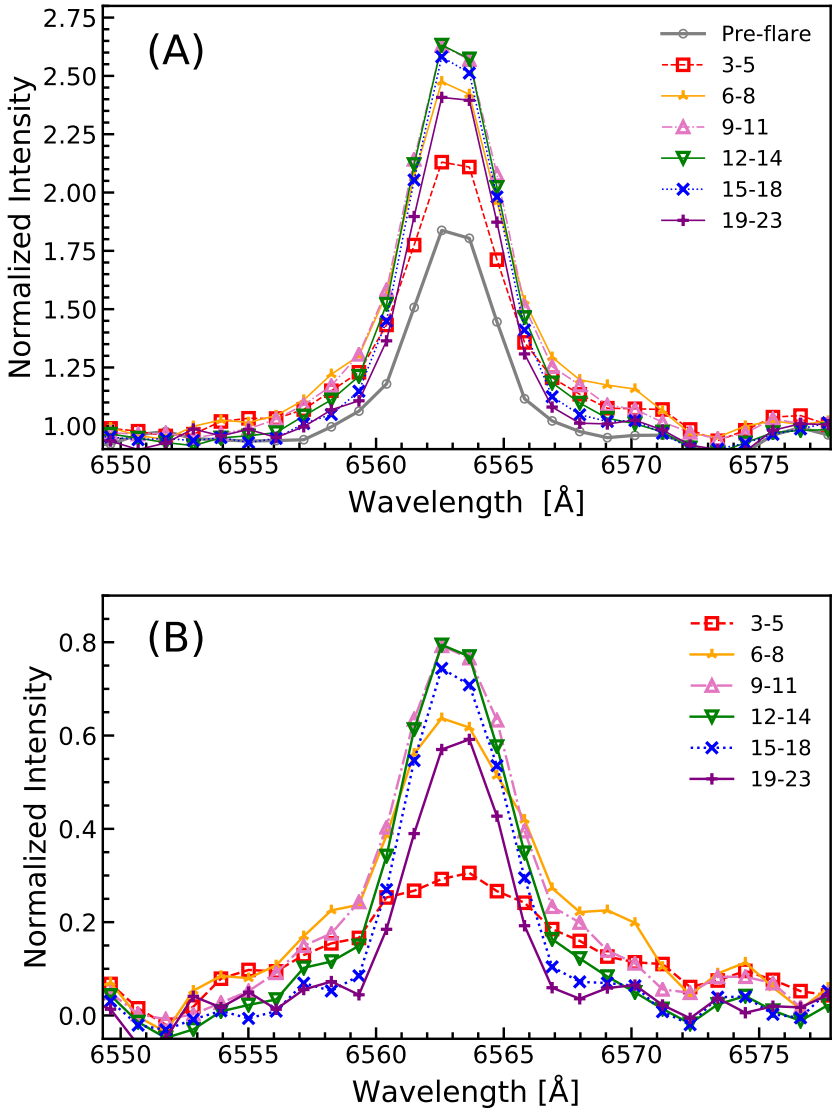


Figure 5.3: (A) H$\alpha$ spectra during the flare #1. The numbers described in the legend is the same ones shown in the Figure 5.2. We combined three to five spectra to make the spectra in the panel (A). (B) Pre-flare subtracted spectra of the flare #1.

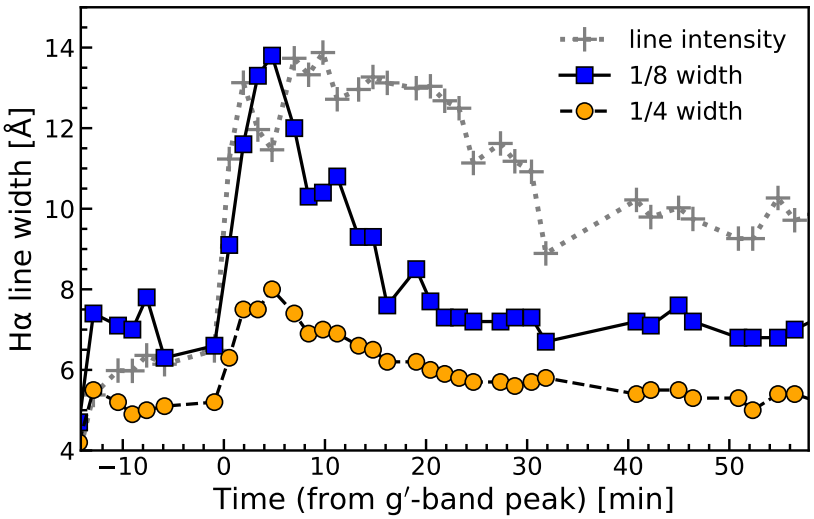


Figure 5.4: Temporal evolution of the H$\alpha$ line width and line intensity of the flare #1. Open squares and open circles indicates the line width where the line intensity is 1/8 and 1/4 of the peak intensity, respectively. Gray crosses are the scaled line peak intensity.

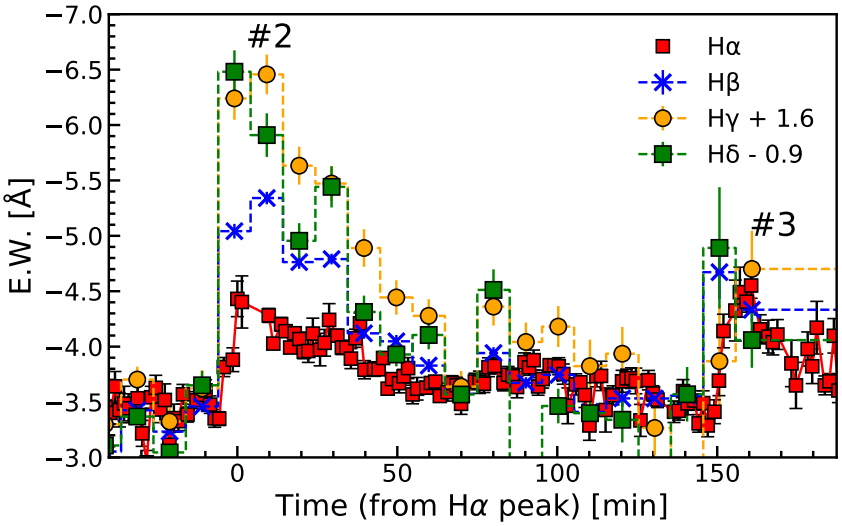


Figure 5.5: Equivalent width (E.W.) of Balmer lines during the flare #2 and #3 observed by Seimei Telescope and SCAT. The relative values are corrected and the pre-flare levels are set to be the same value.

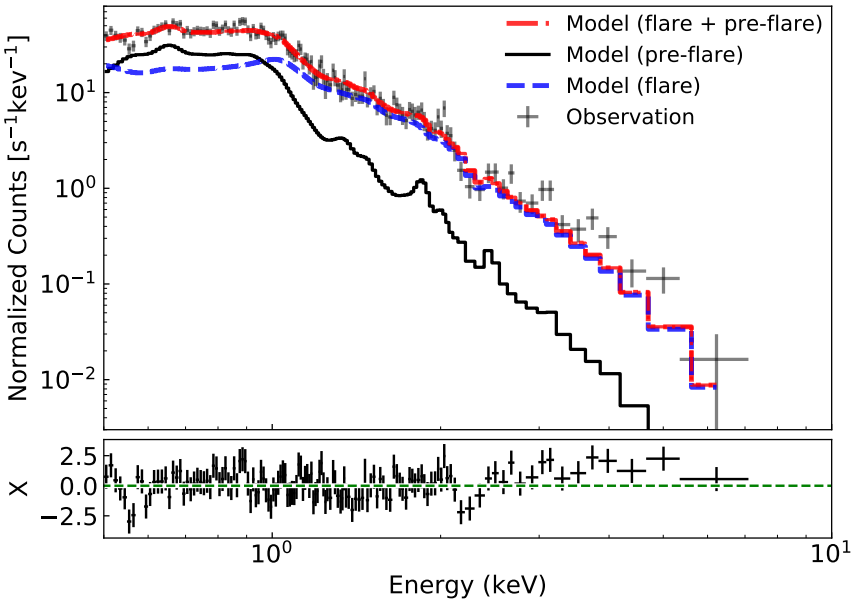


Figure 5.6: X-ray spectra (0.5 - 10 keV) at peak of flare #4. The gray crosses indicate the X-ray spectrum observed by NICER. The red dash-dotted line indicates the model spectra obtained by fitting the observation with a simple thin-thermal model (*apec* model in *XSPEC*). The black solid line is the pre-flare spectra, and the blue dashed line indicate the flare-only spectra (i.e. the red line minus the black line). As a result of the model fitting, the reduced chi-squared is 1.23. The bottom panel indicates values of X = (data - model)/error (normalized by one sigma) for each bin.

terpret because temperature, density, and the difference in opacity for each line contribute to it.

### 5.3.4 Flare #4: a small flare observed by the all Instruments

Figure 5.7 shows the light curve of flare #4, and there are observations by all instruments (Seimei/KOOLS-IFU, SCAT, Nayuta/MALLS, MITSuME, and NICER) during flares. Enhancement of Balmer lines and X-ray are clearly detected, but the continuum emissions are too weak to detect with the MITSuME photometric sensitivity.[††] The enhancement of the equivalent width is the same for all Balmer lines, which is different from the flare #2 although the enhancement level is similar to each other. The total radiated energy in H$\alpha$, H$\beta$, H$\gamma$, and H$\delta$ are calculated to be $1.1\times10^{30}$ erg, $1.6\times10^{30}$ erg, $5.0\times10^{29}$ erg, and $9.6\times10^{29}$ erg, respectively.

[††] As we described, the MITSuME CCDs have the inevitable noise pattern, and the flat flaming can make the photometric sensitivity worse.

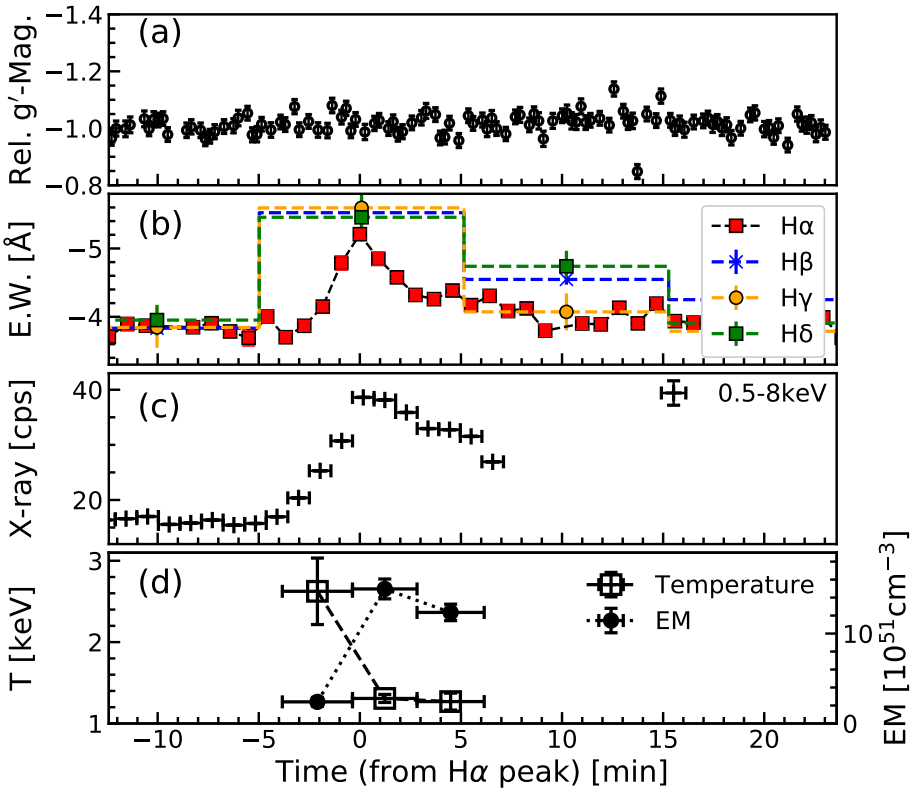


Figure 5.7: Light curves of the flare #4 observed in $g$-band (MITSuME, panel a), Balmer lines (Seimei Telescope and SCAT, panel b), and X-ray (NICER, panel c). The panel (d) shows time variations of the emission measure and temperature during the flare. The values are derived from the pre-flare subtracted X-ray spectra (0.5-8.0 keV).

For the X-ray data, the rise, peak, and initial decay phase were successfully observed. The count rates become about twice the quiescent values. The results of the model fitting of the flare spectra are also plotted in the panel (d) of Figure 5.6. The emission measure and temperature at the flare peak are derived as $1.15\times10^{52}$ cm$^{-3}$ and 1.57 keV (18.2 MK), respectively. After the temperature increases initially, the emission measure increases later, which is similar to the typical X-ray behavior accompanied with chromospheric evaporations in solar flares (e.g. Shibata & Yokoyama (2002)). The observed X-ray flare energy in 0.5 -10 keV is calculated to be $3.4\times10^{31}$ erg, which is larger by about one order of magnitude than the Balmer line energy. Note that even in the initial phase, no significant hard X-ray power-law component is detected and the spectra can be fitted only with the single component thermal spectra.

## 5.4 Rotational modulation

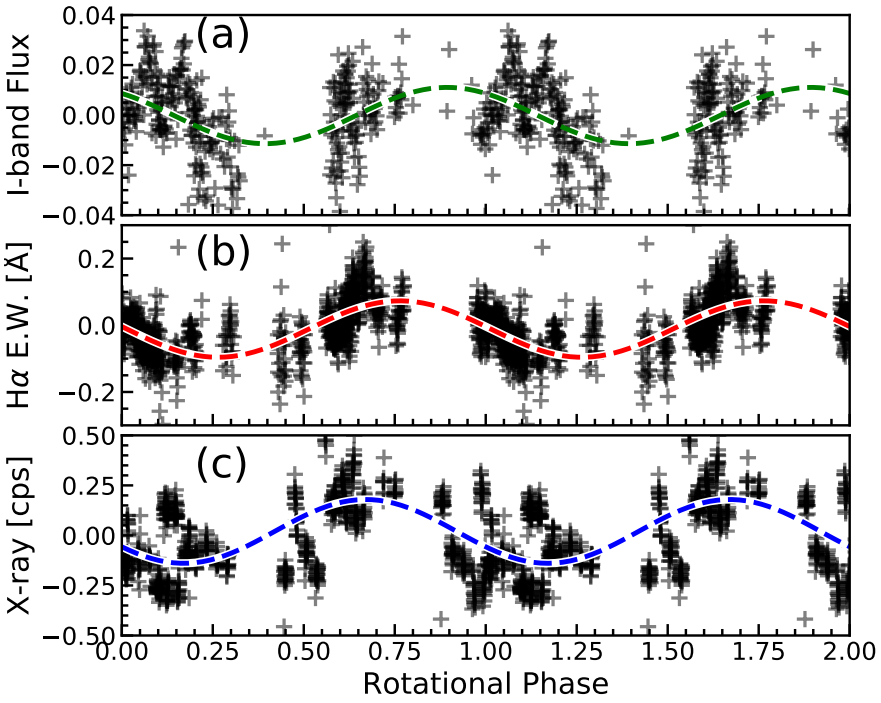


Figure 5.8: Light curves relative to the mean value of (a) I-band continuum, (b) H$\alpha$, and (c) soft X-ray folded by rotational period $\sim$ 2.24 days. Note that flares were removed from the panel. Two rotational phases are plotted. The dotted line in each panel indicates the best-fit sinusoidal curve.

Figure 5.8 (a-c) show the light curves which are folded with the rotational period of 2.2399 days reported in the previous work of Hunt-Walker et al. (2012). We removed the visibly-checked flares to make Figure 5.8. The H$\alpha$ and X-ray phase-folded light curves show the clear periodic feature, which would be the signature of the rotational modulations of the AD Leo with the bright active region in chromosphere and corona. On the other hand, the photometric light curves do not show clear periodicity probably due to the lack of photometric sensitivity. The phase-folded light curves are fitted with a simple sinusoidal curve indicated with the dotted lines. The phase difference between X-ray and H$\alpha$ is only 0.094, and that between X-ray and I-band continuum is 0.22. Although the I-band periodicity is not clear, the phase of X-ray and H$\alpha$ periodicity seems to be highly correlated.

Figure 5.9 shows the comparison between X-ray and H$\alpha$ intensity where both of the data exist at the same time. The X-ray and H$\alpha$ intensity have a positive correlation, while there

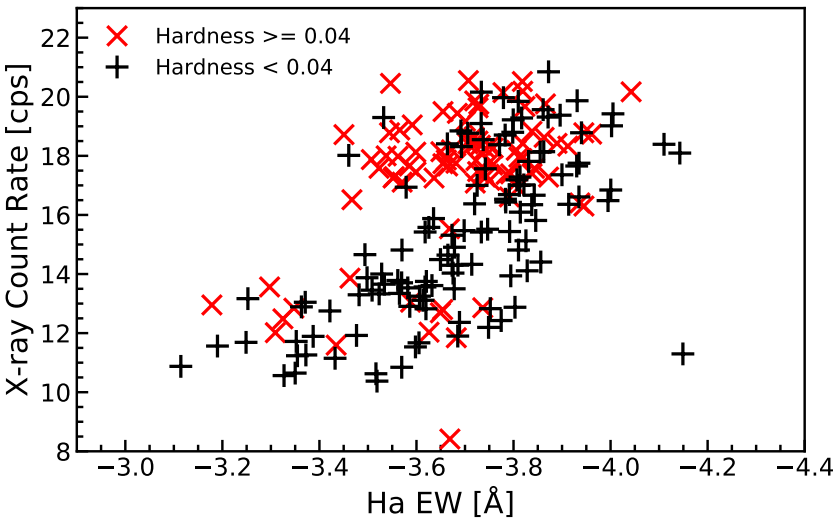


Figure 5.9: Comparison between H$\alpha$ E.W. and X-ray count rates (0.5-8keV) during non-flaring phase. The red pluses and black crosses show the values where the hardness ratio values (i.e. F(2-8 keV)/F(0.5-2 keV)) are $<$ and $>$ 0.04.

looks to be no correlation between them for the high hardness ratio. The amplitude of the X-ray modulations (16 %) is twice larger than that of the H$\alpha$ modulation (8 %), which may be caused by the filling factor or contrast of the active regions.

## 5.5 Radiative-hydrodynamic flare modeling

In Section 5.3, we found that, (1) accompanied by the large white-light enhancement, the H$\alpha$ emission line width dramatically increases to 14 Å from 8 Å, and that (2) some weak H$\alpha$ flares are not accompanied with white-light emission. These observational features motivate us to carry out numerical modelings of stellar flares to know what happens in the atmosphere. In this following section, we report the result of one-dimensional radiative-hydrodynamic (RHD) flare modelings with the RADYN code (Carlsson & Stein (1992, 1995, 1997, 2002)), which calculates hydrogen, helium, and Ca II in non-LTE framework and with non-equilibrium ionization/excitation. We refer the reader to Allred et al. (2015), Kowalski et al. (2015), and Kowalski et al. (2017) for extensive descriptions of the flare simulations.

### 5.5.1 RADYN flare model setup

The pre-flare atmosphere ($\log g$ = 4.75) for an M dwarf in our modeling is described in Appendix A of Kowalski et al. (2017). The pre-flare coronal electron density becomes up to $10^{11}$ cm$^{-3}$. Although this value is larger by one or two orders of magnitude than that of solar atmosphere, it is approximately consistent with the stellar X-ray observations (e.g. Osten et al. (2006)).

Several improvements have been made to the RADYN flare code since Allred et al. (2015), which are worth noting here (they will be described further in Allred (2020), in prep). The hydrogen broadening from Kowalski et al. (2017) and Tremblay & Bergeron (2009) have been included in the dynamic simulations; since we are comparing to H$\alpha$ observations, this update to the hydrogen broadening is a critical improvement (Kowalski (2020), in prep). The pre-flare atmosphere was relaxed with this new hydrogen broadening, and we choose to use the X-ray backheating formulation from Allred et al. (2005) for these models (Kowalski (2020), in prep); the resulting pre-flare apex temperature is $\sim$ 3 MK, with electron density $\sim 10^{11}$ cm$^{-3}$. Finally, we used a new version of the F-P solver (Allred (2020), in prep), which gives a moderately smoother electron beam energy deposition profile over height in the upper chromosphere. These changes have been implemented for the solar flare models presented in Graham et al. (2020).

Recently, this kind of RHD simulations has been widely carried out for the modeling of solar flares and dMe flares. However, the H$\alpha$ behaviors have been not so much well-investigated partly because it is difficult to understand due to its NLTE formation properties and large opacity variations over the line profile. In this study, we revisit the basic properties of the H$\alpha$ lines for dMe flares, and our aim of the numerical simulation is (1) to understand the H$\alpha$ line width behaviors as a function of the injected energy, and (2) to understand the basic relation between H$\alpha$ and optical continuum.

### 5.5.2 Flare heating inputs

In this section, we introduce the flare heating parameters used in our simulations. We aim to know the H$\alpha$/continuum intensity and H$\alpha$ line width as a response to the flare heatings. In this study, we performed two kinds of simulations in which lower atmospheres are heated by (i) the non-thermal high energy electrons (e.g. Kowalski et al. (2017)) and (ii) thermal conduction from the heated loop-top (e.g. Hori et al. (1997); Fisher (1989); Kowalski et al. (2017)). We performed the non-thermal and thermal simulation separately to see their difference in the behavior of the emission atmosphere. Note that we consider only one-dimensional tube in this study, but non-thermal line broadening among multi-

loops (e.g. Fuhrmeister et al. (2011)) may have to be also considered in future (e.g. Warren (2006); Kowalski et al. (2017)).

In the case of non-thermal heating, the energy flux density of non-thermal electrons with a power-law profile ($F(E) \propto E^{-\delta}$) is injected from the loop top. The important parameters are total energy flux density ($F_{\rm NT}$), the lower energy cutoff ($E_{\rm C}$), and the power-law index ($\delta$). Again, we aim to know the H$\alpha$ /continuum intensity and line width by controlling these parameters. For simplicity, the $E_{\rm C}$ is chosen to be 37 keV (Allred et al., 2015). $F_{\rm NT}$ is chosen to be $10^{10}$ cm$^{-2}$ s$^{-1}$ (F10), $10^{11}$ cm$^{-2}$ s$^{-1}$ (F11), $10^{12}$ erg cm$^{-2}$ s$^{-1}$ (F12) (hereafter, we express the flare model with $F_{\rm NT}$ of $10^{10}$ erg cm$^{-2}$ s$^{-1}$ as F10), following the values simulated in previous works of large solar flares (Holman et al. (2003); Allred et al. (2005, 2006); Kowalski et al. (2015)), and the power-law index $\delta$ is determined to be 3 and 5. The heating profile is assumed to be a triangle time variation with the peak time of 2 s where energy flux linearly increases and decreases in the rising and decay phase respectively.

In the cause of thermal-conduction heating, the heating source term is input to the energy equation at the magnetic loop top (e.g. Hori et al. (1997)). The energy flux of the thermal source is $5\times10^{10}$ cm$^{-2}$ s$^{-1}$ (5F10), $10^{11}$ cm$^{-2}$ s$^{-1}$ (F11), $5\times10^{11}$ cm$^{-2}$ s$^{-1}$(5F11), $10^{12}$ erg cm$^{-2}$ s$^{-1}$ (F12) per each magnetic loop. The heating profile is also a triangle time variation with the peak time of 4 s which is twice the non-thermal case.

### 5.5.3 Simulation result I: Hα line broadening for non-thermal/thermal heating

In this section, we show the H$\alpha$ line broadening for the non-thermal/thermal heatings as a response to the different kine of simulation input parameters. First, we show where the H$\alpha$ line and continuum emissions come from in the one-dimensional flare atmosphere in Figure 5.10. Four typical results of the simulated flare atmospheres are shown in Figure 5.10. The upper panels show the detailed atmospheric structure, the middle panels show the contribution function of H$\alpha$ and continuum, and bottom panels show the line formation region of the H$\alpha$. In the middle panels, you can see that the H$\alpha$ (wing and center) and optical continuum enhancements come from the upper to lower chromosphere in the non-thermal electron case (hard case; the right side of Figure 5.10), while they mainly come from the upper chromosphere and transition region in the thermal case (soft case; the left side of Figure 5.10).

Next, let us simply compare the simulated spectra with the observations obtained in the Section 5.3. Figure 5.11 shows the comparison of the H$\alpha$ spectra between observations and models. For the initial phase (red), the observed line shape is more consistent with the hard- and high-energy spectrum model of F12 ($\delta$ = 3). For the later phases, the ob-

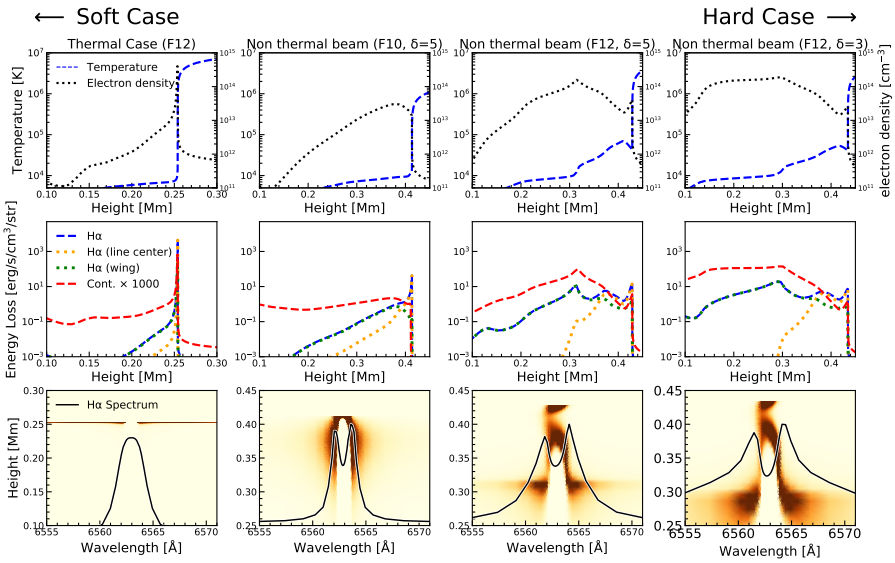


Figure 5.10: Examples of the flaring atmospheric condition at the flare peak calculated by the RADYN code for M-type stars. From left to right, soft to hard energy input cases are shown. Top: the atmospheric temperature (dashed blue line) and electron density (dotted black line) as a function of height from the photosphere at the flare peak of the H$\alpha$ radiation. Middle: contribution functions for H$\alpha$ and 6690 Å continuum as a function of height. For the H$\alpha$, the contribution from line core and wing are separately plotted. Bottom: background show the normalized H$\alpha$ line contribution function in the space of wavelength and atmospheric height. The black curves show the H$\alpha$ spectra.

served line shape is more consistent with the weaker (F10; $\delta$ = 3) or softer (F12; $\delta$ = 5) energy spectrum models. Of course, all the observed spectra is not corresponding “flare peak" (including rising/decay phases) and the readers may think that it is better to compare them with time-dependent H$\alpha$ spectral evolution for a given simulation in a single loop. However, in analogy with solar flares, the stellar flares are expected to be observed as a superposition of many magnetic loops and each footpoint has a different “flare peak". Therefore, under the assumption that one loop quickly decays, the comparison with the peak spectra of each model setup is not so much bad, and it is easy to derive the physical parameters of the energy injection. As a result of comparison between observations and models, one can say that in the initial phase, the high energy electron with large energy deposition rate and hard spectral distribution occurred, and the spectral feature changes to softer/weaker energy injection.

Finally, we show the relation between H$\alpha$ line broadening and some physical parameters such as atmospheric density or energy injections. Figure 5.12 shows the comparison between H$\alpha$ line width and electron density in the chromospheric condensation region

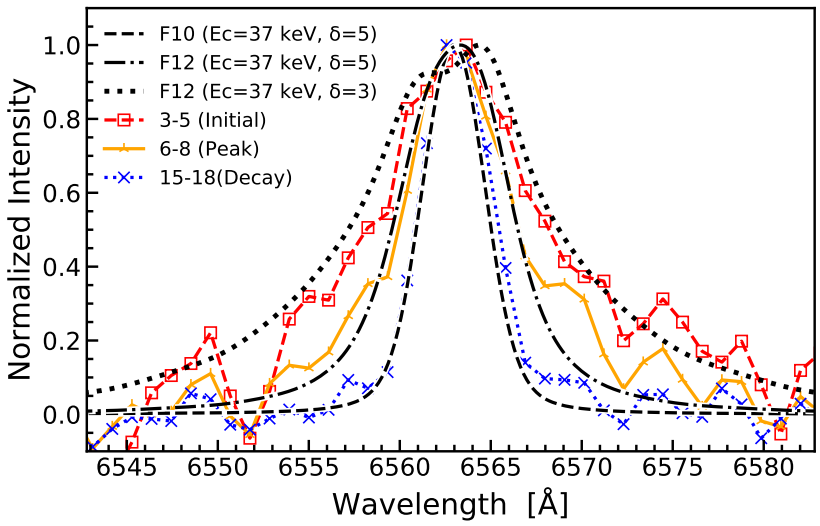


Figure 5.11: Comparison of H$\alpha$ spectra between observations (colored) and model (black). For the observational spectra, the temporal evolution of H$\alpha$ spectra of flare #1 (panel (B) of Figure 5.3) are plotted. For the model spectra, F10 ($\delta$=5), F12 ($\delta$=5), and F12 ($\delta$=3) cases are plotted as references. The model spectra are convolved with the Gaussian-function instrumental profile of Seimei/KOOLS-IFU (R$\sim$2000, $\Delta\lambda \sim 3$ Å; Matsubayashi et al. (2019)), and the central reversal seen in Figure 5.10 is not resolved in the low-resolution spectra.

at the flare emission peak for each case. For the thermal cases, the emission of H$\alpha$ is mostly radiated from the upper chromosphere and transition region where there is less self-absorption[‡‡], so the positive relation for the thermal cases is likely to come from the linear Stark effect (Kowalski et al., 2017). For the non-thermal cases, the harder spectral cases show wider line broadening. If the model atmosphere in F12 ($\delta = 3$) is compared with that in F12 ($\delta = 5$) in Figure 5.10, only the line wing contributions are enhanced in the deep chromosphere for the harder beam of F12 ($\delta$=3). This would be because the hard high energy electrons deposited in the deep chromosphere causes the strong Stark effect and self absorptions. In cases where the electron density is not so much different for each case, the self-absorption can largely contribute to these differences.

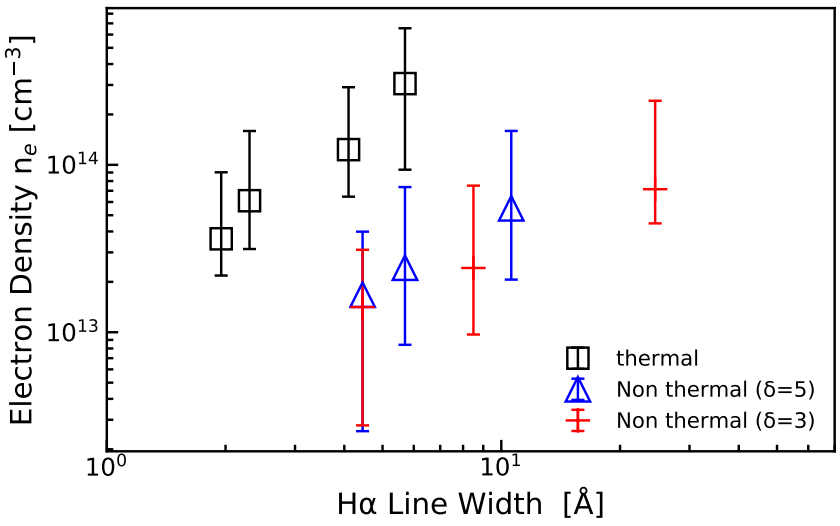


Figure 5.12: Comparison between the H$\alpha$ intensity and electron density weighted by the contribution function of the H$\alpha$ obtained by the RADYN simulations. The squares show the thermal case. The crosses and triangles show the non-thermal electron cases, and the different symbols indicate the different power-law index. As input energy flux (F#; from F10 to F12) increases, the line width and electron density increase.

### 5.5.4 Simulation result II: relation between Balmer-lines and optical-continuum emissions – what are non-white-light flares like?

In this section, we show the relation between H$\alpha$ lines and optical continuum emissions as a response to the different kinds of input parameters of flare simulations. Figure 5.13 shows the comparisons between the continuum and H$\alpha$ emission in the RADYN simulations. We found that the relation between the optical continuum and H$\alpha$ emission is not linear, but expressed as $I_{\mathrm{H}\alpha} \propto I_{\mathrm{cont}}^{\alpha}$, where $\alpha = 0.51 \pm 0.05$. We consider that there are the following two possibilities for this nonlinear relation: (1) an opacity difference between optically-thick H$\alpha$ and optically thin continuum in the chromosphere, and (2) an emissivity difference between H$\alpha$ and continuum (e.g. Kowalski et al. (2019)), (3) or both.

In the case of the possibility (1), since H$\alpha$ is optically thick in the chromosphere, the line shape heavily suffers from the self-absorption, especially in line center. Therefore, the more energetic the flare input is, the less H$\alpha$ emission ($\eta_{H\alpha}$) comes from the lower flaring atmosphere compared with the optical continuum which is optically thin and can escape from a large range of heights. In Figure 5.14, the comparisons between the continuum

[‡‡] Here, self-absorption means that the emissions are absorbed by the upper atmosphere having large opacity not to be able to go out to the surface. The upper layer of the chromosphere/transition region (i.e. corona) have very small opacity in continuum and Balmer lines.

and H$\alpha$ emission are plotted for H$\alpha$ line wing and center separately. You can see that the H$\alpha$ line center is less sensitive to the flare input and continuum emission. This is because the line center is more optically thick than the line wing, and self-absorption more or less affects the nonlinearity (for the absorption line, see e.g. Figure 9.1 in Rutten (2003)).

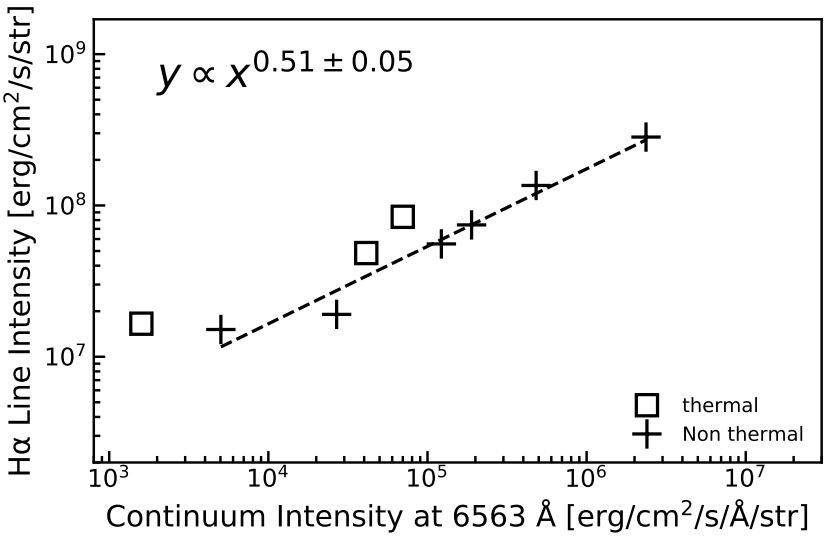


Figure 5.13: Comparison between the H$\alpha$ intensity and continuum intensity at 6563 Å obtained by the RADYN simulations. The H$\alpha$ intensity is wavelength-integrated across the line. Square symbols show the thermal case, and cross symbols show the non-thermal electron cases. As input energy flux (F#; from F10 to F12) increases, H$\alpha$ and continuum intensities increase. The dotted line is the fitted one for the non-thermal case, and the power-law index is derived to be 0.51. Note that the 5F10 thermal case show very week continuum emission, and is not plotted in this figure.

In the case of the possibility (2), the emissivity of the H$\alpha$ can be expressed as

$$\eta_{H\alpha} = \frac{h\nu_0}{4\pi} n_{\rm u} A_{\rm u} \phi(\nu - \nu_0) \propto n_{\rm u} \tag{5.1}$$

where $\eta_{H\alpha}$ is the emissivity of H$\alpha$, $n_{\rm u}$ is the upper level Hydrogen density (n=3), $h$ is a Planck constant, $\nu_0$ is the line center frequency, $A_{\rm u}$ is an Einstein constant, and $\phi$ is the profile function for H$\alpha$. On the other hand, the emissivity of optical continuum ($\eta_{\rm cont}$) can be expressed as

$$\eta_{\rm cont.} = n_{\rm e} n_{\rm p} F(T, \nu) \propto n_{\rm e}^2 \tag{5.2}$$

where $n_{\rm e}$ is the electron density, $n_{\rm p}$ is the proton density, and $F(T, \nu)$ is the function of temperature $T$ and frequency $\nu$ (for the detailed expression, see Kowalski et al. (2019)), if we assume the Paschen continuum is dominant in the optical range. If we assume that the electron density is roughly proportional to the upper-level density of H$\alpha$ and temperature

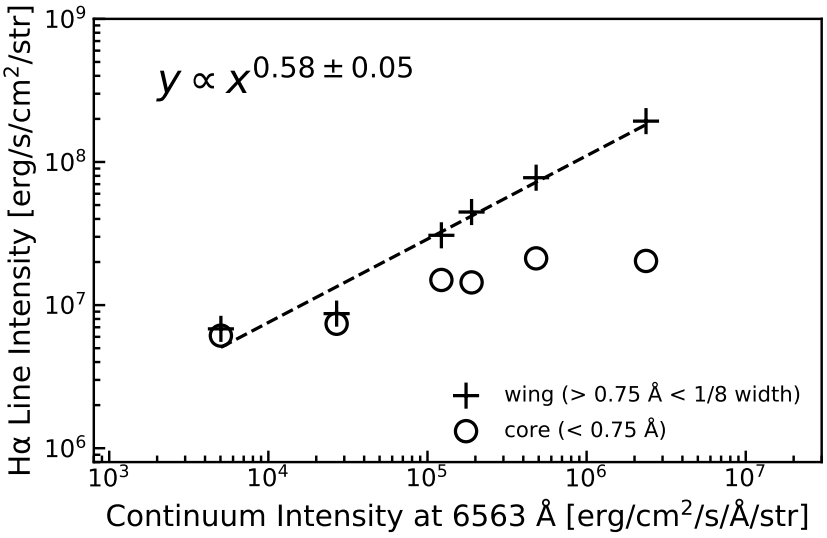


Figure 5.14: Comparison between the H$\alpha$ intensity and continuum intensity at 6563 Å for the non-thermal case obtained by the RADYN simulations. The contribution from line core (circles; $< 0.75$Å from the line center) and wing (crosses; emission integrated over 0.75 Å from line center to 1/8 width) are separately plotted here. The dotted line is the fitted one for line wing, and the power-law index is derived to be 0.58. As input energy flux (F#; from F10 to F12) increases, H$\alpha$ and continuum intensities increase. Since the line center is optically thick compared to the line wing, the emergent intensity of line center cannot become large when the input energy becomes large compared to line wing.

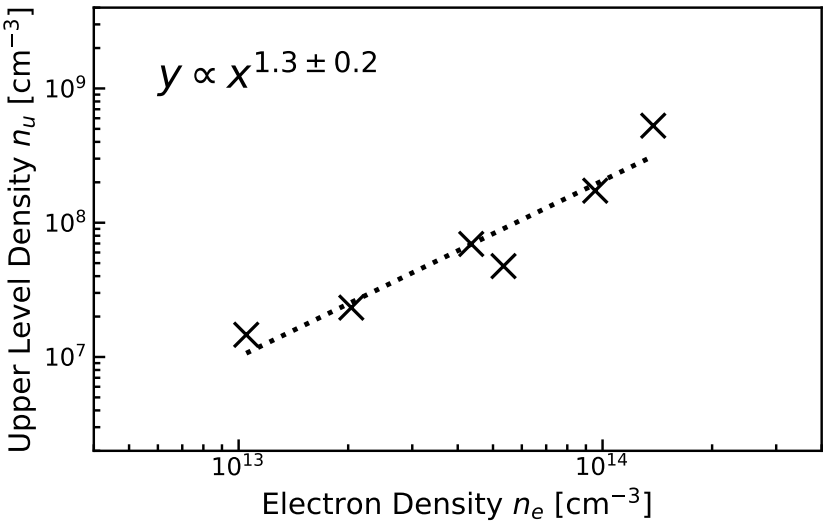


Figure 5.15: Comparison between H$\alpha$ upper level density and electron density weighted the line wing contribution function obtained by the RADYN simulations. The dotted line is the fitted one, and the power-law index is derived to be 1.3.

is not so much different in the chromospheric layers, we can deduce $\eta_{\mathrm{H}\alpha} \propto \eta_{\mathrm{cont}}^{\alpha}$, where $\alpha \sim 0.5$, which may be able to explain the non-linearity. Figure 5.15 shows the comparison between $n_e$ and $n_u$ which are weighted by the continuum and line-wing contribution function, respectively. Considering the obtained relation $n_u \propto n_e^{1.3\pm0.2}$, the equations (5.1) and (5.2) reduce to $I_{\mathrm{H}\alpha} \propto I_{\mathrm{cont}}^{\alpha}$, where $\alpha \sim 0.65$ (with $\tau_{\mathrm{wing}} \ll 1$ in chromosphere), which is simlar to the relations for line wing $I_{\mathrm{H}\alpha wing} \propto I_{\mathrm{cont}}^{\alpha}$, where $\alpha = 0.58 \pm 0.05$.

These results mean that the non-linear relation between H$\alpha$ and continuum intensity comes from both of the (1) opacity effect and (2) emissivity difference. This non-linearity means that the emergent continuum intensity more significantly decreases than the emergent H$\alpha$ intensity when the energy input rate into the chromosphere decreases. For example, the H$\alpha$ intensity decreases by a factor 3 whereas the continuum intensity decreases by one order of magnitude. This can explain why there is no white-light emission on the relatively weak H$\alpha$ flares: white-light emission is difficult to detect compared to the H$\alpha$ emission in the case of weak flares.

## 5.6 Discussion

### 5.6.1 Stellar flares – observations and simulations

Let us summarize the observational results in this work. We found the following three interesting events:

1. During the superflare (flare #1), the H$\alpha$ emission line full width at 1/8 maximum dramatically increases to 14 Å from 8 Å accompanied with the large white-light flares (Section 5.3.2).
2. Some weak H$\alpha$ and X-ray flares (e.g. flare #4) are not accompanied with white-light emissions which are candidates of so-called non-white-light flares in the case of solar flares (Section 5.3.4).
3. Clear rotational modulations are found in X-ray/H$\alpha$ in the same phase whereas the continuum periodicity is not clear due to the photometric sensitivity (Section 5.4, discussed in Section 5.6.2).

We performed a one-dimensional RHD simulation with RADYN code to understand the behavior of H$\alpha$ and optical continuum obtained in the above points (1) and (2) (Section 5.5).

As for the point (1), the numerical simulation (Section 5.5.3) shows that the line width of H$\alpha$ largely depends on both the energy flux density ($F$) and the energy spectrum (a

power-law index $\delta$). By changing the energy spectra, the degree of contribution from Stark broadening and opacity broadening does change, meaning that it is difficult to constrain the input energy spectra from only the H$\alpha$ spectra of the superflare #1. Even if the additional information such as the continuum fluxes is given, there is another degeneracy between intensity ($I$) and emission area ($A_{\rm flare}$), which makes it difficult to constrain the energy spectra.

Considering the large H$\alpha$ broadening during the superflare, it would be at least possible to say that the H$\alpha$ broadening in the initial phase of the superflare indicates a hard- and/or high-energy flare injection via non-thermal electron like the case with $F_{\rm NT}$ = $10^{12}$ erg cm$^{-2}$ s$^{-1}$ and $\delta$ = 3, and the decrease in the line width indicates the decrease of the energy flux density and/or the softening of energy spectra at different locations in the flare ribbon. Previous studies also indicate that $F_{\rm NT}$ = $10^{12}$ erg cm$^{-2}$ (low-energy cutoff $\gg$ 37 keV) or $10^{13}$ erg cm$^{-2}$ s$^{-1}$ is necessary to reproduce the broad-band continua of M-dwarf flares (Kowalski et al., 2016), and fluxes larger than this are sometimes inferred even on the Sun (Krucker et al., 2011). More comparison between observations and modelings can give us a clue to the universality or difference of the particle acceleration on solar and stellar flares.

As for the point (2), our simulation also shows that the H$\alpha$ and optical continuum intensity have non-linear relation $I_{\rm H\alpha} \propto I_{\rm cont}^{\alpha}$, where $\alpha \sim 0.5$, which is largely caused by the opacity and emissivity difference (Section 5.5.4). This non-linearity can contribute to the cause of non-white-light flares: as the energy input rates decrease, the continuum emissions more significantly decrease than H$\alpha$ emissions. In the case of the solar flare, it is reported that non-white-light flares tend to have long durations, i.e. small energy deposition rates (Canfield & Gayley (1987); Matthews et al. (2003); Watanabe et al. (2017)), which is consistent with our simulation and interpretation/analysis. However, it would not be consistent with the relatively a short duration $\sim$ 7 minutes of flare #4, and we need more samples of stellar non-white-light events and the validation in spatially-resolved solar flares would be required. As another possibility, stellar non-white-light flares may be explained by a flare over the limb. In this case, if we assume that white-light emissions originate from only chromosphere/photosphere like solar flares, the white-light emission source at loop footpoints is invisible while the X-ray and H$\alpha$ emission are visible in the flare loop in the corona. However, this possibility may be less likely because white-light emissions can be visibly emitted from the dense (post) flare loops (Heinzel & Shibata (2018); Jejčič et al. (2018)) even though the footpoints are invisible over the stellar limb.

### 5.6.2 Rotational modulations

As summarized in the point (3) of Section 5.6.1, we found X-ray and H$\alpha$ rotational modulations on AD Leo with a period of 2.24 days in almost the same phase (see Section 5.4). It is to our knowledge rare to simultaneously detect the rotational modulation in coronal and chromospheric emissions on M-dwarf, although some previous studies are showing rotational modulations with broadband optical and X-ray (Wargelin et al., 2017) or with only X-ray (e.g. Marino et al. (2003); Hussain et al. (2007)). The correlation between chromospheric and coronal emission would be because both H$\alpha$ and X-ray would come from the magnetically-active regions. Although the small difference of rotational phase ($\sim$ 0.1) between H$\alpha$ and X-ray may indicate the difference of the visibility or location of the bright active region in each wavelength, it may be due to the sparse data sampling and/or the very rough fitting by a sine curve. The amplitude of the brightness variation in X-ray and H$\alpha$ is 32 % and 16 %, respectively. The factor-of-two difference in amplitude between X-ray and H$\alpha$ may be due to that in active region filling factor between chromosphere and corona, but may be due to the contrast between the active region and quiet regions. Saar & Linsky (1985) however inferred that the 73 % of the surface of AD Leo is covered by active regions outside of dark spots. One possibility to explain the difference between the observed brightness amplitude in X-ray/H$\alpha$ and the reported filling factor is that the low inclination angle of AD Leo ($i$ = 20°; Morin et al. (2008)) reduce the brightness amplitude, and the other is that the large filling factor significantly reduced the stellar brightness amplitude (Eker (1994); Schrijver (2020)).

Although the rotational brightness variations were detected for X-ray, we could not detect clear rotational variations in the hardness ratio of X-ray band which is related to the coronal temperature: the spectra show the relatively low hardness ratio even in the high X-ray intensity. This could be because the temperature is not sensitive to the magnetic loop size (Rosner et al., 1978), or may be because the active region consists of group of small magnetic loops and therefore the increase in the number of magnetic loops does not affect the changes in coronal temperature.

The optical rotational modulation is less than $\sim$6 % possibly due to the lack of sensitivity, but maybe it is true considering that optical variability of M dwarfs like GJ 1243 (dMe4.0V) is comparable with this amplitude in *Kepler* (e.g. Hawley et al. (2014); Davenport et al. (2014)). However, considering this low inclination angle, the I-band amplitude of 6% looks rather large, and it is interesting to try a photometric spot modeling on the data as in Chapters 2 and 3. The optical rotational phase is not completely anti-correlated with X-ray/H$\alpha$ ones (0.2–0.3 rotational phase), which may indicate the spotted side of the hemisphere is not the same as coronal/chromospheric active regions, although more precise measurements of the optical rotational modulation would be necessary for conclu-

sions. In this observational period, it is difficult to estimate the active region emergence or decay, but the long-term continuous monitoring observation with multi-wavelength can reveal the signature of magnetic flux emergence/decay in the stellar chromosphere/coronae (c.f. Chapters 2 and 3; e.g. Namekata et al., 2019, 2020a)

## 5.7 Summary and conclusion

We conducted multi-wavelength observation campaign of flaring M-dwarf AD Leo by mainly using newly-developed 3.8-m Seimei telescope and OISTER program. The most prominent features in this campaign is the high time resolutions ($\sim$1 min) spectroscopic observations with the moderate spectral dispersion (R$\sim$2000) that can resolve the H$\alpha$ profiles. We obtained one superflares and 11 small-scalle flares on AD Leo. Here, our findings are listed as follows:

**(i)** During the impulsive phase of the superflare, the H$\alpha$ emission shows enhanced broadenings accompanied with the large white-light flares. These features can be explained by the hard and high-energy non-thermal electron beam injections to the stellar chromosphere but cannot explained by the thermal heatings. This indicates the non-thermal electron can be efficiently accelerated by the superflare and can play an important role to produce radiations as in solar cases.

**(ii)** The line width dramatically changes during the superflares in the time scales of minutes. This kind of dramatical time evolution of line widths was firstly reported in this study thanks to our new instrument. It is found that the electron density with more soft- and/or weak-energy beam are consistent with those in decay phases, indicating the changes in the energy fluxes injected to the lower atmosphere.

**(iii)** Some weak H$\alpha$/X-ray flares are not accompanied with white-light emissions. we found that the relation between optical continuum and H$\alpha$ intensity is nonlinear, which can be one cause of the non-white-light flares. Also, this means that the flare energy budget exhibits diversity in the observations and models, which may an important for the evaluations of its effect on the exoplanet atmosphere.

**(iv)** It is found that coronal emissions are correlated with chromospheric emissions during rotational phases. This indicates solar-like active regions that bright in chromosphere and corona.

First, it can be concluded that most of the above observed features of (super-)flares can be well explained by coupling the RHD models and solar physics in terms of the energy transport and heating via non-thermal electrons, and radiations (results (i)-(iii)). So far, the

information on non-thermal electrons has been limited to some studies using H$\gamma$ lines and broadband continuum (e.g. Kowalski et al., 2016) or radio observations (e.g. MacGregor et al., 2018). Since the particle acceleration mechanism is considered to be one of the biggest mystery in the modern astrophysics, the estimates of high energy particle fluxes in this work will be helpful for the understandings of the particle acceleration in stellar superflares (possibly via the magnetic reconnection; cf. Chapter 4). H$\alpha$ is widely used lines and the approach presented here can help further estimates of high-energy particles in future ground-based observations.

We found that the estimated electron is much higher than solar cases. This indicates that the XUV radiations associated with superflares on M dwarfs can be much stronger than solar cases, which can be radiated to the exoplanet atmosphere around active stars. It is argued that the XUV radiations play an important role in atmospheric escape on exoplanets (Airapetian et al., 2020). In addition, if we assume possible proton fluxes are similarly higher than solar cases, it may be also emitted to the interplanetary space from the reconnection site (observed as type-III radio bursts in solar cases; Webb & Howard, 2012), which may influence the exoplanet atmosphere.

It could be also concluded that the active regions can be similar to solar active regions: the bright corona and chromosphere (see Figure 1.1, 1.5 in the Chapter 1). The result (iv) can be promising to unveil the active levels of active regions (i.e. flare-productivity of spots; see e.g. Toriumi & Wang, 2019) if we had high-quality photometry. The multi-wavelength monitoring observations of spotted stars should be continued in order to reveal how the gigantic spots can produce superflares (as listed as a future works in Chapters 2 and 3)

CHAPTER 6

# Detection of mass ejection from a superflare on a solar-type star

## 6.1 Introduction

As introduced in Chapter 1, mass ejections associated with solar flares releasing the energy of $10^{29}$ to $10^{32}$ erg (Shibata & Magara, 2011; Emslie et al., 2012) often directly affect Earth's environment (Gopalswamy et al., 2003). The mass ejections can be a kind of the "energy transport" of flare energy via kinetic energy (see Section 1.2.5). Active stars including solar-type stars are known to sometimes show larger superflares releasing the energy more than $10^{33}$ erg, and recently it has been proposed that superflares can occur – or have occured – even on the current Sun (see Section 1.2.3; Maehara et al., 2012; Miyake et al., 2012). The superflares may produce much larger mass ejections than the largest solar cases, which can greatly affect the environment of young/current Earth and the habitability and origin of life on exoplanet (Airapetian et al., 2016, 2020). However, no observational indication of mass ejection has been reported especially for solar-type stars, and furthermore, most of the signatures of mass ejections reported before are very controversial even for other kinds of magnetically active stars although some candidates are reported for such as M-type stars (Houdebine et al., 1990; Gunn et al., 1994; Fuhrmeister & Schmitt, 2004; Vida et al., 2016; Honda et al., 2018; Leitzinger et al., 2014; Korhonen et al., 2017; Muheki et al., 2020a), T-tauri stars(Guenther & Emerson, 1997; Tsuboi et al., 1998), close binaries (Favata & Schmitt, 1999), and giant stars (Argiroffi et al., 2019).

Our aim of this chapter is to challenge the detections of stellar mass ejections, especially on solar-type stars. Optical spectroscopic observations can be a promising way to detect the stellar mass ejections (cool mass ejections, e.g. known as filament/prominence eruptions). It should be notable that, for solar-type stars, even the optical spectra of superflare brightenings have never been obtained so far. Koller et al. (2020) surveyed the mass ejections and flares on F-K stars by using the SDSS data, but they report no detection for solar-type

stars (G-type stars). This would be because of the low contrast and the low occurrence frequency of the flares on solar-type stars. Therefore, a detection of the optical spectra is the first gaol of this study, and an ultimate goal is to detect the signature of mass ejections.

EK Draconis (EK Dra) is known to be an active young solar-type star (a G-type, zero-age main-sequence star with an effective temperature of 5560–5700 K and age of 50–125 million years; Waite et al., 2017; Güdel, 2007; Strassmeier, 2009) that exhibits frequent UV stellar flares (Ayres, 2015; Audard et al., 1999) and the gigantic star spots on the low-high latitudes (Waite et al., 2017). With the aim of detecting the optical spectra of superflares as a first step, we conducted optical spectroscopic monitoring of EK Dra for 19 nights between 21 January 2020 and 15 April 2020, simultaneously with optical photometry from the Transiting Exoplanet Survey Satellite (TESS) (Ricker et al., 2015). In Section 6.2, we introduce our observations and analysis. In Section 6.3, we show the results. In Section 6.4, discussions are described. In Section 6.4, we describe the conclusion.

## 6.2 Observation and analysis

### 6.2.1 *TESS* light-curve analysis

*TESS* observed EK Dra (TIC 159613900) in its sector 14-16 (18 July 2019-6 October 2020) and 21-23 (21 January 2020-15 April 2020). The *TESS* light curve from the 2-min time-cadence photometry was processed by the Science Processing Operations Center pipeline, a descendant of the *Kepler* mission pipeline based at the NASA Ames Research Center (Ricker et al., 2015; Fausnaugh, 2020). Figure 6.1 shows the light curve of the EK Dra from BJD (Barycentric Julian Day) 2458945 (= JD 2458944.997 = 5 April 2020 11:56UT ; Sector 23). One stellar superflare was detected by *TESS* when there are simultaneous observations by ground-based telescope (see Section 6.2.2) as indicated with the red arrow in this figure as introduced in Section 6.3.

### 6.2.2 Spectroscopic data analysis

We obtained two spectroscopic datasets of EK Dra. Here, we present the utilization of low-resolution spectroscopic data from KOOLS-IFU (Matsubayashi et al., 2019) (Kyoto Okayama Optical Low-dispersion Spectrograph with optical-fiber Integral Field Unit) of the 3.8-m Seimei Telescope (Kurita et al., 2020) at Okayama Observatory of Kyoto University and MALLS (Ozaki & Tokimasa, 2005; Honda et al., 2018) (Medium And Low-dispersion Long-slit Spectrograph) of the 2-m Nayuta Telescope at Nishi-Harima Astronomical Observatory of University of Hyogo to confirm the flare spectra. KOOLS-IFU is an optical spectrograph with a spectral resolution of R ($\lambda/\Delta\lambda$) $\sim$ 2,000 covering

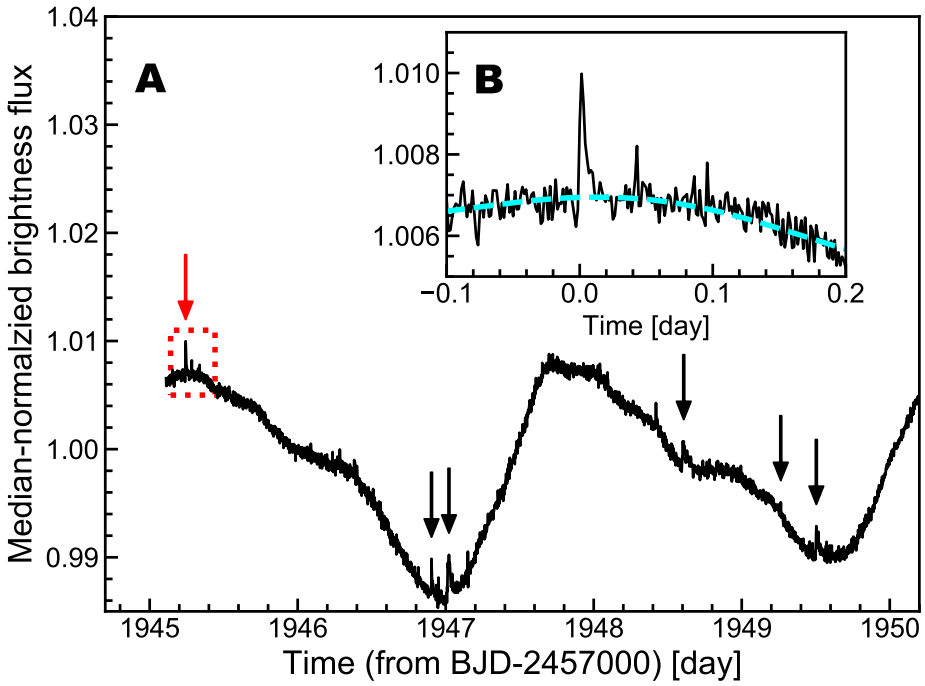


Figure 6.1: Global *TESS* light curve for EK Dra. **(A)** Light curve of a superflare on EK Dra observed by *TESS* from BJD 2457000. The gap before about BJD 2458945 days corresponds to a gap in the data downlink with Earth during the spacecraft's perigee. The arrows indicate stellar flares that occurred during this observational period. The red arrow is a superflare which was observed simultaneously by ground-based spectroscopic observations. **(B)** Enlarged light curve indicated with the red dotted box in panel **(A)**. The cyan dashed line is the global trend of the light curve which is caused by the stellar rotation with large star spots.

a wavelength range from 5800-8000 Å; it is equipped with Ne gas emission lines for wavelength calibration and instrument characterization. The exposure time was set to be 30 sec for this night. The sky spectrum was subtracted by using the sky fibers for each spectrum. The KOOLS-IFU data reduction follows the prescription in Chapter 5 (Namekata et al., 2020b).

MALLS is optical spectroscopy with a spectral resolution of R $\sim$ 10,000 at the H$\alpha$ line covering a wavelength range from 6350-6800 Å; it is also equipped with Fe, Ne, and Ar gas emission lines for wavelength calibration and instrument characterization. Also, the sky spectrum was subtracted by using the spectrum enough separated along with the slit direction for each spectrum. The exposure time was set to be 3 min for this night. The MALLS data reduction follows the prescription in (Honda et al., 2018). We corrected the wavelength for the proper motion velocity of $-20.7$ km s$^{-1}$ of EK Dra based on Gaia Data Release 2 (Lindegren et al., 2018). For the MALLS data, the wavelength corrections are also performed for each spectrum with an accuracy of 0.01 Å by using the Earth

atmospheric absorption lines.

Continuum levels are defined by fitting with the linear line between the wavelength range of H$\alpha$ line wing (6517.8-6537.8 and 6587.8-6607.8 Å). We take the continuum level as the wavelength range of 6517.8-6537.8 and 6587.8-6607.8 Å to measure the equivalent width E.W. (E.W. = $\int(1 - F_\lambda/F_0)d\lambda$, where $F_0$ is the continuum intensity on either side of the absorption feature, while $F_\lambda$ represents the intensity across the entire wavelength range of interest).

### 6.2.3 Flare energy

The *TESS* white-light flare's bolometric energy is derived from the *TESS* light curve in the formula of (Maehara et al., 2012; Shibayama et al., 2013)

$$E_{\rm bol} = \int_{\rm flare} \sigma_{\rm SB} T_{\rm flare}^4 A_{\rm flare} dt, \tag{6.1}$$

where the bolometric flare energy ($E_{\rm bol}$), the flare effective temperature ($T_{\rm flare}$), the area of flare ($A_{\rm flare}$), and the Stefan-Boltzmann constant ($\sigma_{\rm SB}$). For each time, the flare area is calculated based on the flare enhancement, flare effective temperature, stellar radius of 0.94 solar radius, and *TESS* response function (Ricker et al., 2015). The spectrum of white-light flares is assumed as a blackbody spectrum with the 10,000 K effective temperature. Although broadband optical spectra have never been observed for superflares on solar-type stars, the 10,000 K blackbody radiation is a good approximation for the M-dwarf stellar flares (Hawley & Fisher, 1992) or solar flares (Kretzschmar et al., 2010). Even if the flare temperature becomes 6,000-7,000 K, the estimated energies become smaller only by a factor of 0.5.

The H$\alpha$ flare energy is estimated from the enhanced H$\alpha$ E.W. and continuum flux level around H$\alpha$. The continuum flux of EK Dra around H$\alpha$ is derived as 1.57 W m$^{-2}$ nm$^{-1}$ ($\sim$ the solar value) at 1 astronomical unit for flux-calibrated spectra obtained by KOOLS-IFU with the stellar distance given by Gaia Data Release 2 (Lindegren et al., 2018). HR7596 (A0III-type well-known standard star) is used for the flux calibrations as a standard star. The H$\alpha$ flux can contain errors of about a few % due to the difference in the air-mass conditions of HR7596 (1.402) and EK Dra (1.318). Then the H$\alpha$ energy is calculated by just multiplying the enhanced H$\alpha$ E.W. (integrated for H$\alpha$ - 10 Å $\sim$ H$\alpha$ + 10 Å) by the continuum flux and integrating in time.

## 6.3 Result

### 6.3.1 Light curves and spectra

Time-resolved neutral-hydrogen H$\alpha$-line spectra at 6562.8 Å (that is, radiation from cool plasma at a temperature of a few times 10,000 K) were monitored using the low-dispersion spectrograph KOOLS-IFU onboard the 3.8-m Seimei Telescope (Kurita et al., 2020) and the middle-dispersion spectroscopy MALLS onboard the 2-m Nayuta Telescope as introduced in Section 6.2.2. In this observational campaign, we succeeded in obtaining for the first time optical spectra of large superflares on a solar-type star. One that occurred on 5 April 2020 was simultaneously observed using the *TESS* photometry in white light ($\sim$6,000-10,000 Å) and both ground-based spectroscopies in the H$\alpha$ line (Figure 6.2A-B and Figure 6.1). The brightening of the H$\alpha$ line was associated with the *TESS* white-light flares, which had a duration of 16 $\pm$ 2 min. The radiated bolometric energy of the *TESS* white-light flare is estimated to be $2.0\pm0.1\times10^{33}$ erg (20 times the most energetic solar flares) and the radiated H$\alpha$-line energy was $1.7\pm0.1\times10^{31}$ erg; thus the flare is classified as a superflare.

After the impulsive phase of superflare brightening, the *TESS* white-light intensity returned to its pre-flare level in 16 min. However, the equivalent width (E.W.) of H$\alpha$ became lower than the pre-flare level (i.e. it displayed enhanced absorption), returning to the pre-flare level in approximately 2 hours (Figure 6.2B). The blue-shift H$\alpha$ absorption component with a maximum central velocity of about $-510$ km s$^{-1}$ and a half width of $\pm220$ km s$^{-1}$ appeared soon after the superflare. The velocity gradually slowed down with time, and eventually a red-shifted absorption component appeared at a few times 10 km s$^{-1}$ (Figure 6.2C-E and Figure 6.3A). Both ground-based spectroscopic observations simultaneously recorded the same spectral change. This demonstrates that low-temperature and high-density neutral plasma on the stellar disc moves at high speed toward the observer before finally starting to fall back onto the surface. In addition, the deceleration is not monotonic: it was $0.34\pm0.04$ km s$^{-2}$ in the initial phase, dropping to $0.016\pm0.008$ km s$^{-2}$ in the later phase (Figure 6.2C-D and Figure 6.3B). This is interpreted in terms of changes in the height of the ejected mass above the stellar surface. The observed deceleration is in good agreement with that due to the surface gravity of approximately $0.30\pm0.05$ km s$^{-2}$ (Waite et al., 2017), though the initial value is a little larger.

Figure 6.4 shows the time-integrated flare spectra evolution during the events. It is possible to see the differences between pre-flare and flare spectra of blue- or red-shifted absorption components in Figure 6.2C-E (about 1.5 % at most) even by these original spectra, while far-wing continuum levels of flare spectra are well consistent with that of pre-flare spectrum, indicating that the blue-shifted components are real. We made two light curves of

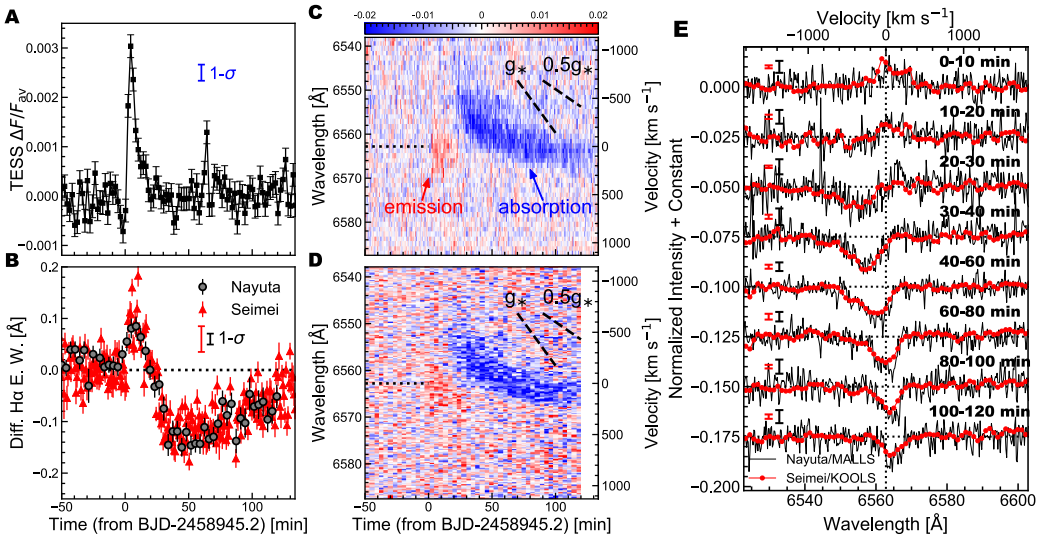


Figure 6.2: Light curves (A-B) and spectra (C-E) of a superflare on EK Dra. **(A)** The light curve observed by *TESS* in white light (∼6000–10,000 Å) on BJD (Balicentric Julian Day) 2458945.2 (5 April 2020). The individual points represent the stellar brightness normalized by the averaged value with the pre-flare level subtracted. The 1-$\sigma$ value of the pre-flare light curve (-150 min to 0 min) is plotted with blue color. **(B)** Light curves of the H$\alpha$ equivalent width (E.W.) observed by the Nayuta telescope (grey circles) and the Seimei telescope (red triangles) during the same observing period as in panel **(A)**. The H$\alpha$ emissions were integrated within $\pm$10 Å from the H$\alpha$ line centre (6562.8 Å) after dividing by the continuum level, and the pre-flare level is subtracted. The positive and negative values represent emissions and absorptions, respectively, compared to the pre-flare level. The 1-$\sigma$ value of the pre-flare light curve (-150 min to 0 min) is plotted with red and black color for Seimei and Nayuta data, respectively. **(C-D)** Tow-dimensional H$\alpha$ spectra obtained by the Seimei Telescope **(C)** and the Nayuta Telescope **(D)**. The red and blue colours correspond to emission and absorption, respectively. The dashed lines indicate the stellar surface gravity ($g_*$) and half of the surface gravity (0.5 $g_*$). The panel **(C-D)** share the upper color bar. **(E)** Temporal evolution of the pre-flare-subtracted H$\alpha$ spectra observed by the Seimei telescope (red) and the Nayuta telescope (black), with the spectra displaced by constant values for clarity. The spectra are binned in time, and the integration periods correspond to the horizontal axes of panel **(A-D)**. The intensities are normalized by the stellar continuum level. The vertical dotted line indicates the H$\alpha$ line centre, and the horizontal dotted lines indicate the zero levels for each spectrum. The 1-$\sigma$ error bar around the line core is also plotted based on the scattering of the residual in line wing.

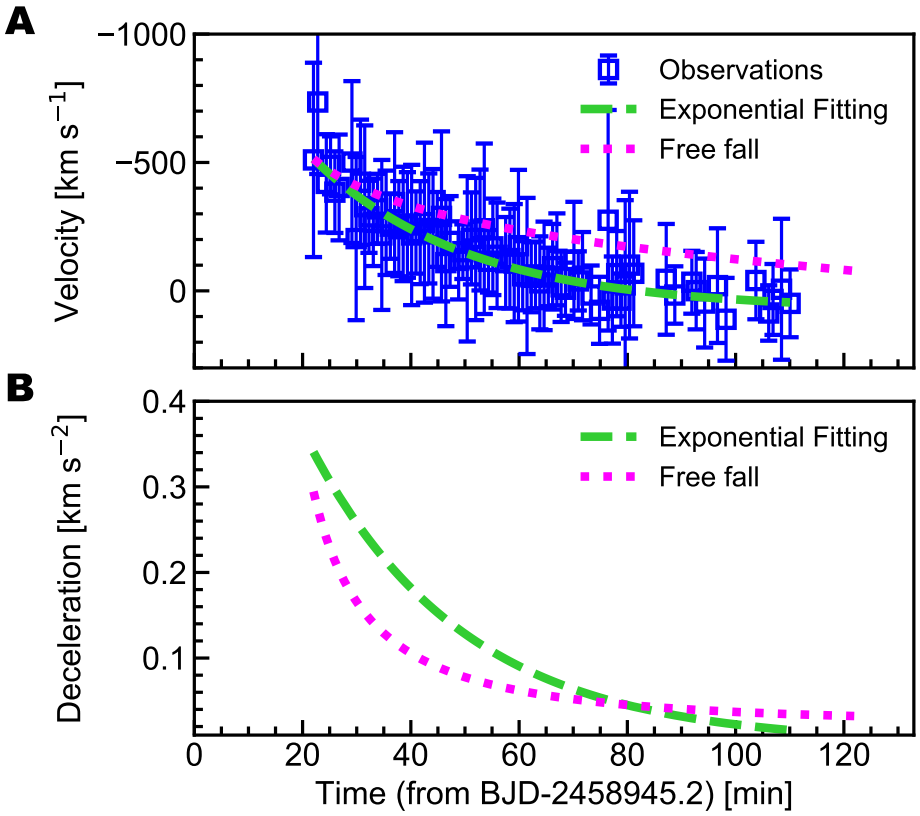


Figure 6.3: Temporal evolution of the velocity and deceleration for the H$\alpha$-line absorption features. **(A)** The blue points indicate the velocity of the H$\alpha$-line absorption features seen after a superflare. The spectra observed by Seimei Telescope were used considering the high S/N and the absorption features are obtained by fitting the absorption features with normal-distribution function. The error bars indicate the standard deviation of the fitted normal distribution. The green dashed line indicates the exponential function which fits the blue symbols, and the magenta dotted line indicates the velocity evolution of the free fall. **(B)** The temporal evolution of deceleration rates is derived from the velocity changes for observation and free-fall model in panel **(A)**.

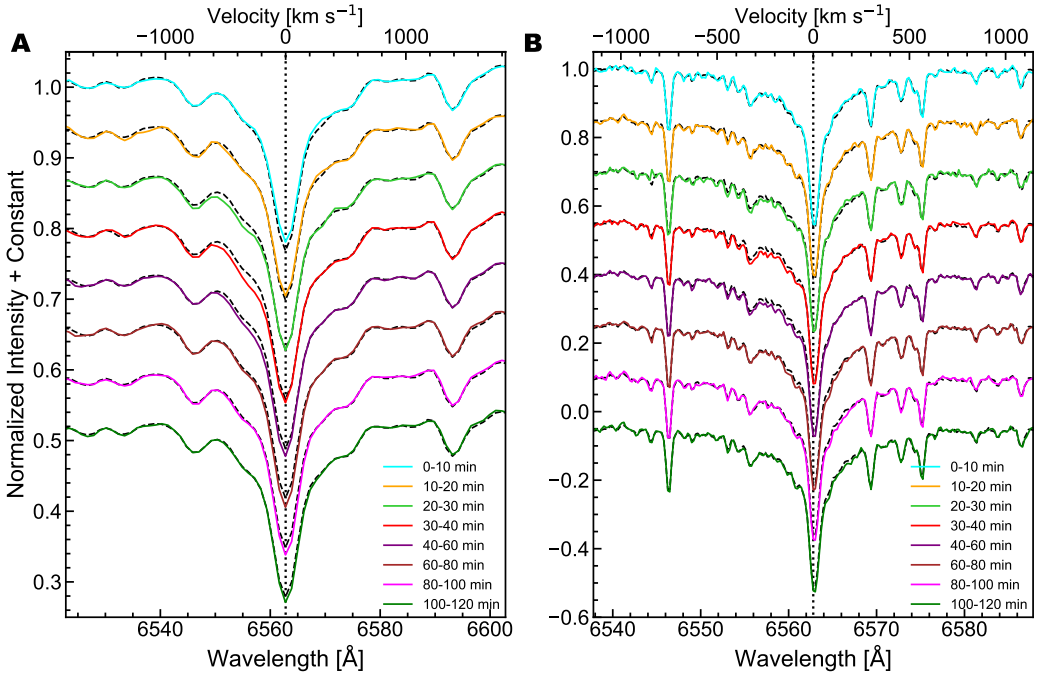


Figure 6.4: Observed H$\alpha$ spectra during a superflare on EK Dra. **(A)** H$\alpha$ spectra observed with Seimei Telescope/KOOLS-IFU (wavelength resolution $\lambda/\Delta\lambda \sim$ 2,000). Each coloured spectrum indicates the averaged spectrum for each time indicated in the legend, and the background black dashed lines are the pre-flare template spectra. The spectra are normalized by the continuum level and the constant values are added to the spectra for visibility. The indicated times in the legend correspond to the times indicated in the horizontal axis of Figure 6.2 **(A-D)**. The dotted vertical line indicates the line centre wavelength (6562.8 Å). **(B)** H$\alpha$ spectra observed with Nayuta Telescope/MALLS (wavelength resolution $\lambda/\Delta\lambda \sim$ 10,000). The plots are almost the same as panel **(A)**. Note that the range of the horizontal axis is different from panel **(A)** for visibility.

the H$\alpha$ E.W. with the integration ranges of H$\alpha$ - 10 Å $\sim$ H$\alpha$ + 10 Å and H$\alpha$ - 20 Å $\sim$ H$\alpha$ + 10 Å, respectively. The narrow-band H$\alpha$ E.W. is used for the measurements of the radiated energy and duration of H$\alpha$ flare because of the high S/N, and the broad-band H$\alpha$ E.W. is used for the measurements of the amount of broad-band features.

### 6.3.2 Comparison between solar and stellar flares

We analyzed solar data as a template of the mass ejection phenomena in order to interpret the stellar H$\alpha$ spectral behaviors. We analyzed a C8.0-class solar flare (i.e. the peak GOES soft X-ray flux $F_{\rm GOES}$ is $8.0\times10^{-6}$ W m$^{-2}$) and associated cool-mass ejection on 02:46 UT observed by the SDDI (Solar Dynamics Doppler Imager; Ichimoto et al., 2017) installed on the SMART (the Solar Magnetic Activity Research Telescope) at Hida Observatory. The SDDI conducted a monitoring observation of the Sun on 2 April 2017. It takes full-

disc solar images at 73 wavelength points at every 0.25 Å from the H$\alpha$ line centre $-9.0$ Å to the H$\alpha$ line centre +9.0 Å. Each set of images is obtained with a time cadence of 15 seconds and a pixel size of about 1.2 arcsec. The SDDI started the daily monitoring observations in 2016, and the C8.0-class solar flare is the largest solar flare with cool mass ejection (classified to known as solar “surge"; Shibata & Magara, 2011) among the events observed by SDDI with good weather condition in this 5 years.

This paper used a 70-min time series of the SDDI images taken from 02:30.05 UT on 2 April 2017. Figure 6.5A shows the full-disc image at the H$\alpha$ wing (6559.8 Å) at 02:30.05 UT. This flare occurred around an active region, named ‘NOAA 12645’, located around solar disc centre and was accompanied by typical cool-plasma ejection. For the period from 02:43:50 to 02:51:44 including flare peak, the full 73 wavelength images are available, while for the other periods, only the 25 images from the H$\alpha$ line centre $-3.0$ Å to the H$\alpha$ line centre +3.0 Å which are enough to cover the whole phenomenon are available in the archive database.

The spectra from the solar flare and the associated solar surge are integrated over the vast region enough to cover the visible phenomena (the magenta region in Figure 6.5A-B). The spectra are reconstructed by using the template solar H$\alpha$ spectrum convolved with SDDI instrumental profile. We first obtained the local pre-flare subtracted spectra which is normalized by partial-image continuum level ($\Delta I(\lambda, t)_{\text{event}}/I(t)_{\text{cont, partial-image}}$). Then, the virtual full-disc pre-flare-subtracted spectra are obtained by multiplying the ratio of the partial-image continuum to full-disc continuum ($I_{\text{cont, partial-image}}$ / $I_{\text{cont, full-disc}}$) [i.e. $\Delta I(\lambda, t)_{\text{event}}$ / $I_{\text{cont, full-disc}}$ = ($\Delta I(\lambda, t)_{\text{event}}$ / $I(t)_{\text{cont, partial-image}}$) × ($I_{\text{cont, partial-image}}$ / $I_{\text{cont, full-disc}}$)], so that we obtained a virtual spectrum of this phenomena as if we observed the Sun as a star. The E.W. of the H$\alpha$ is also calculated by using the full-disc-normalized and pre-flare-subtracted spectra, and we obtained the virtual Sun-as-a-star $\Delta$H$\alpha$ E.W. (i.e. differential H$\alpha$ flux normalized by the full-disc continuum intensity). In Figure 6.5C, temporal evolution of the solar flare and surge are shown for H$\alpha$ centre $-2$ Å ($-91$ km s$^{-1}$), $-1$ Å ($-46$ km s$^{-1}$), $+0$ Å, and $+1$ Å ($+46$ km s$^{-1}$). In the top row, which corresponds to t = 18 min in Figure 6.3, the flare and fast ejected component can be seen at $-2$ Å. In the second row (t = 21 min), the fast ejected components almost disappear, slow components become dominant at $-1$ Å, and total H$\alpha$ E.W. becomes the minimum value as also seen in the stellar case. The fast component is not visible in successive images even in other wavelengths probably because it becomes heated or diluted to be invisible in H$\alpha$ image. In the third line (t = 30 min), both slow upward and downward flows can be seen in $\pm$ 1 Å and flare emissions become very weak but still visible.. In the fourth row (t = 39 min), only the red wing absorption becomes dominant, which means ejected mass was falling back to the solar surface.

Then, how much do the stellar spectral changes obtained here actually resemble those of

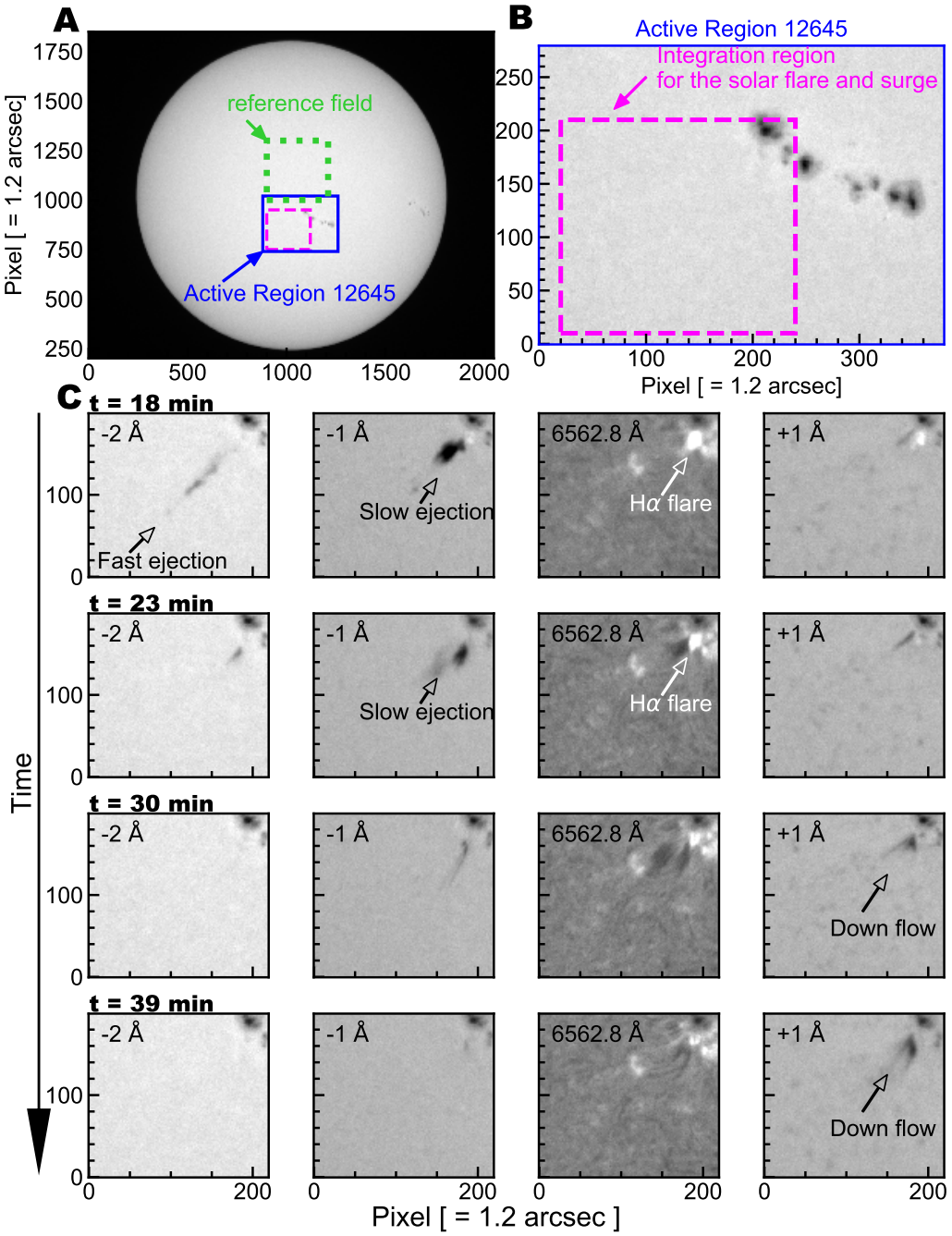


Figure 6.5: A solar flare on April 2, 2017, observed by SMART telescope/SDDI at Hida observatory. **(A)** Full disc image of the Sun at the H$\alpha$ line wing (6559.8 Å). The horizontal and vertical axis mean the image pixels whose size is about 1.2 arcsec in the x-y plane. The green region is a quiet region used as a reference to make the H$\alpha$ spectra. **(B)** the blue region is the enlarged panel of the active region 12645. The magenta region is the region where the solar flare and surge could be seen. **(C)** The temporal evolution of solar images in magenta region at the wavelength of 6560.8 ($-91$ km s$^{-1}$), 6561.8 ($-46$ km s$^{-1}$), 6562.8 (0 km s$^{-1}$), 6563.8 Å (+42 km s$^{-1}$). Emission and absorption features are indicated with white and black, respectively. The movie is available in Movie S1.

solar mass ejections? Blue-shifted H$\alpha$ absorption components are often observed during cool-mass eruptions associated with solar flares (Schmieder et al., 1987; Shibata & Magara, 2011). A space-integrated H$\alpha$ spectrum of a solar eruptive event comparable with stellar events has never been obtained before. We therefore made the space-integrated H$\alpha$ spectra of a solar cool-mass ejection and flare that occurred on solar disc on 2 April 2017 by using the SDDI (Ichimoto et al., 2017) onboard the SMART telescope at Hida Observatory (Figure 6.5), and converted to the full-disc pre-flare subtracted spectra by multiplying partial-region/full-disc ratio (i.e. virtual Sun-as-a-star spectra). We found that the blue-shifted absorption component at several times 10 km s$^{-1}$ due to the cool-mass ejection was predominant after the solar flare, and the spatially integrated H$\alpha$ E.W. showed enhanced absorption (Figure 6.6A). Later, the blue-shifted component decelerated and gradually turned into slow, red-shifted absorption (Figure 6.6B-C). The H$\alpha$ E.W. returned to the pre-flare level in about 30 min (Figure 6.6A). Although the energy scales and velocities are different, these spatially integrated spectra of the solar mass ejection remarkably resemble the spectral changes of the superflare on EK Dra, which supports the suggestion that the observed changes in the stellar absorption spectral change are a signature of a mass ejection similar to a solar one. In addition, the drifted absorption component in time-velocity plane seen in Figure 6.6B is caused not only by the free-falling under the gravity gradient but also by the change in visibility of the dominant plasma caused by the disappearance of the initial fast component, both of which can be possible explanations for the similar spectral changes seen in the stellar case (Figure 6.2C-D)

### 6.3.3 Velocity, mass, and kinetic energy I: stellar data

For the stellar mass ejection, the velocity is derived by fitting the absorption spectra obtained by Seimei telescope with the normal distribution $N(\lambda, \mu, \sigma^2)$ where $\mu$ is the mean wavelength and $\sigma^2$ is the variance. Although the Nayuta telescope has better spectral resolution than the Seimei telescope, the time resolution and signal to noise is worse and spectral shape is more complex; therefore we used the data of the Seimei telescope to derive the velocity. In Figure 6.3A, we plotted the temporal evolution of the velocity ($(\mu - \lambda)/\lambda \times c$, where $\lambda$ is 6562.8 Å, $c$ is light speed) for the fitted absorption feature with the width of $\sigma$. We only plotted the data whose absorption features are clear enough to fit the shape with the threshold of the fitted absorption amplitude $> 0.01$ and fitted velocity dispersion of $< 500$ km s$^{-1}$ and $> 100$ km s$^{-1}$. The threshold was determined by try and error and we found many miss detection of absorption features except for this threshold. The value of 0.01 can be detected enough by the typical S/N$\sim$170 of the Seimei Telescope/KOOLS-IFU, and the lower limit of 100 km s$^{-1}$ is determined not to detect the sharp noisy signals. About 27% were discarded due to this threshold from the initial points (22 min) to final points (110 min), especially for the latter decaying period. The

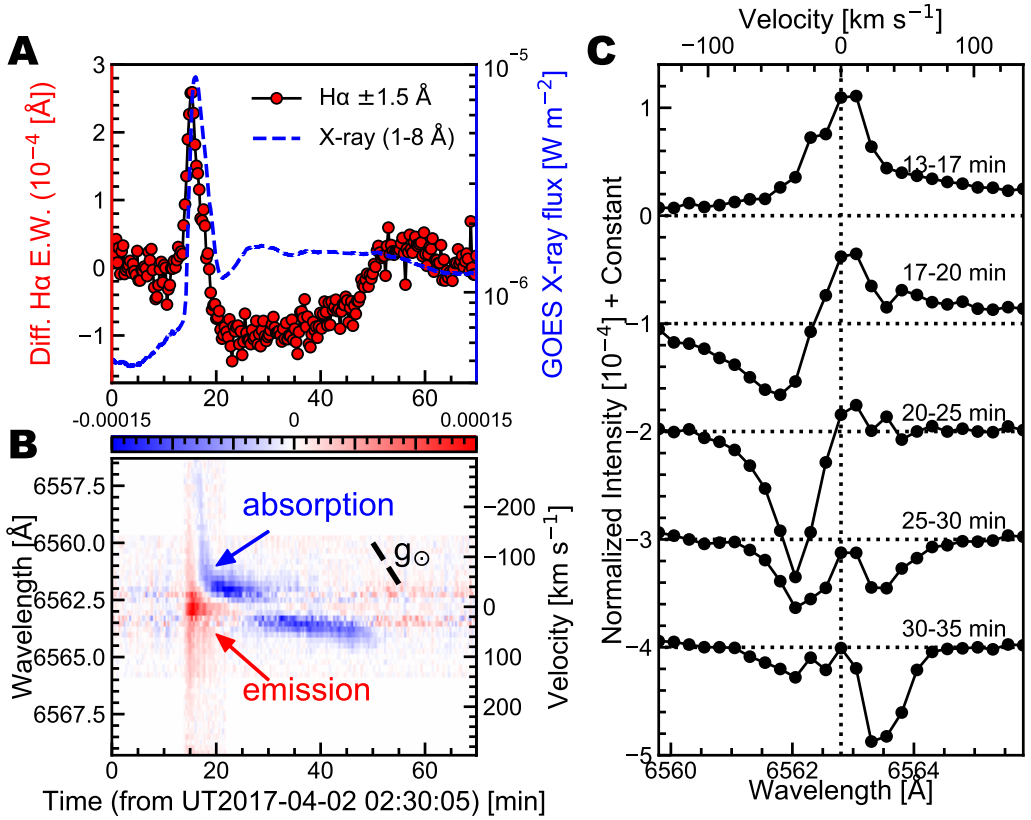


Figure 6.6: The space-integrated light curves (A) and spectra (B-C) of a C8.0-class solar flare and cool-mass ejection on April 2, 2017, observed with the SMART telescope. **(A)** GOES soft X-ray (1-8 Å) and H$\alpha$ E.W. light curves of the solar flare are plotted as a blue dashed line and red circles, respectively. The H$\alpha$ emissions were integrated within $\pm$1.5 Å from the H$\alpha$ line centre (6562.8 Å) and were divided by the full-disk continuum level, and the pre-flare level is subtracted. Time 0 is 14 minutes before the flare begins. **(B)** Two-dimensional pre-flare-subtracted H$\alpha$ spectra. The red and blue colours correspond to emission and absorption compared to the pre-flare levels, respectively. The dashed line indicates surface gravity at the solar surface. For the period from 02:43:50 to 02:51:44, the full 73 wavelengths were available, while for the other periods, only 25 images from the H$\alpha$ line centre $-$3.0 Å to the H$\alpha$ line centre +3.0 Å are available in the archival database (the white regions in the four corners). **(C)** Temporal evolution of the pre-flare-subtracted H$\alpha$ spectrum, shifted vertically by constant values for clarity. The H$\alpha$ spectra were produced by integrating the data over a large enough region to cover the flaring area. The intensities are normalized by the total solar continuum level. The vertical dotted line indicates the H$\alpha$ line centre, and the horizontal dotted lines indicate the zero levels for each spectrum.

blue symbols are fitted with the exponential function indicated with the green line, and it is converted to the deceleration rates plotted in Figure 6.3B. For reference, we also plotted the velocity evolution for the simple free fall with magenta lines. Here, the maximum velocity and its errors are calculated as 510±120 km s$^{-1}$ with its width of 220±90 km s$^{-1}$ from the mean values of the $\mu$ and $\sigma$ of the first five points (t = 22-26 min in Figure 6.2), respectively. The mean values of the velocity when the absorption becomes strong (t = 25-50 min in Figure 6.2) is estimated as 258 km s$^{-1}$.

The plasma mass is simply calculated from the total H$\alpha$ E.W.. We used the simple Becker's cloud model (Mein & Mein, 1988) with optical depth at the line centre of the ejected plasma $\tau_0$ of 5 (a bit optically-thicker case than solar mass ejections; c.f., (Odert et al., 2020)), the two-dimensional aspect ratio of 1 (i.e. cubic), local plasma dispersion velocity $W$ of 20 km s$^{-1}$, and source function $S$ of 0.1 based on the solar observations (Sakaue et al., 2018). The observed half width of 220 km s$^{-1}$ of the stellar blue shifted component is larger by one order of magnitude the solar value, but here we use the solar value as a template. The dispersion velocity of 220 km s$^{-1}$ is considered to be the upper limit of the local velocity dispersion because the ejected mass would have the complex two-dimensional velocity distribution which can lead to larger $W$ in the integrated spectra. First, modeled E.W. of enhanced absorption is calculated by using the Becker's cloud model when the plasma velocity $v_{\rm shift}$ is $-$ 258 km s$^{-1}$ as

$$\text{model} \quad \text{E.W.} \quad = \quad \int_\lambda \frac{I_{0\lambda} - I_\lambda}{I_{0,\text{Cont.}}} d\lambda = \int_\lambda \frac{S - I_{0\lambda}}{I_{0,\text{Cont.}}} \left(1 - e^{-\tau_\lambda}\right) d\lambda \tag{6.2}$$

$$\tau_\lambda \quad = \quad \tau_0 \text{exp} \left[ -\frac{1}{2} \left( \frac{\lambda/\lambda_0 - (1 + v_{\rm shift}/c)}{W/c} \right)^2 \right], \tag{6.3}$$

where $I_{0\lambda}$ is background intensity and $I_{0,\text{Cont.}}$ is continuum intensity. This is the E.W. value for an extreme case when the full disc of the star is totally covered with absorption cool ejected plasma. By comparing the modeled E.W. (Eq. 6.2) with the lowest observed stellar E.W. value of $-0.16$ Å (integrated for H$\alpha$ - 20 Å $\sim$ H$\alpha$ + 10 Å), the cool-plasma filling factor compared to the stellar disc is calculated to be 5.9 % of stellar disc (i.e. modeled E.W./observed E.W.; $Area$ = $1.6\times10^{21}$ cm$^2$). Using the length scale of the ejected plasma $3.9\times10^{10}$ cm (= $Area^{0.5}$), the hydrogen column density is derived as $4.0\times10^{20}$ cm$^{-2}$ from the assumed optical depth based on the plasma model (Tsiropoula & Schmieder, 1997). By multiplying the hydrogen column density by the ejection area, we then obtained the plasma mass as $1.1\times10^{18}$ g. If the two-dimensional aspect ratio becomes 0.1 like jet-like feature (x-width:y-width:z-depth = 1:0.1:0.1), then the estimated mass becomes larger by a factor of 1.78. If optical depth is ranging from 0.8 to 10 (Odert et al., 2020), the source function takes values of 0.02 or 0.5, and the dispersion velocity takes 10 or 220 km s$^{-1}$ (Sakaue et al., 2018), the estimated masses change by a factor of from 0.15 to 4.9. In the following discussions, we used the mass of $1.1^{+4.2}_{-0.9}\times10^{18}$ g for optical depth of 5, and uncertainties of the model (0.15-4.9) is used as the error bars

since the model-based errors are expected to be much larger than the observational errors. The plasma kinetic energy is then calculated as $3.5^{+14.0}_{-3.0}\times10^{32}$ erg by using the velocity of 258 km s$^{-1}$. The observed maximum velocity was 510 km s$^{-1}$ in the early phase, so the kinetic energy can be larger by a factor of 4 although the absorption component was weak at that time.

### 6.3.4 Velocity, mass, and kinetic energy II: solar data

For solar surge observed with SMART/SDDI, we applied the Becker's cloud-model fitting, and derived the surface distributions of ejected mass at a given time of 2 April 2017 03:18:59UT. Figure 6.7 shows the detailed result of the could-model fitting for solar cool-mass ejection. The detailed methods of the cloud model is described in previous studies (Sakaue et al., 2018). As a result of the fitting, the $\tau$-weighted radial velocity is $-31$ km s$^{-1}$, source function is 0.22, and velocity dispersion of 18 km s$^{-1}$ with the mean optical thickness of 0.73. The estimated values of almost all points are in good agreements with the previous study of a solar surge (Sakaue et al., 2018). The distribution of the hydrogen column density is derived from the optical depth and its spatial scale ($2.1\times10^9$ cm) (Tsiropoula & Schmieder, 1997). The plasma mass and kinetic energy are then calculated as $5.1\times10^{14}$ g and $8.5\times10^{27}$ erg, respectively. The kinetic energy is the lower limit because we only considered the line-of-sight velocity, but it would be enough to compare with stellar events. For a comparison with the stellar ejected-mass estimation, we calculated the mass for the solar surge only from the spatially-integrated H$\alpha$ E.W. of $1.0\times10^{-4}$ Å (Figure 6.6A) under the same assumption of the stellar data. As a result, the mass derived only from the H$\alpha$ light curve is estimated to be $3.3\times10^{14}$ g, which is in good agreement with that derived from spatially-resolved analysis within the above model errors (0.15-4.9). This validates our model to estimate the stellar ejected mass.

As for the other solar prominence eruption and surge data plotted in Figure 6.8, the mass, kinetic energies of solar erupting plasma are also plotted whose data are taken from previous studies (Jain & Sorathia, 1987; Liu & Kurokawa, 2004; Ohyama & Shibata, 1999; Christian et al., 2015). The data and references are summarized in Table S6.1. For these flares, we assumed that bolometric energies of B, C, and M class solar flares are $10^{28}$, $10^{29}$, and $10^{30}$ erg from observational estimates of solar flare energies (Emslie et al., 2012; Kretzschmar et al., 2010; Namekata et al., 2017b). The statistical studies of the relation among prominence mass, prominence kinetic energy, and flare energy are now lacking, and more Balmer-lines observations of solar prominence eruptions will be helpful for the understandings of the stellar events.

Table 6.1: Properties of solar cool-mass ejection reported on previous studies.

| Date yyyy/mm/dd | GOES | flare energy [$10^{29}$ erg] | mass [g] | kinetic energy [erg] | reference | event |
|---|---|---|---|---|---|---|
| 1980/10/30 | C4.8 | 4.5 | $10^{14-15}$ | $3.14\times10^{28}$ | Jain & Sorathia (1987) | surge |
| 2001/8/30 | C5.8 | 5.5 | - | $1.4\times10^{27}$ | Liu & Kurokawa (2004) | surge |
| 1993/5/14 | M4.4 | 44 | $10^{15}$ | $1.5\times10^{29}$ | Ohyama & Shibata (1999) | filament eruption |
| 2012/2/11 | C2.7 | 2.7 | $4\times10^{11-13}$ | $2\times10^{28}$ | Christian et al. (2015) | filament eruption |
| 2017/4/2 | C8.0 | 8.0 | $5.1\times10^{14}$ | $8.5\times10^{27}$ | This study | surge |

### 6.3.5 Ejected mass and kinetic energy as a function of flare energy

In Figure 6.8, the data of CME mass and kinetic energy as a function of flare energy are plotted (Drake et al., 2013). The flare energies are originally given by GOES X-ray energies in 1-8 Å ($E_{\mathrm{X,\,GOES}}$), and they are converted to the bolometric energies under the assumption of $100 \times E_{\mathrm{X,\,GOES}}$. This is because the statistical study of solar flares shows that the GOES X-ray band radiates only 1 % of the bolometric energy (≈white-light energy) (Emslie et al., 2012). The relation mass and flare energy are empirically derived as $M \propto E^{0.59\pm0.02}$ (Drake et al., 2013), where $M$ is mass. On the other hand, the relation between mass and peak GOES X-ray flux (that is, the best-used flare energy scale) has been reported by the different authors (Aarnio et al., 2012). The relation between mass and flare energy are empirically derived as $M \propto E^{0.7\pm0.05}$ (Aarnio et al., 2012) under the assumption that bolometric energies of B, C, and M class solar flares are $10^{28}$, $10^{29}$, and $10^{30}$ erg (see Chapter 4; Emslie et al., 2012; Kretzschmar et al., 2010; Namekata et al., 2017b). Both scaling laws are plotted in Figure 6.8A, although the plotted data are taken from (Drake et al., 2013) here. Stellar ejected mass is well described by the latter scaling law (Aarnio et al., 2012), but is relatively more massive than expected from the former scaling law (Drake et al., 2013). Theoretically, the relation between mass and flare energy is derived as $M \propto E^{2/3}$ (Takahashi et al., 2016). which is consistent with both scaling low.

Based on the H$\alpha$ absorption components seen in the EK Dra spectra, the ejected mass is calculated to be $1.1^{+4.2}_{-0.9}\times10^{18}$ g, which is larger than the largest solar mass ejections. This mass estimate corresponds to those predicted from empirical and theoretical solar scaling relations (Aarnio et al., 2012; Drake et al., 2013; Takahashi et al., 2016) between ejected mass and flare energy within the error bars [$\sim 9.4^{+3.2}_{-2.4} \times 10^{16}$ and $3.1^{+1.6}_{-1.1} \times 10^{17}$ g for Drake et al. (2013) and Aarnio et al. (2012), respectively] (Figure 6.8A). This suggests a common relationship between flares and mass ejections of small-scale solar and huge-stellar explosions (i.e. the release of magnetic energy; Shibata & Magara, 2011). This common relation also enables us to estimate the properties of huge stellar mass eruptions based on the empirical solar models (Aarnio et al., 2012; Drake et al., 2013).

Moreover, the kinetic energy is calculated to be $3.5^{+14.0}_{-3.0}\times10^{32}$ erg. Unlike the ejected

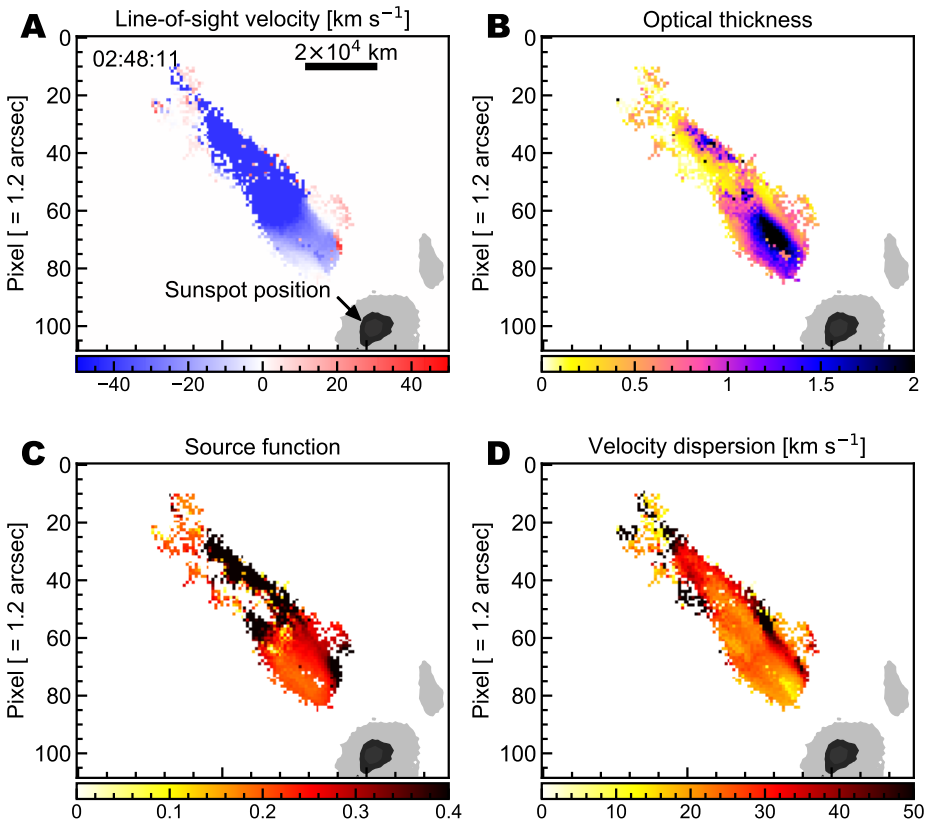


Figure 6.7: Spatial distribution of parameters of the solar cool-mass ejection (solar surge). The spatial distribution of line-of-sight velocity, optical depth, source function, and velocity dispersion for the solar surge in Figure 6.8 and Figure 6.5 is plotted in panel **(A)**, **(B)**, **(C)**, and **(D)**, respectively. Only the cool-plasma regions having enough large area are shown here. Also, black and gray region is the simplified spot umbra and penumbra, respectively. The horizontal and vertical axes represent the x-y plane on the solar disc in the unit of pixel where one pixel corresponds to 1.2 arcsec.

mass, the kinetic energy is 1-2 orders of magnitude smaller than those extrapolated from the solar CME scaling law (Drake et al., 2013) (Figure 6.8B). This trend is common with other mass-ejection candidates (Moschou et al., 2019) and it has been argued that velocity and kinetic energy can be reduced by overlying magnetic fields related to gigantic star spots (Waite et al., 2017; Alvarado-Gómez et al., 2018; Moschou et al., 2019). However, in the solar cases, it is known that the velocities of low-temperature plasma ejections can be much slower than those of the corresponding outer-layer CMEs (Gopalswamy et al., 2003), and the reported kinetic energies of low-temperature plasma ejections are actually 1-2 orders of magnitude smaller than the scaling law (Drake et al., 2013) (Figure 6.8B). By analogy, there is a possibility that the kinetic energy of this stellar event may be the same as–or possibly larger than–the radiated energy (Emslie et al., 2012).

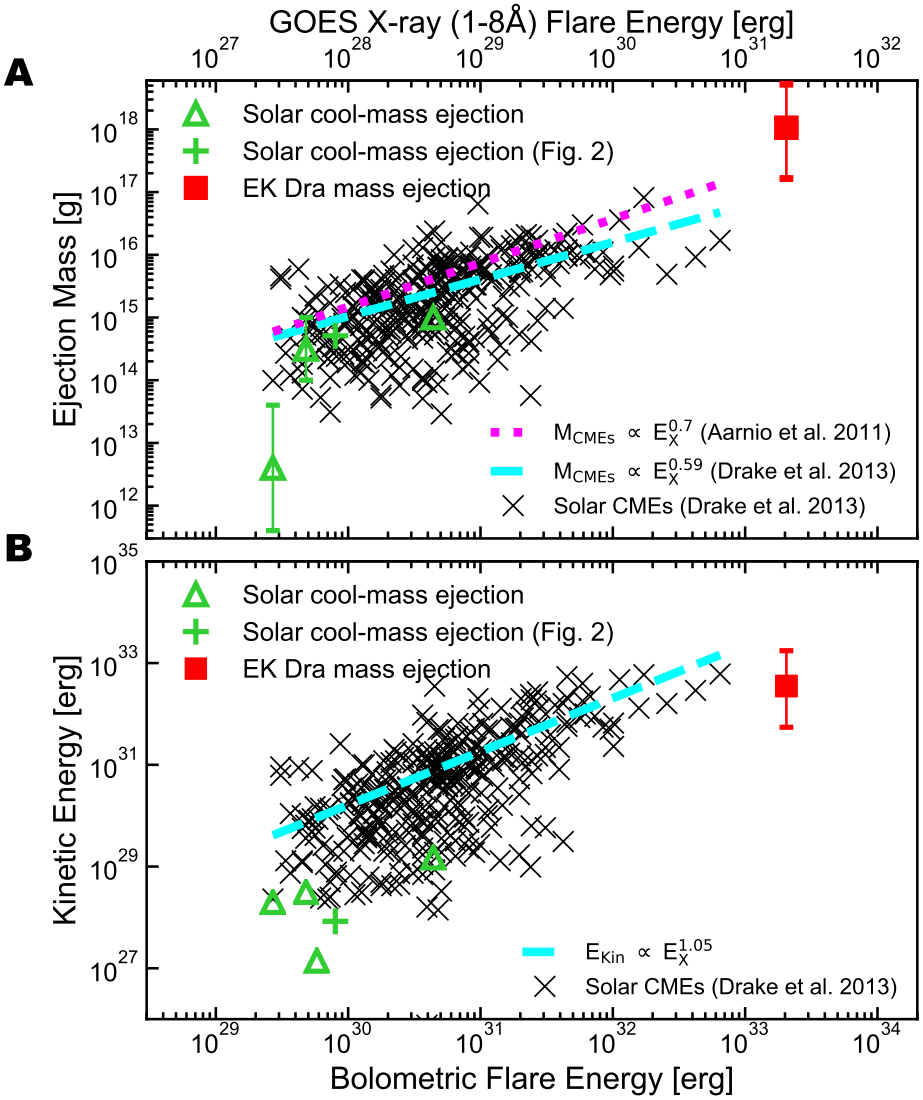


Figure 6.8: Ejected mass and kinetic energy as a function of flare energy for solar and stellar flares. **(A)** Comparison between bolometric flare energy and ejected mass. The red square represents the superflare on EK Dra, the black crosses are data for solar coronal mass ejections, the green triangles are data for solar cool-mass ejections, and the green plus sign represents the solar cool-mass ejection displayed in Figure 6.6 (see Methods for details). The cyan dashed and magenta dotted lines are fits for solar coronal mass ejections expressed as $M_{\rm CMEs} \propto E^{0.59}$ and $M_{\rm CMEs} \propto E^{0.7}$, respectively (see Methods). **(B)** Comparison between flare bolometric energy and ejection kinetic energy. The symbols are the same as in panel **(A)**. The cyan dashed line is a fit for solar coronal mass ejections expressed as $E_{\rm Kin} \propto E_{\rm X}^{1.05}$.

## 6.4 Discussion

### 6.4.1 The source of blue-shifted absorption components

The blue-shifted absorption component on EK Dra cannot be explained other than by a mass ejection from solar-flare observations (Shibata & Magara, 2011). The hypothesis that the blue-shifted absorption on EK Dra might come from upward or downward dynamics in flare kernels must be rejected because they never show H$\alpha$ absorption (Švestka et al., 1962; Ichimoto & Kurokawa, 1984). Also, absorptions from downward flows in cooled flaring magnetic loops (known as post-flare loops; Schmieder et al., 1987) are red shifted, so they cannot explain the blue-shifted components. [However, the observed red-shifted absorption on EK Dra in the later phase might be caused by post-flare loops (Schmieder et al., 1987).] Rotational visibilities of prominences or spots also are not adequate to explain the high velocity, since the rotation speed of EK Dra is only 16.4$\pm$0.1 km s$^{-1}$ (Waite et al., 2017). Thus, we conclude that the stellar blue-shifted absorption component obtained here is the clear evidence for a cool-mass ejection associated with a superflare on a solar-type star.

### 6.4.2 Comparison with the previous studies

Observational signatures for stellar mass ejection have been reported previously for cooler red dwarfs (Honda et al., 2018; Vida et al., 2016) and evolved giant stars (Argiroffi et al., 2019). The previous studies are well summarized in Moschou et al. (2019). The observation of a giant star shows a blue-shifted X-ray emission line of 90 km s$^{-1}$ in post-flare phase and hotter-coronal mass ejections is proposed as a possible explanation (Argiroffi et al., 2019).

In M-dwarf flares, many blue-shifted Balmer line emission components have been reported. However, its interpretations and the relation with solar mass ejections have been quite controversial. This is mostly because no absorption component has been found like solar cool-mass ejection (Honda et al., 2018; Vida et al., 2016) and it is difficult to distinguish from emissions of upward/downward dynamics in chromosphere and/or coronal loop materials.

The number of studies reporting highly-time-resolved velocity variations have been still lacking ($\sim$5-min cadence at the shortest Honda et al., 2018; Vida et al., 2016)) and simultaneous photometry has never been carried out, which prevents us from revealing whether the signatures are related to ejections. Thus, our highly time-resolved ($\sim$50-sec cadence), blue-shifted absorption spectra combined with *TESS* photometry constitutes an unpreced-

ented dataset. In addition, the detailed comparisons with solar events and detections by two different telescopes confirmed the reliability of the detection.

### 6.4.3 How did the stellar mass ejection travel through interplanetary space?

The maximum observed velocity $\sim$-510 km s$^{-1}$ of the blue-shifted component (or up to $\sim -720$ km s$^{-1}$ by considering projection factor of $1/\cos 45^\circ \sim 1.4$) is larger than the typical velocities of solar prominence eruptions (10–400 km s$^{-1}$ Gopalswamy et al., 2003), while it is a little smaller than the escape velocity at the surface ($\sim$670 km s$^{-1}$ Osten & Wolk, 2015). It is estimated that the cool plasma has reached at least $\sim$1.0 stellar radii from the stellar surface (or the initial height) as derived by integrating the velocity over time (or, $\sim$3.2 stellar radii from the stellar surface based on the deceleration rates).

Here we discuss a possibility that the mass is ejected far away. According to the solar cases, how far the ejected mass travels is difficult to estimate just from this cool-plasma observation, because the outer coronal mass ejections (CMEs, with low-density and millions-of-Kelvin-temperature outer layer) are 4–8 times faster than their cool-plasma counterparts (Gopalswamy et al., 2003). In addition, the neutral plasma that emits the H$\alpha$ line gradually accelerated and heated, becoming invisible in H$\alpha$ at several solar radii (still visible in continuum as CME cores Gopalswamy et al., 2003). By these analogy, velocities of some high-speed invisible components in the EK Dra eruption can exceed the escape velocity, although the weak, slow red-shift components in the final phase indicates some masses are going to fall back.

Moreover, our successful measurement of the changes in velocity affords the potential to speculate about what the ejection looks like and how it is affected by the surrounding magnetic field (Alvarado-Gómez et al., 2018; Kay et al., 2019; Airapetian et al., 2016). The deceleration was 10 %–20 % larger than the stellar atmospheric gravity (Figure 6.3B). This may be due not only to high-speed components becoming invisible in H$\alpha$ and low-speed components gradually becoming more dominant, resulting in the apparently high deceleration, but also it may be caused by a large-scale dipole magnetic field slowing down the ejected mass (Alvarado-Gómez et al., 2018).

## 6.5 Conclusion

In this study, the time-resolved optical spectra of a stellar superflare have been successfully on solar-type stars for the first time. By comparing solar observations, we conclude that a huge and fast cool-mass ejection occurred in association with a superflare on the young

solar-type star EK Dra. The detection of mass ejection is the first for the solar-type stars. It is also indicated that some basic nature (e.g. mass) can be understood by analogy with solar observations and models.

The reliability and novelty of our detection can be regarded as prominent because of the following reasons:

- The highest time resolution ($\sim$ 1 min) of spectra among studies reporting signatures [often more than $\sim$5 min for optical line observations; and up to half a day for the X-ray paper (Argiroffi et al., 2019)]
- The multi-wavelength observations in H$\alpha$ and optical continuum. Maehara et al. (2020) performed optical and H$\alpha$ observations, but they cannot detect optical flares.
- The confirmations by two different telescopes in different site.
- The first detection on a solar-type star (G-type main-sequence star).

It is also notable that we detected higher velocity than typical solar cool-mass ejection with eruptive CMEs, although whether it is ejected far away was not directly confirmed. Simultaneous observations with hotter lines may enable us to detect the cool and hot ejected plasma in future (cf. a key problem listed in Section 7.2)

Our findings have important implications to two important astronomical topics:

- its effect on the planet around solar-type stars (e.g. the young and current Sun),
- the stellar mass evolution of solar-type stars.

Young solar-type stars are known to have a very high frequency of superflares (Maehara et al., 2012; Notsu et al., 2019; Güdel, 2007; Ayres, 2015; Audard et al., 1999; Osten & Wolk, 2015), which may have a significant impact on exoplanet atmospheres and habitability (Airapetian et al., 2016, 2020; Alvarado-Gómez et al., 2018; Kay et al., 2019). In addition, it has been suggested recently that superflares may occur even on the current Sun although the frequency is once in several thousand years (Maehara et al., 2012; Notsu et al., 2019; Shibata et al., 2013; Miyake et al., 2012). Therefore, as possible future studies, our findings not only can provide a proxy for huge mass ejections on the young Sun, enabling us to evaluate the effects on the ancient, young Solar-System planets, but also provide a proxy for possible extreme events on the current Sun, which can contribute to research in space-weather prediction. For example, by comparing with simulations (Airapetian et al., 2016) and solar empirical relation (Takahashi et al., 2016), the kinetic energy or high energy particles injected to exoplanet atmosphere can be modeled (Airapetian et al., 2016).

Furthermore, the mass-loss rate due to CMEs on EK Dra has been estimated to be more than $\sim 10^{-12}$ solar mass yr$^{-1}$ (Osten & Wolk, 2015), based on the flare-energy/ejected-mass relation (Aarnio et al., 2012; Drake et al., 2013) shown in Figure 6.8A, while the current solar mass-loss rate is $10^{-14}$ solar mass yr$^{-1}$. Our findings validate this estimate of ejection-related stellar mass loss, which can significantly affect the evolutionary theory of stellar mass, angular momentum, and luminosity (Osten & Wolk, 2015; Aarnio et al., 2012), although the mass-loss values can be an upper limit depending on the association rates. Both the revised stellar luminosity evolution and the proposed generation of greenhouse gases or prebiotic compounds by CME-related particles (Airapetian et al., 2016, 2020) may greatly impact the origins of life on planets.

CHAPTER 7

# Concluding remarks

## 7.1 Conclusion

I first summarize the advantages in my approaches in this thesis. The keyword of my approaches is "time evolution" of extreme stellar magnetic activities. In Chapters 2, 4, and 6, long-term and high-cadence observations by the *Kepler*/*TESS* optical photometry enabled studies of the mid-term spot evolution ($\sim$several hundreds of days) and the rare and short stellar superflare evolution, which have been difficult to obtain from ground/space-based telescopes before the *Kepler*/*TESS* era, especially for solar-type stars*. My strategy in Chapters 2, 3, and 6 (and partly Chapter 4) therefore takes the advantages of the *Kepler*/*TESS* dataset stored in this decade, and the research focusing on solar-type stars are one of the originalities that cannot be achieved without the *Kepler*/*TESS* data. In Chapters 5 and 6, ground-based monitoring observations by the 3.8-m Seimei Telescope, sometimes combined with *TESS* photometry, give us an opportunity to study the highly time-resolved spectroscopic features of stellar superflares not only on solar-type stars but also on cooler M-dwarfs. Since the long-term monitoring observations are costly for other open-use 4-m class telescopes in the world, the high-time-cadence ($\sim$1 min) monitoring observations and plenty of observational times realized here are the advantages in investigating the evolution of the rare and rapid stellar events. In addition, throughout this thesis (cf. Chapters 2$\sim$6), the idea of solar-stellar connection is one of the unique points that bridges the solar physics to stellar observations.

This thesis mainly aimed at whether the extreme stellar magnetic activities can be explained by solar physics established by observations of smaller-scale phenomena on the Sun. Throughout this thesis, it can be concluded that most of the stellar extreme magnetic

*In this thesis, 'solar-type stars' usually mean G-type main-sequence stars with the effective temperature of 5000-6000 K unless additional description is accompanied. The word of 'Sun-like star' means a solar-type star having an old age ($\sim$4.5 Gyr) and slow rotation ($P_{\rm rot} > 20$ days). The word of 'young solar analog' is used for a solar-type star that is very young but has stellar properties similar to the young Sun (it is sometimes described as 'young solar-type star' in Chapter 6). See also the same footnote* in Chapter 1.

activities occur possibly in the same process of the solar counterparts, although the values of physical parameters are different (e.g. scales, magnetic field strength). The main results newly obtained here are summarized as follows:

**(i)** The gigantic star spots with large area ($\sim$10 times larger than the largest sunspots) on solar-type stars can emerge and decay in the same way as sunspots (i.e. emergence from the stellar interiors and decay due to the convection motion). The unified understanding was obtained by my original and first approach to measure the variation rates of star-spots area on solar-type stars in comparison with those of sunspots. This result supports a hypothesis that the magnetic fluxes of gigantic spots are generated inside the star like sunspots (Chapters 2 and 3).

**(ii)** The superflares on solar-type stars can occur through the magnetic reconnection as in the solar flares, although the length scales and magnetic field strength can be largely different from solar ones. This conclusion was obtained from the first direct comparison between solar flares and superflares on the solar-type stars in the "white-light" wavelength. It is suggested that the length scales and magnetic field strength can be indirectly estimated only by the optical photometry on the basis of the magnetic reconnection theory. Based on the theory, it is indicated that the observed superflares on solar-type stars have the magnetic fields of $\sim$200 G ($\sim$3 times the typical solar flares) and length scales of $10^{\sim 10-11}$ cm (up to $\sim$stellar diameter) (Chapter 4).

**(iii)** The optical emissions of the superflare on the M-dwarf AD Leo can be explained by the following model: the non-thermal electrons are injected into the chromosphere and increase the electron density. This picture is consistent with solar observations and recent stellar observations using other wavelengths (Kowalski et al., 2016, 2017). The high-energy electrons are estimated to have the properties of hard spectra ($\delta$=3 in the energy spectra of $\mathrm{d}N/\mathrm{d}E \propto E^{-\delta}$, while the typical value is $\delta$=3-7 in solar cases) and large fluxes (10-100 times of the typical solar value). In addition, the energy injections are found to be changed to the heating with smaller fluxes or thermal-soft spectra in the decay phase of the superflare. The dynamic changes in heating properties during the superflare are shown with the unprecedented high-quality and high-cadence data, which will be helpful for studies on particle accelerations in reconnection sites (Chapter 5).

**(iv)** Stellar mass ejections on the young solar analog* EK Dra was detected by the time-resolved H$\alpha$ spectra. This is the first detection of mass ejection as well as optical spectra of superflares for solar-type stars. The observational spectra and estimated physical quantities share the same properties as solar mass ejections. This indicates the stellar mass ejections occur possibly in the same way as solar cases, although the mass is 10-100 times larger than the largest solar CMEs. The stellar mass ejection

is very helpful to estimate its impact on the exoplanet habitability and stellar mass evolutions, and it is therefore important for the planetary physics and general stellar evolution physics (Chapter 6).

These results provided the universal understandings of small-scale solar magnetic activities and large-scale stellar ones from various perspectives. I consider that the universality of the solar MHD model partly supported here is also meaningful for the general plasma physics.

As for the above results (i)-(iv), possible implications to solar and stellar physics are summarized as follows: The obtained result (iii) can be related to the unified understandings of particle acceleration in solar and stellar flares, which is one of the mysteries in general astrophysics. Also, the result (iv) can mean the significant mass loss on the young Sun (cf. Osten & Wolk, 2015), which is important for general stellar evolution physics. In addition, the universality of the spot and flare mechanism on the Sun and active solar-type stars (cf. (i)-(iii)) can support a hypothesis that the Sun can produce gigantic sunspots and superflares in the same way as smaller events, if the large magnetic fluxes can be generated inside the Sun (see Section 1.2.3). However, for now, the basic assumption of how the sources of the magnetic energy are generated (and stored) inside stars are poorly known (cf. Shibayama et al., 2013; Reinhold et al., 2020). Is the stellar dynamo process the same as that of the Sun? Although this is a very complicated problem, the answer to this question will lead to a very important question for us "Can superflare occur on the Sun?".

One of my aims in this thesis is to investigate the properties of extreme stellar magnetic activities that can be related to the exoplanet habitability (Section 1.3). According to the results in this thesis, it can be also concluded that the huge stellar events can affect the surrounding environment more severely than we experience in the solar system. The important results obtained in this thesis for this topic are summarized as follows:

**(v)** The gigantic star spots (groups) that can potentially produce superflares are found to last from 100 days up to $\sim$1 year, which indicates the extreme space weather can continue for such long periods once the large star spots (groups) emerged, while the periods are typically less than a few months in the case of sunspots. (Chapters 2 and 3).

**(vi)** A large amount of high-energy electrons can be also generated from superflares (Chapter 5). Also, the impulsivity of superflares is found to be higher than solar flares (Chapter 4). These conditions can produce high XUV radiations that severely affect the planet atmosphere (see Airapetian et al., 2020, for review).

**(vii)** Evidence of a huge and fast stellar mass ejection is found to occur on the hyper-active main-sequence star (Chapter 6). This finding is very meaningful because it supports the following possible impact on the exoplanets that have been proposed before: the mass ejection can directly affect the atmospheric erosions in the close-in exoplanets and the CME-related particles can affect the habitability and origin of life on planets (e.g. Airapetian et al., 2016, 2020). Also, it can provide a proxy for possible extreme events on the current Sun (e.g. Maehara et al., 2012; Miyake et al., 2012), which can contribute to research in space-weather prediction (e.g. Kusano et al., 2020).

The results (v)-(vii) provide important informations of real properties of stellar magnetic activities for evaluating its impact on exoplanets, and possibly can provide a proxy for a possible extreme event on the Sun.

I finally introduce the standpoint of this thesis in my overall view. One of the ultimate goals of my study is to know the answer to the general question "How can solar and stellar extreme magnetic activities affect the planet atmosphere, the origin of life, and our human society?". Some problems were addressed in this thesis, but there remain many unsolved problems to answer this question (see Section 7.2 for the detailed future perspectives). Samples with multi-wavelength observations of extreme stellar phenomena has been still lacking for understanding the whole pictures, not only in the optical but also in X-ray, UV, and radio. The coordinated observations are often difficult to perform because of shortness and unpredictability of stellar events. The difficulties have kept us away from the full understanding of stellar extreme events. However, in the past decade, many transient surveys have provided big data which dramatically improve the statistical understanding of stellar magnetic activities (e.g. *Kepler* mission since 2009). Nowadays more and more space X-ray and UV projects are proposed and launched (e.g. NICER since 2017; JAXA's *XRISM* mission; *ESCAPE*, a future EUV satellite by Colorado University). In addition, the nearby optical survey by *TESS* (2018$\sim$) and ground-based telescope (e.g. OISTER in Chapters 5 and 6; Evryscope since 2016, Law et al., 2015) have provided precious opportunities to adjust the multi-wavelength observations. By taking these opportunities, I have just started not only the big-data analysis (Chapters 2$\sim$4) but also the multi-wavelength campaign observations (Chapters 5 and 6). I hope that the results and approaches presented here will greatly advance the solar, stellar, and planetary researches and are helpful for future studies.

## 7.2 Future perspective

Here I overview future perspectives for the main topics presented in this thesis. The following list summarizes several keywords regarding remaining, important problems for star

spots:

- Flare-productive star spots
- Evolution of star spots v.s. flare timing

These questions are raised throughout this thesis (cf. Chapters 2, 3, and 5). Chapters 2 and 3 described the spot emergence/decay mechanism in comparison with sunspot observations. However, the star spot emergence has not been investigated yet in the relation of the occurrence of superflares, which I consider the next step of my study. A significant number of stars have gigantic spots but no superflare (e.g. Namekata et al., 2019; Notsu et al., 2019), indicating another key to trigger the superflares such as emerging fluxes or shear motions. In the case of the Sun, flare-productive sunspots tend to have complex features and large flares are sometimes triggered by the new emergence of magnetic flux from the interior (e.g. Toriumi & Wang, 2019). These insights from the solar observations may help to solve the occurrence condition of stellar superflares by expanding the approach of Chapters 2 and 3 to the *Kepler* superflare stars as a next step. The occurrence condition may be unveiled by multi-wavelength observations of active regions in photospheric, chromospheric, and coronal emissions (cf. Chapter 5), and the investigations of spot evolution by spectroscopic observations with high-dispersion spectroscopy would be also important (e.g. to regularly conduct Doppler Imaging, more preferably, Zeeman Doppler Imaging, cf. Section 1.2.4).

Keywords regarding remaining problems for stellar flares are listed below:

- White-light emission source
- Flare radiation energy budget

Chapters 4 and 5 described the flare occurrence mechanism. However, the origin of white-light flares is still an unsolved problem (even in solar flares; see Chapter 4), and multi-wavelength observations of stellar superflares is lacking. To solve the white-light emission source, broad-band optical to Near-UV (near ultraviolet) spectra need to be characterized (e.g. Kowalski et al., 2013), which can be tried by using the broad-band modes of Seimei Telescope/KOOLS-IFU (Kurita et al., 2020; Matsubayashi et al., 2019). New instruments covering optical to Near-UV and plenty of observational time will be required. In addition, Chapter 5 demonstrates that the energy budget in optical and H$\alpha$ lines can depend on the high-energy electron fluxes ($\sim$flare impulsivity). In order to exactly evaluate the effect of the radiations on the exoplanets, it is necessary to characterize the flare energy budgets by multi-wavelength observations including X-ray, UV, and optical wavelengths.

Keywords regarding remaining problems for stellar mass ejections are listed below:

- Hot-cool mass ejections
- Mass ejection on various types of stars
- Occurrence frequency

In Chapter 6, the stellar mass ejection was detected for the first time on a solar-type star. However, only cool-mass ejection is detected in this thesis, and multi-wavelength observations including hotter lines (e.g. X-ray lines or He lines) are necessary. The relation between hot and cool mass ejections may be able to be characterized by using solar observations by combining the SDDI (see, Chapter 6; Ichimoto et al., 2017) (SMART Telescope at Hida Observatory) and coronagraph as the Sun seen as a star. In addition, most of the detections of mass ejections on other types of stars are still controversial. Multi-wavelength observations (including X-ray, EUV, or radio observations) may be able to unveil the existence of mass ejections on other types of stars. In addition, by solar analogy, the stellar mass ejections do not necessarily accompany superflares, and stellar mass-loss rates and effect on the planets would depend on the occurrence frequency. Recent time-domain astronomy will be able to reveal the occurrence frequency, and I will try this topic by utilizing plenty of observational periods of Seimei telescope.

APPENDIX A

# Supplementary materials in Chapter 2

## A.1 Extended Figures 3.4 for the other observational periods

Figure A.1 and A.2 show the same analyses as Figure 3.4 for *Kepler* quarter 8 to 10 and 12 to 14, respectively. The reconstructed light curve is sometimes consistent with but almost inconsistent with the *Kepler*-30-min light curve. Also, we cannot see positive correlations between in-transit spot area and rotational-modulation spot area. As Lanza et al. (2019) and Davenport (2015) reported, the period of the rotational modulations are slower than that of the equator of Kepler-17 in later quarters, indicating that dominant spots exist out of the transit path.

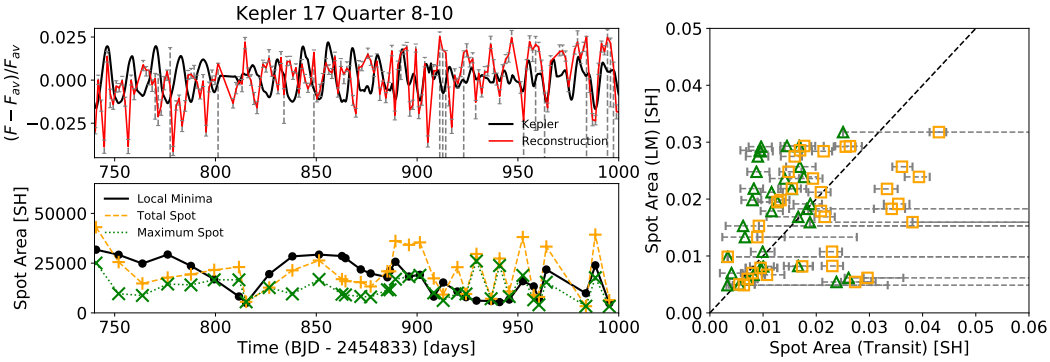


Figure A.1: The same as Figure 3.4, but for Quarter 8-10.

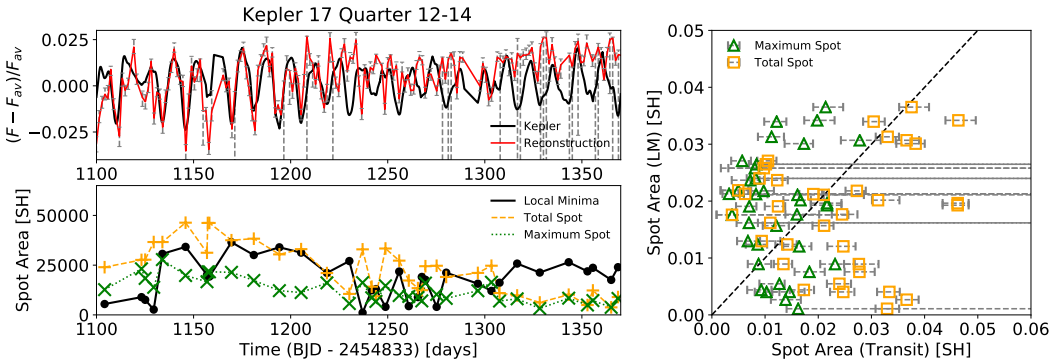


Figure A.2: The same as Figure 3.4, but for Quarter 12-14.

APPENDIX **B**

# Supplementary materials in Chapter 4

## B.1 Validation of Equations 4.7, 4.8

In Chapter 4, we proposed the possibility that the discrepancy of $E$-$\tau$ can be explained by the coronal magnetic field strength, and derived the useful equations. To confirm our suggestions and apply the scaling law to stellar flare observations, we tested the validity of the scaling law on spatially resolved solar flares in our catalogue. The coronal magnetic field $B_{\rm obs}$ and loop length $L_{\rm obs}$ are observationally estimated by using images taken with *SDO*/HMI magnetogram and AIA 94 Å, respectively, and we then compared them with theoretical values ($B_{\rm theor}$, $L_{\rm theor}$) obtained from Equations 4.7 and 4.8. We simply explain the observational method as below. Firstly, flaring regions were defined as the regions with the brightness of AIA 94 Å above 50 DNs$^{-1}$. The loop length scales $L_{\rm obs}$ were defined as square roots of the areas of flaring regions. Secondly, the means of absolute values of photosphetic magnetic field $\bar{B}$ were measured inside the projection of the above flaring area to the photosphere. Using the empirical relation between coronal and photospheric magnetic field ($B_{\rm corona} \sim B_{\rm photosphere}/3$; Isobe et al., 2005; Dulk & McLean, 1978), coronal magnetic field strength $B_{\rm obs}$ were calculated as $\bar{B}/3$. Please refer to Namekata et al. (2017a) for more detail.

The left panel in Figure B.1 is a comparison of the theoretical and observational coronal magnetic field strength. As we expected, there are weak positive correlations between the theoretical and observational estimated magnetic fields. The failure in the power law index may be caused by the rough method of extrapolation of $B_{\rm obs}$ (Namekata et al., 2017a) and the large scattering would be due to the difficulty in accurate measurements of solar WLFs and the contribution of the filling factor to the scaling laws. The right panel in Figure B.1 is the same as the left one for the magnetic loop length ($L$). As one can see, the scaling

law can predict the loop length with a linear relation, which is natural because flare energy and durations are basically determined by the length scales in the case of solar flares.

Although there are positive correlations between the observed values and those estimated by our scaling law, the validity of the scaling laws cannot be completely confirmed, especially for the magnetic field strength. This can be because of the difficulty of the measurement of both physical quantities of solar WLFs and coronal magnetic field strength. As a future study, it is necessary to directly measure stellar magnetic field strengths and compare those estimated from the flare scaling relations.

## B.2 Applications of Equations 4.7, 4.8 to other and future studies

Here we try to apply our scaling relation (Equation 4.7) to other studies and show our prospects for the future stellar observations. Firstly we compared the solar WLFs and flares on a M-type star GJ1243 (Hawley et al., 2014). Figure B.2 is the comparison on the $E$-$\tau$ diagram. Note that the durations are defined as those from the beginning to the end of flares, and the energies are converted into that in the *Kepler* pass band by assuming 10,000 K blackbody. On the basis of our scaling relation (Equation 4.7), the magnetic field strength of GJ 1243 is about 1.7 times stronger than that of solar flares. This is consistent with our understanding that the magnetic field of M-type stars are stronger than that of the Sun. However, the scaling law would not be easily applied in this case because the coronal density is expected to be different from solar atmosphere. Moreover, the emission profile would be expected to be different between solar WLFs and those on M-type stars. It is therefore necessary to investigate the spectral profiles of solar and stellar WLFs as well as stellar atmospheric parameters in detail.

Next let us apply our scaling laws to the previous papers studying the relation between flare energies (or fluxes) and durations. For example, Tsuboi et al. (2016) examined the X-ray flare luminosity ($L$) and its duration ($\tau$) about flares on M-type stars, RS CVn stars and the Sun, and discussed the obtained relations $\tau \propto L^{0.2}$ by using the scaling relation of radiative and conductive cooling. The theories based of radiative/conductive cooling include an uncertainty because X-ray light curves are observed as superpositions of flaring loops which reconnected one after another. If the scaling law (Equation 4.9; $a = 4/7$) is applied, the estimated magnetic field strength of flares on M-type stars, RS CVn stars and the Sun is ranging from 50 G to 500 G and predicts the stronger magnetic field strength on M-type and RS CVn stars than on our Sun. This is consistent with the observation that M-type and RS CVn stars tend to show extremely high activities (e.g. Gershberg, 2005) and M-type stars have about three times stronger magnetic field of star spots than our

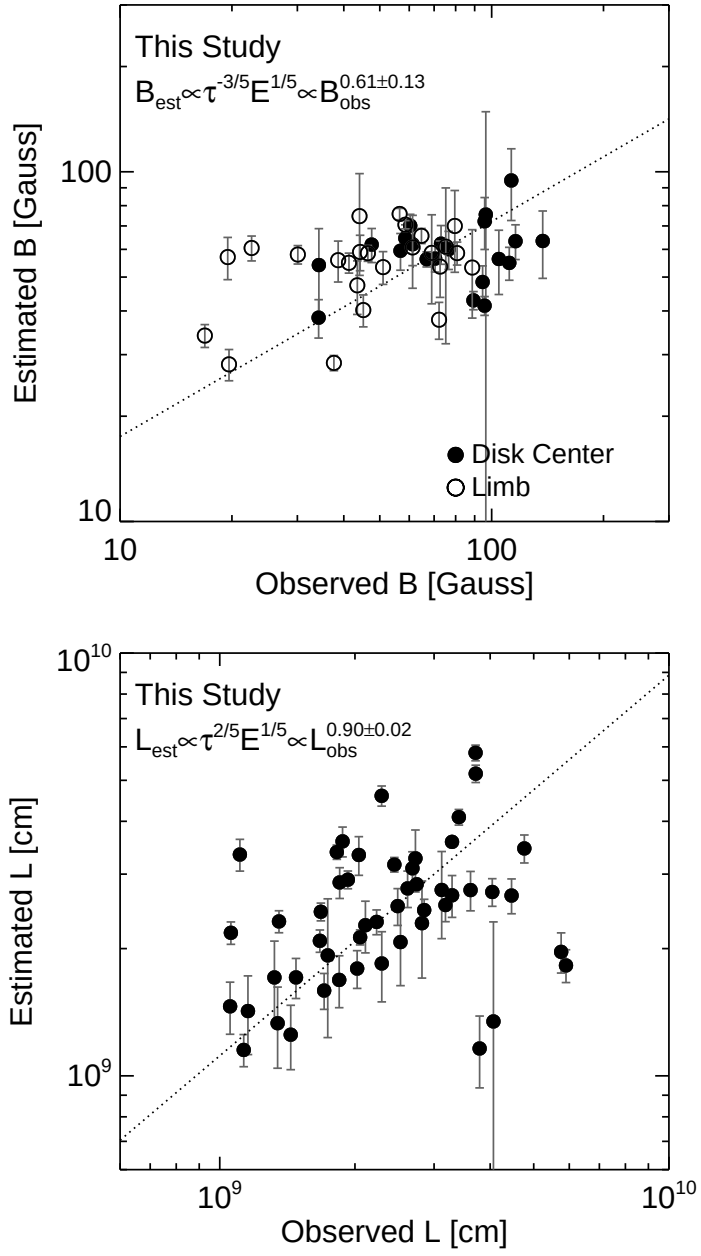


Figure B.1: Comparisons of the theoretical and observational values. The left and right panels show the comparison of coronal magnetic field strengths $B$ and loop lengths $L$, respectively. In the left panel, open circles are flares on the limb (>700) whose magnetic field strength is not reliable. Dotted lines are the fitted lines with linear regression bisecter method. As for the left panel, we fitted the data except for the limb data.

Sun (Johns-Krull & Valenti, 1996). Chang et al. (2015) moreover carried out a statistical study about WLF energy and duration on mid-M stars. The result shows the different distribution on $E$–$\tau$ between nearby M stars (relatively long duration) and open cluster M stars (relatively short duration). This is consistent with our understandings that stars in open clusters are young and then have strong magnetic field strength.

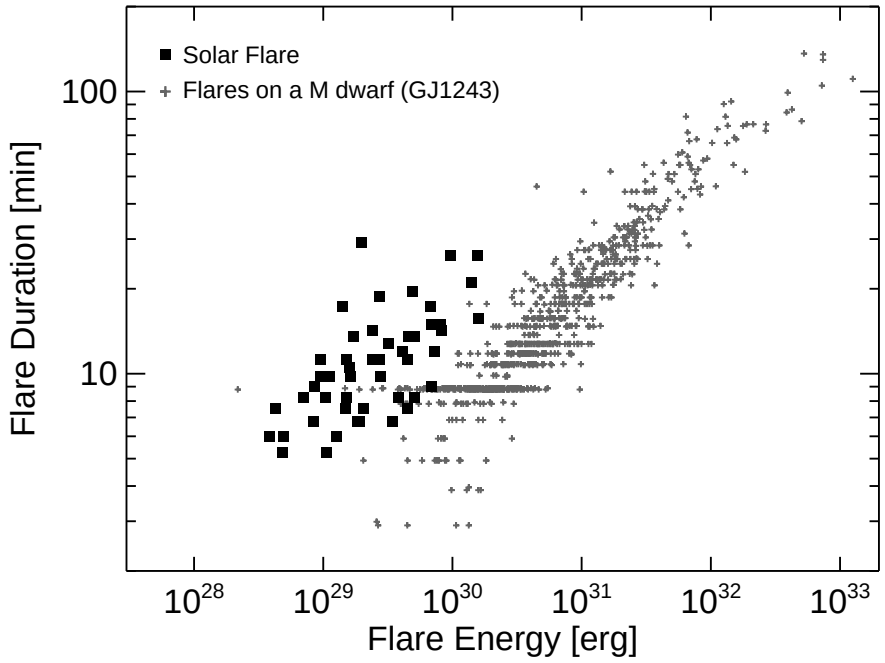


Figure B.2: A comparison between the flare energies and durations for solar and M-dwarf flares. The filled squares are solar WLFs and the gray crosses are flares on a M-type star GJ1243 (Hawley et al., 2014). Note that the durations are defined as that from the beginning to the end of flares, and the energies are converted into that in the *Kepler* pass band by assuming 10,000 K blackbody

As *Kepler* mission have discovered a huge amount of stellar flares, the number of such kind of observations would increase in future (e.g. *TESS*, *PLATO* ; Rauer et al. 2014). In this situation, our scaling law would be helpful for research on stellar activities. The advantage of the scaling law is that only by optical photometry we can estimate physical quantities of unresolved stellar surfaces.

## B.3 List of tables

Here I put the tables for supplementary issues in Chapter 4 like the observational values.

Table B.1: Physical parameters of flares.

| peak time | *GOES* class | Loc.* [deg] | $T_6$† [K] | $EM_{48}$‡ [cm$^{-3}$] | $B_{\rm theor}$§ [G] | $B_{\rm obs}(a)$‖ [G] | $B_{\rm obs}(b)$# [G] | $L_{\rm theor}$§ [$10^9$cm] | $L_{\rm obs}(a)$‖ [$10^9$cm] | $L_{\rm obs}(b)$# [$10^9$cm] | $L_{\rm Reale}$** [$10^9$cm] | $\tau_{\rm SXR}$†† [sec] | $\zeta$‡‡ |
|---|---|---|---|---|---|---|---|---|---|---|---|---|---|
| 2011/02/14-17:26 | M2.2 | S20W04 | 15.5 | 1.2 | 63.7 | 70.0 | 104.7 | 2.2 | 5.2 | 2.0 | 3.9 | 770 | 1.04 |
| 2011/02/15-01:56 | X2.2 | S20W10 | 19.6 | 10.3 | 62.0 | 90.4 | 147.5 | 5.5 | 6.6 | 3.7 | 0.4 | 747 | 0.30 |
| 2011/02/16-07:44 | M1.1 | S19W29 | 14.3 | 0.6 | 63.7 | 121.5 | 180.1 | 1.7 | 3.9 | 1.5 | – | – | – |
| 2011/02/18-10:11 | M6.6 | S21W55 | 18.6 | 3.4 | 71.2 | 81.5 | 129.4 | 3.1 | 4.5 | 1.7 | 0.4 | 233 | 0.42 |
| 2011/02/18-13:03 | M1.4 | S21W55 | 15.7 | 0.8 | 71.3 | 79.7 | 129.9 | 1.7 | 3.5 | 1.4 | 0.2 | 274 | 0.32 |
| 2011/09/23-22:15 | M1.6 | N12E56 | 12.7 | 1.0 | 47.4 | 38.7 | 57.3 | 2.7 | 5.9 | 2.6 | 13.5 | 3209 | 0.97 |
| 2011/11/02-22:01 | M4.3 | N20E77 | 17.2 | 2.1 | 68.2 | 91.5 | 85.7 | 2.6 | 5.2 | 2.5 | – | 1384 | – |
| 2011/11/03-11:11 | M2.5 | N20E70 | 15.9 | 1.3 | 65.6 | 85.0 | 88.1 | 2.2 | 4.7 | 2.2 | 2.7 | 917 | 0.64 |
| 2011/11/03-20:27 | X1.9 | N21E64 | 21.5 | 8.7 | 75.5 | 78.1 | 91.8 | 4.3 | 5.9 | 3.3 | 1.4 | 407 | 0.66 |
| 2011/11/05-03:31 | M3.7 | N20E47 | 15.8 | 1.5 | 63.8 | 82.6 | 112.9 | 2.4 | 7.4 | 4.4 | – | 2209 | – |
| 2011/11/05-20:38 | M1.8 | N21E37 | 17.0 | 0.9 | 79.3 | 114.5 | 130.1 | 1.6 | 4.4 | 2.2 | – | 1427 | – |
| 2011/12/31-13:15 | M2.4 | S25E46 | 17.0 | 1.2 | 74.5 | 75.3 | 98.8 | 1.9 | 3.4 | 1.7 | 1.0 | 352 | 0.61 |
| 2011/12/31-16:26 | M1.5 | S25E42 | 15.1 | 0.9 | 65.9 | 79.5 | 76.8 | 1.9 | 3.7 | 2.2 | – | 636 | – |
| 2012/01/17-04:53 | M1.0 | N18E53 | 14.0 | 0.6 | 61.7 | 55.2 | 46.2 | 1.7 | 4.2 | 1.6 | – | 1429 | – |
| 2012/01/18-19:12 | M1.7 | N17E32 | 14.4 | 1.0 | 59.4 | 76.8 | 81.5 | 2.2 | 4.6 | 1.9 | – | 1476 | – |
| 2012/01/27-18:37 | X1.7 | N33W85 | 15.9 | 9.0 | 44.6 | 17.4 | 37.0 | 7.1 | 9.5 | 6.3 | – | 1480 | – |
| 2012/03/05-04:05 | X1.1 | N19E58 | 18.2 | 5.0 | 63.0 | 51.3 | 63.6 | 4.0 | 7.2 | 4.4 | 1.5 | 2785 | 0.31 |
| 2012/03/06-12:41 | M2.1 | N21E40 | 16.0 | 1.1 | 67.9 | 117.1 | 104.0 | 2.0 | 4.7 | 2.2 | – | 1105 | – |
| 2012/03/06-21:11 | M1.3 | N16E30 | 16.1 | 0.7 | 75.8 | 181.2 | 205.1 | 1.5 | 4.3 | 1.5 | – | – | – |
| 2012/05/07-14:31 | M1.9 | S20W49 | 14.0 | 1.0 | 55.3 | 15.4 | 14.6 | 2.4 | 6.0 | 3.6 | 4.8 | 1777 | 0.66 |
| 2012/05/09-12:32 | M4.7 | N13E31 | 17.8 | 2.3 | 71.4 | 72.2 | 137.5 | 2.6 | 4.4 | 1.8 | 0.6 | 260 | 0.56 |
| 2012/05/09-14:08 | M1.8 | N06E22 | 13.4 | 1.1 | 51.0 | 91.1 | 80.4 | 2.6 | 3.6 | 2.3 | 1.2 | 374 | 0.68 |
| 2012/05/09-21:05 | M4.1 | N12E26 | 17.7 | 2.0 | 72.5 | 83.8 | 88.9 | 2.4 | 3.7 | 2.0 | 1.1 | 346 | 0.66 |
| 2012/05/10-20:26 | M1.7 | N12E12 | 15.7 | 0.9 | 68.8 | 76.7 | 78.4 | 1.9 | 4.1 | 2.1 | 0.5 | 616 | 0.35 |
| 2012/06/13-13:17 | M1.2 | S16E18 | 13.5 | 0.7 | 56.7 | 53.1 | 51.4 | 1.9 | 6.1 | 3.2 | – | – | – |
| 2012/07/05-03:36 | M4.7 | S18W29 | 18.0 | 2.3 | 72.6 | 67.1 | 155.7 | 2.6 | 7.6 | 2.1 | – | 249 | – |
| 2012/07/05-21:45 | M1.6 | S12W46 | 13.4 | 1.0 | 51.6 | 24.6 | 50.5 | 2.5 | 5.6 | 2.0 | – | – | – |
| 2012/07/06-01:40 | M2.9 | S18W41 | 16.3 | 1.5 | 66.7 | 95.2 | 181.8 | 2.3 | 4.5 | 1.7 | – | 176 | – |
| 2012/07/06-08:23 | M1.5 | S17W40 | 15.0 | 0.8 | 64.9 | 102.5 | 175.4 | 1.9 | 4.2 | 1.8 | 2.0 | 727 | 0.64 |
| 2012/07/06-23:08 | X1.1 | S13W59 | 16.6 | 5.5 | 53.1 | 36.2 | 47.4 | 4.9 | 5.6 | 2.3 | 2.7 | 542 | 0.86 |
| 2012/07/08-12:09 | M1.4 | S21W69 | 15.8 | 0.8 | 71.5 | 84.2 | 133.6 | 1.7 | 3.8 | 1.5 | 0.7 | 274 | 0.62 |

Table B.2: Physical paremeters of flares (continued from B.1).

| peak time | *GOES* class | Loc.* [deg] | $T_6$† [K] | $EM_{48}$‡ [cm$^{-3}$] | $B_{\rm theor}$§ [G] | $B_{\rm obs}(a)$‖ [G] | $B_{\rm obs}(b)$# [G] | $L_{\rm theor}$§ [$10^9$cm] | $L_{\rm obs}(a)$‖ [$10^9$cm] | $L_{\rm obs}(b)$# [$10^9$cm] | $L_{\rm Reale}$** [$10^9$cm] | $\tau_{\rm SXR}$†† [sec] | $\zeta$‡‡ |
|---|---|---|---|---|---|---|---|---|---|---|---|---|---|
| 2012/07/12-16:49 | X1.4 | S13W03 | 20.5 | 3.4 | 83.5 | 112.9 | 98.0 | 2.6 | 8.0 | 5.2 | 14.2 | 3536 | 0.77 |
| 2012/07/14-04:58 | M1.0 | S22W36 | 9.7 | 0.7 | 32.1 | 42.5 | 186.8 | 3.4 | 7.8 | 1.7 | – | – | – |
| 2012/10/23-03:17 | X1.8 | S13E58 | 24.2 | 6.7 | 96.9 | 60.3 | 106.9 | 3.0 | 5.0 | 2.8 | 0.7 | 303 | 0.51 |
| 2013/05/02-05:10 | M1.1 | N10W26 | 12.4 | 0.7 | 49.2 | 30.6 | 33.6 | 2.2 | 4.1 | 2.5 | – | 651 | – |
| 2013/05/03-16:55 | M1.3 | N10W38 | 12.3 | 0.8 | 46.3 | 29.5 | 26.6 | 2.6 | 6.1 | 3.6 | – | – | – |
| 2013/05/15-01:40 | X1.2 | N12E64 | 15.8 | 6.6 | 47.1 | 37.7 | 50.2 | 6.0 | 5.9 | 3.7 | – | 909 | – |
| 2013/06/07-22:49 | M5.9 | S32W89 | 17.4 | 2.9 | 65.8 | 23.9 | 33.9 | 3.1 | 5.3 | 3.0 | 3.1 | 1204 | 0.58 |
| 2013/08/17-18:24 | M3.3 | S07W30 | 16.4 | 1.7 | 65.1 | 86.0 | 139.1 | 2.5 | 4.7 | 2.2 | – | – | – |
| 2013/10/22-00:22 | M1.0 | N06E17 | 13.6 | 0.6 | 59.3 | 93.3 | 88.4 | 1.8 | 4.1 | 1.9 | – | 571 | – |
| 2013/10/26-19:31 | M3.1 | S09E81 | 14.2 | 1.7 | 51.1 | 19.1 | 41.9 | 3.2 | 3.7 | 1.7 | – | 380 | – |
| 2013/10/28-15:01 | M2.7 | S08E28 | 15.3 | 1.5 | 60.5 | 68.5 | 83.7 | 2.5 | 4.2 | 2.2 | 0.1 | 141 | 0.37 |
| 2013/10/28-15:15 | M4.4 | S06E28 | 13.6 | 2.5 | 44.1 | 61.1 | 54.3 | 4.2 | 5.3 | 3.6 | 1.4 | 1030 | 0.42 |
| 2013/12/07-07:29 | M1.2 | S16W49 | 11.3 | 0.9 | 39.7 | 19.9 | 25.5 | 3.0 | 5.0 | 3.1 | 9.4 | 2289 | 0.97 |
| 2013/12/22-08:11 | M1.9 | S20W49 | 15.9 | 1.0 | 69.2 | 72.2 | 90.1 | 1.9 | 4.8 | 1.6 | 3.6 | 722 | 0.99 |
| 2013/12/22-15:12 | M3.3 | S19W56 | 15.4 | 1.8 | 58.2 | 59.4 | 100.3 | 2.8 | 4.5 | 2.1 | 3.5 | 739 | 1.02 |
| 2013/12/23-09:06 | M1.6 | S17W63 | 15.4 | 0.9 | 67.5 | 59.7 | 78.9 | 1.8 | 4.5 | 1.6 | 1.6 | 286 | 1.18 |
| 2013/12/31-21:58 | M6.4 | S16W35 | 17.4 | 3.1 | 64.3 | 79.9 | 104.0 | 3.3 | 6.0 | 2.9 | 2.2 | 1593 | 0.42 |
| 2014/01/01-18:52 | M9.9 | S14W47 | 15.9 | 5.1 | 50.3 | 45.7 | 41.8 | 5.0 | 7.7 | 3.8 | – | 1007 | – |
| 2014/01/04-10:25 | M1.3 | S05E48 | 13.6 | 0.8 | 56.1 | 73.2 | 62.3 | 2.1 | 4.3 | 2.3 | – | – | – |
| 2014/01/04-19:46 | M4.0 | S11E34 | 15.2 | 1.5 | 59.5 | 20.0 | 17.7 | 2.6 | 8.6 | 5.0 | – | 3219 | – |
| 2014/02/14-02:57 | M2.3 | S12W25 | 14.6 | 1.3 | 57.2 | 94.7 | 85.6 | 2.5 | 5.0 | 2.6 | 5.2 | 1198 | 0.94 |
| 2014/02/14-12:40 | M1.6 | S15W36 | 13.9 | 0.9 | 56.3 | 35.1 | 34.5 | 2.2 | 6.0 | 1.8 | – | 415 | – |
| 2014/03/13-19:19 | M1.2 | N15W87 | 12.9 | 0.8 | 51.4 | 10.1 | 24.0 | 2.3 | 6.5 | 3.3 | – | 1105 | – |
| 2014/06/12-22:16 | M3.1 | S20W55 | 14.2 | 1.0 | 57.5 | 40.5 | 79.0 | 2.2 | 9.1 | 5.1 | – | 3536 | – |
| 2014/06/16-00:01 | M1.0 | S19E08 | 11.1 | 0.7 | 40.9 | 31.6 | 41.1 | 2.7 | 3.8 | 2.5 | – | 2019 | – |
| 2014/08/01-18:03 | M1.5 | S10E11 | 12.3 | 0.9 | 45.7 | 51.6 | 47.1 | 2.7 | 5.4 | 3.4 | – | 3260 | – |
| 2014/10/21-13:38 | M1.2 | S14E35 | 14.8 | 0.8 | 64.9 | 40.9 | 38.4 | 1.8 | 3.3 | 1.9 | – | 129 | – |
| 2014/10/22-01:59 | M8.7 | S13E21 | 18.4 | 4.0 | 67.2 | 128.0 | 148.6 | 3.5 | 9.5 | 3.8 | 9.9 | 2297 | 0.84 |
| 2014/10/22-14:06 | X1.6 | S14E13 | 20.5 | 5.9 | 75.2 | 110.3 | 91.5 | 3.6 | 9.0 | 5.9 | 7.5 | 1710 | 0.77 |
| 2014/10/24-21:15 | X3.1 | S16W21 | 19.4 | 9.8 | 61.7 | 56.2 | 55.8 | 5.4 | 13.1 | 7.2 | 15.2 | 2646 | 1.00 |
| 2014/10/25-17:08 | X1.0 | S10W22 | 18.7 | 4.8 | 67.0 | 87.5 | 68.5 | 3.7 | 7.5 | 3.9 | – | – | – |
| 2014/10/26-10:56 | X2.0 | S18W40 | 21.9 | 7.3 | 80.2 | 102.3 | 107.2 | 3.8 | 8.5 | 4.2 | 9.0 | 1683 | 0.93 |
| 2014/10/26-20:21 | M2.4 | S15W45 | 15.7 | 1.2 | 65.9 | 115.1 | 95.4 | 2.1 | 6.4 | 2.4 | – | – | – |

Table B.3: Physical parameters of flares (continued from B.2).

| peak time | *GOES* class | Loc.* [deg] | $T_6$† [K] | $EM_{48}$‡ [$\mathrm{cm}^{-3}$] | $B_{\mathrm{theor}}$§ [G] | $B_{\mathrm{obs}}(a)$‖ [G] | $B_{\mathrm{obs}}(b)$# [G] | $L_{\mathrm{theor}}$§ [$10^9$cm] | $L_{\mathrm{obs}}(a)$‖ [$10^9$cm] | $L_{\mathrm{obs}}(b)$# [$10^9$cm] | $L_{\mathrm{Reale}}$** [$10^9$cm] | $\tau_{\mathrm{SXR}}$†† [sec] | $\zeta$‡‡ |
|---|---|---|---|---|---|---|---|---|---|---|---|---|---|
| 2014/10/27-14:23 | X2.0 | S17W52 | 20.9 | 6.7 | 75.4 | 79.0 | 99.1 | 3.8 | 9.3 | 5.1 | 9.1 | 1763 | 0.92 |
| 2014/10/28-02:42 | M3.4 | S14W61 | 15.3 | 1.8 | 57.3 | 91.0 | 111.9 | 2.9 | 7.3 | 4.1 | – | – | – |
| 2014/10/29-10:01 | M1.2 | S18W77 | 13.0 | 0.7 | 52.7 | 76.9 | – | 2.1 | 6.8 | 1.4 | – | – | – |
| 2014/11/05-09:47 | M7.9 | N20E68 | 17.6 | 3.8 | 63.3 | 62.1 | 80.8 | 3.6 | 4.7 | 2.1 | 1.5 | 679 | 0.50 |
| 2014/11/05-19:44 | M2.9 | N17E65 | 15.1 | 1.4 | 58.9 | 40.3 | 50.4 | 2.6 | 5.4 | 3.1 | 4.7 | 2525 | 0.50 |
| 2014/11/07-02:44 | M2.7 | N17E50 | 14.3 | 1.5 | 53.9 | 82.8 | 106.8 | 2.8 | 5.3 | 2.5 | – | – | – |
| 2014/11/07-10:20 | M1.0 | N15E43 | 13.1 | 0.6 | 55.6 | 57.3 | 76.8 | 1.9 | 4.6 | 2.2 | – | 954 | – |
| 2014/11/07-17:26 | X1.6 | N14E36 | 17.3 | 7.9 | 52.9 | 55.1 | 76.4 | 5.7 | 8.3 | 4.7 | 1.7 | 798 | 0.52 |
| 2014/11/15-12:03 | M3.2 | S09E63 | 14.6 | 1.8 | 53.4 | 40.4 | 72.9 | 3.1 | 5.2 | 2.1 | 1.3 | 559 | 0.53 |
| 2014/11/15-20:46 | M3.7 | S13E63 | 15.5 | 2.0 | 58.0 | 41.6 | 34.1 | 3.0 | 4.5 | 1.9 | 0.2 | 276 | 0.35 |
| 2014/12/04-08:03 | M1.3 | S24W27 | 12.9 | 0.8 | 51.5 | 65.3 | 65.5 | 2.2 | 5.3 | 2.4 | – | – | – |
| 2014/12/19-09:44 | M1.3 | S19W27 | 12.6 | 0.8 | 48.8 | 42.6 | 27.3 | 2.4 | 4.0 | 2.3 | 1.1 | 1144 | 0.39 |
| 2014/12/20-00:28 | X1.8 | S21W24 | 18.0 | 8.9 | 55.1 | 89.9 | 105.9 | 5.8 | 8.6 | 4.6 | – | 2975 | – |

*Locations where flares occurred.
†Temperature in unit $10^6$K when emission measure is maximum value.
‡Emission measure in unit $10^{48}\mathrm{cm}^{-3}$.
§Theoretically estimated physical quantities by Shibata & Yokoyama (2002).
‖Observationally measured physical quantities in the case of (a).
#Observationally measured physical quantities in the case of (b).
**Theoretically estimated loop length by Reale et al. (1997).
††Flare duration defined as e-folding decay time of soft X-ray intensity.
‡‡The trajectory of $\sqrt{EM} - T$ diagram.

Table B.4: Physical parameters of flares.

| No | Day* | GOES Class | Loc.† [arcsec] | $E^{\ddagger}$ [$10^{29}$erg] | $E_{\rm C}{}^{\S}$ [$10^{29}$erg] | $\Delta E^{\|\|}$ [$10^{29}$erg] | $F^{\#}$ [$10^5$DN] | $F_{\rm C}{}^{\S}$ [$10^5$DN] | $\Delta F^{\|\|}$ [$10^5$DN] | $\tau_{\rm decay}{}^{**}$ [min] | $\Delta\tau_{\rm decay}$ [min] | $\tau_{\rm HXR}{}^{\dagger\dagger}$ [min] | $F_C/F_{\rm sun}$ [ppm] | $B_{\rm est}{}^{\ddagger\ddagger}$ [G] | $B_{\rm obs}{}^{\S\S}$ [G] | $L_{\rm est}{}^{\ddagger\ddagger}$ [$10^9$cm] | $L_{\rm obs}{}^{\S\S}$ [$10^9$cm] |
|---|---|---|---|---|---|---|---|---|---|---|---|---|---|---|---|---|---|
| 1 | 2011/02/15-01:56 | X2.2 | (210,-220) | 66.1 | 71.1 | 7.7 | 29.8 | 32.0 | 1.5 | 8.37 | 0.375 | 2.12 | 7.04 | 62.0 | 89.3 | 5.50 | 3.71 |
| 2 | 2011/02/18-10:11 | M6.6 | (755,-270) | 5.99 | 8.64 | 1.33 | 10.9 | 15.7 | 1.0 | 2.47 | 0.00 | 0.467 | 3.46 | 71.2 | 80.7 | 3.05 | 1.67 |
| 3 | 2011/02/18-13:03 | M1.4 | (765,-275) | 2.21 | 3.21 | 2.03 | 5.42 | 7.90 | 1.28 | 1.32 | 0.375 | 0.0833 | 1.73 | 71.3 | 79.6 | 1.67 | 1.35 |
| 4 | 2011/02/24-07:35 | M3.5 | (-925,275) | 9.45 | 31.2 | 2.2 | 5.37 | 17.7 | 0.8 | 9.35 | 0.750 | 2.63 | 3.93 | 50.3 | 16.9 | 3.37 | 2.29 |
| 5 | 2011/03/07-20:12 | M3.7 | (615,560) | 4.51 | 6.84 | 1.72 | 6.28 | 9.53 | 1.17 | 2.38 | 0.375 | 2.07 | 2.12 | 42.4 | 19.5 | 4.17 | 5.76 |
| 6 | 2011/03/09-23:23 | X1.5 | (190,275) | 3.55 | 3.84 | 4.27 | 8.80 | 9.52 | 3.22 | 1.23 | 1.50 | 0.833 | 2.12 | 55.1 | 96.4 | 5.38 | 4.07 |
| 7 | 2011/03/14-19:52 | M4.2 | (705,340) | 6.65 | 9.33 | 2.44 | 10.1 | 14.2 | 1.7 | 2.93 | 0.375 | 0.133 | 3.18 | 60.7 | 72.7 | 2.99 | 2.11 |
| 8 | 2011/03/15-00:22 | M1.0 | (750,325) | 1.32 | 1.94 | 0.71 | 2.37 | 3.48 | 0.48 | 2.13 | 0.375 | 0.100 | 0.779 | 77.6 | 43.5 | 1.35 | 1.05 |
| 9 | 2011/07/30-02:09 | M9.3 | (-525,170) | 17.6 | 20.5 | 2.7 | 24.3 | 28.2 | 1.7 | 2.43 | 0.375 | 0.200 | 6.73 | 60.9 | 60.4 | 4.01 | 2.85 |
| 10 | 2011/09/24-20:36 | M5.8 | (-740,155) | 2.88 | 3.89 | 1.17 | 5.64 | 7.63 | 0.63 | 1.87 | 0.00 | 0.633 | 1.79 | 75.7 | 44.2 | 2.63 | 1.71 |
| 11 | 2011/09/24-09:40 | X1.9 | (-815,165) | 24.8 | 37.7 | 3.7 | 33.2 | 50.4 | 1.3 | 3.33 | 0.00 | 0.317 | 11.7 | 78.3 | 64.7 | 3.93 | 2.45 |
| 12 | 2011/09/26-05:08 | M4.0 | (-520,120) | 4.99 | 5.77 | 1.65 | 8.26 | 9.55 | 1.33 | 2.07 | 0.375 | 0.133 | 2.24 | 73.2 | 76.6 | 2.40 | 2.02 |
| 13 | 2011/12/26-20:30 | M2.3 | (635,-325) | 4.95 | 6.42 | 3.06 | 5.01 | 6.51 | 0.88 | 2.10 | 0.375 | 0.0333 | 1.49 | 70.9 | 61.3 | 1.89 | 2.29 |
| 14 | 2011/12/31-13:15 | M2.4 | (-620,-395) | 5.62 | 7.41 | 5.11 | 7.78 | 10.3 | 2.6 | 2.18 | 1.12 | 0.217 | 2.35 | 74.5 | 75.3 | 1.93 | 1.74 |
| 15 | 2012/03/09-03:53 | M6.3 | (50,380) | 11.3 | 12.4 | 3.7 | 11.6 | 12.7 | 1.6 | 3.82 | 0.375 | 3.27 | 3.00 | 71.4 | 94.6 | 1.88 | 4.46 |
| 16 | 2012/05/10-04:18 | M5.7 | (-360,255) | 14.1 | 15.7 | 4.6 | 17.5 | 19.5 | 3.2 | 2.93 | 0.375 | 0.600 | 4.81 | 60.5 | 56.8 | 3.38 | 2.49 |
| 17 | 2012/06/03-17:55 | M3.3 | (-565,275) | 5.96 | 7.23 | 3.32 | 8.49 | 10.3 | 1.4 | 2.65 | 0.750 | 0.500 | 2.56 | 51.3 | 34.3 | 3.29 | 2.53 |
| 18 | 2012/07/04-09:55 | M5.3 | (290,-340) | 6.22 | 6.93 | 2.86 | 8.64 | 9.63 | 1.58 | 1.62 | 0.375 | 0.317 | 2.41 | 79.8 | 95.8 | 2.42 | 1.84 |
| 19 | 2012/07/05-03:36 | M4.7 | (415,-335) | 7.31 | 8.45 | 0.98 | 10.4 | 12.0 | 0.7 | 2.62 | 0.00 | 0.417 | 3.01 | 72.6 | 66.9 | 2.55 | 2.05 |
| 20 | 2012/07/05-11:48 | M6.1 | (500,-350) | 19.1 | 23.0 | 4.9 | 19.4 | 23.3 | 1.7 | 3.08 | 0.375 | 1.12 | 5.82 | 64.8 | 73.1 | 3.22 | 2.62 |
| 21 | 2012/07/06-01:40 | M2.9 | (590,-330) | 5.52 | 6.95 | 0.75 | 5.90 | 7.42 | 0.30 | 4.08 | 0.00 | 0.0833 | 1.86 | 66.7 | 95.7 | 2.33 | 1.68 |
| 22 | 2012/07/19-05:58 | M7.7 | (925,-200) | 3.64 | 9.03 | 1.04 | 1.11 | 2.75 | 0.16 | 8.48 | 1.50 | 8.42 | 0.688 | 57.0 | 19.6 | 3.52 | 4.77 |
| 23 | 2012/08/06-04:38 | M1.6 | (-915,-230) | 1.83 | 4.33 | 0.58 | 2.21 | 5.22 | 0.23 | 3.88 | 0.375 | 0.267 | 1.30 | 64.4 | 7.23 | 1.91 | 1.06 |
| 24 | 2012/10/23-03:17 | X1.8 | (-800,-260) | 20.6 | 31.6 | 1.4 | 28.0 | 43.0 | 0.8 | 2.78 | 0.00 | 0.267 | 10.4 | 96.9 | 58.6 | 3.03 | 2.74 |
| 25 | 2012/11/20-12:41 | M1.7 | (950,200) | 0.674 | 2.22 | 0.40 | 1.85 | 6.09 | 0.36 | 1.10 | 0.00 | 0.683 | 1.46 | 55.2 | 5.07 | 2.33 | 1.13 |
| 26 | 2013/05/13-02:17 | X1.7 | (-930,200) | 4.19 | 10.9 | 1.6 | 2.69 | 7.02 | 0.51 | 2.78 | 1.50 | 1.15 | 1.79 | 74.8 | 3.24 | 3.92 | 2.82 |
| 27 | 2013/05/13-16:05 | X2.8 | (-925,180) | 27.7 | 64.0 | 2.0 | 15.6 | 36.1 | 0.4 | 4.88 | 0.750 | 3.10 | 9.17 | 64.3 | 30.1 | 5.75 | 3.41 |
| 28 | 2013/05/15-01:48 | X1.2 | (-850,200) | 26.4 | 43.9 | 6.1 | 9.01 | 15.0 | 1.0 | 14.1 | 0.375 | 3.78 | 3.81 | 47.1 | 37.6 | 5.96 | 3.71 |
| 29 | 2013/10/25-08:01 | X1.7 | (-910,-160) | 18.1 | 36.8 | 2.2 | 16.9 | 34.2 | 0.7 | 4.00 | 0.375 | 1.47 | 8.49 | 82.0 | 46.4 | 3.67 | 1.82 |
| 30 | 2013/10/28-15:15 | M4.4 | (-440,-195) | 19.7 | 22.2 | 6.4 | 8.77 | 9.89 | 1.52 | 3.07 | 0.375 | 0.400 | 2.45 | 60.5 | 61.3 | 2.52 | 3.62 |
| 31 | 2013/10/28-02:03 | X1.0 | (910,40) | 16.9 | 32.3 | 8.5 | 11.0 | 21.0 | 2.6 | 2.55 | 1.12 | 0.750 | 5.20 | 58.2 | 44.1 | 4.33 | 3.12 |
| 32 | 2013/11/10-05:14 | X1.1 | (215,-275) | 21.5 | 23.3 | 4.8 | 28.2 | 30.7 | 2.7 | 2.92 | 0.375 | 1.38 | 7.55 | 65.2 | 58.6 | 4.00 | 4.04 |
| 33 | 2014/01/07-10:13 | M7.2 | (-220,-170) | 30.9 | 33.0 | 9.1 | 39.9 | 42.7 | 3.5 | 3.38 | 0.00 | 0.500 | 10.4 | 73.6 | 115 | 2.95 | 2.69 |
| 34 | 2014/01/27-22:10 | M4.9 | (-940,-260) | 4.46 | 14.7 | 1.3 | 3.58 | 11.8 | 0.5 | 6.12 | 0.750 | 1.03 | 2.87 | 72.4 | 72.2 | 2.63 | 1.11 |
| 35 | 2014/02/07-10:29 | M1.9 | (765,265) | 3.27 | 4.76 | 2.06 | 5.83 | 8.49 | 1.16 | 2.02 | 0.750 | 0.0833 | 2.08 | 78.8 | 69.0 | 1.79 | 1.32 |
| 36 | 2014/03/12-22:34 | M9.3 | (910,270) | 8.11 | 20.6 | 1.4 | 8.37 | 21.3 | 0.6 | 3.67 | 0.375 | 0.817 | 5.28 | 78.1 | 41.3 | 3.05 | 1.93 |
| 37 | 2014/03/29-17:48 | X1.0 | (515,265) | 14.7 | 17.3 | 3.2 | 19.8 | 23.3 | 1.8 | 2.83 | 0.375 | 0.800 | 5.84 | 61.5 | 47.5 | 4.05 | 3.18 |
| 38 | 2014/06/11-09:06 | X1.0 | (-820,-305) | 12.5 | 20.7 | 3.5 | 8.17 | 13.6 | 1.1 | 6.17 | 0.750 | 0.633 | 3.52 | 76.5 | 45.1 | 3.24 | 1.88 |
| 39 | 2014/10/16-13:03 | M4.3 | (-935,-225) | 3.85 | 12.7 | 1.0 | 5.27 | 17.4 | 0.5 | 2.65 | 0.00 | 0.233 | 4.35 | 126 | 22.6 | 1.40 | 1.35 |
| 40 | 2014/10/22-01:59 | M8.7 | (-390,-295) | 1.54 | 1.74 | 1.25 | 3.93 | 4.46 | 0.95 | 1.27 | 0.00 | 0.267 | 1.12 | 67.2 | 137 | 3.47 | 3.79 |

Table B.5: Physical parameters of flares (continued from B.4).

| No | Day* | GOES Class | Loc.† [arcsec] | $E^{\ddagger}$ [$10^{29}$erg] | $E_C{}^{\S}$ [$10^{29}$erg] | $\Delta E^{\|\|}$ [$10^{29}$erg] | $F^{\#}$ [$10^5$DN] | $F_C{}^{\S}$ [$10^5$DN] | $\Delta F^{\|\|}$ [$10^5$DN] | $\tau_{\rm decay}{}^{**}$ [min] | $\Delta\tau_{\rm decay}$ [min] | $\tau_{\rm HXR}{}^{\dagger\dagger}$ [min] | $F_C/F_{\rm sun}$ [ppm] | $B_{\rm est}{}^{\ddagger\ddagger}$ [G] | $B_{\rm obs}{}^{\S\S}$ [G] | $L_{\rm est}{}^{\ddagger\ddagger}$ [$10^9$cm] | $L_{\rm obs}{}^{\S\S}$ [$10^9$cm] |
|---|---|---|---|---|---|---|---|---|---|---|---|---|---|---|---|---|---|
| 41 | 2014/10/22-14:28 | X1.6 | (-170,-320) | 4.67 | 5.08 | 1.31 | 7.84 | 8.53 | 0.61 | 2.30 | 0.374 | 0.733 | 2.14 | 75.2 | 111 | 3.64 | 5.90 |
| 42 | 2014/10/24-07:48 | M4.0 | (80,-410) | 7.02 | 7.77 | 3.44 | 4.66 | 5.16 | 1.16 | 4.83 | 0.00 | 1.32 | 1.29 | 62.4 | 34.2 | 2.81 | 3.29 |
| 43 | 2015/03/02-15:28 | M3.7 | (909,366) | 3.77 | 12.4 | 1.7 | 2.47 | 8.16 | 0.41 | 6.62 | 1.50 | 0.500 | 2.02 | 54.3 | 6.37 | 3.13 | 2.04 |
| 44 | 2015/03/10-03:24 | M5.1 | (-600,-170) | 9.03 | 10.9 | 1.8 | 10.9 | 13.3 | 0.7 | 2.83 | 0.375 | 0.483 | 3.31 | 61.0 | 70.4 | 3.17 | 2.23 |
| 45 | 2015/03/11-00:02 | M2.9 | (-429,-157) | 4.33 | 4.85 | 1.39 | 11.2 | 12.5 | 1.2 | 0.917 | 0.375 | 0.133 | 3.12 | 71.2 | 112 | 2.14 | 1.44 |
| 46 | 2015/03/11-16:22 | X2.1 | (-350,-174) | 27.9 | 30.7 | 12.9 | 19.6 | 21.6 | 3.4 | 4.02 | 0.750 | 0.117 | 5.38 | 69.8 | 104 | 4.78 | 2.73 |
| 47 | 2015/05/05-22:11 | X2.7 | (-902,259) | 32.2 | 72.8 | 3.0 | 31.4 | 71.1 | 0.8 | 3.27 | 0.00 | 0.517 | 18.4 | 68.4 | 56.5 | 5.33 | 3.29 |
| 48 | 2015/08/28-19:04 | M2.1 | (869,-273) | 1.19 | 2.27 | 0.76 | 2.30 | 4.38 | 0.55 | 1.85 | 0.750 | 0.350 | 1.14 | 91.5 | 88.7 | 1.46 | 1.16 |
| 49 | 2015/10/02-00:13 | M5.5 | (826,-377) | 9.94 | 18.6 | 3.4 | 10.8 | 20.3 | 1.3 | 3.72 | 0.375 | 2.00 | 5.18 | 63.8 | 51.0 | 3.14 | 1.85 |
| 50 | 2015/11/04-12:03 | M2.5 | (887,231) | 2.24 | 4.33 | 1.26 | 3.08 | 5.95 | 0.59 | 2.12 | 0.375 | 4.65 | 1.49 | 54.7 | 38.6 | 3.11 | 1.48 |

*Flare peak time of the GOES soft X-ray flux. †Event locations (EW, NS) in the unit of arcsec. ‡Flare energy radiated in the white light. §Corrected values for limb darkening.
$\|\|1\ \sigma$ error of each value. (Note that the error bars on the Figure 4 are 3-$\sigma$ values) #Total counts of the white-light flares. **E-folding decay time. ††Decay time of the HXR flare (30-80keV).
‡‡Theoretically estimated values from the scaling laws. §§Observationally measured values with *SDO*.

Table B.6: Detailed Observations.

| No | WL Start* | WL End* | HXR Area† [%] | Detecter‡ No | No | WL Start* | WL End* | HXR Area† [%] | Detecter‡ No |
|---|---|---|---|---|---|---|---|---|---|
| 1 | 2011/02/15-01:31:35 | 2011/02/15-01:54:05 | 30 | (4,5,6,7,8) | 26 | 2013/05/13-01:49:45 | 2013/05/13-02:07:45 | 30 | (3,5,6,7,8) |
| 2 | 2011/02/18-09:47:19 | 2011/02/18-09:54:04 | 30 | (4,5,6,7,8) | 27 | 2013/05/13-15:43:45 | 2013/05/13-16:04:00 | 30 | (3,5,6,7,8,9) |
| 3 | 2011/02/18-12:45:04 | 2011/02/18-12:51:04 | 30 | (4,5,6,7,8) | 28 | 2013/05/15-01:23:31 | 2013/05/15-01:47:31 | 30 | (3,5,6,7,8,9) |
| 4 | 2011/02/24-07:19:35 | 2011/02/24-07:33:50 | 30 | (4,5,6,7,8) | 29 | 2013/10/25-07:47:22 | 2013/10/25-08:01:37 | 20 | (3,5,6,7,8,9) |
| 5 | 2011/03/07-19:36:51 | 2011/03/07-19:43:36 | 30 | (4,5,6,7,8) | 30 | 2013/10/28-15:01:37 | 2013/10/28-15:19:37 | 50 | (3,5,6,7,8) |
| 6 | 2011/03/09-22:57:52 | 2011/03/09-23:03:07 | 30 | (4,5,6,7,8) | 31 | 2013/10/28-01:51:06 | 2013/10/28-02:04:36 | 10 | (3,5,6,7,8,9) |
| 7 | 2011/03/14-19:32:22 | 2011/03/14-19:42:07 | 20 | (4,5,6,7,8) | 32 | 2013/11/10-04:51:05 | 2013/11/10-04:57:50 | 20 | (3,4,5,6,8) |
| 8 | 2011/03/15-00:03:07 | 2011/03/15-00:09:52 | 70 | (4,5,6,7,8) | 33 | 2014/01/07-09:47:17 | 2014/01/07-10:00:47 | 30 | (3,5,6,7,8,9) |
| 9 | 2011/07/30-02:01:03 | 2011/07/30-02:08:33 | 30 | (4,5,6,7,8) | 34 | 2014/01/27-22:00:02 | 2014/01/27-22:10:32 | 20 | (3,4,5,6,7,8) |
| 10 | 2011/09/24-20:23:27 | 2011/09/24-20:29:27 | 50 | (4,5,6,7,8) | 35 | 2014/02/07-10:03:48 | 2014/02/07-10:13:33 | 10 | (3,5,6,7,8,9) |
| 11 | 2011/09/24-09:24:57 | 2011/09/24-09:34:42 | 30 | (4,5,6,7,8) | 36 | 2014/03/12-22:11:22 | 2014/03/12-22:21:52 | 10 | (3,5,6,7,8,9) |
| 12 | 2011/09/26-04:56:27 | 2011/09/26-05:02:27 | 50 | (4,5,6,7,8) | 37 | 2014/03/29-17:38:24 | 2014/03/29-17:46:39 | 20 | (3,5,6,7,8,9) |
| 13 | 2011/12/26-20:06:48 | 2011/12/26-20:16:33 | 30 | (3,4,5,6,7,8,9) | 38 | 2014/06/11-08:43:48 | 2014/06/11-08:56:33 | 10 | (3,5,6,7,8,9) |
| 14 | 2011/12/31-13:06:03 | 2011/12/31-13:14:18 | 10 | (3,4,5,6,7,8) | 39 | 2014/10/16-12:44:23 | 2014/10/16-12:51:53 | 30 | (3,5,6,7,9) |
| 15 | 2012/03/09-03:17:23 | 2012/03/09-03:27:53 | 50 | (3,5,6,7,8) | 40 | 2014/10/22-01:20:23 | 2014/10/22-01:24:08 | 30 | (3,4,5,6,7,8,9) |
| 16 | 2012/05/10-03:54:16 | 2012/05/10-04:01:46 | 20 | (3,5,6,7,8,9) | 41 | 2014/10/22-14:00:07 | 2014/10/22-14:06:07 | 50 | (3,5,6,7,9) |
| 17 | 2012/06/03-17:25:48 | 2012/06/03-17:32:33 | 20 | (3,5,6,7,8,9) | 42 | 2014/10/24-07:29:21 | 2014/10/24-07:40:36 | 30 | (3,6,8) |
| 18 | 2012/07/04-09:28:03 | 2012/07/04-09:40:48 | 10 | (3,5,6,7,8,9) | 43 | 2015/03/02-15:00:05 | 2015/03/02-15:14:20 | 30 | (3,5,6,7,9) |
| 19 | 2012/07/05-03:04:48 | 2012/07/05-03:12:18 | 30 | (3,5,6,7,8,9) | 44 | 2015/03/10-03:02:22 | 2015/03/10-03:13:37 | 30 | (3,5,6,7,9) |
| 20 | 2012/07/05-11:18:18 | 2012/07/05-11:28:48 | 10 | (3,5,6,7,8,9) | 45 | 2015/03/10-23:41:22 | 2015/03/10-23:47:22 | 20 | (3,5,6,7,9) |
| 21 | 2012/07/06-01:13:48 | 2012/07/06-01:23:33 | 30 | (3,5,6,7,8,9) | 46 | 2015/03/11-16:00:52 | 2015/03/11-16:13:37 | 10 | (4,5,6,7,8) |
| 22 | 2012/07/19-05:07:03 | 2012/07/19-05:32:33 | 30 | (3,5,6,7,8) | 47 | 2015/05/05-21:45:14 | 2015/05/05-21:59:29 | 30 | (3,5,6,7,8) |
| 23 | 2012/08/06-04:10:47 | 2012/08/06-04:20:32 | 30 | (3,5,6,7,8,9) | 48 | 2015/08/28-18:55:44 | 2015/08/28-19:03:14 | 20 | (3,5,6,7,8,9) |
| 24 | 2012/10/23-03:03:08 | 2012/10/23-03:12:53 | 30 | (3,5,6,7,8,9) | 49 | 2015/10/01-23:44:25 | 2015/10/01-23:52:40 | 50 | (5,6,7,8) |
| 25 | 2012/11/20-12:24:49 | 2012/11/20-12:29:19 | 10 | (3,5,6,7,8) | 50 | 2015/11/04-11:36:50 | 2015/11/04-11:42:50 | 50 | (3,5,6,7,8) |

*The start and end time of white-light flare we defined by eye on the basis of the pre-flare subtracted movies in Section 2.

†The contour levels of the mask of the hard X-ray images where we extracted white-light emission as in Section 2.

‡The *RHESSI* detectors we used in this analysis.

Table B.7: Physical paremeters of flares with *Hinode*.

| No | Day | $E_C$ [$10^{29}$erg] | $\tau_{\rm HMI}$ [min] | $\tau_{\rm red}$* [min] | $\tau_{\rm green}$* [min] | $\tau_{\rm blue}$* [min] |
|---|---|---|---|---|---|---|
| 2 | 2011/02/18-10:10 | 8.64 | 2.47 | 2.10 | 2.07 | 1.85 |
| 14 | 2011/12/31-13:13 | 7.41 | 2.18 | 1.98 | 3.20 | 0.983 |
| 24 | 2012/10/23-03:15 | 31.6 | 2.78 | 3.15 | 3.13 | 3.30 |
| 41 | 2014/10/22-14:06 | 5.08 | 2.30 | 2.55 | 2.70 | 2.80 |

*Observed e-folding decay time with SOT/Red, Green, and Blue continuum.

APPENDIX C

# Supplementary materials in Chapter 5

## C.1 Flare atlas

In this section, we will show the observed flares which are not discussed in the main part but important for our future studies. Figure C.1 shows the light curves observed with 40cm KU (Kyoto University) Telescope (B-band photometry), Seimei Telescope, and NICER on April 12th. Five small but clear flares are detected in this period (see flare #7 – 11).

Figure C.2 shows the light curves observed with only NICER on April 13th. We estimated the emission measure and temperature of the flare #12, and it is found that the peak timing of temperature is similar to that of the emission measure. The flare energy in X-ray (0.5 - 10 keV) is estimated to be $9.7 \times 10^{31}$ erg, which is very large and comparable to the largest scale of solar flares.

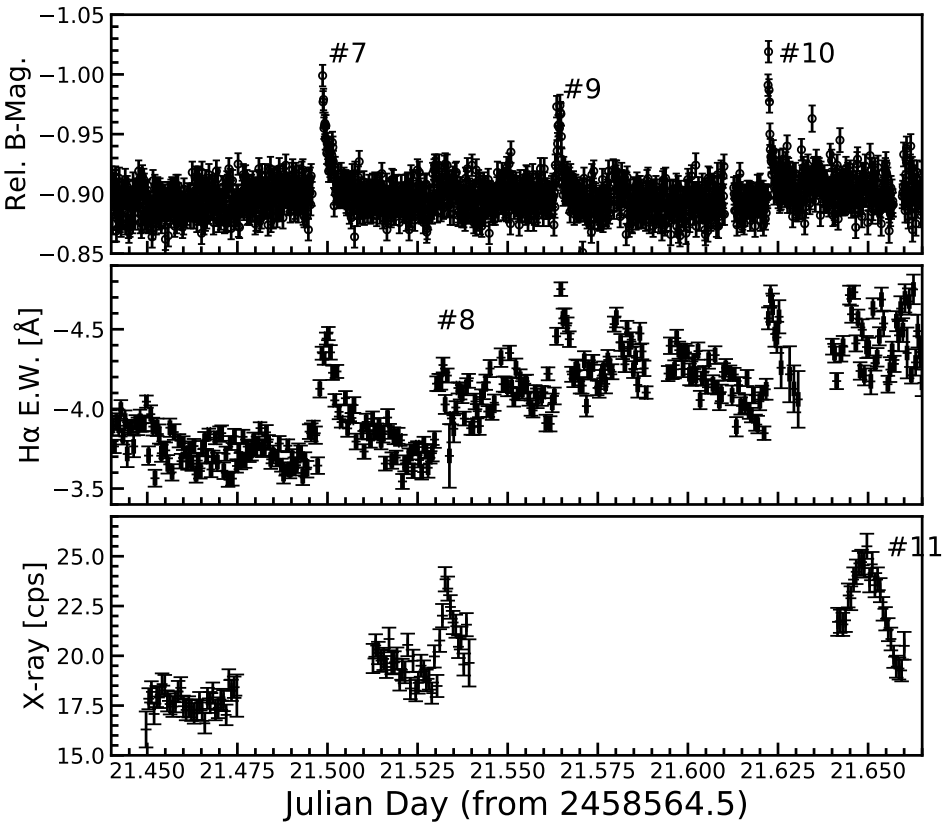


Figure C.1: B-band, H$\alpha$, X-ray light curve during April 12th. The detected flare #7 – #11 are labeled in the figure.

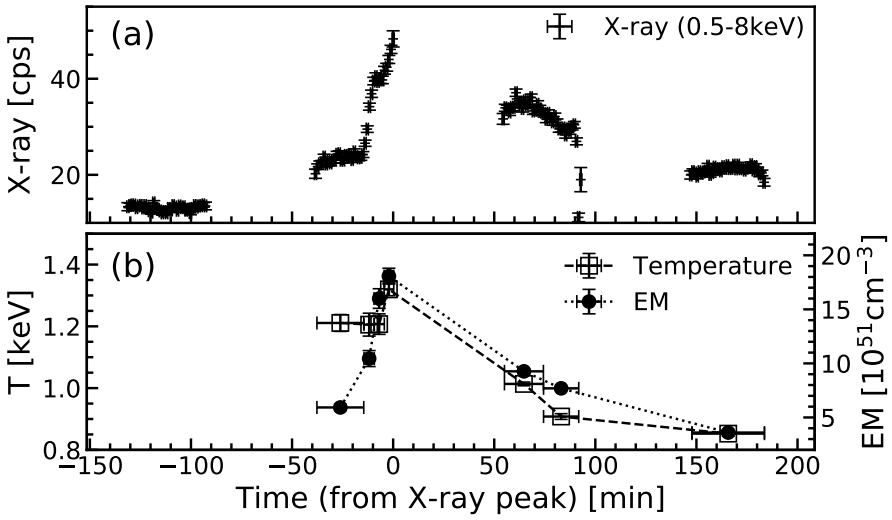


Figure C.2: X-ray large flares (SF #12) detected only with NICER. The panel (a) shows the X-ray light curve (0.5 - 8.0 keV). The panel (b) shows the temporal evolution of emission measure and temperature. The radiated energy in 0.5 - 10 keV band is estimated to be $9.7 \times 10^{31}$ erg.

APPENDIX D

# Supplementary materials in Chapter 6

## D.1 Low-mass companion

Although a faint low-mass companion is reported about 20 AU away from EK-Dra solar-type primary star (projected distance), they are so separated from and believed to be not magnetically coupled with each other Waite et al. (2017). UV stellar flares have been observed on EK Dra so far Audard et al. (1999); Telleschi et al. (2005); Ayres (2015), and they are thought to occur on the solar-type primary star. The absorption of blue-shift component is 1.5 % of the continuum leve while the low-mass companion is as about six magnitudes faint in V-band as the solar-type primary star König et al. (2005); therefore it is unlikely to be explained by the low-mass companion even if the whole continuum levels of the companion star is absorbed. Also, a hypothesis that the mass ejection generated on the low-mass companion passed the solar-type primary star and produce the absorption is rejected considering the difference between the traveling timescale across the projected distance of 20 AU and the short time lag between flares and ejection phenomenon.

Also, the rotational brightness variations would be caused by the solar-type primary star, considering the luminosity differences. The total flare radiated energies are positively related to the spot filling factor changes measured for each *TESS* observational sector (Figure D.1), indicating that superflares are also related to the solar-type primary star.

Figure D.2 shows temporal variations of distance between EK Dra's sky location at each time and pre-flare location in the unit of pixel during the superflare based on the TESS pixel-level photometric data. No centroid motion is observed during this flare, suggesting that it is associated with EK-Dra system rather than an instrumental systematic error or contamination from scattered background light or a distant star.

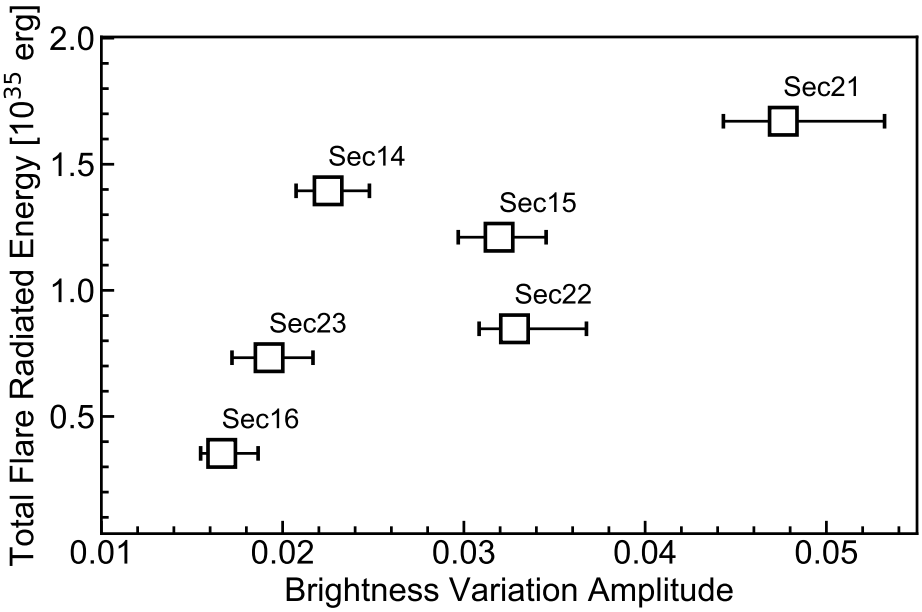


Figure D.1: Total flare radiated energy v.s. brightness variation amplitude on EK Dra. The total flare radiated energy represents the integrated radiated energy for all flares whose energy is more than $10^{33}$ erg during each *TESS*-sector. The brightness modulation amplitude is normalized by the stellar averaged luminosity and it is derived as a difference between its top 95 % and 5% brightness level for each sector.

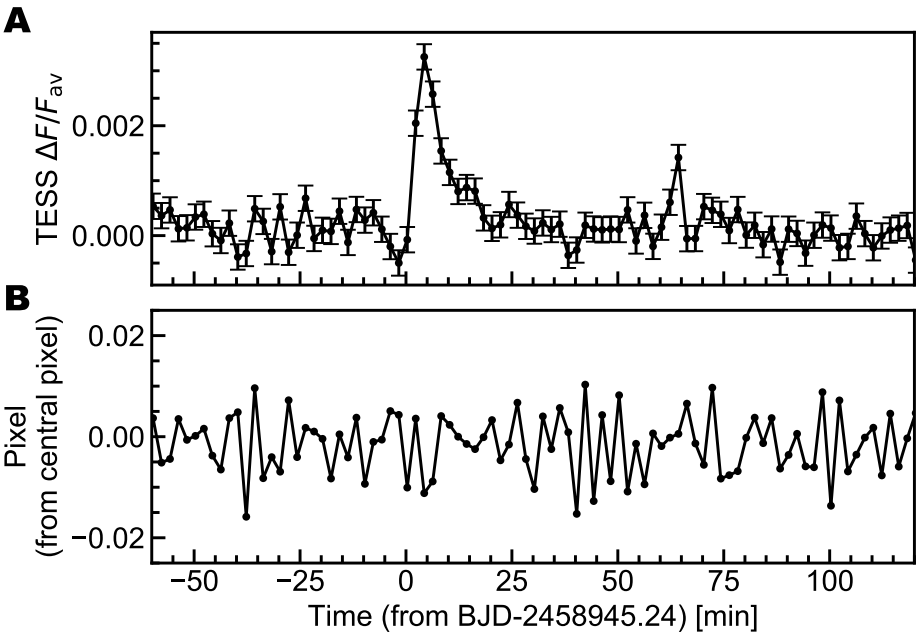


Figure D.2: Light curve and count-weighted central pixel variation during the superflare on EK Dra. **(A)** Optical light curve of the superflare observed by *TESS*. **(B)** Count-weighted central pixel variation during the superflare.

## D.2 Stability of pre-flare spectra

Figure D.3 shows the extended light curve of the superflare and pre-flare brightness on EK Dra. The light curve shows that the pre-flare H$\alpha$ E.W. and continuum level are stable enough to detect the flare emission above the 1-$\sigma$ level in each. The 1-$\sigma$ levels were calculated based on the scattering of E.W. for -150 to 0 min before the flare onsets. The differences of duration between optical and H$\alpha$ flares were not significantly measured by considering the error bars in H$\alpha$ E.W., and the flare evolution on the different emission bands/lines should be investigated in future study as seen in other stellar flare events (Flaccomio et al., 2018).

We obtained the pre-flare template spectra by averaging the 30 frames before the flare started. The periods used for the pre-flare spectra are indicated with black arrows in the Figure D.3A-B. 2-m Nayuta Telescope has a smaller mirror than 3.8-m Seimei Telescope, and it is necessary to use longer periods to make the pre-flare template spectrum. Figure D.4 shows temporal variations of the H$\alpha$ spectra in pre-flare phase on time scales similar to the mass ejection event. The panel shows that the pre-flare H$\alpha$ spectra is quite stable for enough long time. Considering the enough stability of spectra and E.W. in pre-flare phase, we can exclude that the observed variations in the H$\alpha$ profile could be due to background variations of the stellar chromosphere.

## D.3 Time-resolved spectra with higher time cadence

Figure D.5 shows the pre-flare-subtracted H$\alpha$ spectra during and after the superflare on EK Dra with higher time cadence than Figure 6.2E. Basically, the spectra are plotted every 10 min. As for the period during 20 - 50 min, the spectral changes are more dynamic than others as in the light curves in Figure 6.2B, and the spectra are plotted every 5 min. The error bars are plotted on the left side of the each spectrum.

## D.4 Relation between magnetic field structure of EK Dra and mass ejection

Some studies with the Doppler imaging technique showed that there are large star spots around the equator without any polar spots from the observation data in 2015 (Järvinen et al., 2018), and Waite et al. (2017) reported that there is a small polar spot from the observation data in 2015. The polar spot may be related to a possible strong large-scale dipole magnetic field. Zeeman Doppler imaging of EK Dra showed that mean surface magnetic field strength is 66-89 G during 2007-2012 (Waite et al., 2017).

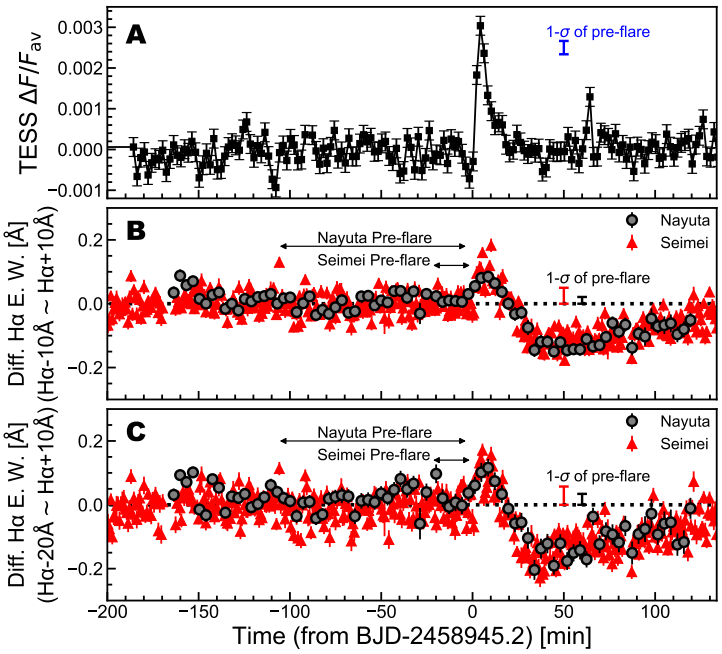


Figure D.3: Light curve of a superflare on EK Dra with longer period than Figure 6.2. **(A)** TESS white-light light curve. The blue point indicates the 1-$\sigma$ value (0.00033) of the pre-flare brightness variation during -150 min – 0 min. **(B)** Light curves of the H$\alpha$ E.W.. The H$\alpha$ emissions were integrated within $\pm$10 Å from the H$\alpha$ line center (6562.8 Å. The black and red error bars indicate the 1-$\sigma$ value (0.050 and 0.021) of the pre-flare light curves observed by Nayuta Telescope/MALLS and Seimei Telescope/KOOLS-IFU, respectively. These error values are measured for -150 min – 0 min. The periods to make the pre-flare reference spectra are also indicated with black arrows in the panel (i.e. 30 frame before the flare onset). **(C)** The panel is basically same as panel **(B)**, but the H$\alpha$ emissions were integrated between 6562.8 - 20 Å and 6562.8 + 10 Å.

It is proposed that the large-scale overlaying strong magnetic fields can suppress the stellar mass ejections (Alvarado-Gómez et al., 2018). Alvarado-Gómez et al. (2018) simulated stellar mass ejections under the large scale magnetic field of 75 G and proposed that the particular large-scale magnetic field configuration establishes a suppression threshold around $\sim 3 \times 10^{32}$ erg in the kinetic energy of mass ejections. Although the similar large scale field is not always prominent for EK Dra as mentioned above, the assumed magnetic field strength $\sim$75 G is similar to the past observations of 66-89 G on EK Dra. If we simply apply the simulation result to our observation, the observed kinetic energy of EK Dra eruption $3.5 \times 10^{32}$ erg is comparable to the suppression threshold $\sim 3 \times 10^{32}$ erg. This may mean that the ejected mass have a potential to escape from the magnetic field suppression, although they can significantly loose the kinetic energy. However, we need to be careful for this discussion because there are no magnetic field maps covering our observation period. The maps of magnetic field and spots depend on the observational periods

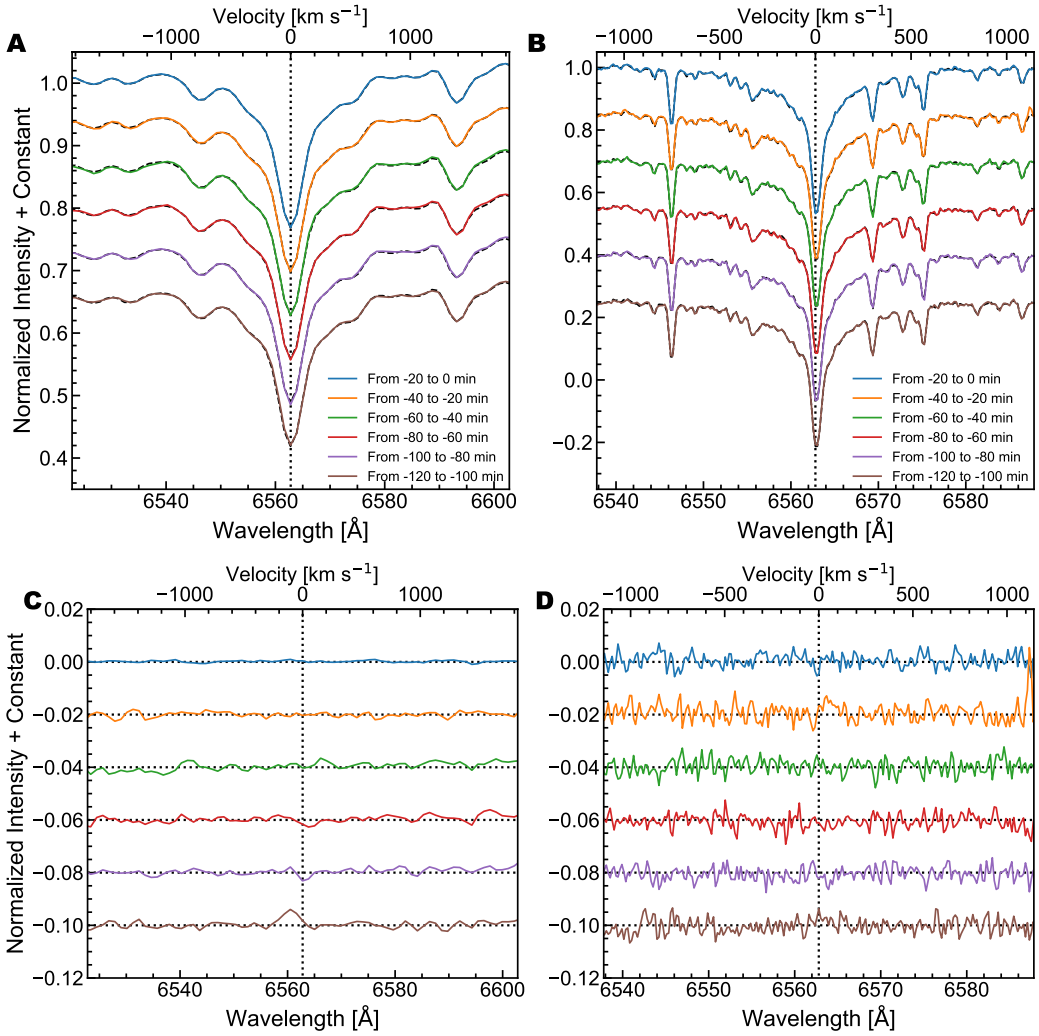


Figure D.4: Time-resolved pre-flare H$\alpha$ spectra observed by Seimei Telescope/KOOLS-IFU (A, C) and Nayuta Telescope/MALLS (B, D). **(A, B)** colored lines indicate pre-flare H$\alpha$ spectra from -120 min to 0 min before the flare starts. Each colored spectrum indicates the averaged spectrum for the periods in the legend. The background black dashed lines are the pre-flare template spectra averaged for the all 30 frames before the flare onset. The frame 1-30 correspond to the observational period indicated with black arrows in Figure D.3 **(B,C)**. The vertical dotted vertical line indicates the line center wavelength (6562.8 Å). **(C, D)** The residual of the pre-flare H$\alpha$ spectra (colored lines in panel **(A, B)**) subtracted by the 30-frames-averaged spectra (black lines in **(A, B)**).

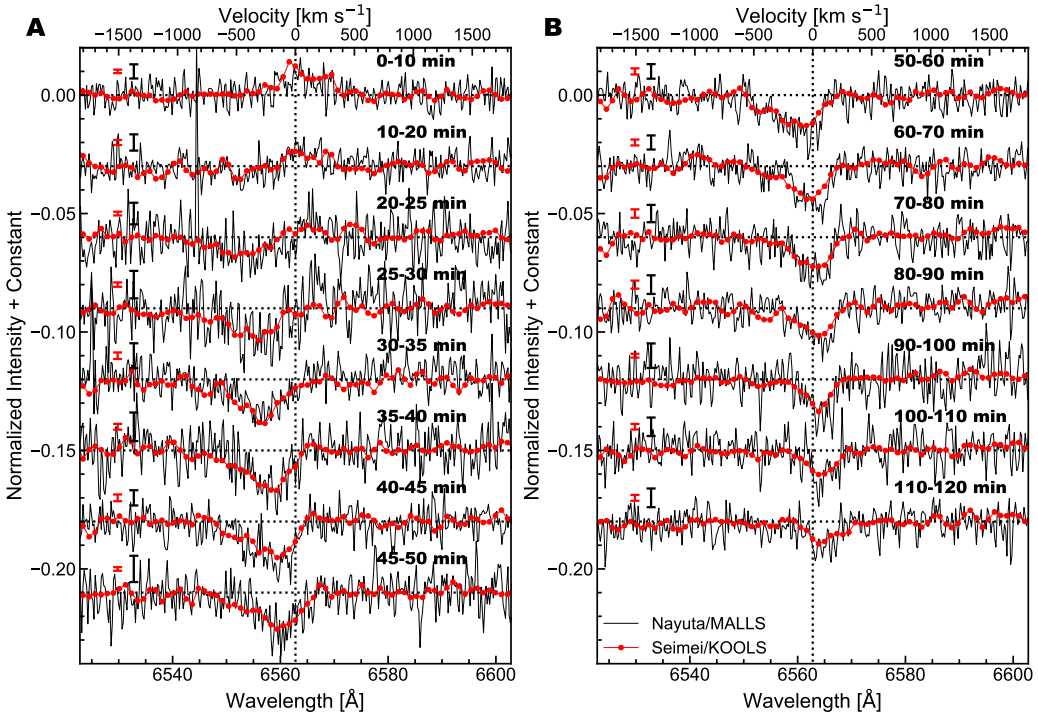


Figure D.5: Pre-flare-subtracted H$\alpha$ spectra during and after the superflare on EK Dra with higher time cadence than panel **(E)** in Figure 6.2. **(A, B)** The red and black lines are the data observed by the Seimei Telescope and the Nayuta Telescope. The spectra are binned in time, and the integration periods correspond to the horizontal axes of panel **(A-D)** in Figure 6.2. The intensities are normalized by the stellar continuum level. The vertical dotted line indicates the H$\alpha$ line center, and the horizontal dotted lines indicate the zero levels for each spectrum. The 1-$\sigma$ values for the line center are indicated with red (Seimei Telescope) and black (Nayuta Telescope) error bars for each time bin. The 1-$\sigma$ values are basically calculated by the scattering in line wing (6522.8 - 6532.8 Å and 6592.8 - 6602.8 Å).

(Järvinen et al., 2018; Waite et al., 2017) probably due to new spot emergence/decay, long-term stellar activity cycles, or stellar differential rotations.

As in Figure 6.1, the superflare occurred near the local brightness maximum, although some of the starspots are expected to be visible from the observer (Waite et al., 2017; Roettenbacher & Vida, 2018; Doyle et al., 2018; Namekata et al., 2020a; Doyle et al., 2020). This may mean that the ejected mass was not suppressed at least by the strong overlaying 'local' magnetic field of large spots.

# Bibliography


Aarnio, A. N., Matt, S. P., & Stassun, K. G. 2012, ApJ, 760, 9, doi: 10.1088/0004-637X/760/1/9

Airapetian, V. S., Glocer, A., Gronoff, G., Hébrard, E., & Danchi, W. 2016, Nature Geoscience, 9, 452, doi: 10.1038/ngeo2719

Airapetian, V. S., Barnes, R., Cohen, O., et al. 2020, International Journal of Astrobiology, 19, 136, doi: 10.1017/S1473550419000132

Allen, J., Frank, L., Sauer, H., & Reiff, P. 1989, EOS Transactions, 70, 1479, doi: 10.1029/89EO00409

Allred, J. C., Hawley, S. L., Abbett, W. P., & Carlsson, M. 2005, ApJ, 630, 573, doi: 10.1086/431751

—. 2006, ApJ, 644, 484, doi: 10.1086/503314

Allred, J. C., Kowalski, A. F., & Carlsson, M. 2015, ApJ, 809, 104, doi: 10.1088/0004-637X/809/1/104

Allred, J. C. e. a. i. p. 2020

Alvarado-Gómez, J. D., Drake, J. J., Cohen, O., Moschou, S. P., & Garraffo, C. 2018, ApJ, 862, 93, doi: 10.3847/1538-4357/aacb7f

Araki, T., & Ikeda, K. 2013, Neural Networks, 43, 33

Argiroffi, C., Reale, F., Drake, J. J., et al. 2019, Nature Astronomy, 3, 742, doi: 10.1038/s41550-019-0781-4

Asai, A., Yokoyama, T., Shimojo, M., et al. 2004, ApJ, 611, 557, doi: 10.1086/422159

Aschwanden, M. J., Xu, Y., & Jing, J. 2014, ApJ, 797, 50, doi: 10.1088/0004-637X/797/1/50

Aschwanden, M. J., Caspi, A., Cohen, C. M. S., et al. 2017, ApJ, 836, 17, doi: 10.3847/1538-4357/836/1/17

Audard, M., Güdel, M., & Guinan, E. F. 1999, ApJL, 513, L53, doi: 10.1086/311907

Aulanier, G., Démoulin, P., Schrijver, C. J., et al. 2013, A&A, 549, A66, doi: 10.1051/0004-6361/201220406

Ayres, T. R. 1997, J. Geophys. Res., 102, 1641, doi: 10.1029/96JE03306

—. 2015, AJ, 150, 7, doi: 10.1088/0004-6256/150/1/7

Baliunas, S. L., Donahue, R. A., Soon, W. H., et al. 1995, ApJ, 438, 269, doi: 10.1086/175072

Balona, L. A., & Abedigamba, O. P. 2016, MNRAS, 461, 497, doi: 10.1093/mnras/stw1443

Basri, G. 2018, ApJ, 865, 142, doi: 10.3847/1538-4357/aade45

Basri, G., & Nguyen, H. T. 2018, ApJ, 863, 190, doi: 10.3847/1538-4357/aad3b6

Bastien, F. A., Stassun, K. G., Basri, G., & Pepper, J. 2016, ApJ, 818, 43, doi: 10.3847/0004-637X/818/1/43

Battersby, S. 2019, Proceedings of the National Academy of Science, 116, 23368, doi: 10.1073/pnas.1917356116

Benz, A. O. 2017, Living Reviews in Solar Physics, 14, 2, doi: 10.1007/s41116-016-0004-3

Benz, A. O., & Güdel, M. 2010, ARA&A, 48, 241, doi: 10.1146/annurev-astro-082708-101757

Berdyugina, S. V. 2005, Living Reviews in Solar Physics, 2, 8, doi: 10.12942/lrsp-2005-8

Berdyugina, S. V., & Usoskin, I. G. 2003, A&A, 405, 1121, doi: 10.1051/0004-6361:20030748

Berger, T. A., Huber, D., Gaidos, E., & van Saders, J. L. 2018, ApJ, 866, 99, doi: 10.3847/1538-4357/aada83

Bogdan, T. J., Gilman, P. A., Lerche, I., & Howard, R. 1988, ApJ, 327, 451, doi: 10.1086/166206

Bonomo, A. S., Hébrard, G., Santerne, A., et al. 2012, A&A, 538, A96, doi: 10.1051/0004-6361/201118323

Bradshaw, S. J., & Hartigan, P. 2014, ApJ, 795, 79, doi: 10.1088/0004-637X/795/1/79

Brasseur, C. E., Osten, R. A., & Fleming, S. W. 2019, ApJ, 883, 88, doi: 10.3847/1538-4357/ab3df8

Brun, A. S., & Browning, M. K. 2017, Living Reviews in Solar Physics, 14, 4, doi: 10.1007/s41116-017-0007-8

Bumba, V. 1963, Bulletin of the Astronomical Institutes of Czechoslovakia, 14, 91

Caballero-García, M. D., Šimon, V., Jelínek, M., et al. 2015, MNRAS, 452, 4195, doi: 10.1093/mnras/stv1565

Canfield, R. C., & Gayley, K. G. 1987, ApJ, 322, 999, doi: 10.1086/165795

Carlsson, M., & Stein, R. F. 1992, ApJL, 397, L59, doi: 10.1086/186544

—. 1995, ApJL, 440, L29, doi: 10.1086/187753

—. 1997, ApJ, 481, 500, doi: 10.1086/304043

—. 2002, ApJ, 572, 626, doi: 10.1086/340293

Carrington, R. C. 1858, MNRAS, 19, 1, doi: 10.1093/mnras/19.1.1

—. 1859, MNRAS, 20, 13, doi: 10.1093/mnras/20.1.13

Carroll, T. A., Strassmeier, K. G., Rice, J. B., & Künstler, A. 2012, A&A, 548, A95, doi: 10.1051/0004-6361/201220215

Chang, S. W., Byun, Y. I., & Hartman, J. D. 2015, ApJ, 814, 35, doi: 10.1088/0004-637X/814/1/35

Chen, F., & Ding, M. D. 2010, ApJ, 724, 640, doi: 10.1088/0004-637X/724/1/640

Chen, P. F. 2011, Living Reviews in Solar Physics, 8, 1, doi: 10.12942/lrsp-2011-1

Cheung, M. C. M., & Isobe, H. 2014, Living Reviews in Solar Physics, 11, 3, doi: 10.12942/lrsp-2014-3

Cheung, M. C. M., Schüssler, M., Tarbell, T. D., & Title, A. M. 2008, ApJ, 687, 1373, doi: 10.1086/591245

Christe, S., Hannah, I. G., Krucker, S., McTiernan, J., & Lin, R. P. 2008, ApJ, 677, 1385, doi: 10.1086/529011

Christian, D. J., Jess, D. B., Antolin, P., & Mathioudakis, M. 2015, ApJ, 804, 147, doi: 10.1088/0004-637X/804/2/147

Cleveland, W. S. 1979, J. Amer. Statist. Assoc., 74, 829

Cliver, E. W., & Dietrich, W. F. 2013, Journal of Space Weather and Space Climate, 3, A31, doi: 10.1051/swsc/2013053

Croll, B. 2006, PASP, 118, 1351, doi: 10.1086/507773

Crosby, N. B., Aschwanden, M. J., & Dennis, B. R. 1993, SoPh, 143, 275, doi: 10.1007/BF00646488

Crosley, M. K., Osten, R. A., & Norman, C. 2017, ApJ, 845, 67, doi: 10.3847/1538-4357/aa7edc

Davenport, J. 2015, PhD thesis, University of Washington

Davenport, J. R. A., Hebb, L., & Hawley, S. L. 2015, ApJ, 806, 212, doi: 10.1088/0004-637X/806/2/212

Davenport, J. R. A., Hawley, S. L., Hebb, L., et al. 2014, ApJ, 797, 122, doi: 10.1088/0004-637X/797/2/122

Désert, J.-M., Charbonneau, D., Demory, B.-O., et al. 2011, ApJS, 197, 14, doi: 10.1088/0067-0049/197/1/14

Dikpati, M., & Charbonneau, P. 1999, ApJ, 518, 508, doi: 10.1086/307269

Ding, M. D., Fang, C., & Yun, H. S. 1999, ApJ, 512, 454, doi: 10.1086/306776

Doyle, L., Ramsay, G., & Doyle, J. G. 2020, MNRAS, 494, 3596, doi: 10.1093/mnras/staa923

Doyle, L., Ramsay, G., Doyle, J. G., Wu, K., & Scullion, E. 2018, MNRAS, 480, 2153, doi: 10.1093/mnras/sty1963

Drake, J. J., Cohen, O., Yashiro, S., & Gopalswamy, N. 2013, ApJ, 764, 170, doi: 10.1088/0004-637X/764/2/170

Dulk, G. A. 1985, ARA&A, 23, 169, doi: 10.1146/annurev.aa.23.090185.001125

Dulk, G. A., & McLean, D. J. 1978, SoPh, 57, 279, doi: 10.1007/BF00160102

Eastwood, J. P., Nakamura, R., Turc, L., Mejnertsen, L., & Hesse, M. 2017, SSRv, 212, 1221, doi: 10.1007/s11214-017-0399-8

Eker, Z. 1994, ApJ, 420, 373, doi: 10.1086/173567

Emslie, A. G., Dennis, B. R., Shih, A. Y., et al. 2012, ApJ, 759, 71, doi: 10.1088/0004-637X/759/1/71

Estrela, R., & Valio, A. 2016, ApJ, 831, 57, doi: 10.3847/0004-637X/831/1/57

Fausnaugh, M. M. e. a. 2020, TESS Data Release Notes: Sector 23, DR32

Favata, F., & Schmitt, J. H. M. M. 1999, A&A, 350, 900. https://arxiv.org/abs/astro-ph/9909041

Feldman, U., Laming, J. M., & Doschek, G. A. 1995, ApJL, 451, L79, doi: 10.1086/309695

Fisher, G. H. 1989, ApJ, 346, 1019, doi: 10.1086/168084

Fisher, G. H., Canfield, R. C., & McClymont, A. N. 1984, ApJL, 281, L79, doi: 10.1086/184290

—. 1985, ApJ, 289, 414, doi: 10.1086/162901

Fisher, G. H., & Hawley, S. L. 1990, ApJ, 357, 243, doi: 10.1086/168911

Flaccomio, E., Micela, G., Sciortino, S., et al. 2018, A&A, 620, A55, doi: 10.1051/0004-6361/201833308

Fletcher, L., & Hudson, H. S. 2008, ApJ, 675, 1645, doi: 10.1086/527044

Forbes, T. G. 2000, J. Geophys. Res., 105, 23153, doi: 10.1029/2000JA000005

Forbes, T. G., & Acton, L. W. 1996, ApJ, 459, 330, doi: 10.1086/176896

Fröhlich, H. E., Frasca, A., Catanzaro, G., et al. 2012, A&A, 543, A146, doi: 10.1051/0004-6361/201219167

Fuhrmeister, B., Lalitha, S., Poppenhaeger, K., et al. 2011, A&A, 534, A133, doi: 10.1051/0004-6361/201117447

Fuhrmeister, B., & Schmitt, J. H. M. M. 2004, A&A, 420, 1079, doi: 10.1051/0004-6361:20035644

Gendreau, K. C., Arzoumanian, Z., Adkins, P. W., et al. 2016, in Society of Photo-Optical Instrumentation Engineers (SPIE) Conference Series, Vol. 9905, Space Telescopes and Instrumentation 2016: Ultraviolet to Gamma Ray, ed. J.-W. A. den Herder, T. Takahashi, & M. Bautz, 99051H, doi: 10.1117/12.2231304

Gershberg, R. E. 2005, Solar-Type Activity in Main-Sequence Stars, doi: 10.1007/3-540-28243-2

Giles, H. A. C., Collier Cameron, A., & Haywood, R. D. 2017, MNRAS, 472, 1618, doi: 10.1093/mnras/stx1931

Gilks, W., R. G. S. S. 1998, Adaptive Markov chain Monte Carlo through regeneration. Journal of the American Statistical Association, 93, 1045

Gnevyshev, M. N. 1938, Izvestiya Glavnoj Astronomicheskoj Observatorii v Pulkove, 16, 36

Gopalswamy, N., Shimojo, M., Lu, W., et al. 2003, ApJ, 586, 562, doi: 10.1086/367614

Graham, D. R., Cauzzi, G., Zangrilli, L., et al. 2020, ApJ, 895, 6, doi: 10.3847/1538-4357/ab88ad

Grosso, N., Montmerle, T., Feigelson, E. D., et al. 1997, Nature, 387, 56, doi: 10.1038/387056a0

Güdel, M. 2007, Living Reviews in Solar Physics, 4, 3, doi: 10.12942/lrsp-2007-3

Guenther, E. W., & Emerson, J. P. 1997, A&A, 321, 803

Gunn, A. G., Doyle, J. G., Mathioudakis, M., Houdebine, E. R., & Avgoloupis, S. 1994, A&A, 285, 489

Hale, G. E. 1908, ApJ, 28, 315, doi: 10.1086/141602

Hale, G. E., Ellerman, F., Nicholson, S. B., & Joy, A. H. 1919, ApJ, 49, 153, doi: 10.1086/142452

Hall, D. S., & Henry, G. W. 1994, International Amateur-Professional Photoelectric Photometry Communications, 55, 51

Harra, L. K., Schrijver, C. J., Janvier, M., et al. 2016, SoPh, 291, 1761, doi: 10.1007/s11207-016-0923-0

Harvey, K. L. 1992, in Astronomical Society of the Pacific Conference Series, Vol. 27, The Solar Cycle, ed. K. L. Harvey, 335

Harvey, K. L., & Zwaan, C. 1993, SoPh, 148, 85, doi: 10.1007/BF00675537

Hastings, W. 1994, International Amateur-Professional Photoelectric Photometry Communications, 57(1), 97

Hathaway, D. H. 2015, Living Reviews in Solar Physics, 12, 4, doi: 10.1007/lrsp-2015-4

Hathaway, D. H., & Choudhary, D. P. 2008, SoPh, 250, 269, doi: 10.1007/s11207-008-9226-4

Hawley, S. L., Davenport, J. R. A., Kowalski, A. F., et al. 2014, ApJ, 797, 121, doi: 10.1088/0004-637X/797/2/121

Hawley, S. L., & Fisher, G. H. 1992, ApJS, 78, 565, doi: 10.1086/191640

Hawley, S. L., & Pettersen, B. R. 1991, ApJ, 378, 725, doi: 10.1086/170474

Hawley, S. L., Fisher, G. H., Simon, T., et al. 1995, ApJ, 453, 464, doi: 10.1086/176408

Hawley, S. L., Allred, J. C., Johns-Krull, C. M., et al. 2003, ApJ, 597, 535, doi: 10.1086/378351

Hayakawa, H., Iwahashi, K., Ebihara, Y., et al. 2017, ApJL, 850, L31, doi: 10.3847/2041-8213/aa9661

Heinzel, P., & Kleint, L. 2014, ApJL, 794, L23, doi: 10.1088/2041-8205/794/2/L23

Heinzel, P., Kleint, L., Kašparová, J., & Krucker, S. 2017, ApJ, 847, 48, doi: 10.3847/1538-4357/aa86ef

Heinzel, P., & Shibata, K. 2018, ApJ, 859, 143, doi: 10.3847/1538-4357/aabe78

Henry, G. W., Eaton, J. A., Hamer, J., & Hall, D. S. 1995, ApJS, 97, 513, doi: 10.1086/192149

Henwood, R., Chapman, S. C., & Willis, D. M. 2010, SoPh, 262, 299, doi: 10.1007/s11207-009-9419-5

Hertzsprung, E. 1924, BAN, 2, 87

Hildner, E., Gosling, J. T., MacQueen, R. M., et al. 1976, SoPh, 48, 127, doi: 10.1007/BF00153339

Hirayama, T. 1974, SoPh, 34, 323, doi: 10.1007/BF00153671

Hodgson, R. 1859, MNRAS, 20, 15, doi: 10.1093/mnras/20.1.15

Holman, G. D., Sui, L., Schwartz, R. A., & Emslie, A. G. 2003, ApJL, 595, L97, doi: 10.1086/378488

Honda, S., Notsu, Y., Namekata, K., et al. 2018, PASJ, 70, 62, doi: 10.1093/pasj/psy055

Hori, K., Yokoyama, T., Kosugi, T., & Shibata, K. 1997, ApJ, 489, 426, doi: 10.1086/304754

Hotta, H., Iijima, H., & Kusano, K. 2019, Science Advances, 5, 2307, doi: 10.1126/sciadv.aau2307

Hotta, H., & Yokoyama, T. 2011, ApJ, 740, 12, doi: 10.1088/0004-637X/740/1/12

Houdebine, E. R., Foing, B. H., Doyle, J. G., & Rodono, M. 1993, A&A, 274, 245

Houdebine, E. R., Foing, B. H., & Rodono, M. 1990, A&A, 238, 249

Hudson, H. S., Acton, L. W., Hirayama, T., & Uchida, Y. 1992, PASJ, 44, L77

Hudson, H. S., Wolfson, C. J., & Metcalf, T. R. 2006, SoPh, 234, 79, doi: 10.1007/s11207-006-0056-y

Hukushima, K., & Nemoto, K. 1996, Journal of the Physical Society of Japan, 65, 1604, doi: 10.1143/JPSJ.65.1604

Hunt-Walker, N. M., Hilton, E. J., Kowalski, A. F., Hawley, S. L., & Matthews, J. M. 2012, PASP, 124, 545, doi: 10.1086/666495

Hurford, G. J., Schmahl, E. J., Schwartz, R. A., et al. 2002, SoPh, 210, 61, doi: 10.1023/A:1022436213688

Hussain, G. A. J., Jardine, M., Donati, J. F., et al. 2007, MNRAS, 377, 1488, doi: 10.1111/j.1365-2966.2007.11692.x

Huttunen, K., & Koskinen, H. 2004, Annales Geophysicae, 22, 1729, doi: 10.5194/angeo-22-1729-2004

Ichimoto, K., & Kurokawa, H. 1984, SoPh, 93, 105, doi: 10.1007/BF00156656

Ichimoto, K., Ishii, T. T., Otsuji, K., et al. 2017, SoPh, 292, 63, doi: 10.1007/s11207-017-1082-7

Ikuta, K., Maehara, H., Notsu, Y., et al. 2020, ApJ, 902, 73, doi: 10.3847/1538-4357/abae5f

Ishii, T. T., Kawate, T., Nakatani, Y., et al. 2013, PASJ, 65, 39, doi: 10.1093/pasj/65.2.39

Isobe, H., Takasaki, H., & Shibata, K. 2005, ApJ, 632, 1184, doi: 10.1086/444490

Isobe, H., Kubo, M., Minoshima, T., et al. 2007, PASJ, 59, S807, doi: 10.1093/pasj/59.sp3.S807

Isobe, T., Feigelson, E. D., Akritas, M. G., & Babu, G. J. 1990, ApJ, 364, 104, doi: 10.1086/169390

Işik, E., Schüssler, M., & Solanki, S. K. 2007, A&A, 464, 1049, doi: 10.1051/0004-6361:20066623

Jain, R., & Sorathia, B. 1987, Journal of Astrophysics and Astronomy, 8, 295, doi: 10.1007/BF02714894

Järvinen, S. P., Strassmeier, K. G., Carroll, T. A., Ilyin, I., & Weber, M. 2018, A&A, 620, A162, doi: 10.1051/0004-6361/201833496

Jejčič, S., Kleint, L., & Heinzel, P. 2018, ApJ, 867, 134, doi: 10.3847/1538-4357/aae650

Jess, D. B., Mathioudakis, M., Crockett, P. J., & Keenan, F. P. 2008, ApJL, 688, L119, doi: 10.1086/595588

Johns-Krull, C. M., & Valenti, J. A. 1996, ApJL, 459, L95, doi: 10.1086/309954

Kahler, S., Golub, L., Harnden, F. R., et al. 1982, ApJ, 252, 239, doi: 10.1086/159551

Kane, S. R. 1974, in Coronal Disturbances, ed. G. A. Newkirk, Vol. 57, 105

Karoff, C., Knudsen, M. F., De Cat, P., et al. 2016, Nature Communications, 7, 11058, doi: 10.1038/ncomms11058

Kasting, J. F., Whitmire, D. P., & Reynolds, R. T. 1993, Icarus, 101, 108, doi: 10.1006/icar.1993.1010

Katsova, M. M., & Livshits, M. A. 2015, SoPh, 290, 3663, doi: 10.1007/s11207-015-0752-6

Kawate, T., Ishii, T. T., Nakatani, Y., et al. 2016, ApJ, 833, 50, doi: 10.3847/1538-4357/833/1/50

Kay, C., Airapetian, V. S., Lüftinger, T., & Kochukhov, O. 2019, ApJL, 886, L37, doi: 10.3847/2041-8213/ab551f

Kerr, G. S., & Fletcher, L. 2014, ApJ, 783, 98, doi: 10.1088/0004-637X/783/2/98

Kippenhahn, R., & Weigert, A. 1990, Stellar Structure and Evolution

Kipping, D. M. 2012, MNRAS, 427, 2487, doi: 10.1111/j.1365-2966.2012.22124.x

Kleint, L., Heinzel, P., Judge, P., & Krucker, S. 2016, ApJ, 816, 88, doi: 10.3847/0004-637X/816/2/88

Koch, D. G., Borucki, W. J., Basri, G., et al. 2010, ApJL, 713, L79, doi: 10.1088/2041-8205/713/2/L79

Koller, F., Leitzinger, M., Temmer, M., et al. 2020, arXiv e-prints, arXiv:2012.00786. https://arxiv.org/abs/2012.00786

König, B., Guenther, E. W., Woitas, J., & Hatzes, A. P. 2005, A&A, 435, 215, doi: 10.1051/0004-6361:20040462

Kopecky, M. 1984, SoPh, 93, 181, doi: 10.1007/BF00156663

Kopparapu, R. K., Ramirez, R., Kasting, J. F., et al. 2013, ApJ, 765, 131, doi: 10.1088/0004-637X/765/2/131

Korhonen, H., Vida, K., Leitzinger, M., Odert, P., & Kovács, O. E. 2017, in Living Around Active Stars, ed. D. Nandy, A. Valio, & P. Petit, Vol. 328, 198–203, doi: 10.1017/S1743921317003969

Kotani, T., Kawai, N., Yanagisawa, K., et al. 2005, Nuovo Cimento C Geophysics Space Physics C, 28, 755, doi: 10.1393/ncc/i2005-10190-5

Kowalski, A. F., Butler, E., Daw, A. N., et al. 2019, ApJ, 878, 135, doi: 10.3847/1538-4357/ab1f8b

Kowalski, A. F., Hawley, S. L., Carlsson, M., et al. 2015, SoPh, 290, 3487, doi: 10.1007/s11207-015-0708-x

Kowalski, A. F., Hawley, S. L., Wisniewski, J. P., et al. 2013, ApJS, 207, 15, doi: 10.1088/0067-0049/207/1/15

Kowalski, A. F., Mathioudakis, M., Hawley, S. L., et al. 2016, ApJ, 820, 95, doi: 10.3847/0004-637X/820/2/95

Kowalski, A. F., Allred, J. C., Uitenbroek, H., et al. 2017, ApJ, 837, 125, doi: 10.3847/1538-4357/aa603e

Kowalski, A. F. e. a. 2020, in preparation

Koyama, K., Hamaguchi, K., Ueno, S., Kobayashi, N., & Feigelson, E. D. 1996, PASJ, 48, L87, doi: 10.1093/pasj/48.5.L87

Kretzschmar, M. 2011, A&A, 530, A84, doi: 10.1051/0004-6361/201015930

Kretzschmar, M., de Wit, T. D., Schmutz, W., et al. 2010, Nature Physics, 6, 690, doi: 10.1038/nphys1741

Kron, G. E. 1947, PASP, 59, 261, doi: 10.1086/125964

Krucker, S., Hudson, H. S., Jeffrey, N. L. S., et al. 2011, ApJ, 739, 96, doi: 10.1088/0004-637X/739/2/96

Kubo, M., Lites, B. W., Shimizu, T., & Ichimoto, K. 2008, ApJ, 686, 1447, doi: 10.1086/592064

Kuhar, M., Krucker, S., Martínez Oliveros, J. C., et al. 2016, ApJ, 816, 6, doi: 10.3847/0004-637X/816/1/6

Künstler, A., Carroll, T. A., & Strassmeier, K. G. 2015, A&A, 578, A101, doi: 10.1051/0004-6361/201525687

Kurita, M., Kino, M., Iwamuro, F., et al. 2020, PASJ, 72, 48, doi: 10.1093/pasj/psaa036

Kusano, K., Iju, T., Bamba, Y., & Inoue, S. 2020, Science, 369, 587, doi: 10.1126/science.aaz2511

Lanza, A. F., Das Chagas, M. L., & De Medeiros, J. R. 2014, A&A, 564, A50, doi: 10.1051/0004-6361/201323172

Lanza, A. F., Netto, Y., Bonomo, A. S., et al. 2019, A&A, 626, A38, doi: 10.1051/0004-6361/201833894

Law, N. M., Fors, O., Ratzloff, J., et al. 2015, PASP, 127, 234, doi: 10.1086/680521

Leenaarts, J. 2020, Living Reviews in Solar Physics, 17, 3, doi: 10.1007/s41116-020-0024-x

Leitzinger, M., Odert, P., Greimel, R., et al. 2014, MNRAS, 443, 898, doi: 10.1093/mnras/stu1161

Lemen, J. R., Title, A. M., Akin, D. J., et al. 2012, SoPh, 275, 17, doi: 10.1007/s11207-011-9776-8

Lin, R. P., & Hudson, H. S. 1976, SoPh, 50, 153, doi: 10.1007/BF00206199

Lin, R. P., Dennis, B. R., Hurford, G. J., et al. 2002, SoPh, 210, 3, doi: 10.1023/A:1022428818870

Lindegren, L., Hernández, J., Bombrun, A., et al. 2018, A&A, 616, A2, doi: 10.1051/0004-6361/201832727

Lingam, M., & Loeb, A. 2017, ApJ, 848, 41, doi: 10.3847/1538-4357/aa8e96

Liu, J. 2001, Monte Carlo strategies in scientific computing. New York: Springer.

Liu, Y., & Kurokawa, H. 2004, ApJ, 610, 1136, doi: 10.1086/421715

Livingston, W. 2002, SoPh, 207, 41, doi: 10.1023/A:1015555000456

MacGregor, M. A., Weinberger, A. J., Wilner, D. J., Kowalski, A. F., & Cranmer, S. R. 2018, ApJL, 855, L2, doi: 10.3847/2041-8213/aaad6b

Machado, M. E., Emslie, A. G., & Avrett, E. H. 1989, SoPh, 124, 303, doi: 10.1007/BF00156272

Machado, M. E., Emslie, A. G., & Mauas, P. J. 1986, A&A, 159, 33

Maehara, H., Notsu, Y., Notsu, S., et al. 2017, PASJ, 69, 41, doi: 10.1093/pasj/psx013

Maehara, H., Shibayama, T., Notsu, Y., et al. 2015, Earth, Planets, and Space, 67, 59, doi: 10.1186/s40623-015-0217-z

Maehara, H., Shibayama, T., Notsu, S., et al. 2012, Nature, 485, 478, doi: 10.1038/nature11063

Maehara, H., Notsu, Y., Namekata, K., et al. 2020, PASJ, doi: 10.1093/pasj/psaa098

Marino, A., Micela, G., Peres, G., & Sciortino, S. 2003, A&A, 407, L63, doi: 10.1051/0004-6361:20031053

Martin, E., H. K. J. S. e. a. 1996, Proceedings of the Second International Conference on Knowledge Discovery and Data Mining (KDD-96). AAAI Press., 226

Martínez Oliveros, J.-C., Hudson, H. S., Hurford, G. J., et al. 2012, ApJL, 753, L26, doi: 10.1088/2041-8205/753/2/L26

Martinez Pillet, V., Moreno-Insertis, F., & Vazquez, M. 1993, A&A, 274, 521

Masuda, S., Kosugi, T., Hara, H., Tsuneta, S., & Ogawara, Y. 1994, Nature, 371, 495, doi: 10.1038/371495a0

Mathur, S., Huber, D., Batalha, N. M., et al. 2017, ApJS, 229, 30, doi: 10.3847/1538-4365/229/2/30

Matsubayashi, K., Ohta, K., Iwamuro, F., et al. 2019, PASJ, 71, 102, doi: 10.1093/pasj/psz087

Matthews, S. A., van Driel-Gesztelyi, L., Hudson, H. S., & Nitta, N. V. 2003, A&A, 409, 1107, doi: 10.1051/0004-6361:20031187

Mauas, P. J. D. 1990, ApJS, 74, 609, doi: 10.1086/191511

McIntosh, P. S. 1981, in The Physics of Sunspots, ed. L. E. Cram & J. H. Thomas, 7–54

McQuillan, A., Mazeh, T., & Aigrain, S. 2014, ApJS, 211, 24, doi: 10.1088/0067-0049/211/2/24

Mein, P., & Mein, N. 1988, A&A, 203, 162

Metropolis, N., Rosenbluth, A. W., Rosenbluth, M. N., Teller, A. H., & Teller, E. 1953, JChPh, 21, 1087, doi: 10.1063/1.1699114

Meyer, F., Schmidt, H. U., Weiss, N. O., & Wilson, P. R. 1974, MNRAS, 169, 35, doi: 10.1093/mnras/169.1.35

Miyake, F., Masuda, K., & Nakamura, T. 2013, Journal of Geophysical Research (Space Physics), 118, 7483, doi: 10.1002/2012JA018320

Miyake, F., Nagaya, K., Masuda, K., & Nakamura, T. 2012, Nature, 486, 240, doi: 10.1038/nature11123

Morin, J., Donati, J. F., Petit, P., et al. 2008, MNRAS, 390, 567, doi: 10.1111/j.1365-2966.2008.13809.x

Morris, B. M., Hebb, L., Davenport, J. R. A., Rohn, G., & Hawley, S. L. 2017, ApJ, 846, 99, doi: 10.3847/1538-4357/aa8555

Moschou, S.-P., Drake, J. J., Cohen, O., et al. 2019, ApJ, 877, 105, doi: 10.3847/1538-4357/ab1b37

Muheki, P., Guenther, E. W., Mutabazi, T., & Jurua, E. 2020a, MNRAS, 499, 5047, doi: 10.1093/mnras/staa3152

—. 2020b, A&A, 637, A13, doi: 10.1051/0004-6361/201936904

Nagai, F. 1980, SoPh, 68, 351, doi: 10.1007/BF00156874

Nagai, F., & Emslie, A. G. 1984, ApJ, 279, 896, doi: 10.1086/161960

Najita, K., & Orrall, F. Q. 1970, SoPh, 15, 176, doi: 10.1007/BF00149484

Namekata, K., Maehara, H., Honda, S., et al. submitted

Namekata, K., Sakaue, T., Watanabe, K., Asai, A., & Shibata, K. 2017a, PASJ, 69, 7, doi: 10.1093/pasj/psw111

Namekata, K., Sakaue, T., Watanabe, K., et al. 2017b, ApJ, 851, 91, doi: 10.3847/1538-4357/aa9b34

Namekata, K., Maehara, H., Notsu, Y., et al. 2019, ApJ, 871, 187, doi: 10.3847/1538-4357/aaf471

Namekata, K., Davenport, J. R. A., Morris, B. M., et al. 2020a, ApJ, 891, 103, doi: 10.3847/1538-4357/ab7384

Namekata, K., Maehara, H., Sasaki, R., et al. 2020b, PASJ, 72, 68, doi: 10.1093/pasj/psaa051

Neidig, D. F. 1989, SoPh, 121, 261, doi: 10.1007/BF00161699

Neupert, W. M. 1968, ApJL, 153, L59, doi: 10.1086/180220

Norton, A. A., Jones, E. H., Linton, M. G., & Leake, J. E. 2017, ApJ, 842, 3, doi: 10.3847/1538-4357/aa7052

Notsu, Y., Honda, S., Maehara, H., et al. 2015a, PASJ, 67, 32, doi: 10.1093/pasj/psv001

—. 2015b, PASJ, 67, 33, doi: 10.1093/pasj/psv002

Notsu, Y., Shibayama, T., Maehara, H., et al. 2013, ApJ, 771, 127, doi: 10.1088/0004-637X/771/2/127

Notsu, Y., Maehara, H., Honda, S., et al. 2019, ApJ, 876, 58, doi: 10.3847/1538-4357/ab14e6

Odert, P., Leitzinger, M., Guenther, E. W., & Heinzel, P. 2020, MNRAS, 494, 3766, doi: 10.1093/mnras/staa1021

O'Hare, P., Mekhaldi, F., Adolphi, F., et al. 2019, Proceedings of the National Academy of Science, 116, 5961, doi: 10.1073/pnas.1815725116

Ohyama, M., & Shibata, K. 1999, in Proceedings of the Nobeyama Symposium, ed. T. S. Bastian, N. Gopalswamy, & K. Shibasaki, 367–370

Oka, M., Phan, T. D., Krucker, S., Fujimoto, M., & Shinohara, I. 2010, ApJ, 714, 915, doi: 10.1088/0004-637X/714/1/915

Okamoto, S., Notsu, Y., Maehara, H., et al. 2020, arXiv e-prints, arXiv:2011.02117. https://arxiv.org/abs/2011.02117

Osten, R. A., Hawley, S. L., Allred, J., et al. 2006, ApJ, 647, 1349, doi: 10.1086/504889

Osten, R. A., & Wolk, S. J. 2015, ApJ, 809, 79, doi: 10.1088/0004-637X/809/1/79

Osten, R. A., & Wolk, S. J. 2017, in Living Around Active Stars, ed. D. Nandy, A. Valio, & P. Petit, Vol. 328, 243–251, doi: 10.1017/S1743921317004252

Otsuji, K., Kitai, R., Ichimoto, K., & Shibata, K. 2011, PASJ, 63, 1047, doi: 10.1093/pasj/63.5.1047

Ozaki, S., & Tokimasa, N. 2005, Annual Report of the Nishi-Harima Astronomical Observatory (ISSN 0917-6926), 15, 15

Parker, E. N. 1955, ApJ, 121, 491, doi: 10.1086/146010

Paulson, D. B., Allred, J. C., Anderson, R. B., et al. 2006, PASP, 118, 227, doi: 10.1086/499497

Petrovay, K., & van Driel-Gesztelyi, L. 1997, SoPh, 176, 249, doi: 10.1023/A:1004988123265

Pettersen, B. R., Coleman, L. A., & Evans, D. S. 1984, ApJS, 54, 375, doi: 10.1086/190934

Poe, C. H., & Eaton, J. A. 1985, ApJ, 289, 644, doi: 10.1086/162928

Priest, E. R. 1981, Solar flare magnetohydrodynamics

Pulkkinen, T. 2007, Living Reviews in Solar Physics, 4, 1, doi: 10.12942/lrsp-2007-1

Rauer, H., Catala, C., Aerts, C., et al. 2014, Experimental Astronomy, 38, 249, doi: 10.1007/s10686-014-9383-4

Reinhold, T., Shapiro, A. I., Solanki, S. K., et al. 2020, Science, 368, 518, doi: 10.1126/science.aay3821

Rempel, M., & Cheung, M. C. M. 2014, ApJ, 785, 90, doi: 10.1088/0004-637X/785/2/90

Rempel, M., & Schlichenmaier, R. 2011, Living Reviews in Solar Physics, 8, 3, doi: 10.12942/lrsp-2011-3

Rich, F. J., & Denig, W. F. 1992, Canadian Journal of Physics, 70, 510, doi: 10.1139/p92-086

Ricker, G. R., Winn, J. N., Vanderspek, R., et al. 2015, Journal of Astronomical Telescopes, Instruments, and Systems, 1, 014003, doi: 10.1117/1.JATIS.1.1.014003

Riley, P., Baker, D., Liu, Y. D., et al. 2018, SSRv, 214, 21, doi: 10.1007/s11214-017-0456-3

Roettenbacher, R. M., & Vida, K. 2018, ApJ, 868, 3, doi: 10.3847/1538-4357/aae77e

Roettenbacher, R. M., Monnier, J. D., Korhonen, H., et al. 2016, Nature, 533, 217, doi: 10.1038/nature17444

Rosner, R., Tucker, W. H., & Vaiana, G. S. 1978, ApJ, 220, 643, doi: 10.1086/155949

Rubenstein, E. P., & Schaefer, B. E. 2000, ApJ, 529, 1031, doi: 10.1086/308326

Rust, D. M., & Bar, V. 1973, SoPh, 33, 445, doi: 10.1007/BF00152432

Rutten, R. J. 2003, Radiative Transfer in Stellar Atmospheres

Saar, S. H., & Linsky, J. L. 1985, ApJL, 299, L47, doi: 10.1086/184578

Sakaue, T., Tei, A., Asai, A., et al. 2018, PASJ, 70, 99, doi: 10.1093/pasj/psx133

Sammis, I., Tang, F., & Zirin, H. 2000, ApJ, 540, 583, doi: 10.1086/309303

Savanov, I. S., & Strassmeier, K. G. 2008, Astronomische Nachrichten, 329, 364, doi: 10.1002/asna.200710963

Schaefer, B. E., King, J. R., & Deliyannis, C. P. 2000, ApJ, 529, 1026, doi: 10.1086/308325

Scherrer, P. H., Schou, J., Bush, R. I., et al. 2012, SoPh, 275, 207, doi: 10.1007/s11207-011-9834-2

Schmieder, B., Forbes, T. G., Malherbe, J. M., & Machado, M. E. 1987, ApJ, 317, 956, doi: 10.1086/165344

Schrijver, C. J. 2020, ApJ, 890, 121, doi: 10.3847/1538-4357/ab67c1

Schrijver, C. J., & Title, A. M. 1999, SoPh, 188, 331, doi: 10.1023/A:1005281526160

Schrijver, C. J., Beer, J., Baltensperger, U., et al. 2012, Journal of Geophysical Research (Space Physics), 117, A08103, doi: 10.1029/2012JA017706

Schrijver, C. J., Kauristie, K., Aylward, A. D., et al. 2015, Advances in Space Research, 55, 2745, doi: 10.1016/j.asr.2015.03.023

Schwartz, P., Jejčič, S., Heinzel, P., Anzer, U., & Jibben, P. R. 2015, ApJ, 807, 97, doi: 10.1088/0004-637X/807/1/97

Schwenn, R. 2006, Living Reviews in Solar Physics, 3, 2, doi: 10.12942/lrsp-2006-2

Segura, A., Walkowicz, L. M., Meadows, V., Kasting, J., & Hawley, S. 2010, Astrobiology, 10, 751, doi: 10.1089/ast.2009.0376

Sharma, S. 2017, ARA&A, 55, 213, doi: 10.1146/annurev-astro-082214-122339

Shibata, K., & Magara, T. 2011, Living Reviews in Solar Physics, 8, 6, doi: 10.12942/lrsp-2011-6

Shibata, K., & Yokoyama, T. 1999, ApJL, 526, L49, doi: 10.1086/312354

—. 2002, ApJ, 577, 422, doi: 10.1086/342141

Shibata, K., Isobe, H., Hillier, A., et al. 2013, PASJ, 65, 49, doi: 10.1093/pasj/65.3.49

Shibayama, T., Maehara, H., Notsu, S., et al. 2013, ApJS, 209, 5, doi: 10.1088/0067-0049/209/1/5

Shimizu, T. 1995, PASJ, 47, 251

Shkolnik, E., Liu, M. C., & Reid, I. N. 2009, ApJ, 699, 649, doi: 10.1088/0004-637X/699/1/649

Silva, A. V. R. 2003, ApJL, 585, L147, doi: 10.1086/374324

Solanki, S. K. 2003, A&A Rv, 11, 153, doi: 10.1007/s00159-003-0018-4

Solanki, S. K., Krivova, N. A., & Haigh, J. D. 2013, ARA&A, 51, 311, doi: 10.1146/annurev-astro-082812-141007

Solanki, S. K., Walther, U., & Livingston, W. 1993, A&A, 277, 639

Strassmeier, K. G. 2009, A&A Rv, 17, 251, doi: 10.1007/s00159-009-0020-6

Strassmeier, K. G., & Bopp, B. W. 1992, A&A, 259, 183

Strassmeier, K. G., Hall, D. S., & Henry, G. W. 1994, A&A, 282, 535

Strassmeier, K. G., Lupinek, S., Dempsey, R. C., & Rice, J. B. 1999, A&A, 347, 212

Svestka, Z. 1976, Solar Flares

Tajima, T., & Shibata, K. 2002, Plasma astrophysics

Takahashi, T., Mizuno, Y., & Shibata, K. 2016, ApJL, 833, L8, doi: 10.3847/2041-8205/833/1/L8

Takasao, S., Matsumoto, T., Nakamura, N., & Shibata, K. 2015, ApJ, 805, 135, doi: 10.1088/0004-637X/805/2/135

Tei, A., Sakaue, T., Okamoto, T. J., et al. 2018, PASJ, 70, 100, doi: 10.1093/pasj/psy047

Telleschi, A., Güdel, M., Briggs, K., et al. 2005, ApJ, 622, 653, doi: 10.1086/428109

Thompson, S., & Caldwell, D. 2016, Kepler Data Release 25 Notes, KSCI-19065-002

Toriumi, S., Hayashi, K., & Yokoyama, T. 2014, ApJ, 794, 19, doi: 10.1088/0004-637X/794/1/19

Toriumi, S., & Hotta, H. 2019, ApJL, 886, L21, doi: 10.3847/2041-8213/ab55e7

Toriumi, S., Schrijver, C. J., Harra, L. K., Hudson, H., & Nagashima, K. 2017, ApJ, 834, 56, doi: 10.3847/1538-4357/834/1/56

Toriumi, S., & Wang, H. 2019, Living Reviews in Solar Physics, 16, 3, doi: 10.1007/s41116-019-0019-7

Tremblay, P. E., & Bergeron, P. 2009, ApJ, 696, 1755, doi: 10.1088/0004-637X/696/2/1755

Tsiropoula, G., & Schmieder, B. 1997, A&A, 324, 1183

Tsuboi, Y., Koyama, K., Murakami, H., et al. 1998, ApJ, 503, 894, doi: 10.1086/306024

Tsuboi, Y., Yamazaki, K., Sugawara, Y., et al. 2016, PASJ, 68, 90, doi: 10.1093/pasj/psw081

Tsuneta, S. 1996, ApJ, 456, 840, doi: 10.1086/176701

Tsuneta, S., Acton, L., Bruner, M., et al. 1991, SoPh, 136, 37, doi: 10.1007/BF00151694

Tsuneta, S., Ichimoto, K., Katsukawa, Y., et al. 2008, SoPh, 249, 167, doi: 10.1007/s11207-008-9174-z

Usoskin, I. G. 2017, Living Reviews in Solar Physics, 14, 3, doi: 10.1007/s41116-017-0006-9

Usoskin, I. G., Kromer, B., Ludlow, F., et al. 2013, A&A, 552, L3, doi: 10.1051/0004-6361/201321080

Uusitalo, J., Arppe, L., Hackman, T., et al. 2018, Nature Communications, 9, 3495, doi: 10.1038/s41467-018-05883-1

Valio, A., Estrela, R., Netto, Y., Bravo, J. P., & de Medeiros, J. R. 2017, ApJ, 835, 294, doi: 10.3847/1538-4357/835/2/294

Van Doorsselaere, T., Shariati, H., & Debosscher, J. 2017, ApJS, 232, 26, doi: 10.3847/1538-4365/aa8f9a

van Driel-Gesztelyi, L., & Culhane, J. L. 2009, SSRv, 144, 351, doi: 10.1007/s11214-008-9461-x

Veronig, A., Temmer, M., Hanslmeier, A., Otruba, W., & Messerotti, M. 2002, A&A, 382, 1070, doi: 10.1051/0004-6361:20011694

Vida, K., Kriskovics, L., Oláh, K., et al. 2016, A&A, 590, A11, doi: 10.1051/0004-6361/201527925

Švestka, Z., Kopecký, M., & Blaha, M. 1962, Bulletin of the Astronomical Institutes of Czechoslovakia, 13, 37

Waite, I. A., Marsden, S. C., Carter, B. D., et al. 2017, MNRAS, 465, 2076, doi: 10.1093/mnras/stw2731

Waldmeier, M. 1955, Ergebnisse und Probleme der Sonnenforschung.

Walkowicz, L. M., Basri, G., & Valenti, J. A. 2013, ApJS, 205, 17, doi: 10.1088/0067-0049/205/2/17

Walter, F. M., & Bowyer, S. 1981, ApJ, 245, 671, doi: 10.1086/158842

Wargelin, B. J., Saar, S. H., Pojmański, G., Drake, J. J., & Kashyap, V. L. 2017, MNRAS, 464, 3281, doi: 10.1093/mnras/stw2570

Warren, H. P. 2006, ApJ, 637, 522, doi: 10.1086/497904

Watanabe, K., Kitagawa, J., & Masuda, S. 2017, ApJ, 850, 204, doi: 10.3847/1538-4357/aa9659

Watanabe, K., Shimizu, T., Masuda, S., Ichimoto, K., & Ohno, M. 2013, ApJ, 776, 123, doi: 10.1088/0004-637X/776/2/123

Webb, D. F., & Howard, T. A. 2012, Living Reviews in Solar Physics, 9, 3, doi: 10.12942/lrsp-2012-3

Weber, M. A., Fan, Y., & Miesch, M. S. 2011, ApJ, 741, 11, doi: 10.1088/0004-637X/741/1/11

Wright, N. J., Drake, J. J., Mamajek, E. E., & Henry, G. W. 2011, ApJ, 743, 48, doi: 10.1088/0004-637X/743/1/48

Xu, Y., Cao, W., Liu, C., et al. 2006, ApJ, 641, 1210, doi: 10.1086/500632

Yamada, Y., Uemura, M., Fukazawa, Y., Tanaka, Y., & Itoh, R. 2017, in Proceedings of the 7th International Fermi Symposium, 30

Yamashiki, Y. A., Maehara, H., Airapetian, V., et al. 2019, ApJ, 881, 114, doi: 10.3847/1538-4357/ab2a71

Yokoyama, T., & Shibata, K. 1998, ApJL, 494, L113, doi: 10.1086/311174

Yuda, S., Hiei, E., Takahashi, M., & Watanabe, T. 1997, PASJ, 49, 115, doi: 10.1093/pasj/49.1.115

Zharkova, V. V., Arzner, K., Benz, A. O., et al. 2011, SSRv, 159, 357, doi: 10.1007/s11214-011-9803-y

Zirin, H., & Liggett, M. A. 1987, SoPh, 113, 267, doi: 10.1007/BF00147707

Zwaan, C. 1987, ARA&A, 25, 83, doi: 10.1146/annurev.aa.25.090187.000503